An exploration of oceanic fine-scale dynamics in the Strait of Gibraltar : numerical simulation, observation, and mixing

Margaux Hilt

To cite this version:

Margaux Hilt. An exploration of oceanic fine-scale dynamics in the Strait of Gibraltar : numerical simulation, observation, and mixing. Ocean, Atmosphere. Université Paul Sabatier - Toulouse III, 2022. English. NNT : 2022TOU30049 . tel-03728144

HAL Id: tel-03728144
https://theses.hal.science/tel-03728144

Submitted on 20 Jul 2022

THÈSE

En vue de l'obtention du

DOCTORAT DE L'UNIVERSITÉ DE TOULOUSE

Délivré par l'Université Toulouse 3 - Paul Sabatier

Présentée et soutenue par

Margaux HILT

Le 8 mars 2022

Exploration des fines échelles océaniques dans le Détroit de Gibraltar: simulation numérique, observation et mélange induit

---

Ecole doctorale : **SDU2E - Sciences de l'Univers, de l'Environnement et de l'Espace**

Spécialité : **Océan, Atmosphère, Climat**

Unité de recherche :
LAERO - Laboratoire d'Aérologie

Thèse dirigée par
Francis AUCLAIR et Franck DUMAS

Jury
M. Jesús GARCíA LAFUENTE, Rapporteur
M. Xavier CARTON, Rapporteur
Mme Maria-Eletta NEGRETTI, Examinatrice
Mme Lucie BORDOIS, Examinatrice
M. Sylvain COQUILLAT, Examinateur
M. Patrick MARCHESIELLO, Examinateur
M. Francis AUCLAIR, Directeur de thèse
M. Franck DUMAS, Co-directeur de thèse

Avant-propos et remerciements

En regardant en arrière, on voit le chemin parcouru et à quel point il a été long. Le constat étant ici, pour tout ce que ce chemin a eu de sinueux, je me retrouve assez loin du point de départ. Bon, je vais arrêter ici la métaphore avant de me retrouver dans le fossé. Le principal c'est que je m'étais dit que je tenterais l'aventure si l'occasion se présentait, et c'est chose faite.

Pour avoir permis l'existence de ce travail scientifique, je tiens d'abord à remercier mon directeur de thèse, Francis Auclair, auprès duquel j'ai beaucoup appris de la rigueur scientifique au cours de ces années et qui m'a fait confiance pour développer mes idées, depuis le stage de fin de master jusqu'à aujourd'hui. Je remercie aussi mon co-directeur, Franck Dumas, avec qui c'était toujours un plaisir d'échanger même si les occasions étaient plus rares. Et un grand merci à Laurent Roblou et Cyril Nguyen, avec qui j'ai beaucoup travaillé, pour toute l'aide qu'ils m'ont apporté dans la réalisation de ce travail.

Merci aux équipes du Laboratoire d'Aérologie pour leur accueil, et d'autant plus pour leur travail durant les confinements. Merci à Sylvain Coquillat d'avoir accepté de présider le jury pour ma soutenance.

Je remercie aussi les autres membres de mon jury de soutenance : Maria-Eletta Negretti pour avoir accepté d'en faire parti et ses retours pour la correction de ce manuscrit ; Lucie Bordois, dont cette thèse est la continuation d'un travail de simulation numérique qu'elle avait amorçé et qui a mis au point la campagne à la mer Gibraltar 2020 ; Yves Morel, Patrick Marchesiello, et Xavier Capet, tous les trois aussi membres de mon commité de thèse, pour leur intérêt sur ce travail et leur exigence ; et enfin mes rapporteurs Xavier Carton et Jesùs García Lafuente d'avoir lu ce manuscrit. Merci Xavier pour tes remarques pertinentes. Thank you Jesùs for reading this manuscript and for all your insight on the Strait of Gibraltar.

Merci Leeko, puis Pauline, puis Sorën, qui ont partagé le bureau A101 avec moi, de la relative fraîcheur de l'hiver toulousain à l'été parfois étouffant. Et merci à tous ces gens que j'ai pu rencontrer, principalement les stagiaires, doctorants et post-doctorants du laboratoire d'Aérologie, dont Azusa, Carlos (et Zoé), Marina, Laurent, Nicolas, Gaëtan, Joris, et tous les autres, pour les bons moments de convivialités passés ensemble. Un merci particulier à Roxane avec qui j'ai partagé une cabine sur l'Atalante (dont des premiers jours mouvementés en mer), aux autres membres de l'équipe scientifique de la campagne Gibraltar 2020, aux hydrographes du SHOM, et bien sûr aux membres de l'équipage.

D'un point de vu plus personnel, merci Alix pour tous nos rendez-vous hebdomadaires, les visites à Nancy ou à Metz, et une virée à la plage de Gruissan. Et merci à mes parents, en particulier à ma mère, Véronique, pour l'hébergement alors que je rédigeais ce manuscrit. Et enfin bravo à mon frère, Jérémy, pour être devenu interne en médecine. Même si je suis 'docteur Hilt' la première, ce sera bientôt ton tour.

Table des matières

Table des Acronymes

ADCP	Acoustic Doppler Current Profiler	
AJ	Atlantic Jet	Jet Atlantique
APE	Available Potential Energy	Énergie potentielle disponible
BPE	Background Potential Energy	Énergie potentielle de référence
CROCO	Coastal & Regional Ocean Community mOdel	
CS	Camarinal Sill	Seuil de Camarinal
CTD	Conductivity, Temperature, and Depth	
EAG	East Alboran Gyre	Gyre est de la mer d'Alboran
EOS	Equation Of State	Équation d'état
ES	Espartel Sill	Seuil d'Espartel
ISW	Internal Solitary Wave	Onde interne solitaire
LAIW	Large Amplitude Internal Wave	Onde Interne de Grande Amplitude
LES	Large Eddy Simulation	Simulation (numérique) des grandes structures turbulentes
LIW	Levantine Intermediate Water	Eau Intermédiaire Lévantine
NACW	North Atlantic Central Water	Eau centrale Nord-Atlantique
PE	(gravitational) Potential Energy	Énergie Potentielle (de gravité)
RHS	Right-Hand Side (term of an equation)	Terme de droite dans une équation
SAR	Synthetic Aperture Radar	
SAW	Surface Atlantic Water	Eau de surface Atlantique
SVD	Singular Value Decomposition	Décomposition en Valeurs Singulières
WAG	West Alboran Gyre	Gyre ouest de la mer d'Alboran
WMDW	West Mediterranean Deep Water	Eau profonde du bassin ouest-Méditerranée

-1- Introduction

1.1 Un voyage en *Terra Incognita* [1]

1.1.1 Dynamique océanique : vers les fines échelles

La dynamique de l'océan est variée, et le *spectre* des processus qui la composent s'étend sur une large gamme autant spatiale que temporelle. La houle, les courants d'Ekman, les systèmes d'upwelling ou de downwelling, les ondes de marée, les marées internes, la convection profonde, les courants de gravité ou encore les panaches fluviaux, en représentent une fraction. Ces processus constituent la réponse de l'océan, vu comme un *système dynamiquement ouvert* à un ensemble de forçages externes : la pression atmosphérique à sa surface, les marées astronomiques, les flux de quantité de mouvement induits par le vent, les flux de chaleur radiatifs, ou les flux de matière par les précipitations, les fleuves ou encore par évaporation, *et cetera*...

Mais l'océan ne se résume toutefois pas non plus à une somme de processus "forcés" dont la combinaison linéaire suffirait à expliquer sa dynamique propre. Ces processus interagissent entre eux induisant d'importants *mécanismes de transferts* de propriétés physiques (par exemple sous forme d'énergie...) et dynamiques (par exemple sous forme d'enstrophie [2]...) entre les différentes gammes d'échelles spatiales et temporelles du spectre. Ces mécanismes sont en partie évoqués ci-après et schématisés dans la Figure 1.1.

Lorsque les transferts prennent spatialement et temporellement une forme cohérente, on parle de *cascades d'échelles* ou de *cascades turbulentes* (Lapeyre, 2000). Les mécanismes débouchant sur ces transferts sont, quant à eux, généralement associés à des *instabilités dynamiques* dont la nature va varier d'une région du spectre spatio-temporelle à l'autre, en particulier car l'effet de la rotation de la Terre sur leur développement n'est pas pris en compte de la même façon selon la taille des structures impliquées.

Ainsi, à méso-échelle [3] (région 1 de la Figure 1.1), la stratification de la colonne d'eau et la rotation du globe terrestre jouent tous deux des rôles prépondérants et peuvent localement être associées à des équations de bilan de quantité de mouvement équilibrées. Ainsi, par exemple, l'action de la rotation de la Terre peut donner à l'océan un comportement de colonnes de Taylor.

A cette échelle, Charney (1971) parle de régime de *turbulence géostrophique* (ou quasi-géostrophique) qui met en jeu instabilités *barotropes* [4] et *baroclines* [5]. Salmon (1980) montre

---

[1] Scotti (2010)

[2] A l'image de l'énergie cinétique pour la vitesse, l'enstrophie est définie comme la moitié du carré de la vorticité relative, i.e. du rotationnel de la vitesse.

[3] Région du spectre constitué d'échelles plus grandes que le premier rayon de Rossby de l'ordre de la dizaine voir de la centaine de kilomètres.

[4] Littéralement "qui ne dépend que de la pression", i.e. dont les surfaces isopycnales sont confondues avec les surfaces isobares.

[5] Qui ne sont pas barotropes

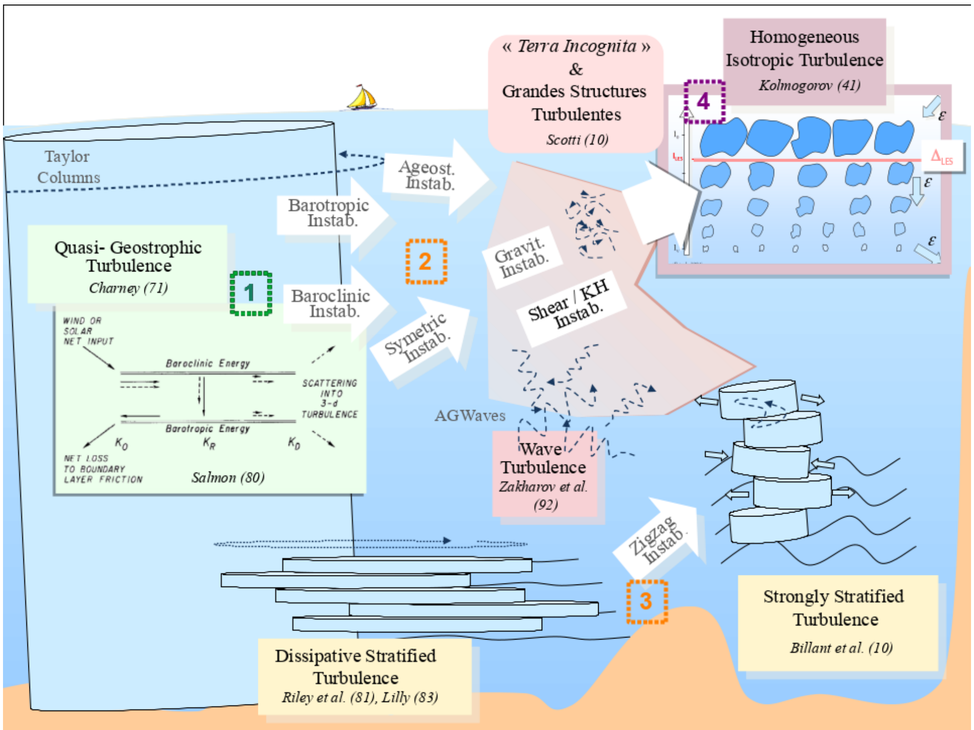

FIGURE 1.1: L'océan vu à travers ses cascades d'échelles, ses instabilités et ses principaux modèles de turbulence. (1) La méso-échelle. (2) et (3) la sous-mésoéchelle. (4) la micro-échelle. Δ_{LES} est l'échelle juste en-deçà des grandes structures turbulentes. D'après Charney (1971); Salmon (1980); Riley et al. (1981); Lilly (1983); Zakharov et al. (1992); Billant et al. (2010); Kolmogorov (1941); Scotti (2010).

que les transferts s'organisent de façon cohérente sous la forme d'une *cascade inverse* associée à des transferts énergétiques barotropes dirigés majoritairement vers de plus grandes échelles dites synoptiques [6]. Les transferts d'enstrophie sont quant à eux majoritairement dirigés vers de plus fines échelles. La cascade inverse demeure toutefois un modèle qualitatif fournissant une grille de lecture pour les processus complexes et "non localisés" du spectre océanique.

Dans la gamme d'échelles spatio-temporelles inférieures, les structures dites de *sous- mésoéchelle* (région 2 sur la Figure 1.1) sont elles aussi sujettes à un large éventail d'instabilités (McWilliams, 2016) : instabilité agéostophique, symétrique, frontale, convective, ou encore instabilités de cisaillement, instabilités baroclines dans la couche de mélange océanique, instabilités paramétriques des ondes internes... Dans cette région du spectre, l'impact de la rotation du globe terrestre est plus faible qu'à mésoéchelle mais la stratification contraint fortement la dynamique océanique, débouchant sur des formes de turbulence dites "stratifiées" (région 3 de la Figure 1.1) : la *turbulence stratifiée dissipative*, la *turbulence fortement stratifiée* (Augier, 2012), avec l'instabilité "zig-zag" faisant office de pont entre ces deux formes de turbulence (Billant et al., 2010).

En deçà de cette sous-mésoéchelle (on parle de *microéchelle*, région 4 de la Figure 1.1), une autre cascade présentant elle-aussi une certaine cohérence peut prendre naissance : la *cascade directe* ou cascade de Richardson. Là, l'énergie est transférée "directement" vers l'échelle de Kolmogorov au-delà de laquelle la dissipation moléculaire est majoritairement active. Si les théories décrivant les transferts à mésoéchelle ne s'accordent pas à montrer de routes directes

---

[6] Une telle cascade "inverse" est caractéristique de régimes de turbulence 2D.

vers la dissipation, les transferts depuis la sous-mésoéchelle le permettent, mais de façon locale et intermittente.

En parallèle de cette route depuis la sous-mésoéchelle, la micro-échelle émerge aussi de la propagation en continue des ondes de gravité internes et des ondes de gravité de surface dans l'océan. L'interaction de ces nombreuses ondes donne lieu à une forme particulière de turbulence, appelée *la turbulence d'onde*. Le déferlement de ces ondes, leurs instabilités donnent généralement naissance à des "patchs turbulents" intermittents annoncés par l'apparition de grandes structures turbulentes.

Ces *grandes structures turbulentes* marquent en effet l'entrée de la cascade directe, elles sont associées à des instabilités de cisaillement telles que les instabilités de Kelvin-Helmholtz. Le reste de la cascade directe à micro-échelle est ensuite décrit par un modèle de turbulence homogène et isotrope 3D. Mais comme les mécanismes entraînant ces instabilités de cisaillement vont être variés les échelles spatiales et temporelles des grandes structures turbulentes ne sont pas clairement définies : elles peuvent atteindre quelques dizaines de mètres au sein de la colonne d'eau (cisaillement au bord d'un courant) mais peuvent aussi ne pas dépasser le mètre dans les couches de surface ou de fond (cisaillement de couches limite).

Cascades d'échelles et modèles de turbulence décrivent ainsi des régions spécifiques du spectre spatio-temporel de l'océan présentant une certaine cohérence. Les instabilités dynamiques tissent quant à elles des ponts entre ces régions. En toute rigueur, comprendre, expliquer, *simuler* (explicitement) ou *modéliser* (implicitement) le mélange turbulent, implique donc évidemment de représenter correctement l'ensemble du spectre océanique, ses transferts, ses cascades... La cascade turbulente directe, i.e. le transfert "inertiel" d'énergie aboutissant à la région "dissipative" du spectre doit faire l'objet d'un soin tout particulier. Le point d'origine de cette cascade au sein du spectre océanique n'est cependant pas clairement défini et la localisation physique de cette cascade varie aussi bien dans le temps que dans l'espace. Seule l'apparition souvent intermittente de grandes structures turbulentes semble permettre de localiser spatialement et temporellement ce point de départ.

A. Scotti (Scotti, 2010), dans une revue sur la modélisation de l'océan, conclut qu'avec l'étude des grandes structures turbulentes, s'ouvrent les portes de la *Terra Incognita*. Il reprend ainsi la conclusion de J.C. Wyngaard (Wyngaard, 2004) rédigée quelques années auparavant pour l'atmosphère. Cette terre inconnue, souvent aussi qualifiée de "zone grise" abritant les *fines échelles océaniques*, est plus largement considérée comme la région particulièrement mal connue du spectre océanique dans laquelle la dynamique peut localement et temporairement basculer d'un équilibre simple entre un nombre limité de processus à une dynamique non-linéaire complexe induisant une cascade (directe) d'instabilités dynamiques aboutissant à la dissipation moléculaire.

1.1.2 Mélange et rétroactions

A l'aboutissement de ces transferts et cascades d'échelles, la dissipation moléculaire va modifier les propriétés du fluide océan, c'est le mélange. Il ne constitue toutefois pas un puits sans fond ou un aller sans retour. Les flux diapycnaux[7] modifient en effet les propriétés thermohalines des masses d'eau, et la dissipation visqueuse près du fond "injecte" de la vorticité potentielle[8]. L'accumulation de telles modifications va *in fine* se répercuter sur la réponse de

---

[7] normal aux surfaces isopycnales

[8] La vorticité potentielle est une quantité, une substance d'après Haynes and McIntyre (1990), essentielle dans la description des écoulements stratifiés en rotation qui est conservée par advection

l'océan à ses forçages et sont donc autant d'exemples de rétroactions sur la grande échelle.

La région du détroit de Gibraltar séparant la mer Méditerranée de l'océan Atlantique est à ce titre tout à fait exemplaire. Il s'agit d'un point de passage entre les deux bassins ; c'est en particulier le point d'entrée de la majorité des eaux qui circulent en Méditerranée, et l'origine de la masse d'eaux méditerranéennes participant à la circulation dans le bassin Nord-Atlantique. Comme indiqué dans le paragraphe suivant, le croisement d'eaux atlantiques et méditerranéennes dans une région géographiquement limitée et à forte amplitude de marée induit un mélange qui va modifier salinité et quantité de mouvement de ces masses d'eau. Il exerce donc un contrôle sur la dynamique de l'ensemble de la mer Méditerranée (Farmer and Armi, 1988), décidant en quelque sorte le régime dynamique de l'ensemble de ce bassin et fixant vraisemblablement le contenu en vorticité potentielle de la veine méditerranéenne en Atlantique Nord.

La dissipation turbulente exerce donc une rétroaction sur les plus grandes échelles du spectre océanique : elle structure les masses d'eau mais aussi la circulation océanique.

1.1.3 Le détroit de Gibraltar [9]

Les talus continentaux, dorsales océaniques, monts sous-marins isolés et autres détroits sont autant d'accidents bathymétriques qui canalisent, perturbent, modifient la circulation générale des masses d'eau océaniques et plus généralement la dynamique de l'océan. Les accidents bathymétriques sont localement le siège de régimes de couches limites particuliers entraînant quasi-systématiquement l'apparition de structures turbulentes très localisées spatialement et ouvrant ainsi les portes de la *Terra Incognita*.

Le détroit de Gibraltar a déjà été cité dans le paragraphe précédent (§1.1.2) comme exemple de région abritant des processus de fines échelles structurant la dynamique océanique de grande échelle. Il constitue l'archétype de l'accident topographique contraignant fortement la dynamique océanique. Le détroit est en effet la seule connexion de la mer Méditerranée à l'océan global. Ses dimensions spatiales sont réduites sur la verticale (de 300 m à 1 km de profondeur seulement) et sur l'horizontale (de l'ordre de la quinzaine de kilomètres entre les côtes marocaines et espagnoles). L'échange de masses d'eaux entrantes et sortantes, dit *échange barocline*, entre les deux bassins méditerranéen et nord-atlantiques est ainsi canalisé. Le croisement de ces deux flux donne un transport net barotrope qui, en moyenne temporelle, est positif pour la Méditerranée et compense l'évaporation annuelle dans ce bassin (Bryden et al., 1994).

La circulation dans le détroit à l'échelle locale ne se résume cependant pas à l'alimentation de la Méditerranée. L'accélération des courants par effet de canalisation par la bathymétrie et les côtes se cumule au courants induits par la marée semi-diurne pour engendrer des courants relativement élevés (de l'ordre de ou dépassant le m/s) qui vont évoluer à l'échelle de l'heure (voire de la demi-heure). En particulier, les courants peuvent être suffisamment élevés pour dépasser la vitesse de propagation de certaines ondes internes de gravité : on dit alors que le *flot est surcritique* (Baines, 1995). La canalisation par la côte et la bathymétrie variant sur de courtes distances, le flot peut passer localement d'un régime sur-critique à sous-critique en modifiant les conditions d'écoulement des eaux atlantiques et méditerranéennes. Au niveau du seuil principal du détroit de Gibraltar, le seuil de Camarinal, une telle transition entraîne la formation puis la relaxation d'un *ressaut hydraulique interne* au cours du cycle de marée (Farmer and Armi, 1988).

Le seuil de Camarinal est l'accident bathymétrique le moins profond du détroit et se présente comme une véritable barrière que les eaux méditerranéennes qui circulent sous les eaux

---

[9] Une revue bibliographique plus détaillée est présentée au Chapitre 4 (§4.2.1).

atlantiques doivent franchir. Une fois franchis cet obstacle, les eaux méditerranéennes s'écoulent vers l'ouest comme un *courant de gravité*. A cet écoulement s'ajoute la dynamique du *ressaut hydraulique interne*, provoquant un mélange fort, local et intermittent des eaux méditerranéennes et atlantiques (Wesson and Gregg, 1994; García-Lafuente et al., 2011).

La relaxation du ressaut hydraulique interne qui a lieu lors de la renverse de marée se fait de surcroît sous la forme d'une onde interne de très grande amplitude qui se propage vers la Méditerranée en évoluant en solibore puis en un train d'ondes solitaires (ou solitons). Ces structures de grande amplitude sont elles-mêmes associées à une augmentation locale du mélange pendant leur propagation mais aussi et surtout lors de leur déferlement (Vlasenko et al., 2009).

La dissipation turbulente est répartie de façon très hétérogène dans la colonne d'eau océanique, souvent préférentiellement dans les couches de surface et de fond et généralement sous la forme d'événements intermittents (on parle de bouffées turbulentes). Ces caractéristiques compliquent grandement sa localisation et sa quantification même si son impact sur la circulation générale est maintenant reconnu et décrit de façon très qualitative (de Lavergne et al., 2017). La région du détroit de Gibraltar offre cependant un terrain d'étude particulièrement pertinent pour qui souhaite explorer cette dissipation turbulente et ses rétroactions. En effet les bouffées turbulentes semblent être associées aux régimes dynamiques présentant de fortes amplitudes de marée (donc facilement localisables dans le temps) et être préférentiellement localisées au-dessus des principaux seuils parsemant le détroit (facilement localisables géographiquement et relativement peu profonds).

Le choix du détroit de Gibraltar comme région d'étude privilégiée pour mes travaux de doctorat se justifie donc à plusieurs titres. Elle est particulièrement adaptée pour une première exploration en *Terra Incognita* puisque les portes ouvrant une voie vers cette terre inconnue semblent y être facilement localisables : des structures turbulentes "intenses" peuvent être plus facilement observables au sein de la colonne d'eau et simulées numériquement de façon explicite. Le détroit de Gibraltar est de plus une région de choix pour mieux appréhender l'impact (la rétroaction) que pourrait imposer la dissipation turbulente sur la circulation générale dans les bassins méditerranéen et nord-atlantique : il s'agit donc d'une région privilégiée pour étudier comment cette dissipation peut structurer la dynamique océanique à beaucoup plus grande échelle.

1.2 Une exploration des fines échelles océaniques

1.2.1 Définir les fines échelles océaniques

Objet central de mes travaux de doctorat, les *fines échelles* océaniques doivent en premier lieu être clairement définies. Jusqu'ici, ces fines échelles ont plus spécifiquement été associées dans notre introduction (§1.1.1) à la région du spectre océanique identifiée comme *Terra Incognita*.

Les fines échelles sont donc définies par la suite comme les échelles spatiales et temporelles de l'ensemble des processus et autres mécanismes dynamiques de *sous-mésoéchelle* (McWilliams, 2016) auxquels s'ajoutent les grandes structures turbulentes qui ouvrent la voie à la cascade directe et marquent l'entrée de la *micro-échelle*.

1.2.2 Les verrous dynamiques et numériques

Toute entrée dans un territoire inconnu tel que la *Terra Incognita* est associée à la reconnaissance et à la levée d'un certain nombre de difficultés. Dans le cas présent, ces "difficultés" prennent la forme de véritables *verrous* d'ordres dynamiques et numériques.

Verrous dynamiques.

Un certain nombre de "verrous" dynamiques peuvent être identifiés. Les grandes structures turbulentes dont il est en particulier question ici sont le résultat de diverses instabilités "primaires" peuplant la méso et la sous-mésoéchelle océaniques : instabilités de type barotrope, barocline, symétrique, zig-zag, agéostrophique, paramétrique des ondes internes, etc... Ces mécanismes de déstabilisation peuvent être vus comme brisant de façon intermittente des structures, des processus, des équilibres subtils régissant localement et de façon parfois éphémère la dynamique de l'océan. Leur exploration relève par conséquent plus d'une approche stochastique que purement déterministe.

Les grandes structures turbulentes elles-mêmes constituent de plus des processus certes importants mais néanmoins indissociables des transferts d'échelles auxquels elles sont associées, et donc de leur localisation dans le spectre spatio-temporel. Ainsi ni les échelles spatiales ni les échelles temporelles des instabilités de cisaillement ne sont clairement identifiables à partir de grandeurs caractéristiques comme le peuvent être les rayons de Rossby pour la méso-échelle et ses instabilités barotropes et baroclines. Leur étude requiert donc la prise en compte simultanée de régions étendues du spectre océanique.

Le mélange turbulent lui-même se présente comme un véritable verrou d'ordre conceptuel. Comment en effet le localiser et le quantifier à partir d'observations ou de simulations numériques ? Quelles grandeurs évaluer ? Comment faire le lien entre les flux turbulents et une évolution diabatique supposée faible de l'énergie potentielle des masses d'eau et de l'énergie cinétique de la circulation ?

Ce lien est généralement représenté par le rapport de ces deux dernières quantités, l'*efficacité du mélange*. Cependant ni la définition, ni la mesure de ces quantités n'est triviale et il n'existe pas encore de consensus parmi les divers approches de mesures, que ce soit dans l'océan réel, en laboratoire, ou en simulations numériques (Gregg et al., 2018).

Concernant l'évaluation de l'évolution de l'énergie potentielle, Lorenz (Lorenz, 1955) a construit un cadre théorique rigoureux depuis maintenant plus d'un demi-siècle. Quelques décennies plus tard Winters et al. (1995) ont proposé un algorithme de calcul basé sur une équation d'évolution de l'énergie potentielle s'appuyant sur un certain nombre d'hypothèses pour certaines assez restrictives (dont un domaine d'application fixe au cours du temps...). L'implémentation de cet algorithme dans un contexte réaliste demeure toutefois un défi tant sur le niveau de précision des calculs requis (pour déterminer une quantité d'amplitude relativement faible telle que le mélange turbulent) que du coût numérique de cet algorithme.

Verrous numériques.

Les grandes structures turbulentes sont traditionnellement prises en charge par les modèles "sous-maille" dans les configurations océaniques côtières, régionales et *a fortiori* globales. N'étant pas universels, ces modèles "sous-maille" rendent leur prise en compte (implicite) très dépendante du lieu et de la période étudiés : les "modèles de fermeture" doivent en effet être ajustés et confrontés à la réalité avec comme principal enjeu le choix du modèle et la détermination des paramètres physiques ou numériques.

Si la mise en place de configurations LES (*Large Eddy Simulation*, ou 'Simulation des Grandes Échelles Turbulentes') est envisageable et peut donc être appuyée sur des modèles "sous-maille" plus universels et plus simples, elle demeure hors d'atteinte pour l'amorce de la cascade directe qui a lieu dans les couches limites de surface et de fond. Dans ces régions, les échelles spatiales caractéristiques des grandes structures turbulentes peuvent en effet considérablement décroître pour être finalement de l'ordre du mètre. La simulation (explicite) de ces échelles particulières est encore inenvisageable du fait de leur coût calcul dans des configurations qui cherchent à représenter des régions océaniques riches de processus variés.

Des *approches hybrides LES / RANS*[10] *dites "zonales"* (Friess, 2010) doivent par conséquent être envisagées afin d'associer une approche LES là où cela est possible avec une approche RANS là où cela est indispensable.

La simulation explicite des grandes structures turbulentes, même partielle, engendre l'utilisation de grilles de calcul à très haute résolution sur des régions océaniques *a priori* relativement étendues. Elle requiert donc un nouvel effort de réduction du coût de calcul et s'inscrit de fait dans le cadre d'approches numériques massivement parallèles associées au *Calcul dit à Hautes Performances (HPC).*

De telles simulations numériques engendrent par ailleurs un grand volume de champs de sorties. Leur traitement demande par conséquent la mise en place de nouveaux outils, précipitant le numéricien dans l'ère du *Big Data* et lui imposant de construire de nouveaux diagnostiques pour localiser et quantifier les processus et les mécanismes de fine échelle (grandes structures turbulentes, flux diapycnaux...).

1.2.3 Simuler explicitement les fines échelles

Explorer numériquement les fines échelles océaniques implique de simuler explicitement les grandes structures turbulentes et l'on entre ainsi de plain-pied dans une approche numérique LES ou plus spécifiquement dans une approche hybride dite "LES zonale" (§1.2.2).

La promesse d'une puissance de calcul pétaflopique puis exaflopique a, en théorie au moins, ouvert les portes de la simulation des grandes structures turbulentes (LES) pour l'océan et l'atmosphère. Les météorologues ont par exemple rapidement pu tirer parti des moyens de calcul disponibles : des algorithmes dédiés ont vu le jour dès le début des années 2000 débouchant sur des codes numériques tels que WRF (Skamarock et al., 2001) en version compressible ou Méso-NH (Lac et al., 2018) en version anélastique. Ces deux types de codes permettent, chacun avec leurs spécificités, d'aborder la simulation de la cascade turbulente directe en représentant explicitement les plus grandes structures turbulentes dans l'atmosphère.

Les modèles océaniques n'ont pas été immédiatement en mesure de franchir le cap de la LES en grande partie à cause de la présence d'une surface libre aux conséquences dynamiques multiples. Cette dernière rend en particulier plus complexe la relaxation de l'hypothèse hydrostatique : elle est en effet parcourue par des ondes de gravité se propageant très rapidement et présentant des dynamiques différentes selon que l'hypothèse "onde longue" (hydrostatique) est, ou non, imposée.

Plusieurs pré-requis ont dus être satisfaits avant de lancer une exploration numérique des

---

[10] Pour Reynolds Averaged Simulations.

grandes structures turbulentes dans un contexte réaliste aussi complexe que celui par exemple du détroit de Gibraltar. Pour ce faire, dans la foulée de l'ANR COMMODO rassemblant au milieu des années 2010 l'ensemble des équipes françaises travaillant sur la modélisation de l'océan, les équipes de recherche en océanographie physique et en mathématiques se sont associées au sein du projet CROCO (www.croco-ocean.org). Un Groupement de Recherche éponyme est né associant les principaux organismes de recherche en informatique et en océanographie français (l'IRD, INRIA, le CNRS-INSU, l'IFREMER et le SHOM) avec l'Université de Toulouse Paul Sabatier. En 2021, l'IRD a entériné la constitution du GdRinternational CROCO (gdri-croco.cnrs.fr) tourné vers les partenaires du projet au Sud.

L'héritage reçu du code américain ROMS (Shchepetkin and McWilliams, 2005) avait fait de CROCO un code particulièrement efficace dont le coeur numérique (time-splitting, schémas numériques...) a été spécifiquement conçu pour limiter les coûts de calcul et l'utilisation de l'espace mémoire. L'hypothèse hydrostatique, elle-aussi héritée du code ROMS, a dû être remise en cause dans le contexte d'un océan à surface libre, et intégré à la séparation des pas de temps (*time splitting*). Ceci fut chose faite en relaxant aussi l'hypothèse de Boussinesq comme préconisé par Auclair et al. (2018), tout en maintenant un bon niveau de performance dans un contexte massivement parallèle.

Afin de s'attaquer à l'ensemble des verrous dynamiques et numériques identifiés, de nouvelles recherches ont été entamées en parallèle de mes travaux de thèse pour (i) porter le code sur une nouvelle génération de processeurs dits hétérogènes (associant processeurs CPU et GPU), (ii) permettre le raffinement local de la dynamique océanique par imbrication de configurations LES dans des maquettes numériques régionales très étendues et (iii) repenser la simulation des grandes structures turbulentes dans un contexte "stochastique" Mémin (2014). Les maquettes que j'ai développées ou co-développées dans le cadre de mes travaux de thèse ont servi durant ces trois années et servent actuellement de configurations-tests pour l'ensemble de ces développements, transformant le détroit de Gibraltar en une véritable région de démonstration.

1.2.4 Où l'on justifie une démarche scientifique pour cette exploration...

Ma thèse s'appuie essentiellement sur des résultats de simulations numériques. En effet, mes travaux ont débouché (i) sur la mise en place et l'évaluation de maquettes réalistes du détroit de Gibraltar en intégrant les évolutions du code CROCO, et (ii) sur la proposition de diagnostics dédiés à l'étude de la fine échelle. En particulier, les maquettes tri-dimentionnelles du détroit de Gibraltar (dites LES zonales) représentent un volume important de données difficile à exploiter et ont fait émerger l'intérêt de diagnostics précis de quantification du mélange diapycnal. La piste choisie pendant ma thèse a été le diagnostique de ce mélange via l'évaluation de l'énergie potentielle dans les simulations numériques, avec un travail de développement important pour l'implémentation dans les cas d'écoulements régionaux à bathymétrie accidentée et à surface libre. Ce travail reste encore évidemment préliminaire et il a vocation à être généralisé dans des configurations de plus en plus sophistiquées.

Un article a d'ores et déjà été publié sur la dynamique bi-dimensionnelle du détroit de Gibraltar (Hilt et al., 2020) et j'ai eu l'occasion de présenter mes résultats sur la dynamique tri-dimensionnelle du détroit lors du colloque international *Ocean Sciences 2020*[11].

Le développement de ces maquettes et des diagnostics associés ont aussi été motivés par la préparation d'une campagne de mesure (PROTEVS GIBRALTAR 2020) *in situ*, à laquelle j'ai

---

[11] https ://hal.archives-ouvertes.fr/hal-02884740v1

eu l'occasion de participer à l'automne 2020.

Mes travaux de thèse s'inscrivent dans une démarche scientifique que j'ai eu à coeur de rendre rigoureuse. Ils s'appuient sur :

— le choix d'une région océanique (le détroit de Gibraltar) présentant une dynamique de fine échelle intense dont la rétroaction sur la grande échelle est particulièrement intéressante,
— la mise en place et l'évaluation de techniques de simulation numérique originales en conditions océaniques réalistes associées à la LES zonale,
— le développement d'outils diagnostiques dédiés à la dynamique de fine échelle,
— l'évaluation des résultats numériques à partir d'observations via des allers-retours entre l'océan réel et l'océan numérique,
— le tout dans le contexte d'un travail d'équipe s'inscrivant dans le cadre du Groupement de Recherche CROCO.

1.3 Plan du manuscrit

Le Chapitre 2 présente le *modèle d'océan* sur lequel s'appuie ma thèse. Ce modèle est classiquement basé sur la conservation de la masse, de la quantité de mouvement, de la chaleur et des traceurs. En particulier, le passage à un système de coordonnées curvilignes est adressé. Le modèle CROCO pour la simulation numérique de l'océan régional et/ou côtier est aussi présenté dans ce chapitre.

Les simulations numériques des fines échelles du détroit de Gibraltar sont présentées dans les Chapitres 3 et 4. Elles sont abordées tout d'abord dans un modèle simplifié à deux dimensions dans le Chapitre 3, constitué d'un article publié au cours de mes années de thèse (Hilt et al., 2020). Le Chapitre 4 poursuit cette démarche de simulation numérique en proposant une maquette océanique réaliste tri-dimensionnelle. Le Chapitre 4 présente aussi l'analyse d'un premier jeu d'observations issues de la campagne de mesures PROTEVS Gibraltar 2020.

Enfin, dans un dernier Chapitre 5, sont présentés les derniers travaux menés à bien pendant ma thèse avec plusieurs applications d'un algorithme dédié à la quantification et à la localisation du mélange turbulent. Ces applications se font graduellement vers des cas de plus en plus réalistes, jusqu'à celui de la simulation 2D du détroit de Gibraltar présentée au Chapitre 3.

-2- Vers une simulation des grandes structures turbulentes (LES [1])

2.1 Résumé en français

Le présent chapitre présente de façon détaillée le *modèle d'océan* utilisé dans le cadre de ma thèse pour simuler numériquement les grandes échelles turbulentes (ou LES[1]) dans la région du détroit de Gibraltar mais aussi, plus généralement, pour développer des modèles analytiques simplifiés de processus au service de cette approche numérique. Plusieurs sections du chapitre ont été intégrées à des publications acceptées (Hilt et al., 2020), (Auclair et al., 2021a) ou en cours de rédaction (Auclair et al., 2021b) mais aussi au rapport d'études du programme amont PROTEVS Gibraltar du SHOM (Auclair et al., 2019). L'ensemble du chapitre est par conséquent rédigé en anglais.

Dans une première partie (§2.2) sont introduites les équations de conservations usuelles de l'océanographie physique, dont les équations de Navier-Stokes, point de départ du développement du *modèle d'océan*. Le choix est ensuite fait de se placer dans le contexte d'une grille verticale curviligne qui permet d'épouser la forme des fonds marins et de suivre les mouvements de la surface libre de l'océan (dont un certain nombres de développements ont aussi présentés en Annexe 2.5.1).

Dans la deuxième partie du chapitre (Section 2.3), est présenté le fonctionnement du code communautaire à cœur non-hydrostatique, compressible et à surface libre CROCO, basé sur le *modèle d'océan* de la première partie. L'implémentation numérique de ce *modèle d'océan* a demandé d'importants développements tant algorithmiques que numériques, développements qui ne peuvent être menés à bien s'ils miment directement la physique de l'océan. Parce qu'il est très général, ce *modèle d'océan* peut réaliser la synthèse de processus dynamiques dans une gamme très étendue d'échelles spatio-temporelles depuis la circulation basse fréquence, jusqu'aux ondes acoustiques. Ce sont plus spécifiquement les plus fines échelles et les plus hautes fréquences qui peuvent imposer les plus fortes restrictions à l'approche numérique envisagée ; ce sont donc les processus associés et en particulier les processus ondulatoires acoustiques ou gravitaires qui ont été étudiés en priorité.

J'ai participé à une partie des développements de CROCO durant ma thèse, sur le plan purement numérique tout d'abord, avec l'implémentation et l'évaluation de nouveaux schémas numériques dans un contexte pleinement réaliste et la mise en œuvre de stratégies originales pour la LES. Sur le plan de la dynamique océanique ensuite, avec la réalisation d'études de processus de fines échelles et l'étude des interactions complexes entre ces processus.

En parallèle des développements numériques et des travaux sur la dynamique de la région du détroit de Gibraltar menés dans le cadre de la présente thèse de doctorat, a été développé et

---

[1] LES : Large Eddy Simulation.

publié un modèle analytique suffisamment général pour décrire la dispersion des ondes et des modes acoustiques, des ondes et des modes internes de gravité ou encore des ondes de gravité de surface (Auclair et al., 2021a). Le modèle analytique de dispersion a de plus été utilisé pour explorer la dynamique ondulatoire dans la région du détroit de Gibraltar. J'ai participé et co-signé cette étude en support du développement numérique de CROCO, étude qui n'a pas été incluse dans le présent manuscrit.

2.2 A non-hydrostatic, compressible, free-surface ocean model

2.2.1 Continuous free-surface compressible equations in z-coordinates

Model equations in conservative form

Conservation of mass, conservation of momentum (Newton's second law of motion), conservation of total energy (first law of thermodynamics) and conservation of any tracers are the backbones of ocean dynamics. In the ocean, the conservation of mass can be written as a prognostic equation for density (written ρ), the conservation of momentum leads to prognostic equations for the three components of momentum (written $\rho\mathbf{v}$) and the conservation of total energy (or first law of thermodynamics) can be stated as a prognostic equation for potential temperature (θ). The conservation of chemical species can then be expressed as a prognostic equation for salinity (S). These conservation equations consequently lead to the following general system of prognostic equations (expressed in flux form) :

$$\frac{\partial \rho}{\partial t} = -\nabla \cdot (\rho \mathbf{v}) \tag{2.2.1a}$$

$$\frac{\partial \rho \mathbf{v}}{\partial t} = -\nabla \cdot (\rho \mathbf{v} \otimes \mathbf{v}) - 2\rho\, \mathbf{\Omega} \times \mathbf{v} - \nabla p + \nabla \cdot \Big(\mu(\nabla \mathbf{v} + \nabla \mathbf{v}^{\,T}) + \mu_2 (\nabla \cdot \mathbf{v})\, \mathbf{I}\Big) + \rho \mathbf{g} \tag{2.2.1b}$$

$$\frac{\partial \rho \theta}{\partial t} = -\nabla \cdot (\rho \theta \mathbf{v}) + \nabla \cdot (\kappa_\theta \nabla \theta) \tag{2.2.1c}$$

$$\frac{\partial \rho S}{\partial t} = -\nabla \cdot (\rho S\, \mathbf{v}) + \nabla \cdot (\kappa_S \nabla S) \tag{2.2.1d}$$

with μ, μ_2, κ_T and κ_S respectively the dynamical and bulk viscosities and the thermal and salt diffusivities. $\mathbf{\Omega}$ is the earth instant rotation vector. Assuming that variables are in thermodynamic equilibrium, the equation of state (EOS) can be formulated as a non-linear, diagnostic functional relation between temperature, salinity, density and (total) pressure (written p) :

$$\rho = \rho_{eos}[\theta, S, p] \tag{2.2.2}$$

Boundary conditions

The position of the interface separating the ocean and the atmosphere must additionally be calculated and is introduced as a boundary condition. This can be achieved by stating that a salty-water particles that is just below this interface in the ocean, remains at the interface, leading to the surface kinematic relation :

$$\frac{\partial \zeta}{\partial t} = w(\mathbf{x}_{\scriptscriptstyle H}, z = \zeta) - \mathbf{v}_H(\mathbf{x}_{\scriptscriptstyle H}, z = \zeta) \cdot \nabla_H \zeta \tag{2.2.3}$$

where ζ is the free-surface anomaly in the vicinity of the geoid and subscribe H indicates that only the horizontal component is considered. Assuming then no-slip condition and that ocean water cannot penetrate the ocean bottom (at depth $z = -H$) :

$$\mathbf{v}(\mathbf{x}_H, z = -H) = \mathbf{0} \tag{2.2.4}$$

Neglecting surface-tension pressure drop, the boundary condition for pressure at the surface of the ocean is given by :

$$p(\mathbf{x}_H, z = \zeta, t) = p_{atm} \tag{2.2.5}$$

with p_{atm} the atmospheric pressure above the surface of the ocean. The resulting system of prognostic equations, diagnostic relations and boundary conditions leads to a non-linear problem whose main characteristics is the wild spectrum of dynamic processes involved (see for instance Gill (1982) or Vallis (2006)). Periodic processes such as ocean waves can give a comprehensive overview of the extension of space-time spectrum of transient processes which can propagate in the ocean and Auclair et al. (2021a) derive a compressible, free-surface, stratified model of two dispersion relations for wave-numbers and pulsation gathering acoustic, surface and internal waves and insisting on the modification of the dispersion of gravity (acoustic) waves by compressibility (gravity and stratification).

Formulated thus, the system of Navier-Stokes and conservation equations for a free-surface ocean can, at least in theory, be integrated straightforwardly. All variables but the pressure have their own prognostic equation and pressure can be diagnosed from the equation of state 2.2.2. Note that the system can be reformulated so that pressure is also given by a prognostic equation.

Evolution of the density field for a Boussinesq fluid

For a linear approximation of the equation of state used in a Boussinesq framework (incompressible fluid), a simple evolution equation of ρ can be obtained as a combination of Equations 2.2.1c and 2.2.1d leading to :

$$\frac{d\rho}{dt} = \nabla \cdot (\kappa_\rho \nabla \rho) \tag{2.2.6}$$

where κ_ρ is the equivalent diffusivity of density.

2.2.2 Terrain-following coordinates

Definition

The capacity of numerical models to mimic the evolution of global or regional oceanic circulation relies on horizontal and vertical definition of the grid on which the Navier-Stokes and conservation equations previously defined are solved and integrated in time.

Due to considerations of the representation of bathymetric features and free-surface evolution, terrain-following coordinates, or S-coordinates, are chosen for the vertical discretization. They are generally defined on generalized constant-s surfaces with s given by :

$$s = s(x, y, z, t) = s(\mathbf{x}, t) \tag{2.2.7}$$

requiring thus that s be a monotonic function of the vertical coordinate z :

$$\left.\frac{\partial s}{\partial z}\right|_{xyt} \neq 0 \tag{2.2.8}$$

$\partial s/\partial z$ is continuous and single-signed (either strictly positive or negative).

Examples

Several examples and comparisons on the choice of $s(\mathbf{x}, t)$ are given in chapter 6 of Griffies (2004). Following Shchepetkin and McWilliams (2005), less general σ-coordinates can be defined by :

$$z(\mathbf{x}, \sigma, t) = \sigma H(\mathbf{x_h}) \quad or \quad z(\mathbf{x}, \sigma, t) = \sigma(H(\mathbf{x_h}) + \zeta(\mathbf{x_h}, t)) + \zeta(\mathbf{x_h}, t) \tag{2.2.9}$$

where $H(\mathbf{x_h}) = H(\mathbf{x}, \mathbf{y})$ is the bottom topography and $\zeta(\mathbf{x_h}, t)$ the surface elevation anomaly. Its generalization to s-coordinates is defined by :

$$z(\mathbf{x}, s, t) = \mathcal{S}(s) H(\mathbf{x_h}) \tag{2.2.10}$$

which is currently written :

$$z(\mathbf{x}, \sigma, t) = \mathcal{S}(\sigma) H(\mathbf{x_h}) \tag{2.2.11}$$

and $S(\sigma)$ can be a non-linear function. Some current definitions are presented on the Wiki-Roms web-site[2].

Vertical velocities

The definition of such a new vertical coordinate requires the derivation of the associated vertical velocity at the grid point. Using the coordinate transformation presented in Section 2.5.1 of Appendix 2.5, $w \equiv v_z$ can be decomposed as :

$$\begin{aligned}
v_z &\equiv \frac{dz}{dt} && \text{(2.2.12a)}\\
&= \underbrace{\underbrace{\left.\frac{\partial z}{\partial s}\right|_{tx}}_{\equiv h} \frac{ds}{dt}}_{\equiv v_s} + \underbrace{\left.\frac{\partial z}{\partial x}\right|_{ts} \underbrace{\frac{dx}{dt}}_{\equiv u} + \left.\frac{\partial z}{\partial t}\right|_{xs} \underbrace{\frac{dt}{dt}}_{=1}}_{=\left.\frac{dz}{dt}\right|_s} && \text{(2.2.12b)}\\
&= \left.\frac{\partial z}{\partial s}\right|_{tx} \frac{ds}{dt} + \left.\frac{dz}{dt}\right|_s && \text{(2.2.12c)}\\
&= h\frac{ds}{dt} \quad + \left.\frac{dz}{dt}\right|_s && \text{(2.2.12d)}\\
&= v_s \quad + \underbrace{\left.\frac{\partial z}{\partial t}\right|_{xs} + u\left.\frac{\partial z}{\partial x}\right|_{ts}}_{\left.\frac{dz}{dt}\right|_s = v_{\Sigma,z}} && \text{(2.2.12e)}
\end{aligned}$$

where :

$$h \equiv \left.\frac{\partial z}{\partial s}\right|_{tx} \quad \text{and} \quad v_s \equiv h\frac{ds}{dt} \tag{2.2.13}$$

In other words, the vertical velocity is the composition of $v_{\Sigma,z}$ (the vertical component of the velocity of the constant-s surface as it moves), and v_s (the velocity through this same surface).

---

[2] `https://www.myroms.org/wiki/Vertical_S-coordinate`

An important aspect of this computation is that v_s remains a velocity along the vertical axes since no change of direction of the axes is made.

In the more restrictive case where σ-coordinates are used :

$$\sigma = \frac{z-\zeta}{H+\zeta} \tag{2.2.14}$$

and as a consequence :

$$v_z = w = \mathbf{u}_z.\mathbf{v} = \frac{dz}{dt} = \underbrace{(H+\zeta)\frac{d\sigma}{dt}}_{\equiv v_\sigma} + (\sigma-1)\frac{dH}{dt} + \sigma\frac{d\zeta}{dt} \tag{2.2.15}$$

where in σ-coordinates :

$$v_\sigma = (H+\zeta)\frac{d\sigma}{dt} \tag{2.2.16}$$

2.3 CROCO : a numerical implementation of the non-hydrostatic, compressible, free-surface *ocean model*

2.3.1 From Boussinesq, hydrostatic models to a compressible, non-hydrostatic kernel

Ocean models whether dedicated to global, regional or even coastal scales are traditionally based on the Boussinesq, hydrostatic assumptions (Griffies, 2012; Shchepetkin and McWilliams, 2005). The present study is a step toward the explicit simulation of at least the largest turbulent eddies in a realistic context and, as a consequence, a non-hydrostatic numerical approach is required. Auclair et al. (2018) concluded that an efficient non-hydrostatic, free-surface, mode-splitting numerical model of the ocean could be designed relaxing also the Boussinesq approximation. Doing so, the authors chose to work with local equations and they do not solve for a 3D Poisson equation to diagnose total pressure. They consequently follow the choices made in meso-scale atmospheric modeling by Skamarock et al. (2001). The compressible (non-Boussinesq) approach is original in ocean modeling and in particular in free-surface, ocean modeling. Indeed Marshall et al. (1997) or Auclair et al. (2011) chose to retain the Boussinesq assumption. A consequence of Auclair et al. (2018)'s choice is that the complete *ocean model* presented in §2.2 can be solved numerically.

The computing cost of such a non-hydrostatic, compressible, free-surface approach can quickly become prohibitive especially because the explicit modeling of fine scales requires high-resolution grids. Following the conclusions of the COMODO french community[3], the compressible and free-surface algorithm developed by Auclair et al. (2018) has been implemented in the ROMS-AGRIF branch of the ROMS ocean models (Shchepetkin and McWilliams, 2005). This choice was justified by the great efficiency of Shchepetkin's time-splitting and time-stepping and more generally by the experience accumulated in ROMS community during the last two decades.

The simulations of the strait of Gibraltar presented in Chapters 3 and 4 were the very first realistic implementation of the non-hydrostatic, compressible, free-surface kernel of CROCO (Hilt et al., 2020).

---

[3] COMODO gathered the french ocean modeling community. It was sponsored by the French ANR eponymous project (2011-2016).

2.3.2 Time-splitting

Dynamical time-scales

Numerical constraints can conveniently be enumerated in terms of time-scales of dynamical "transfers" of tracer, pressure or velocity anomalies in the ocean. Advection, diffusion or radiation by gravity or acoustic waves are examples of such transfers. For a given length-scale (such as a model grid scale), maximum characteristic velocities can give an order of magnitude for the most restrictive time-scales for each type of "transfer".
To derive the main characteristic length scales, the pressure and density anomalies are first conveniently defined with respect to the hydrostatic rest state leading to the pressure decomposition :

$$p(\mathbf{x},t) = p_h(\mathbf{x},t) + \delta p(\mathbf{x},t) \tag{2.3.1}$$

with $p_h(\mathbf{x},t)$ the hydrostatic pressure component and $\delta p(\mathbf{x},t)$ an anomaly. The former is defined by $\partial_z p_h = -\rho_h(\mathbf{x},t)g$ where $\rho_h(\mathbf{x},t)$ can be chosen as the slowly-varying, statically-stable field of density. Based on this pressure decomposition, a first-order Taylor expansion of the density field can be carried out :

$$\rho(T,S,p) = \rho_{\theta S}(T,S,p_0) + \frac{p_h + \delta p - p_0}{c_s^2} + O(\delta p^2) \tag{2.3.2}$$

for a reference, slow component of pressure p_0 which is most often chosen different from the hydrostatic pressure in numerical models. Numerical constraints relative to the various transfers of anomalies can basically be classified into three categories depending if they are associated to compressibility (acoustic waves..), surface-induced processes (surface gravity waves...) or internal-ocean (incompressible) processes (internal gravity waves, advection, diffusion, buoyancy-induced processes...). Orders of magnitude of maximum velocities in a deep ocean of each category are respectively given by $v[\delta p] \approx O(1500\ m/s)$, $v[p_\zeta] \approx \sqrt{gH} \approx O(100\ m/s)$ and $v[p_{int},\ ...] \approx O(1\ m/s)$ leading to at least two spectral gaps in terms of velocities in the ocean :

$$v[p_{int},\ ...] \ll v[p_\zeta] \ll v[\delta p] \tag{2.3.3}$$

This hierarchy of velocity scales (and thus timescales for a fixed grid-scale) and the associated gaps constitute the basis to develop time-splitting approaches for numerical models of the ocean. Under free-surface, Boussinesq and hydrostatic assumptions, the time-splitting procedure implemented in ROMS model (Shchepetkin and McWilliams, 2005) filters for instance acoustic and non-hydrostatic processes and takes advantage of the gap $v[p_{int},\ ...] \ll v[p_\zeta]$. It can be formulated as a decomposition of the pressure between a 2D surface-induced pressure-component (named external or barotropic-like component) $\bar{p}_h(\mathbf{x},t)$ and a 3D density-induced (internal or baroclinic-like) pressure-component $p'_h(\mathbf{x},t)$. The time-splitting approach for a more general free-surface, non-hydrostatic and compressible ocean can also be based on the ranking of Equation 2.3.3. The procedure is yet different from that used for hydrostatic ocean models. In the latter, coupling is based on the separation of the velocity field between a barotropic-like, depth-averaged component and a baroclinic-like anomaly. The faster, surface-induced component of the pressure force is integrated with a small time-step and after each integration sequence of the external mode, the depth-averaged component of the internal-mode velocity is forced to fit to the external-mode, depth-averaged velocity. Separating the "fast" and "slow" components of momentum in a compressible model to integrate them separately is not that simple and more importantly, it is not even necessary. The time-splitting procedure proposed in CROCO compressible kernel is indeed based on the splitting of the terms on the Right-Hand-Side (hereafter RHS) of the prognostic and diagnostic equations of the ocean model. Two coupled models (hereafter called the slow and fast numerical kernels) are then integrated in turn. The slow (respectively fast) kernel is advanced with a large (small) time-step computing explicitly slowly-varying (rapidly-varying) terms at the RHS and implicitly the remaining terms. A time-filtering procedure is additionally implemented to force both the slow and fast mode in a similar way as Shchepetkin and McWilliams (2005).

Pressure and density decomposition

The splitting of the processes based on the magnitude of their time-scale relies essentially on a decomposition of the pressure and density fields. Following Auclair et al. (2021a), the pressure decomposition in Equation 2.3.1 can be further developed for a free-surface ocean :

$$p(\mathbf{x},t) = \underbrace{p_{atm}(\mathbf{x}_H,t) + g\int_z^{\zeta} \rho_h(\mathbf{x}_H,z',t)\, dz'}_{p_h(\mathbf{x},t)} + \delta p(\mathbf{x},t) \tag{2.3.4a}$$

$$= \underbrace{\underbrace{p_{atm}(\mathbf{x}_H,t) + \rho_0 g\,(\zeta(\mathbf{x}_H,t) - z)}_{\bar{p}_h(\mathbf{x},t)} + \underbrace{g\int_z^{\zeta} (\rho_h(\mathbf{x}_H,z',t) - \rho_0)\, dz'}_{p'_h(\mathbf{x},t)}}_{p_h(\mathbf{x},t)} + \delta p(\mathbf{x},t) \tag{2.3.4b}$$

where ρ_0 is a constant reference density. The Taylor expansion of density with respect to total pressure (Equation 2.3.2) leads then to :

$$\rho(\mathbf{x},t) = \rho_{\theta S}(\mathbf{x},t) + \underbrace{\frac{1}{c_s^2}\left(p_h(\mathbf{x},t) + \delta p(\mathbf{x},t) - p_0(\mathbf{x},t)\right)}_{(p(\mathbf{x},t)-p_0(\mathbf{x},t))/c_s^2} + \mathrm{O}(\delta p^2) \tag{2.3.5a}$$

$$\approx \underbrace{\rho_h(\mathbf{x},t) + \rho_{nh}(\mathbf{x},t) + \frac{1}{c_s^2}\left(p_h(\mathbf{x},t) - p_0(\mathbf{x},t)\right)}_{\rho_s(\mathbf{x},t)} + \underbrace{\frac{\delta p(\mathbf{x},t)}{c_s^2}}_{\rho_f(\mathbf{x},t)} \tag{2.3.5b}$$

with $\partial p/\partial\rho|_\eta = c_s^2$ at constant entropy η, $\rho_{\theta S} = \rho_{eos}(\theta,\ S,\ p_0)$, $\rho_{nh} = \rho_{\theta S} - \rho_h$, ρ_s (and ρ_f) are respectively the components of the density field treated by the slow (fast) kernel (see below). This decomposition of the pressure and density fields clearly demonstrates, if necessary, the inextricable relationships between compressibility and hydrostaticity assumptions.

Slow vs fast components

Based on the decomposition of the pressure and density fields (Equations 2.3.4b and 2.3.5b), the terms at the RHS of the momentum equations can be split in two categories depending on the time-scales they are associated with :

$$\partial_t \rho \mathbf{v} = \underbrace{-\nabla.\,(\rho \mathbf{v} \otimes \mathbf{v}) - \rho f \mathbf{u_z} \wedge \mathbf{v} - \nabla(\int_z^{\zeta} (\rho_s - \rho_0) g \, dz') + \mu \Delta \mathbf{v}}_{\mathbf{\Lambda}_s} \tag{2.3.6a}$$

$$\underbrace{-\rho_0 g \nabla \zeta - \nabla \delta p - \rho f' \mathbf{u_y} \wedge \mathbf{v} + (\rho_{nh} + \rho_f)\mathbf{g} + \mu_2 \nabla(\nabla.\mathbf{v})}_{\mathbf{\Lambda}_f} \tag{2.3.6b}$$

Note that the Coriolis pseudo-force is itself splitted : the traditional component (with $f = 2\Omega sin(\phi)$, $\mathbf{u}_z$ the vertical unit vector in Cartesian coordinates and ϕ the latitude) is integrated with the slow kernel whereas the non-traditional component (with $f' = 2\Omega cos(\phi)$ and $\mathbf{u}_y$ the south-north horizontal unit vector in Cartesian coordinates). This latter component can indeed be associated with horizontal-axis rolls and is integrated with the fast kernel. The nonlinear advective terms are integrated with the slow kernel, i.e. a priori with a larger time-step and thus at a lower cost. Diffusion terms associated to dynamical (respectively bulk) viscosity are integrated with the slow (fast) kernel. The momentum equation (Equation 2.3.6) can thus be rewritten in a compact, conservative form and in s-coordinates as :

$$\partial_t \rho_s h_s \mathbf{v}_s = \quad \Lambda_s \ + \ll \Lambda_f \gg \tag{2.3.7a}$$

$$\partial_t \rho_f h_f \mathbf{v}_f = [[\Lambda_s]] + \quad \Lambda_f \tag{2.3.7b}$$

This splitting conserves basically the formulation of the horizontal momentum equations proposed in Shchepetkin and McWilliams (2005) : the length-scales of the processes and the fast-mode forcing are yet obviously different but the filtering procedure $\ll . \gg$ is the "flat" filter proposed by Shchepetkin and McWilliams (2005) (top left in Figure 16 of the aforementioned paper). [[.]] notation indicates the extrapolation in time of the slow-kernel terms to be used at the fast-kernel RHS (see §2.3.8).

2.3.3 Time-stepping

The time-splitting and time-stepping proposed in the following build both on Shchepetkin and McWilliams (2005) and on Auclair et al. (2018). Shchepetkin and McWilliams (2005)'s LFAM3[4], predictor-corrector time-stepping is indeed implemented in the slow kernel while a Forward-Backward (FB) scheme is used to integrate the fast-mode. The introduction of a compressible, non-hydrotatic kernel is taken from Auclair et al. (2018) and adapted to a two-mode implementation.

Figure 2.1 shows the predictor-corrector implementation of the slow and fast kernels based on ROMS barotropic/baroclinic time-splitting. Both the time-splitting and the various time-stepping are summarized in Equations 2.3.8.

Note that in these equations and in the following, to simplify notations and to be coherent with CROCO's variables, s (for "slow") and f (for "fast") subscripts are indicated for right-most variable only : $\rho h \mathbf{v}_s = \rho_s h_s \mathbf{v}_s$ and $\rho h \mathbf{v}_f = \rho_f h_f \mathbf{v}_f$. This means that $\rho h \mathbf{v}$, for example, is a CROCO variable. The decomposition of the density field into its fast and slow components is given by Equation 2.3.5b.

---

[4] Leap-Frog Adams-Moulton 3 steps

I.a Time-interpolation : $t_s - \Delta t_s/2$

$$[\Theta]^{n-\frac{1}{2}} = \alpha_{n-1}\Theta_s^{n-1} + \alpha_n\Theta_s^n \tag{2.3.8a}$$

I.b Predictor step : $t_s + \Delta t_s/2$

$$\rho h\mathbf{v}_s^{n+\frac{1}{2}} = \rho h\mathbf{v}_s^{n-\frac{1}{2}} + \Delta t_s\left(\Lambda_{s,v}^n + <\Lambda_{f,v}>^n\right) \tag{2.3.8b}$$

$$\rho h(\theta_s,\ S_s)^{n+\frac{1}{2}} = \rho h(\theta_s,\ S_s)^{n-\frac{1}{2}} + \Delta t_s\Lambda_{s,(\theta,S)}^n \tag{2.3.8c}$$

$$\rho_s^{n+\frac{1}{2}} = \rho_{eos}\left(\theta_s^{n+\frac{1}{2}},\ S_s^{n+\frac{1}{2}},\ z_s^{n+\frac{1}{2}}\right) \tag{2.3.8d}$$

$$\partial_s\rho\omega_s^{n+\frac{1}{2}} = -\partial_t\rho h_s^{n+\frac{1}{2}} + \nabla\cdot\rho h\mathbf{u}_s^{n+\frac{1}{2}} \tag{2.3.8e}$$

I.c AB3-extrapolation : $t_s + \Delta t_s/2$

$$[[\Psi_s]]^{n+\frac{1}{2}} = \beta_{n-2}\Psi_s^{n-2} + \beta_{n-1}\Psi_s^{n-1} + \beta_n\Psi_s^n \tag{2.3.8f}$$

II. Fast-mode steps : $t_f \in (t_s,\ t_s + \Delta t_s]\ or\ m \in [0,\ N_f)_{\mathcal{N}}$

$$\zeta_f^{m+1} = \zeta_f^m + \Delta t_f\left(w_{surf}^m - \mathbf{u}_{surf}^m.\nabla\zeta^m\right) \tag{2.3.8g}$$

$$\rho hu_f^{m+1} = \rho hu_f^m + \Delta t_f\left([[\Lambda_{s,u}]]^{n+\frac{1}{2}} - [[\overline{\Lambda_{s,u}}]]^{n+\frac{1}{2}} + \Lambda_{f,u}^m + \overline{\overline{\Lambda_{f,u}}}^{\,m} + \overline{\overline{\Lambda_{f,-\nabla\zeta}}}^{\,m+1}\right) \tag{2.3.8h}$$

$$\overline{\overline{\rho hU}}_f^{\,m+1} = \overline{\overline{\rho hU}}_f^{\,m} + \Delta t_f\left(\overline{\Lambda_{f,u}^m} + \overline{\overline{\Lambda_{f,u}}}^{\,m} + \overline{\overline{\Lambda_{f,-\nabla\zeta}}}^{\,m+1}\right) \tag{2.3.8i}$$

$$\rho hw_f^{m+1} = \rho hw_f^m + \Delta t_f\left([[\Lambda_{s,w}]]^{n+\frac{1}{2}} + \Lambda_{f,w}^{m+1*}\right) \tag{2.3.8j}$$

$$\rho h_f^{m+1} = \rho h_f^m - \Delta t_f\left([[\partial_t\rho h_s]]^{n+\frac{1}{2}} + \nabla\cdot\{\rho h\mathbf{v}\}_f^{m+1}\right) \tag{2.3.8k}$$

$$m = N_f - 1 :\ \bar{\rho}\zeta_s^{n+1} = \bar{\rho}(H + \zeta_f)^m - \bar{\rho}H_s^{m+1} - \Delta t_f\nabla\cdot\overline{\overline{\rho h\mathbf{u}}}^{\,m+1} \tag{2.3.8l}$$

$$Update\ grid :\rho h_f^{m+1},\ z_f^{m+1} \tag{2.3.8m}$$

III.a Filtering : $t_s + \Delta t_s\ and\ t_s + \Delta t_s/2$

$$<\Phi_f>^{n+1} = \Phi_f^{m=n+1} \tag{2.3.8n}$$

$$\ll\Phi_f\gg^{n+\frac{1}{2}} = \frac{1}{N_f}\sum_{m=1}^{N_f}\Phi_f^m \tag{2.3.8o}$$

III.b Corrector step : $t_s + \Delta t_s$

$$\rho h\mathbf{v}_s^{n+1} = \rho h\mathbf{v}_s^n + \Delta t_s\left(\Lambda_s^{n+\frac{1}{2}*} + \ll\Lambda_f\gg^{n+\frac{1}{2}}\right) \tag{2.3.8p}$$

$$\partial_s\rho\omega_s^{n+1} = -\partial_t\,\rho h_s^{n+1} + \nabla\cdot\rho h\mathbf{u}_s^{n+1} - \overline{\nabla\cdot\rho h\mathbf{u}_s}^{\,n+1} - \overline{<\nabla\cdot\rho h\mathbf{u}_s>}^{\,n+1} \tag{2.3.8q}$$

$$\rho h(\theta_s,\ S_s)^{n+1} = \rho h(\theta_s,\ S_s)^n + \Delta t_s\Lambda_{s,(\theta,S)}^{n+\frac{1}{2}*} \tag{2.3.8r}$$

$$\rho_s^{n+1} = \rho_{eos}\left(\theta_s^{n+1},\ S_s^{n+1},\ z_s^{n+1}\right) \tag{2.3.8s}$$

$$\rho h\mathbf{u}_s^{n+1} = \rho h\mathbf{u}_s^{n+1} - \overline{\rho h\mathbf{u}_s}^{\,n+1} + \overline{\rho h\mathbf{u}_f}^{\,m=N_f-1} \tag{2.3.8t}$$

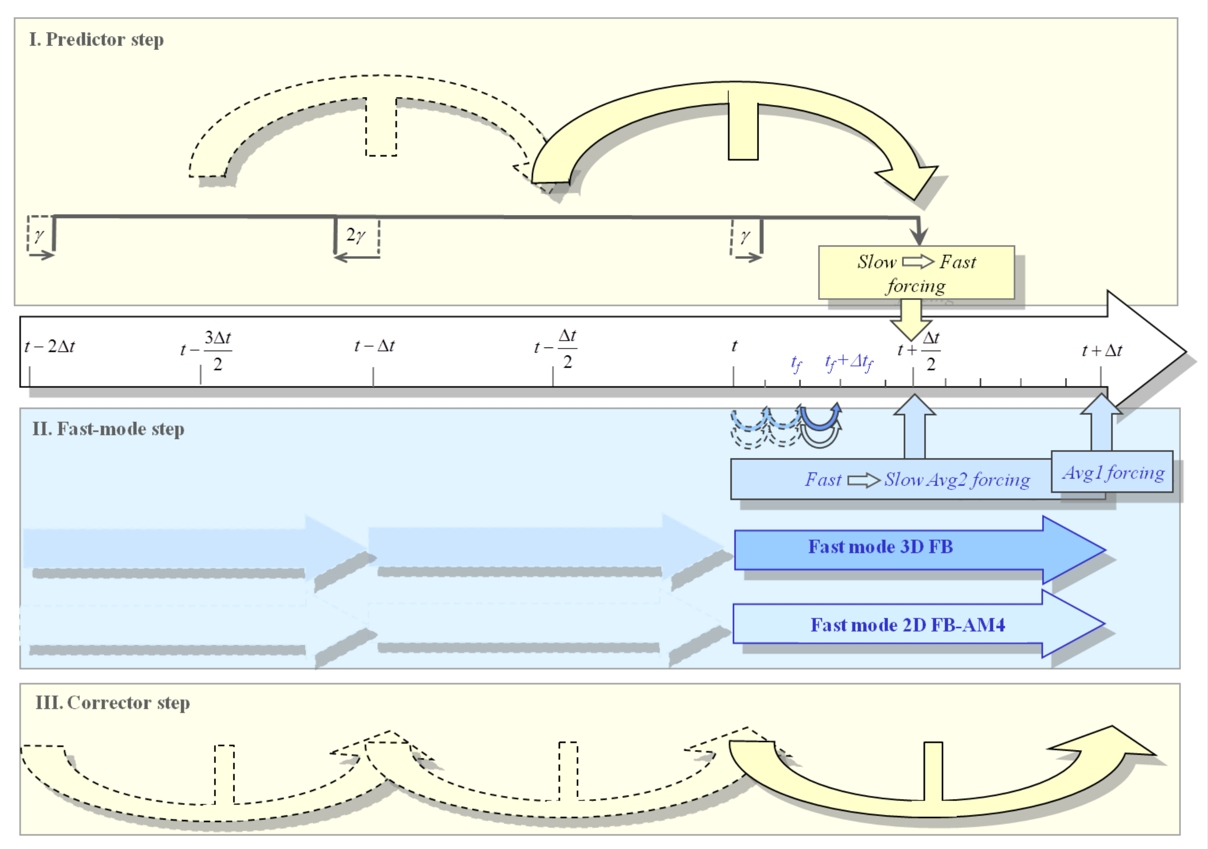

FIGURE 2.1: *Time-splitting and time-stepping of CROCO model with its non-hydrostatic, compressible (NBQ) kernel. Yellow (blue) background color : slow (fast) kernel.*

Predictor (I), fast-kernel Forward-Backward (II) and Corrector (III) steps are shown in horizontal color bands on Figure 2.1 (yellow for the slow kernel, blue for the fast kernel). After time-interpolating slow-kernel variables to $t_s - \varDelta t_s/2$ (step I.a, notation [.]), the slow kernel is advanced from $t_s - \varDelta t_s/2$ to $t_s + \varDelta t_s/2$ with a centered, leap-frog-like, time-stepping (step I.b). Then, to prepare the integration of the fast kernel, the slow-kernel RHS is extrapolated to $t_s + \varDelta t_s/2$ based on an AB3 scheme using its previous evaluations at $t_s - 2\varDelta t_s$, $t_s - \varDelta t_s$ and t_s (step I.c, notation [[.]]). The fast kernel can in turn be advanced from t_s to $t_s + \varDelta t_s$ using a forward-backward like time-stepping (step II) with time-step $\varDelta t_f$ satisfying $N_f = \varDelta t_s/\varDelta t_f \in \mathcal{N}$. The vertical momentum equation can optionally be integrated with semi-implicit scheme over the vertical direction.

The vertical grid is updated at each fast time-step (Equation 2.3.8m) but slow-kernel components of the RHS remain constant during the fast-kernel integration. At the last fast time-step, surface elevation displacement for the slow kernel can be recomputed to ensure perfect numerical coherence between the surface kinematic relation and depth-integrated mass conservation (Equations 2.3.8g and 2.3.8l).

Further numerical details such as the values of the interpolation (α_n) or extrapolation (β_n) coefficients, the expressions of the slow-kernel RHS terms ($\varLambda_s$), the expressions of the fast-kernel surface-related pressure force terms ($\varLambda_{f,-\nabla\zeta}$), the fast-kernel RHS remaining terms ($\varLambda_f$) or the implicit fast and slow-kernel RHS terms (indicated by an asterisk) can be found in CROCO dedicated manuals and publications. A major difference with the hydrostatic time-splitting is that the surface elevation displacement is given by the kinematic condition (Equation 2.3.8g) and not by the depth-integral of the mass conservation equation. Once the fast-kernel RHS and variables have been filtered both at $t_s + \Delta t_s$ and $t_s + \Delta t_s/2$ (step III.a, notations $< . >$ and $\ll . \gg$), the slow kernel is finally advanced from t to $t_s + \Delta t_s$ during the leap-frog-like Corrector step (III.b). A star following the time-index superscript indicates the use of an implicit numerical schemes.

Note that the 2D depth-averaged, barotropic-like, horizontal momentum Equations 2.3.8i (double over-bar notation) are advanced in the same way as in Shchepetkin and McWilliams (2005). The result of this 2D integration is indeed used to correct both the horizontal momentum itself and the RHS of the horizontal momentum equation at Corrector step. It can also be used to require a perfect coherence of the surface elevation displacement and the depth-average transport (at machine precision) during the slow-mode integration.

2.4 Conclusion, discussion of the *ocean model*

In the present chapter, we proposed a rigorous framework (a "map") for our exploration of ocean *fine scales* in the *Terra Incognita*. An analytical, terrain-following s-coordinate model for the conservation of mass, momentum, heat and tracers has first been proposed under general assumptions of a compressible, free-surface ocean (§2.2).

We then considered the numerical implementation of this general *ocean model* (§2.3). After a consideration of the space-time scales potentially involved in fine scale ocean dynamics, an original time-splitting has been detailed as an extension of Shchepetkin and McWilliams (2005)'s barotropic/baroclinic time-splitting. It is also a restriction to a two-mode time-splitting of Auclair et al. (2018)'s three-mode time-splitting. This time-splitting allows the integration of both acoustic and surface-induced processes with a smaller time-step in order to make the integration of a compressible, free-surface realistic ocean affordable. It is based on the spectral gaps identified in Equation 2.3.3 between acoustic, surface and internal processes.

The region of the Strait of Gibraltar has been chosen as the region of demonstration for fine-scale dynamics in CROCO. As a consequence, the LES configurations presented in Chapters 3, 4 and 5 are not only based on the two-mode CROCO kernel of Section 2.3 ; these configurations have indeed been part of the development process itself.

2.5 Appendices to the *ocean model*

2.5.1 *s*-coordinate transformation

The present appendix gathers several formula and relations essential to the development of the numerical implementation of the *ocean model.*

Transformation matrices

The transformation matrix of the generalized coordinate transformation is :

$$\Lambda_s^z = \begin{pmatrix} 1 & 0 & 0 & 0 \\ 0 & 1 & 0 & 0 \\ 0 & 0 & 1 & 0 \\ \frac{\partial z}{\partial t} & \frac{\partial z}{\partial x} & \frac{\partial z}{\partial y} & h = \frac{\partial z}{\partial s} \end{pmatrix} \tag{2.5.1}$$

and the inverse transformation is given by :

$$\Lambda_z^s = \begin{pmatrix} 1 & 0 & 0 & 0 \\ 0 & 1 & 0 & 0 \\ 0 & 0 & 1 & 0 \\ \frac{\partial s}{\partial t} & \frac{\partial s}{\partial x} & \frac{\partial s}{\partial y} & \frac{\partial s}{\partial z} \end{pmatrix} \tag{2.5.2}$$

The Jacobian of the transformation $J = det(\Lambda_s^z)$ is the (specific) thickness :

$$J = h = \frac{\partial z}{\partial s} = \left.\frac{\partial z}{\partial s}\right|_{xyt} \tag{2.5.3}$$

Griffies (2004) further define the infinitesimal thickness for modelling developments :

$$\delta h = \frac{\partial z}{\partial s}\delta s \tag{2.5.4}$$

Formula and identities

Base on the transformation matrices, the s-coordinate transformations can be rewritten :

$$\left.\frac{\partial A}{\partial t}\right|_{xz} = \left.\frac{\partial A}{\partial t}\right|_{xs} - \frac{1}{h}\left.\frac{\partial A}{\partial s}\right|_{tx}\left.\frac{\partial z}{\partial t}\right|_{xs} \tag{2.5.5a}$$

$$\left.\frac{\partial A}{\partial x}\right|_{tz} = \left.\frac{\partial A}{\partial x}\right|_{ts} - \frac{1}{h}\left.\frac{\partial A}{\partial s}\right|_{tx}\left.\frac{\partial z}{\partial x}\right|_{ts} \tag{2.5.5b}$$

$$\left.\frac{\partial A}{\partial z}\right|_{tx} = \frac{1}{h}\left.\frac{\partial A}{\partial s}\right|_{tx} \tag{2.5.5c}$$

whereas material derivatives satisfy :

$$\frac{d}{dt} = \left.\frac{\partial}{\partial t}\right|_{z} + \mathbf{u}.\nabla_z + w\frac{\partial}{\partial z} \tag{2.5.6a}$$

$$= \left.\frac{\partial}{\partial t}\right|_{s} + \mathbf{u}.\nabla_s + \dot{s}\frac{\partial}{\partial s} \tag{2.5.6b}$$

This leads to :

$$\dot{z} = \left.\frac{dz}{dt}\right|_{s} = \left.\frac{\partial z}{\partial t}\right|_{s} + \mathbf{u}.\nabla_s z + \dot{s}\frac{\partial z}{\partial s}, \quad r \quad \dot{s} = \left.\frac{ds}{dt}\right|_{z} = \left.\frac{\partial s}{\partial t}\right|_{z} + \mathbf{u}.\nabla_z s + w\frac{\partial s}{\partial z} \tag{2.5.7}$$

Using the identities :

$$\left.\frac{\partial s}{\partial t}\right|_{z} = \left(\left.\frac{\partial t}{\partial s}\right|_{z}\right)^{-1}, \quad \left.\frac{\partial s}{\partial x}\right|_{z} = \left(\left.\frac{\partial x}{\partial s}\right|_{z}\right)^{-1}, \quad \left.\frac{\partial s}{\partial y}\right|_{z} = \left(\left.\frac{\partial y}{\partial s}\right|_{z}\right)^{-1}, \quad \left.\frac{\partial s}{\partial z}\right|_{x} = \left(\left.\frac{\partial z}{\partial s}\right|_{x}\right)^{-1} \tag{2.5.8}$$

several relations can be obtained from the triple product rule and the coordinate transformations are given by :

$$\left.\frac{\partial z}{\partial t}\right|_{s} = -\left.\frac{\partial s}{\partial t}\right|_{z}\left.\frac{\partial z}{\partial s}\right|_{s}, \quad \left.\frac{\partial z}{\partial x}\right|_{s} = -\left.\frac{\partial s}{\partial x}\right|_{z}\left.\frac{\partial z}{\partial s}\right|_{s}, \quad \left.\frac{\partial z}{\partial y}\right|_{s} = -\left.\frac{\partial s}{\partial y}\right|_{z}\left.\frac{\partial z}{\partial s}\right|_{s} \tag{2.5.9}$$

Local orthonormal coordinates

Griffies (2004) further defines in his chapter (6.4) a system of orthonormal coordinates :

$$\mathbf{e}_{x^*} = \frac{\mathbf{y} \wedge \nabla s}{||\mathbf{y} \wedge \nabla s||}, \quad \mathbf{e}_{y^*} = \mathbf{e}_s \wedge \mathbf{e}_{x^*}, \quad \mathbf{e}_s = \frac{\nabla s}{||\nabla s||} \tag{2.5.10}$$

In this particular case ($\mathbf{e}_s.\mathbf{z}$) has a unique sign, the basis vectors can be rewritten :

$$\mathbf{e}_{x^*} = \frac{\mathbf{x} + S_x \mathbf{z}}{\sqrt{1 + S_x^2}}, \quad \mathbf{e}_{y^*} = \frac{-S_x S_y \mathbf{x} + (1 + S_x^2)\mathbf{y} + S_y \mathbf{z}}{\sqrt{(1 + S^2)(1 + S_x^2)}}, \quad \mathbf{e}_s = \frac{(-\mathbf{S}, 1)}{\sqrt{1 + S^2}} \tag{2.5.11}$$

The s-coordinate transformation is a rotation and :

$$\mathbf{e}_{x^* y^* s} = \Lambda_s^z \mathbf{e}_{xyz} \tag{2.5.12}$$

Note in particular the definition of the slope $\mathbf{S}$ and its norm $S = ||\mathbf{S}||$ used to rewrite the orthonormal basis :

$$\mathbf{S} = \nabla_s z = -\frac{\partial z}{\partial s} \nabla_z s = \left(S_x,\ S_y,\ 0\right) \tag{2.5.13}$$

where $\nabla_s z$ is "the horizontal gradient of the height of a fluid parcel as taken along surfaces of constant generalized vertical coordinate s" (Griffies, 2004).

Note that this orthonormal basis is not used to project the equations of the model. S-coordinates are "only" used as a change of variable whereas equations and vector quantities remain written in the original Cartesian or spherical basis. The present s-coordinate orthonormal basis is presented here to be latter used in the computation of fluxes through s-surfaces.

2.5.2 Operators & relations in s-coordinates

Divergence of the velocity field in s-coordinates

Using :

$$\left.\frac{\partial}{\partial t}\frac{\partial z}{\partial s}\right|_{tx} = \frac{\partial h}{\partial t} \qquad \textit{and} \qquad \left.\frac{\partial}{\partial x}\frac{\partial z}{\partial s}\right|_{tx} = \frac{\partial h}{\partial x} \tag{2.5.14}$$

the expression of the divergence of the velocity field in s-coordinates can be written :

$$h\,\nabla.(\mathbf{v}) = h\left.\frac{\partial u}{\partial x}\right|_{zt} + h\left.\frac{\partial v_z}{\partial z}\right|_{xt} \tag{2.5.15a}$$

$$= h\left.\frac{\partial u}{\partial x}\right|_{st} - \left.\frac{h\,\partial u}{h\,\partial s}\right|_{tx}\left.\frac{\partial z}{\partial x}\right|_{ts} + \frac{h\,\partial}{h\,\partial s}\left(v_s + \left.\frac{\partial z}{\partial t}\right|_{xs} + u\left.\frac{\partial z}{\partial x}\right|_{ts}\right) \tag{2.5.15b}$$

$$= h\left.\frac{\partial u}{\partial x}\right|_{st} - \left.\frac{\partial u}{\partial s}\right|_{tx}\left.\frac{\partial z}{\partial x}\right|_{ts} + \frac{\partial v_s}{\partial s} + \frac{\partial h}{\partial t} + u\frac{\partial h}{\partial x} + \left.\frac{\partial u}{\partial s}\right|_{tx}\left.\frac{\partial z}{\partial x}\right|_{ts} \tag{2.5.15c}$$

$$= \left.\frac{\partial v_s}{\partial s}\right|_{tx} + \left.\frac{\partial hu}{\partial x}\right|_{ts} + \left.\frac{\partial h}{\partial t}\right|_{xs} \tag{2.5.15d}$$

Note that this is a particular case of the formulation of a change of variables with its Jacobian ($J = h$ in the present case).

Conservative "flux" forms : kinematics & dynamics

Two general conservative formulations can be obtained combining this with the continuity equation (Auclair, 2011)[5].

A is a property given per unit mass (thermodynamically intensive) (see the demonstration on web site). The first two (conservative) relations are fundamentals to analytical and numerical modeling.

Based on the conservation of mass :

$$\rho\frac{dA}{dt} = \left.\frac{\partial \rho A}{\partial t}\right|_{xz} + \left.\frac{\partial \rho A u}{\partial x}\right|_{tz} + \left.\frac{\partial \rho v_s}{\partial z}\right|_{tx} \tag{2.5.16}$$

Based on the conservation of mass & in s-coordinates :

$$\rho h\frac{dA}{dt} = \left.\frac{\partial \rho h A}{\partial t}\right|_{xs} + \left.\frac{\partial \rho h A u}{\partial x}\right|_{ts} + \left.\frac{\partial \rho A v_s}{\partial s}\right|_{tx} \tag{2.5.17}$$

A kinematic, non-conservative formulation can be obtained without the continuity equation :

$$\frac{dA}{dt} = \left.\frac{\partial A}{\partial t}\right|_{xs} + u\left.\frac{\partial A}{\partial x}\right|_{ts} + \left.\frac{v_s}{h}\frac{\partial A}{\partial s}\right|_{tx} \tag{2.5.18}$$

The demonstration is given in (Auclair, 2011)[5].

Conservation of mass : note finally that the conservation of mass $A = 1$ can then be rewritten :

$$h\frac{d\rho}{dt} = \left.\frac{\partial \rho h}{\partial t}\right|_{xs} + \left.\frac{\partial \rho h u}{\partial x}\right|_{ts} + \left.\frac{\partial \rho v_s}{\partial s}\right|_{tx} \tag{2.5.19}$$

Additionally, the evolution of ρ in Equation 2.2.6 can be rewritten in s-coordinates as :

$$h\frac{d\rho}{dt} \approx \frac{\partial}{\partial x}\left(h\kappa^h\left.\frac{\partial \rho}{\partial x}\right|_{ts}\right)_{ts} + \frac{\partial}{\partial s}\left(\frac{\kappa^v}{h}\left.\frac{\partial \rho}{\partial s}\right|_{tx}\right)_{tx} \tag{2.5.20}$$

with : $\kappa_c^h \approx \kappa^h$ and $\kappa_c^v \approx \kappa^v$.

---

[5] WOcean.fr Web Site : `http://poc.omp.obs-mip.fr/auclair/WOcean.fr/SNH/Restricted/NH-NBQ/Sources/Images/png/Coord_demo.png`

-3- Fines échelles dans le détroit de Gibraltar : simulation numérique et analyse de la dynamique dans une section verticale 2D

3.1 Résumé en français

Ce chapitre s'appuie sur l'article *"Numerical Modeling of Hydraulic Control, Solitary Waves and Primary Instabilities in the Strait of Gibraltar"* (Hilt et al., 2020) publié dans la revue *Ocean Modelling*. Si la démarche numérique présentée dans cet article avait été proposée lors de mon stage de fin d'étude, la rédaction même de l'article ainsi qu'une grande majorité des éléments d'analyses présentés (décomposition en valeurs singulières, tests de sensibilité...) ont été réalisés durant la première année de mon doctorat. Ces travaux constituent un véritable socle sur lequel est appuyé le reste de l'étude menée à bien durant ma thèse de doctorat, et sont référencés dans le reste du manuscrit, d'où leur inclusion.

Une configuration numérique simplifiée basée sur une section verticale (2D) est implémentée dans le détroit de Gibraltar avec le code communautaire à surface libre CROCO dans sa version non-hydrostatique, compressible, non-Boussinesq (voir Section 2.3). Cette configuration est peu coûteuse en temps de calcul malgré sa haute résolution (environ 45 m sur l'horizontale) et s'appuie sur une bathymétrie réaliste le long de l'axe du détroit avec sa configuration de seuils (Farmer and Armi (1988), programme *Gibraltar Experiment*). Durant l'élaboration de cette configuration, une attention toute particulière a été apportée à l'impact de la pseudo-force de Coriolis sur l'échange moyen simulé lors de l'initialisation.

La simulation est initialisée par *lock-exchange* : deux profils de stratification type 'nord Atlantique' et 'Méditerranéen' sont choisis pour initialiser cette configuration simplifiée de part et d'autre du seuil de Camarinal, point central du passage du détroit. Au début de la simulation, le front au-dessus du seuil évolue rapidement en un écoulement bicouche avec des eaux méditerranéennes s'écoulant en courant de gravité dans la moitié ouest du domaine et une intrusion en surface des eaux atlantiques sur la partie est.

Après une période de simulation d'ajustement de trois jours, la marée semi-diurne est ajoutée par un courant barotrope oscillant à la frontière ouest. Dans une simulation où la rotation de la Terre n'est pas prise en compte, le mélange induit par les courants de marée détruit la stratification obtenue après relaxation du *lock exhange*, modifiant en particulier la profondeur de l'interface où se propagent les solitons. Lorsque la pseudo-force de Coriolis est introduite en même temps que le forçage par la marée, la stratification induite par le mécanisme de *lock-exchange* se maintient, au détriment de la valeur moyennée dans le temps de l'échange au niveau du seuil de Camarinal.

Durant quelques périodes de marée M2, cette configuration simplifiée permet donc de simuler explicitement et de façon réaliste les variations des processus à l'oeuvre dans le détroit à l'échelle de la marée, et en particulier les processus de fines échelles : propagation de trains d'ondes solitaires, contrôles hydrauliques aux seuils, ressauts hydrauliques internes et mélange turbulent avec la simulation explicite d'instabilités primaires de cisaillement qui ont un effet local sur la stratification.

Ainsi les ondes internes de grande amplitude de mode 1 se propageant dans l'est du détroit sont caractérisées comme étant des ondes solitaires (ou solitons) par comparaison avec le modèle analytique non-linéaire de Korteweg de Vries.

La modulation des phénomènes observés par divers paramètres (bathymétrie, intensité des courants de marée, hypothèse hydrostatique, résolution spatiale) est étudiée en détail. A haute résolution (environ 45 m), la relaxation de l'hypothèse non-hydrostatique est indispensable pour représenter les instabilités de cisaillement qui apparaissent dans le jet Méditerranéen, et qui constituent l'amorce de la cascade turbulente directe.

Malgré les défauts inhérents à une représentation 2D-verticale (nécessairement limitée dynamiquement et non représentative des effets longitudinaux comme le contrôle hydraulique dans le détroit de Tarifa), la configuration proposée permet de représenter de façon réaliste et de proposer une première analyse des mécanismes de *fine échelle* dans le détroit à la fréquence de la marée barotrope.

3.2 Numerical Modeling of Hydraulic Control, Solitary Waves and Primary Instabilities in the Strait of Gibraltar (Hilt et al., 2020)

Authors M. Hilt, L. Roblou, C. Nguyen, P. Marchesiello, F. Lemarié, S. Jullien, F. Dumas, L. Debreu, X. Capet, L. Bordois, R. Benshila, F. Auclair

Abstract A two-dimensional, vertical section of the Strait of Gibraltar is simulated numerically with the nonhydrostatic / non-Boussinesq three-dimensional CROCO model to investigate details of small-scale dynamics. The proposed configuration is simple, computationally efficient and incorporates the configuration of sills characteristic of this region. Despite the shortcomings of a 2D representation, this configuration provides a realistic depiction of small-scale mechanisms in the strait during a typical tidal cycle : internal solitary waves generation and propagation, occurrence of hydraulic controls and hydraulic jumps at the sills and presence of active turbulent patches. In particular, the well-known eastward propagation of large amplitude internal waves is assessed using the Korteweg de Vries (KdV) propagation model for solitary waves.

As a step towards establishing a realistic three-dimensional Large Eddy Simulation (LES), the sensitivity of the configuration to various choices (e.g., resolution, amplitude of tidal forcing or numerical schemes) is investigated. Our analyses indicate that the representation of small-scale dynamics in the Strait of Gibraltar can be much improved by increasing resolution and relaxing the hydrostatic assumption. Further studies are necessary to grasp the mechanisms of mixing and/or stirring induced by this fine scale processes.

3.2.1 Introduction

The Strait of Gibraltar connects two major basins : the Northern Atlantic and the Mediterranean Sea, over which evaporation exceeds precipitation and river run-off. To compensate the resulting loss, exchanges of mass and salt are required through the strait. Figure 3.1 illustrates the rather complex exchanges occurring there. Inflowing Atlantic water is less salty (salinity $S_A \approx 36$) than the outflowing Mediterranean water ($S_M > 38$), and spreads as a surface layer

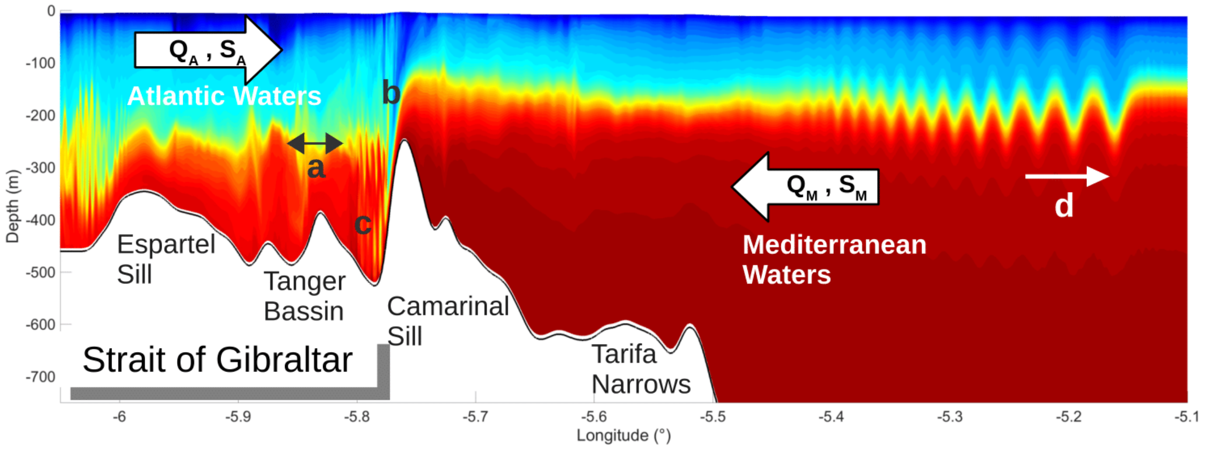

FIGURE 3.1: Illustration of small-scale processes in the Strait of Gibraltar induced by tidal interaction with stratification and bathymetry. (a) Linear / Small amplitude internal wave. (b) Hydraulic Jump. (c) Kelvin-Helmholtz instabilities. (d) Large-amplitude internal waves or internal solitary waves (ISW).

in the Alboran Sea. The interface between the two water masses is distorted by undulations that are not precisely periodic with regard to the tidal cycle but exhibit regularity in some areas. One of the paper objectives is to better understand the small-scale processes that lead to the Atlantic and Mediterranean water masses transformation in the vicinity of the Strait of Gibraltar.

To further illustrate the exchange between the Northern Atlantic and the Mediterranean, a very simple steady-state model can be expressed as a system of two basic conservation equations.

Volume conservation is expressed as :

$$Q_A + Q_M = E - P \tag{3.2.1}$$

while the conservation of salt requires :

$$Q_A S_A + Q_M S_M = 0 \tag{3.2.2}$$

where Q_A is the Atlantic water volume flux (positive), Q_M is the Mediterranean water volume flux (negative), both localized in the Strait of Gibraltar, and $E - P$ is the space-averaged Evaporation minus Precipitation (and river runoff) water budget integrated over the whole Mediterranean Sea. $E - P$ is positive. S_A (S_M) stands for Atlantic (Mediterranean) water mean salinity and $S_M - S_A \approx 2$ (Bethoux, 1979). The water budget $E - P$ is positive in the Mediterranean due to excess evaporation that correspond to a yearly averaged loss of water of about 1 meter over the whole basin (Garrett et al., 1990).

A major dynamical feature in the Strait of Gibraltar is the so-called "flow criticality" usually characterized by the Froude number (F) : it compares the internal wave phase speed with a flow characteristic velocity. Several definitions of the non-dimensional Froude number can be found in the literature : it can notably be defined for each layer, resulting in a composite number for the whole water column, as in Farmer and Armi (1988) or in Sannino et al. (2009b).

A "subcritical" (respectively "supercritical") regime lies in the range of small (respectively large) values of the Froude number $F < 1$ (respectively $F > 1$), with an intermediate "critical" regime for $F \approx 1$. The upstream propagation of internal waves is inhibited for supercritical flow so that a hydraulic control occurs at the transition from subcritical to supercritical flow;

it persists during periods and within regions of large Froude numbers. As such, the hydraulic regime at a given point will vary in time according to substantial currents variations occurring along the tidal cycle. It is, for example, well established that large amplitude solitary waves in the Strait of Gibraltar can develop due to the hydraulic control at Camarinal Sill (Farmer and Armi, 1988), making it a crucial process to represent.

Several analytical models have been proposed to investigate the hydraulic control in the Gibraltar region (Bryden and Stommel, 1984; Farmer and Armi, 1986; Garrett et al., 1990). The hydraulic control usually occurs in these models at Camarinal Sill (CS), Espartel Sill (ES), and Tarifa Narrows (TN), although the modelled hydraulic control location and frequency vary according to the model refinement :

1. Farmer and Armi (1986)'s two-layer model accounts for the strait geometry (depth and width), the exchanged volumes (Q_A and Q_M) and the salinity contrast ($S_A - S_M$). This simple model is able to simulate two hydraulic controls : the first one located by the sill, the other in the TN contraction, defining "maximal exchange regime" (further details are given below).
2. In a slightly more elaborated model, the inclusion of entrainment between the two layers and the subsequent interfacial layer introduction modify the left-hand terms of Equations 3.2.1 and 3.2.2 with the introduction of horizontal and vertical transports in the interfacial layer (Bray et al., 1995). Critical conditions are changed within such two interfaces model which may support two baroclinic modes and new hydraulic controls (Sannino et al., 2009b).
3. Considering a three-dimensional flow, the definition of the control needs to account for cross-strait variations such as the tilt of the density interface in the latitudinal direction. In the maximal exchange solution, control in TN may induce the detachment of the surface layer from the northern coast (Sannino et al., 2009b).

The hydraulic control effect within the strait is illustrated in Figure 3.1. The flow is initially subcritical in the Strait ; the propagation of internal waves is not hindered at the interface between Atlantic and Mediterranean waters (denoted “a” in Figure 3.1) ; then the tidal flood in the vicinity of the Camarinal Sill becomes supercritical. In the supercritical to subcritical transition, downstream of the sill, a "hydraulic jump" (“b” in Figure 3.1) may occur.

Hydraulic jumps are large-amplitude depressions in the regions where hydraulic controls occur. There, intense mixing between the Atlantic and Mediterranean waters takes place as observed by Wesson and Gregg (1994). Shear flow instabilities can develop in the hydraulic jump of the Camarinal Sill (denoted “c” in Figure 3.1).

The release of hydraulic jumps generates large-amplitude, non-linear, nonhydrostatic Internal Solitary Waves (ISW) trains (denoted “d” in Figure 3.1) (Farmer and Armi, 1988). As the barotropic tide is constrained by the bathymetry, large vertical velocities appear and induce energy transfer to several normal modes of internal waves. Some observations in the Strait of Gibraltar identify the largest ISW amplitude to the first baroclinic mode ; for which vertical velocities have the same direction throughout the water column and all isopycnal surface displacements are in phase. The signature of Mode 2 waves (the vertical velocity profile exhibits one node) has also been observed in the region of Gibraltar strait (Farmer and Armi, 1988; Vázquez et al., 2006). The internal waves propagate at the interface of Mediterranean and Atlantic waters.

As the strait flow varies at various timescales during the year, some deviation is expected in the occurrence of the hydraulic control in the strait. This may have a wide impact since local flow conditions combined with the above two conservation Equations 3.2.1 and 3.2.2 determine the relation between the volume fluxes, the evaporation minus precipitation budget ($E - P$) and the salinity difference ($S_A - S_M$) (Bryden and Kinder, 1991). Practically, an "overmixed" solution corresponds to a minimal salinity difference and a maximal exchange of water mass in the strait : it would thus constrict the formation of Mediterranean waters and diapycnal mixing over the Mediterranean basin (Bryden and Stommel, 1984; Garrett et al., 1990). Moreover, the small-scale processes occurring in the strait itself can directly modify the local characteristics of Mediterranean waters (García-Lafuente et al., 2011; Naranjo et al., 2015) and Atlantic waters (Millot, 2014). This can affect their characteristics as they enter respectively in the North Atlantic sub-basin and in the Mediterranean Sea.

To study the flow dynamics in the strait in further details, more realistic numerical modelling is of great help. Early attempts used two-layer models (Brandt et al., 1996; Izquierdo et al., 2001). The increase of computational power led to 3D modelling (Sannino et al., 2004) with increasing vertical and horizontal resolution, explicitly addressing the tidal cycle and flow characteristics. More recently, even nonhydrostatic models have been used (Sánchez Garrido et al., 2011; Sannino et al., 2014) to explicitly represent the ISW. Other configurations include the Strait of Gibraltar into a Mediterranean circulation model (Soto-Navarro et al., 2015). In this case, the increased resolution locally in the strait (Naranjo et al., 2014) — or the nesting of high-resolution grids within a coarse resolved regional model (Sannino et al., 2009a) — shows a clear impact on Mediterranean stratification and improves the representation of convective events in the northwestern Mediterranean basin.

The coastal and regional ocean modelling community model (CROCO [1]) is based on a new nonhydrostatic and non-Boussinesq solver (Auclair et al., 2018) developed within the former ROMS kernel (Shchepetkin and McWilliams, 2005), for an optimal accuracy and cost efficiency. CROCO opens up new perspectives in terms of modelling of small-scale processes (Fox-Kemper et al., 2019; Lemarié et al., 2019). In this sense, the present study objectives are also numerical : we show that a new generation of nonhydrostatic ocean models can be used efficiently to simulate complex nonlinear, fine scale physics in a realistic but computationally-affordable configuration. The complete solution of Navier-Stokes equations are thus solved numerically for the very first time in a complex realistic regional configuration.

The present configuration of the Strait of Gibraltar is based on a classical lock-exchange initialization (Sannino et al., 2002). A 2D vertical section of the strait is adopted in order to reduce the number of parameters impacting the studied dynamics. This rather simple configuration is thus of weak computational cost and reduces the implementation burden ; it allows to reach the horizontal and vertical scales of the largest turbulent structures observed in this area. In the strait, where most transverse dynamical feature are an order of magnitude weaker, our numerical approach is some kind of ersatz of a large-eddy simulation (LES [2]), for which at least the generation process of primary instabilities is correctly represented. However, LES is a 3D concept as the route to molecular dissipation differs in 2D and 3D turbulence. The present study is focused on the description of the largest primary instabilities in the Strait of Gibraltar ; as well as providing order of magnitudes for explicit simulations of these dynamics. Along with these physical aims, the relevance of the chosen numerical methods is a major concern. A quantified impact of the largest turbulent structures on the water masses is out of the scope of what is presented hereafter : it would require a fully three dimensional LES (also achievable with the CROCO model), in complement with dedicated relevant experimental measurements.

---

[1] http ://www.croco-ocean.org/

[2] LES (Large Eddy Simulation) : LES, as opposed to DNS (Direct Numerical Simulation) does not cope with the full 3D Kolmogorov energy cascade down to molecular scales. However at least the onset of this cascade (the largest turbulent structures) is explicitly represented, unlike in RANS (Reynolds Averaged Navier-Stokes).

In Section 2, we present an overview of CROCO equations and the implementation for the 2D lock-exchange experiment. We describe the implementation of the bathymetry profile, water masses, and the exchange and tidal flows. In Section 3.2.3, we analyse the physics of the 2D configuration, comparing the model solution to already published data (e.g., in Farmer and Armi (1988)). Emphasis is then made on the hydraulic control (Section 3.2.3), the hydraulic jump (Section 3.2.3) and the mode-1 and mode-2 ISW (non-linear internal trains of solitary waves) propagation (Section 3.2.3). Last, the sensitivity to the tidal forcing amplitude and to the numerical choices are analysed respectively in Sections 3.2.4 and 3.2.4, with a focus on the fine-scales dynamics listed in Figure 3.1.

3.2.2 Model Description and Configuration

The Numerical Modeling System

The proposed numerical model of the Strait of Gibraltar simulates explicitly the fine-scale processes (from tens to hundreds of meters) discussed previously. This assumes that (i) a sufficient grid resolution is provided in the strait and (ii) a well-suited numerical kernel is used.

The nonhydrostatic (non-Boussinesq) CROCO version is chosen for its ability to allow the explicit representation of primary instabilities that cascade the kinetic energy injected at large scale down to the smaller scales. This direct transfer ends at the finest scale resolved ; the subgrid dissipation of energy is performed both by the implicit mixing of the advection schemes and the explicit closure schemes. The dissipation is solely performed by (quasi-)monotonic numerical advection schemes (Grinstein et al., 2007) when no parametrized turbulent closure scheme accounts for the subgrid-scale mixing.

CROCO is an extension of ROMS from which it inherited the robustness and efficiency of its time-splitting implementation, the accuracy of high-order methods, including its pressure gradient scheme for terrain-following coordinates, and computing performances (Shchepetkin and McWilliams, 2005; Debreu et al., 2012; Soufflet et al., 2016). In CROCO's time-splitting algorithm, the "slow mode" is similar to ROMS internal (baroclinic) mode (Shchepetkin and McWilliams, 2005) ; its "fast mode" includes the usual external (barotropic) mode and a new pseudo-acoustic mode that allows computation of the nonhydrostatic pressure within a non-Boussinesq formalism (Auclair et al., 2018). A two-level time-splitting kernel is thus conserved in CROCO (as opposed to the first implementation of the 3-level time-splitting by Auclair et al. (2018)) but the fast time step integrates a 3D-compressible flow. Furthermore the slow internal mode is enhanced by a prognostic equation of the vertical velocity, replacing the hydrostatic equation.

Continuous, Free-Surface, Compressible Equations

The full set of Navier-Stokes equations for a free-surface ocean is explicitly integrated, including the continuity and momentum equations, the surface kinematic relation, the heat, salt and state equations in Cartesian coordinates :

$$\partial_t \rho = -\vec{\nabla}.(\rho\vec{v}) \tag{3.2.3}$$

$$\partial_t \rho\vec{v} = -\vec{\nabla}.\left(\rho\vec{v}\otimes\vec{v}\right) - 2\rho\vec{\Omega}\wedge\vec{v} - \vec{\nabla}p + \rho\vec{g} + \mu\Delta\vec{v} + \lambda\vec{\nabla}(\vec{\nabla}.\vec{v}) \tag{3.2.4}$$

$$\partial_t \zeta = w_{(z=\zeta)} - \vec{v}_{(z=\zeta)}.\vec{\nabla}\zeta \tag{3.2.5}$$

$$\partial_t \rho\theta = -\vec{\nabla}.\left(\rho\theta\vec{v}\right) + \kappa_\theta\Delta\theta \tag{3.2.6}$$

$$\partial_t \rho S = -\vec{\nabla}.\left(\rho S\vec{v}\right) + \kappa_S\Delta S \tag{3.2.7}$$

$$\rho = \varrho\left(\theta, S, P\right) \tag{3.2.8}$$

where $\vec{v} = (u, v, w)$ is the velocity, p the total pressure, ζ the free-surface anomaly, ρ the density, θ and S the potential temperature and salinity respectively. $\vec{\Omega}$ is the instantaneous earth rotation vector, $\vec{g}$ is the acceleration of gravity and μ, λ, κ_θ and κ_S are respectively the dynamical and second (bulk) viscosity and the thermal and salinity diffusivities. $\varrho\left(\theta, S, P\right)$ is a linear approximation of the seawater equation of state.

Density and Pressure Decomposition

As part of the time-splitting, the density is splitted into one slow and one fast component based on a first-order decomposition with respect to the total pressure. In the following, s and f subscripts refer to these slow and fast components respectively [3].

$$\rho = \rho_s\left(\theta, S, P\right) + \overbrace{\left.\frac{\partial\rho}{\partial P}\right|_{\theta,S}\delta P}^{\delta\rho=\rho_f} + O\left(\delta P^2\right) \tag{3.2.9}$$

$$P = \underbrace{P_{atm} + \int_z^\zeta (\rho_s - \rho_0) g \, dz'}_{Slow\ mode} + \underbrace{\rho_0 g(\zeta - z) + \underbrace{\delta P}_{P_f}}_{Fast\ mode} \tag{3.2.10}$$

No further decomposition is required for the other variables. Note that δP is the nonhydrostatic pressure.

Slow vs Fast Components

Navier-Stokes equations are integrated with two different time-steps in a time-splitting algorithm. The slow mode is identical to ROMS whereas the fast mode is now 3D and includes the integration of the compressible terms of the momentum and continuity equations. The free-surface anomaly is computed through the surface kinematic condition.

---

[3] ρ_0 is a reference density that will be specified later on.

$$
\begin{aligned}
\partial_t \rho_f &= -\partial_t \rho_s \quad -\vec{\nabla}.(\rho\vec{v}) \\
\partial_t \rho\vec{v} &= \overbrace{-\vec{\nabla}.\,(\rho\vec{v}\otimes\vec{v}) - 2\rho\vec{\Omega}\wedge\vec{v} - \vec{\nabla}\Big(\int_z^{\zeta_f}(\rho_s-\rho_0)g\,dz'\Big) + \mu\Delta\vec{v}}^{\vec{\Lambda}_s} \\
&\quad \underbrace{-\rho_0 g\vec{\nabla}\zeta_f - \vec{\nabla}P + \rho\vec{g} + \lambda\vec{\nabla}(\vec{\nabla}.\vec{v})}_{\vec{\Lambda}_f} \qquad (3.2.11) \\
\partial_t \zeta_f &= w_{f(z=\zeta)} - \vec{v}_{f(z=\zeta)}.\vec{\nabla}\zeta_f \\
\partial_t \rho\theta_s &= \Theta_s = -\vec{\nabla}.\,(\rho\theta_s\vec{v}) + \kappa_\theta\Delta\theta_s \\
\partial_t \rho S_s &= \Sigma_s = -\vec{\nabla}.(\rho S_s\vec{v}) + \kappa_S\Delta S_s \\
\rho_s &= \varrho(\theta_s, S_s, \zeta_f) \\
\rho_f &= c_s^{-2}P_f
\end{aligned}
$$

The momentum equations are integrated both in the slow and fast modes but the right-hand-side of the equation is split in two parts : a "slow" part ($\vec{\Lambda}_s$) made of slowly varying terms (advection, Coriolis force, baroclinic pressure force and viscous dissipation) and a "fast" part ($\vec{\Lambda}_f$), made of fast-varying terms (the surface-induced and compressible pressure force, the weight and dissipation associated with bulk-viscosity). This momentum equation is numerically integrated twice, once with a large time-step keeping $\vec{\Lambda}_f$ constant, and once with a smaller time-step keeping $\vec{\Lambda}_s$ constant. This time-splitting is much more computationally efficient than integrating the whole set of equations at the same short time step.

The general, compressible Equations set 3.2.11 can basically propagate three types of waves : internal and external gravity waves, and acoustic waves propagating at c_s, the speed of sound. The nonhydrostatic pressure anomaly is not a solution of a diagnostic elliptic Poisson-like equation as it is for a Boussinesq equations set. The pressure anomalies travel at the acoustic waves velocity. The acoustic solver is not global anymore (as it is in the Poisson-like set) ; it is now local in space, meaning that no 3D global linear system of equations needs to be inverted anymore. The price of solving fast acoustic waves is however enhanced due to a more restrictive CFL conditions. Both acoustic and surface waves are integrated in CROCO's fast mode with a smaller time-step to cope with this. As a linear set of simplified compressible equations needs to be integrated in this fast mode the whole computations remain affordable. In addition, since the sound speed is at least one order of magnitude larger than the phase-velocity of the fastest propagating waves and much larger than any ocean advection velocity, it can be artificially reduced. The only requirement is that the speed of sound remains larger than any other propagating wave or flow velocity in the domain. In particular, it must remain larger than the phase-velocity of long surface waves so that nonhydrostatic anomalies can be propagated vertically fast enough to set up the corresponding wave structure over the water column. Sensitivity tests show that, in this case, a slower sound speed has no impact on lower-frequency dynamics in the region of the strait : more details on that point can be found in Auclair et al. (2018).

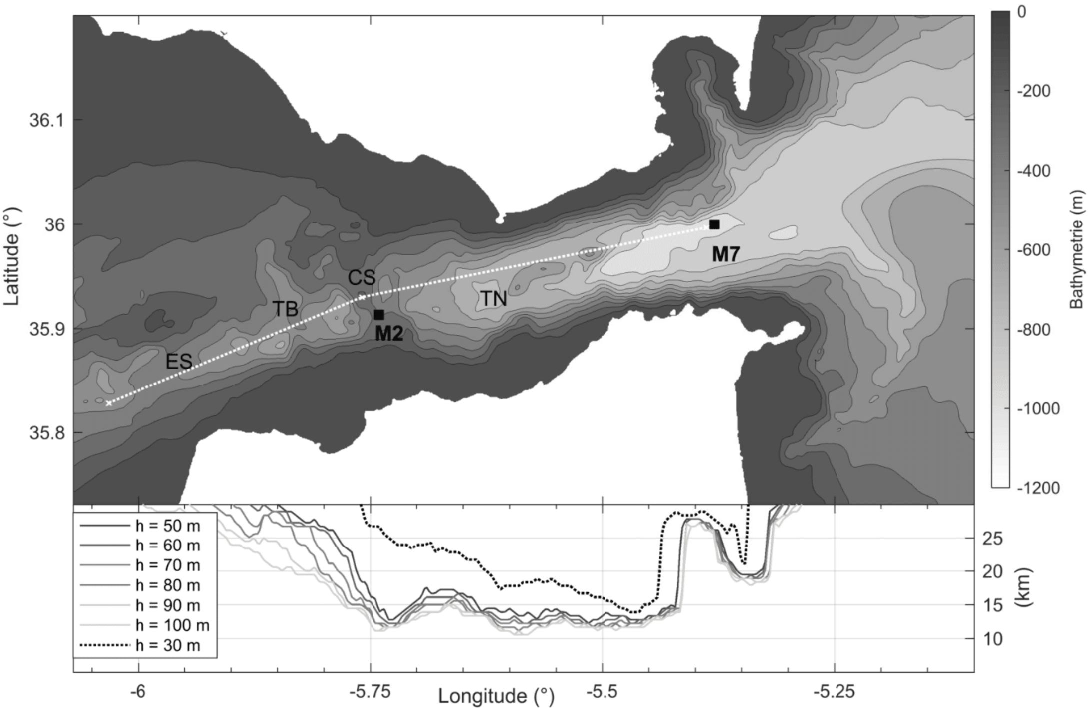

FIGURE 3.2: a) Bathymetry of the strait of Gibraltar, with the section used for the present model configuration (white dotted line). Black squares indicate the position of moorings from Candela et al. (1990); ES : Espartel Sill, TB : Tanger Basin, CS : Camarinal Sill , TN : Tarifa Narrows. b) Width of the Gibraltar Strait along transverse direction (y) between 2 isobaths of depth h[4].

Bathymetry

Figure 3.2.a presents the 500-m-resolution bathymetry gathered in the framework of the HOMONIM project coordinated by the French Navy (SHOM) and MeteoFrance, and as provided by the French Navy (Biscara et al., 2016). The main bathymetric features as well as the localization of the studied 2D vertical section are exhibited. This section is chosen as close as possible to the transect of Farmer and Armi's Gibraltar Experiment performed in April 1986 (Farmer and Armi, 1988) and coincides in the western area with the Mediterranean waters privileged path. Hereafter, u is the velocity in the longitudinal direction of the section and v the velocity in the transverse direction. Figure 3.2.b presents the Gibraltar Strait width according to different reference depths. This plot shows that an averaged thirteen kilometer width can be used, featuring steep slopes at the lateral boundaries of the strait, especially in Tarifa Narrows.

Simulations are performed with 50m and 220m horizontal resolutions. The bathymetry used in the simulations is averaged laterally to limit the unrealistic effect of local seamounts in the transverse direction such as those found in TN (which can end up acting as another sill in a 2D vertical section). To that end, a Gaussian interpolation of the bathymetry along the section in Figure 3.2.a is used with a greater Gaussian radius in the transverse direction than in the longitudinal direction. The Gaussian radius in the transverse direction is set to 1500 m (i.e. lower than the width of the strait in Figure 3.2.b). As a consequence, the bathymetry only reflects the deepest areas in the canal. In the longitudinal direction, the Gaussian interpolation radius is set to 300 m to preserve the bathymetry variability in this direction.

The minimum depth thus assessed at Camarinal Sill (i.e. the main sill in the Strait), along the

---

[4] in other words, the distance along the meridional direction between two isobaths of equal depth.

TABLE 3.1: Numerical parameters of simulation **SimRef**

Number of horizontal points	2661x3	
Horizontal scale (Δx)	50 m	
Number of vertical σ-levels	40	
Depth	Min	Max
	247 m	900 m
Vertical scale (Δz)	6 m	23 m
Slow time step (t_s)	1 s	
Fast time step (t_f)	1/8 s	
Spin up period	72 h	
Vertical Viscosity	10^{-6} m^2/s	
Lateral Viscosity	10^{-5} m^2/s	
Diffusivity	10^{-6} m^2/s	
Momentum Advective Scheme	TVD - Van Leer	
Turbulent Closure Scheme	none	
T, S Advective Scheme	WENO5	
Quadratic bottom drag coefficient	10^{-3}	
Atmospheric forcing/fluxes	none	

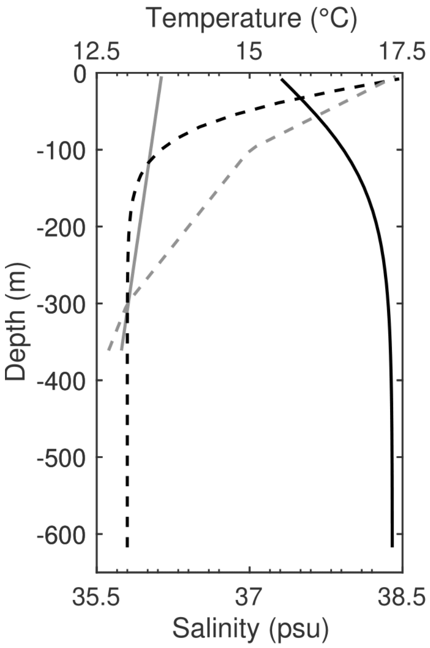

FIGURE 3.3: Initial salinity (solid) and temperature (dashed) profiles of Mediterranean water (black) and Atlantic water (grey).

transect's path goes from the value of approximately 200 m to 245 m. The model bathymetry used is the one shown in Figure 3.1. A reference simulation (hereafter named **SimRef**) is carried out at 50-m horizontal resolution with additional characteristics and parameters listed in Table 3.1.

Initial Water Masses, Tidal Forcing and Boundary Conditions

The temperature and salinity reference profiles are chosen to initialise the density field of the simulations. A minimum of two profiles for each of those variables is needed to initialize gradients associated with sloping isopycnal surfaces in a given direction. According to Sannino et al. (2002), a lock-exchange initialization is performed with homogeneous Atlantic water initially to the west of the CS and homogeneous Mediterranean water to the east. A three-day spin-up described in Section 3.2.2) is then performed to set up the exchange flow in the strait.

The initial temperature and salinity profiles are presented in Figure 3.3. The contrast in salinity between Atlantic and Mediterranean waters is noticeable, with respective mean values of 35.9 and 38.2.

In the following, the interface between Atlantic and Mediterranean layers is taken as the 37 isohaline, following Bryden et al. (1994). Density is now expressed as an anomaly (written ρ') relative to a reference (mean) density ρ_0. From now on, the implicit reference density (unless contraindicated) will be $\rho_0 = 1033.7$ kg/m^3 : a value reached in the pycnocline separating the two water masses.

An idealized M2 tidal forcing (of period T = 12.4 h) is prescribed at the open boundaries after the spin-up period (at t = 3 days = 5.8 T). It is introduced thanks to a barotropic current of amplitude 0.4 m/s at the western boundary (0.8 m/s at CS), corresponding to a moderate regime according to the TPXO-8 tidal atlas (Egbert and Erofeeva, 2002). Lateral forcing is introduced at the open eastern and western boundaries through mixed active passive radiation conditions (Marchesiello et al., 2001) ; cyclic conditions are imposed to the northern and southern open boundaries.

Initial Flow and Effect of Coriolis Force

The Gibraltar strait lateral boundaries are distant of about 15 km, with a clear funneling effect from the CS to the eastern end of the strait (5.4°W ; see Figure 3.2.b). The internal Rossby radius R (see Appendix 3.2.6) is usually found to vary from 10 to 20 km (Bormans and Garrett, 1989; Candela et al., 1990; Vlasenko et al., 2009). The width of the strait and the Rossby radius R being of the same order of magnitude, rotational effects can be neglected as a rather good approximation. Therefore, the momentum balance is mainly between the acceleration and the pressure force in the Equation 3.2.4 and the geostrophic adjustment in the along-strait direction is locally neglected. In their observations (Farmer and Armi, 1988) and the 3D-modeling configurations (Sannino et al., 2002), the consequence of Earth's rotation is a cross-strait shear of along-strait velocity (Bormans and Garrett, 1989) and a tilt of the isopycnals : along the southern boundary (i.e. along the Moroccan coast), the interfacial isopycnal is deeper and the flow reaches larger velocities.

As the transverse flow, the coastal boundaries, and the resulting "funnelling effect" cannot be simulated in a 2D vertical section, it is necessary to examine whether completely ignoring rotational effects is viable in a 2D vertical approximation. To that end, three different numerical simulations of the stratification and the mean circulation are compared : (i) one simulation with the Coriolis force activated from start to end (**SimAllCor** ; $f = 8.5\ 10^{-5} s^{-1}$), (ii) the second one without the Coriolis force (**SimNoCor** ; $f = 0$), and (iii) the last one with the Coriolis force activated only after a three days spin-up period (**SimRef**). Apart from the Coriolis parameter, all the three simulations where performed with the characteristics given in Table 3.1 for **SimRef**. During the very first hours of simulation time, the 'Lock-Exchange dam' separating the Atlantic and Mediterranean water-masses disappears ; a gravity current is generated with dense Mediterranean waters flowing down the western slope of CS and light Atlantic water spreading in the surface layer east of the sill.

Figure 3.4 presents the field of the longitudinal velocity (u) as well as some isopycnals for **SimAllCor** (a) and **SimNoCor** (b) at t = 72 h (i.e., the end of the spinup period). The bold isopycnal surface $\rho' = -0.7\ kg/m^3$ corresponds at that time to the 37psu-isohaline. Figures 3.4.a-b also present the transverse-velocity (v) isotachs ± 0.5 m/s. Figures 3.4.c-d show the tidal residual components u and v in the water column at the two dashed vertical lines on Figures 3.4.a-b. These locations correspond to the moorings indicated in Figure 1 of Candela et al. (1990). Using the 37psu-isohaline as a frontier between the two water masses, the 3T time-averaged transport through the left dashed line at the CS is given in the columns labelled 'Transport' of the Table 3.2.

In **SimNoCor** (Figure 3.4.b), a clear vertical shear of the along-section velocity can be seen between the two water masses. The shear is still featured in the 3T-averaged current profiles of Figure 3.4.c and is, for station M2, in accordance with the observations given by the moorings at the CS. This shear has decreased since initialization as progressive mixing of the two water masses reduces the baroclinicity. The currents in **SimAllCor** and **SimRef** are weaker, with locally negative currents in the upper layer (see Figure 3.4.c). This is confirmed by the layer-averaged transports presented in Table 3.2, where values in **SimAllCor** and **SimRef** are one order of magnitude smaller than in **SimNoCor**. Using an average strait's width of 13 km, an approximate baroclinic transport for the strait can be estimated from the values in Table 3.2 ; for **SimNoCor** it would be of 0.6 Sv : it is slightly weaker than the range of 0.7-1 Sv estimated from various field observations (see a review in Sammartino et al. (2015)). In **SimAllCor** and **SimRef**, the cross-section velocity is due to the inclusion of the Coriolis force. More precisely, during the spin-up phase of **SimAllCor**, the effect of rotation can no more be neglected after 6 hours. At that time, the upper Atlantic layer has spread over a distance of about 26 km and the cross-section velocity featured in Figure 3.4.a is already significant.

With no coastal boundaries to hinder the geostrophic adjustment within the strait, the initially longitudinal gravity current is almost completely converted into transverse geostrophic current with spurious (non physical) consequences on the slope of the isopycnals. Geostrophy enables a thermal-wind balance for the transverse v component :

$$\frac{\partial v}{\partial z} = -\frac{g}{\rho_0 f}\frac{\partial \rho}{\partial x} \tag{3.2.12}$$

This is particularly apparent to the east of the CS in Figure 3.4.a where the pycnocline is located at the transition between positive and negative transverse velocities. As a consequence, the pycnocline slope is $\Delta z/\Delta x = 6.10^{-3}$ (Table 3.2) and the Atlantic water cannot spread further than the resulting surface front. In **SimRef**, the Coriolis force is introduced only after a 72-h-spin-up period leading to the state presented in Figure 3.4.b. In this case, the resulting slope and transverse velocity are smaller than in **SimAllCor**. The pycnocline in the eastern part of the domain is deeper whereas it is shallower in the western part. However, longitudinal currents remain weak. In contrast, in **SimNoCor** the thermal-wind balance is not allowed and, away from the sills, $\Delta z/\Delta x$ vanishes. In the longitudinal direction, the main balance is between the pressure force ($-1/\rho_0\ \partial p/\partial x$) and the acceleration term. In this case, the shear of the longitudinal velocity is better represented at the two moorings. The larger transports in both layers indicate that a larger amount of Mediterranean water enters the Tangier basin than in **SimAllCor**. This is confirmed by the stratification (Figure 3.4.a and Table 3.2) since the pycnocline is shallower over the Espartel Sill (and deeper within the TN).

A perfect balance between the transports in the upper and lower layers is not achieved in

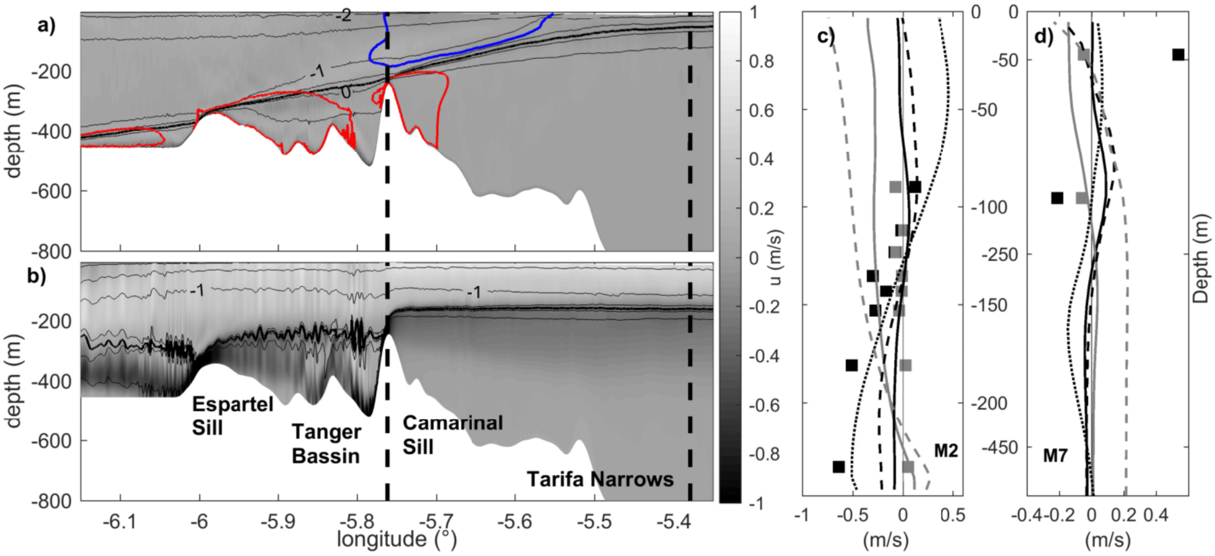

FIGURE 3.4: a - b) Longitudinal currents u (greyscale) and isopycnals (thin black lines) of density anomaly between -2 kg m^{-3} and 0.5 kg m^{-3} with an interval of 0.5 kg m^{-3} at t = 72 h at the end of the spin-up phase for **SimAllCor** (a) and **SimNoCor** (b). The bold line is for isopycnal $\rho' = -0.7\ kg/m^3$. The vertical dashed lines indicate the location of the profiles given in c and d. Color contours in (a) indicate the values of transverse currents v. Inside the red contours $v \geq 0.5\ m/s$, while inside the blue contours $v \leq -0.5\ m/s$. c - d) 3T-averaged longitudinal currents (black) and transverse currents (grey) for **SimRef** (plain), **SimAllCor** (dashed) and **SimNoCor** (dotted). Observation of tidal-mean currents at stations M2 and M7 (Figure 3.2) from Candela et al. (1990) (squares).

any of these three numerical experiments. While there is no numerical challenge in achieving longer simulation, the fluxes of Mediterranean and Atlantic waters are not realistically specified to re-stratify properly the water column in these academic configurations. After the spin-up period, the intense tidal mixing and other dissipative processes may end up homogenizing the initial water masses. The gap between the transports in the upper and lower layers disappears as the depth-averaged absolute transports decrease. This process is faster in **SimNoCor** than in the other configurations in which the thermal-wind balance maintains the isopycnal slopes. In this case, the depth of the 37 psu-isohaline, taken as a moving average over one tidal period at x = 5.4°W, increases from 130 to 175 m in **SimNoCor** over three tidal periods (not shown). This impacts the large-amplitude internal waves propagation.

The difficulty to obtain both realistic ambient stratification and circulation is a limitation of the restriction to a 2D vertical section of the dynamical problem targeted. In the proposed implementation, an initial state is obtained by lock-exchange with a spin-up period of 72 h dedicated to the adjustment of the gravity current produced by the 'dam break'. For the remainder of this paper, the reference simulation (**SimRef**) is chosen as the simulation whose adjustment is made in a non-rotating framework. This initial state has a correct mean exchange but it is weakened as the tidal forcing is introduced and changes the stratification conditions.

To mitigate this problem, the rotation is restored at the end of the spin-up period : the geostrophic balance that ensues stabilizes the slopes of isopycnals by generating a transverse current. The mean exchange is nevertheless reduced but the stratification (i.e. both the slope of the isopycnals and the vertical density gradient) thus saved is crucial to the generation and propagation of the large-amplitude solitary waves. Furthermore, the small-scale processes discussed hereafter take place during the tidal cycle. At this time-scale, the barotropic exchange is dominated by the tidal currents, so that in the reference simulation, the amplitude of the baroclinic exchange is correct. Note that if rotation is activated from the beginning of the spin-up period (**SimAllCor**), it leads to unrealistically-large slopes of the isopycnals (see Table 3.2).

3.2.3 The Reference Simulation

The reference simulation presented previously is now evaluated thanks to the observational data from the Gibraltar Experiment (Farmer and Armi, 1988). We describe the hydraulic controls, the primary instabilities and the dynamics of the ISW in this reference simulation.

Comparison with in situ Observations

In the present section, observations from the Gibraltar Experiment (Farmer and Armi, 1988) are investigated in order to evaluate the quality of the model solution obtained with the reference configuration **SimRef**.

Table 3.2 presents the pycnocline depth and slope at different locations along the section for the three configurations and the observational data. The depth and slope for **SimAllCor** and **SimNoCor** are calculated after 72 h of simulation and correspond to the isopycnal surface $\rho'=$ -0.7 kg/m^3 in Figures 3.4.a-b, whereas for configuration **SimRef** the same isopycnal taken in a 3T-averaged stratification corresponding to Figure 3.5. In **SimAllCor**, the isopycnals have a greater slope than the reported observations from Gibraltar Experiment (0.006 vs 0.003). In **SimNoCor**, there is no slope away from the sills, while as discussed before, the slope obtained in **SimRef** is small. The stratification in **SimRef** is close to that of **SimNoCor** in the eastern part with an isopycnal close to the horizontal. In the western part and over the CS, the pycnocline is shallower than in the other two simulations (Table 3.2).

In the following, we further investigate small-scale dynamical processes such as hydraulic jump and ISW propagation in configuration **SimRef**. This is also the baseline configuration used to perform all sensitivity tests presented hereafter.

TABLE 3.2: 3T time-averaged transports (m^2/s) at CS, depth (m) and slope of the interface.

	Transport (m^2/s)		Pycnocline Depth (m)			Pycnocline Slope	
	Upper layer	Lower layer	ES (5.91°W)	CS (5.71°W)	TN (5.52°W)	ES-CS	CS-TN
Farmer and Armi (1988)	/	/	190	125	60	0.003	0.003
SimAllCor	-5	-13	300	175	70	0.006	0.006
SimNoCor	50	-45	290	200	220	0.005	-0.001
SimRef	0.7	-6	245	175	160	0.004	0.001

Tidal Currents & Hydraulic Control.

In the present study, the Froude number (F) is simply defined at each grid point as the ratio between the local longitudinal velocity u and the theoretical speed c_1 of the first internal wave

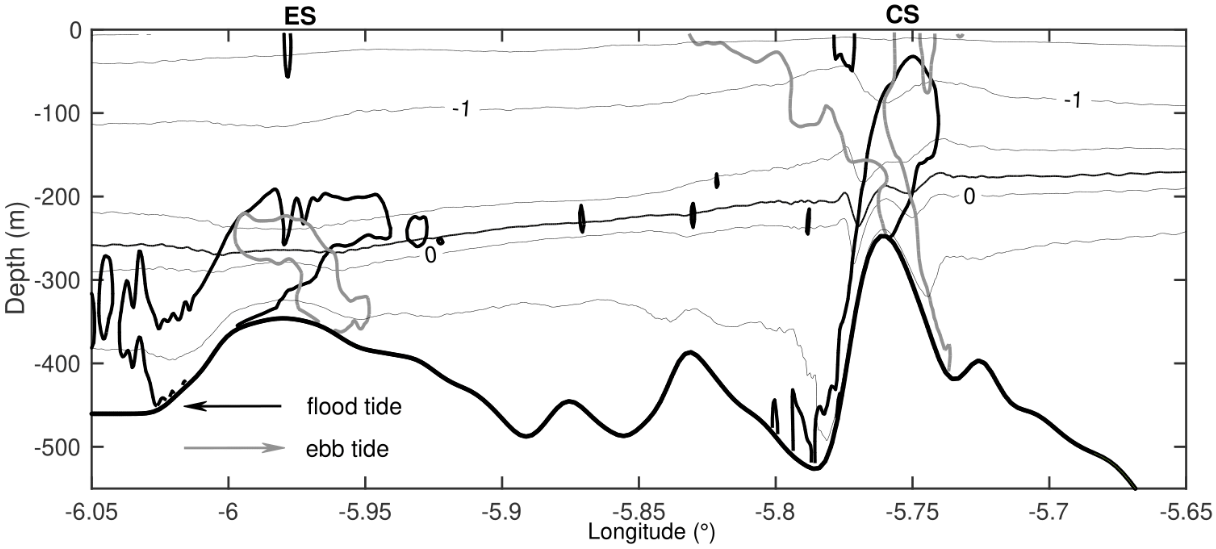

Figure 3.5: Isopycnal position averaged over a 3T time interval in **SimRef** (thin black lines are density anomaly contours between -1.5 kg m^{-3} and 0.5 kg m^{-3} with an interval of 0.5 kg m^{-3}; Thick black (grey) contours indicate critical Froude number $F = 1$ during flood (ebb) tide, inside which the flow is supercritical.

mode, computed with the modal decomposition for each point of the x-axis (see Appendix 3.2.6 for details).

For single-layer flows, hydraulic control occurs in the region of transition between subcritical and supercritical flows. In this region, the condition $F > 1$ is met over the whole water column. For multi-layer flows, the Froude number condition may be satisfied in a few layers only. In this case, the layers where the flow becomes supercritical are considered as "hydraulically controlled".

Three areas of potential hydraulic control in Gibraltar Strait are identified from previous studies : the CS, the ES and the narrowest part of the TN (near 5.5°W longitude in Figure 3.2). Farmer and Armi (1988) found persistent controls for first internal wave mode at the ES, the CS and the TN. Sannino et al. (2009b) found only ephemeral appearances of such controls, except at the ES where it is permanent. The discrepancy is likely lying in the definition and the estimation of the composite Froude number.

Figure 3.5 shows the regions where the flow is critical. Closed contours indicate the locations of critical Froude number ($F = 1$), inside which the flow is supercritical. The longitudinal velocity fields (u) used to estimate F are taken at maximum outflow (grey) at $t = 7.5\ T$ and maximum inflow (black) at $t = 8\ T$. The internal waves phase speed c_1 is computed from the 3T-time-averaged stratification represented in Figure 3.5. No control of the first mode is ever seen in TN : this is a consequence of the 2D simplification which excludes the representation of the tidal flow intensification by the narrowing of the strait at TN. On the other hand, hydraulic control is expected at both sills. The location where it should occur alternate between the eastern (during ebb) and western (during flood) sides of the sills, with a return to subcritical flow when tidal current slackens. The Froude number easily goes beyond 2 in the Mediterranean outflow at CS, where the flow is supercritical through most of the water column, except sometime at the surface. At ES, the lower layer may become supercritical with Froude number that never exceeds 1.5. The lack of persistent control at ES may be a consequence of the crudely imposed stratification.

Primary Instabilities in the Hydraulic Jump Area

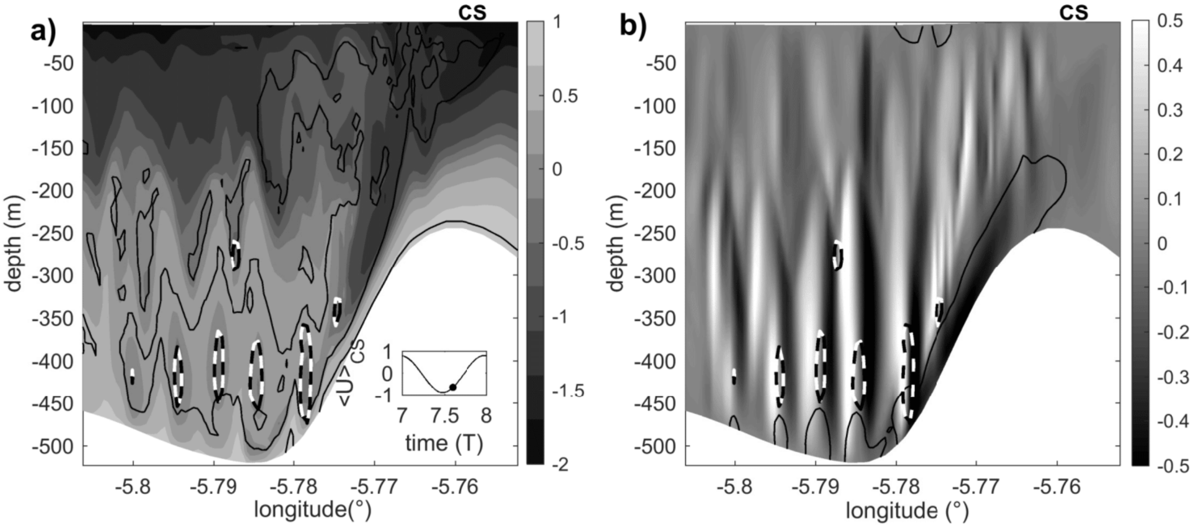

FIGURE 3.6: a) Density anomaly (greyscale ; kg/m^3) in the lee side of Camarinal Sill in **SimRef** at t = 7.56 T. Black contours indicate the location where the Richardson number is 0.25. b) Vertical velocity (greyscale ; m/s) in the lee side of Camarinal Sill in **SimRef** at t = 7.56 T. The black contour indicates the location where the Froude number is 1. a) and b) The black and white contour represents $OW = -4 * 10^{-4}\ s^{-2}$.

One manifestation of the hydraulic control is the formation of hydraulic jumps in specific regions where the flow transitions from supercritical to subcritical. This is a complex area with steep slopes and high shears where flow-topography interaction can generate small-scale coherent structures. The largest ones are resolved in **SimRef** and are characterised here with various methods. First, the Okubo-Weiss parameter (Appendix 3.2.6) is computed to investigate the presence of new 'coherent structures' in the hydraulic jump area. Their dynamics are further investigated using Empirical Orthogonal Functions (EOFs) computed with a Singular Value Decomposition (SVD). Their typical length and velocity scales are finally compared with the expected analytical values of shear instabilities and lee waves.

The dynamics of the CS hydraulic jump are illustrated in Figure 3.6, in which the density field (Figure 3.6.a) and the vertical velocity field (Figure 3.6.b) over the western slope of the CS are represented during flood. Several flow parameters were also computed and are depicted in Figure 3.6.a and b. These parameters are :

1. The Froude number defined in Appendix 3.2.6. The contours of critical Froude number $F = 1$ are shown in Figure 3.6.b, inside which the flow is supercritical.
2. The Richardson gradient number defined as $Ri = N^2 / (\partial u/\partial z)^2$, with N the Brunt-Väisälä frequency defined in Equation 3.2.13. Contours of $Ri = 0.25$ are depicted in Figure 3.6.a, as $Ri < 0.25$ is a required condition for the development of shear instabilities.

$$N = \sqrt{-\frac{g}{\rho_0}\frac{\partial \rho}{\partial z}} \tag{3.2.13}$$

3. The Okubo-Weiss parameter defined in Appendix 3.2.6. Negative values of OW indicate vortical circulation, and so contours of $OW = -4 * 10^{-4}\ s^{-2}$ are shown in both Figure 3.6.a and b.

In Figure 3.6.b, the supercritical flow region (F > 1) follows the slope of the sill where the velocity in the Mediterranean outflow is larger than 2 m/s (see the contour F = 1 running approximately parallel to isopycnals between 5.76°W and 5.77°W). At 5.77°W, the density field in Figure 3.6.a shows a sharp transition (e.g., isopycnal $\rho' = -0.5 kg/m^3$ rises from 350 to 225 m depth), and forms a wedge-shaped region over the supercritical Mediterranean outflow. This is the signature of an internal hydraulic jump.

Downstream of the hydraulic jump, several small-scale structures are visible. Figure 3.6.a shows patches of lighter water (billows) associated with areas of negative OW values at a depth of 400 m, and large-amplitude disturbances of isopycnals at 150 m. Negative OW values are also located at troughs and can reach $OW = -4 * 10^{-4} s^{-2}$. Both types of structures are propagating westward and are quite probably shed from the internal hydraulic jump at the tip of the wedge-shaped region at 5.773°W, with the size of billows growing rapidly as they travel down-slope. In the potential generation area, Richardson number values are less than 0.25, indicating favorable conditions for generation of primary shear instabilities.

Further identification of the simulated new features of Figure 3.6 is achieved by proceeding with a complex singular value decomposition (SVD) (Pairaud and Auclair, 2005) of the velocity field ($w + iu$) in the water column between 5.795°W and 5.78°W longitude, during outflow conditions. This region is highlighted in Figure 3.7.a, in which the time mean field of longitudinal velocity u is presented, showing the intense outflow below layers of lesser velocities. The mean density field and location of $Ri < 0.25$ are also indicated, the former showing a homogeneous area between 50-150 m above the seafloor. The SVD gives a first singular vector responsible for 28 % of the total variance corresponding to the evolution of the barotropic forcing (not shown). The remaining singular eigenvectors have lesser corresponding variance and show smaller structures with high-frequency variations in the singular right eigenvector. Two consecutive singular vectors often have very close eigenvalues and temporal variations.

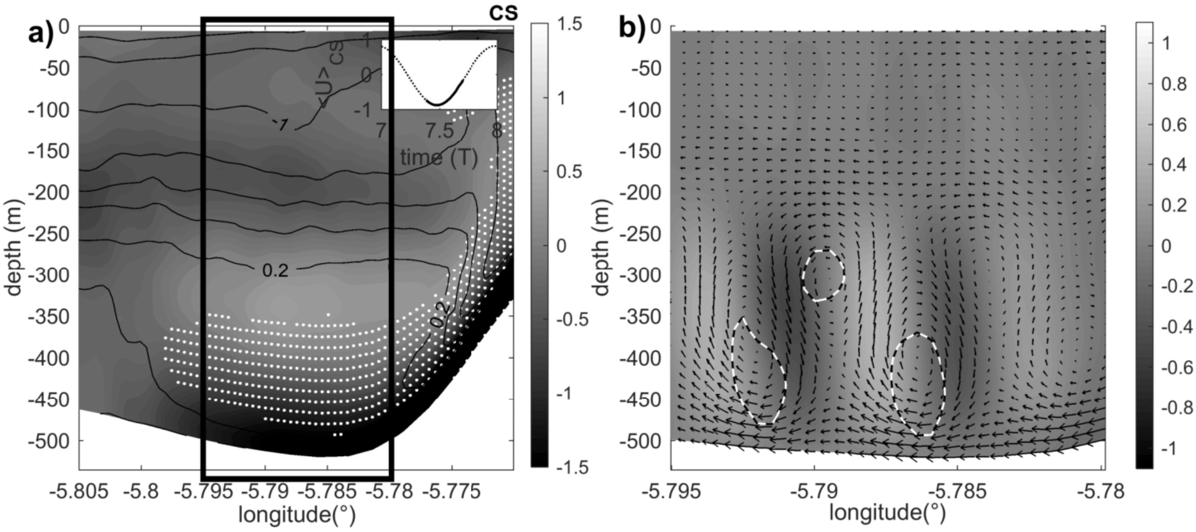

FIGURE 3.7: a) Mean field of longitudinal velocity u (m/s) ; greyscale) and isopycnals (black lines, density anomaly between -1.6 kg m^{-3} and 0.5 kg m^{-3} with an interval of 0.3 kg m^{-3}) with location of Ri<0.25 (white dots). b) Vertical velocity w (greyscale ; m/s) and velocity vectors of the superposition of the second and third singular vectors of the SVD decomposition added to the mean velocity field of (a). Black and white contours are OW=$-1.5 * 10^{-4}$ s^{-2}

Figure 3.7.b shows the reconstructed field of the combination of the second and third singular vectors (respectively responsible for 13 % and 11 % of total variance) added to the mean field

shown in Figure 3.7.a. The Okubo-Weiss parameter is again computed for the resulting velocity field, which shows two rows of y-axis vortices centered at z = -300 m (anti clockwise) and -400 m (clockwise). The upper row of vortices appears to generate the observed interface oscillations.

Based on OW=0 contours, the lower clockwise vortices have an estimated horizontal scale of 200 m and a vertical scale of 150 m, corresponding to horizontal and vertical wavenumbers 3.10^{-2} and 4.10^{-2} m^{-1} respectively. Their propagation speed can be estimated as -0.7 m/s by following the center of the billows defined by areas of negative OW values. The distance between the centers of two consecutive vortices is L = 530 m. The centers of the upper anti-clockwise and lower clockwise vortices are shifted along flow by L/2, so that the extrema of their respective vertical velocities are aligned vertically. It seems that a transfer of momentum occurs between the two rows of vortices in a way reminiscent of the Vallis model of edge waves in a stratified region of a shear flow (pp 254-258 in Vallis (2006)).

The length scales deduced from this SVD analysis can now be compared with expected scales from simple analytical models for shear instabilities and internal waves based on the general characteristics of the flow on the western slope of Camarinal.

Shear flow instability in a two-layer system of infinite depth results in a mixed interface of vertical extent ΔH expressed by equation 14.6 of Cushman-Roisin and Beckers (2011) :

$$\Delta H \approx \frac{1}{k_{min}} = \frac{\rho_0(u_1-u_2)^2}{2(\rho_2-\rho_1)g} \tag{3.2.14}$$

with k_{min} the wave-number of the most unstable mode in this system, taken as the scale of the primary instability that will develop. In the generation area of CS, (u_1-u_2) is in the range of 1.2 to 2 m/s and $(\rho_2-\rho_1)$ is in the range of 1.2 to 1.7 kg/m^3. Additional values are $\rho_0 = 1033.7$ kg/m^3 and g = 9.81 m^2/s. This gives a range of vertical scales between 44 m and 183 m and k_{min} between 2.10^{-2} m^{-1} and 5.10^{-3} m^{-1}. The scales of the simulated lower row of vortices are in the upper part of this range.

Lee waves are another candidate for small-scale transient flow and the interfacial oscillations observed in our solutions. Their generation over topography is expected when tidal excursion is larger that the topographic length scale $1/k_b$, i.e, $k_b u_0/\omega > 1$ (St. Laurent and Garrett, 2002). The slopes of Camarinal Sill are not symmetrical, as can be seen for example in Figure 3.4. On the western side of the sill, the depth increases from 250 m (at 5.76°W) to 510 m (at 5.78°W) over only 1.8 km, whereas on the eastern side it increases from 250 m to 620 m (at 5.65°W) over 9.4 km. k_b is thus chosen in a range between 3.10^{-3} m^{-1} and 6.10^{-4} m^{-1}. $u_0 = 0.4$ m/s is the amplitude of the barotropic tidal current away from the sill. In these conditions, the ratio $k_b u_0/\omega$ ranges between 1.7 (over the west slope) and 8.9 (over the east slope). Based on this, we cannot rule out the possibility that lee waves are generated over the CS.

If the simulated small-scale structures would originate from lee waves, their phase speed would be comparable to a mode-1 internal gravity wave. This can be estimated using the same method as in Appendix 3.2.6 for the average stratification presented in Figure 3.7.a. It yields a value of 1.4 m/s in the area down-flow of the hydraulic jump, which is twice the estimated propagation speed of both rows of simulated structures. Therefore, even though lee-wave generation is theoretically possible, the interfacial oscillations observed in the simulation appear more consistent with the stirring effect of the bottom coherent vortices, whose scales fall within the range of expected values for KH instability.

We conclude that coherent structures are clearly identified in our simulations. They are generated in an area of potentially unstable shear ($Ri < 0.25$) and are associated with billows of lighter mixed fluid. The deeper row of vortices can reasonably be interpreted as Kelvin-Helmholtz primary instabilities. Their downstream behaviour further corresponds to a 2D pairing of two consecutive Kelvin-Helmholtz billows. These billows are advected in a region of westward flow between the Mediterranean vein and Atlantic waters up until 5.8°W. At this location, advection is reduced as the lower layer decelerates and the billows are uplifted in a flow recirculation and mixed in the pycnocline. These small-scale features appear in the simulation for as long as the hydraulic jump is present, injecting water from the pycnocline in the outflow and vigorously mixing the Atlantic and Mediterranean waters until the tidal currents weaken sufficiently for the flow to become subcritical.

However, the dynamics simulated in a 2D vertical section with no transverse flow and no transverse instability may differ from the real ocean. In a fully 3D configuration, primary Kelvin-Helmholtz instabilities should decay faster as secondary Kelvin-Helmholtz instabilities develop along the transverse rotation axis of the primary billows. This is precluded in the present 2D configuration, even with enhanced resolution, as only y-axis billows can occur.

Wesson and Gregg (1994) observed billow structures in the area of CS with an extension of several tens of meters. This length scale is much smaller than the one simulated in the present numerical configuration. However, these observations were made in shallower regions, i.e. probably closer to the generation area : larger billows more in line with those simulated in the present study could thus develop downstream. Further observations on site are needed, although short length-scales and fast propagation speed would require adapted measurement strategies.

Internal Tide Dynamics

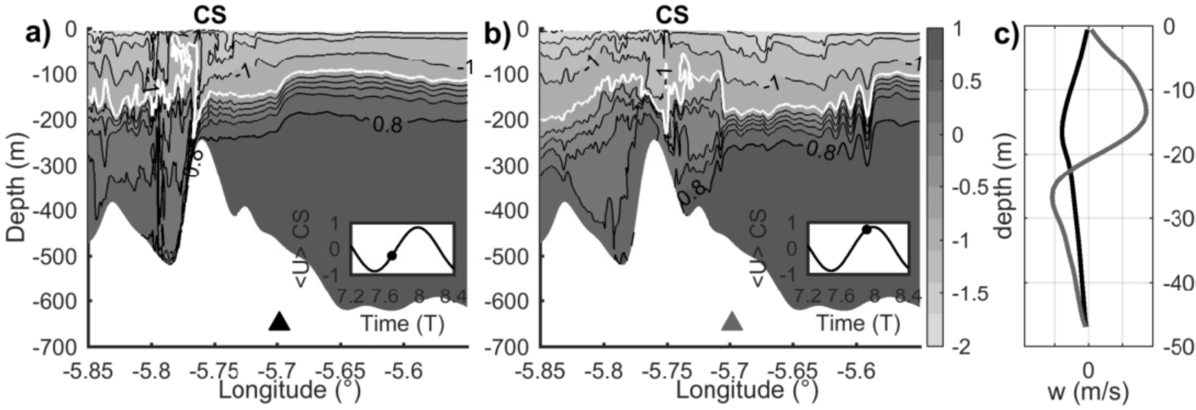

FIGURE 3.8: Density anomaly fields ($\rho\,;\,kg/m^3$) of **SimRef** zoomed over CS at t = 7.7 T (a) and t = 7.9 T (b). The position of $\rho' = -0.7\ kg/m^3$ isopycnal is shown in white. c) Profiles of vertical velocity at the position marked by a triangle in (a)-black and (b)-grey.

In **SimRef**, two main types of large amplitude wave propagating eastward can be observed. Both of them are generated at CS while tidal currents reverse from westward to eastward. This is illustrated in Figure 3.8.a-b. First, a mode-1 wave appears as a bore over the sill's crest approximately 2.25 hours after the westward flow peaks. In Figure 3.8.a, it has propagated over the eastern slope of the sill's crest and is now at 5.7°W longitude : the corresponding profile in Figure 3.8.c has only one maximum as expected for a mode-1 internal wave. This wave rapidly steepens while a hydraulic control is maintained on the western side of the sill with lower values of the Froude number. One hour and 15 minutes later, the flow becomes subcritical and a large-amplitude mode-2 wave crosses the sill. In Figure 3.8.b, this new wave is propagating over the eastern slope of the sill ; its vertical velocity profile is presented in Figure 3.8.c. It exhibits

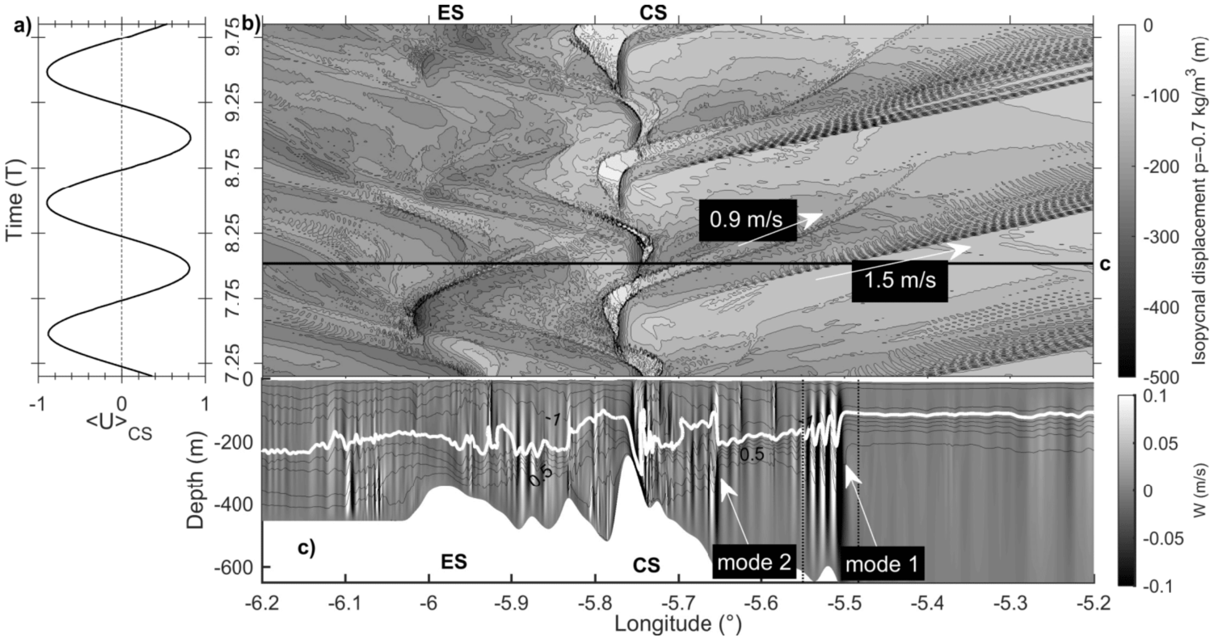

FIGURE 3.9: (a) Depth-averaged currents over CS. (b) Space-time diagram of the vertical displacement of isopycnal $\rho' = -0.7\ kg/m^3$ of **SimRef** ($\Delta z = 50\ m$ between two contours). The black line indicates the time used in the bottom panel. (c) vertical velocity field (greyscale) and isopycnals (black lines ; density anomaly between -1.9 kg m^{-3} and 0.5 kg m^{-3} with an interval of 0.3 kg m^{-3}) at the time indicated in panel (b). In white is the isopycnal $\rho' = -0.7\ kg/m^3$.

two maxima of opposite signs and a zero-crossing at the pycnocline's depth as expected for a mode-2 internal wave. Additionally, it can be seen in this figure that the bore-like wave has evolved into a train of internal solitary waves, whose propagation is discussed below.

The propagation of internal waves can be characterized by plotting a space-time evolution of a particular isopycnal. In Figure 3.9.b, the depth evolution of the $-0.7\ kg/m^3$ isopycnal is represented (also in a white contour in Figure 3.8). Regions of sharp horizontal density gradients can be identified periodically in the region of the CS next to 5.76°W longitude. They correspond to the generation of hydraulic jumps. The propagation of internal waves are identified by the tilt of isolines, whose slopes provide an estimate of wave propagation speed. There are differences from one tidal cycle to the next because mixing progressively changes the background stratification in the domain. In the following, we focus on the tidal cycle $t = 7.5\ T - 8.5\ T$ (second cycle after the end of the spin-up phase), for which the three-tidal-cycle averaged velocity shear and stratification are shown in Figures 3.4 and 3.5.

The mode-1 bore of Figure 3.8.a propagates down-slope of the CS into the TN, where it experiences a transition into a train of solitary waves moving at a speed of 1.5 m/s. In Figure 3.9.c, such a train made of four mode-1 waves can be seen at 5.5°W longitude. The amplitude of the first wave reaches 100 m. The solitons train amplitude momentarily increases and exceeds 150 m as it propagates over the slope near 5.5°W longitude in the TN (still during ebb tide). From then on, the wave amplitude decreases as it propagates towards the deeper region. Meanwhile the dispersion increases the number of waves as well as their wavelength as noticed in the space-time diagram which shows the envelop of the train of solitons expanding while it propagates eastward. The dispersion as simulated in CROCO is compared with the Korteweig deVries model in Appendix 3.2.6.

Similarly, the mode-2 wave shown in Figure 3.8.b propagates through the shallowest part of the TN at a speed of 0.9 m/s as a new hydraulic jump is being generated over the eastern slope of CS. It is located at 5.65°W longitude in Figure 3.9.c, with an amplitude of approximately 100 m. The propagation speed of this mode-2 internal wave subsequently decreases when it reaches the deepest part of the domain while simultaneously the tidal phase shifts to flood. The amplitude of these waves is simultaneously strongly reduced.

The signatures of other large-amplitude internal waves can be seen propagating to the west of the CS in Figure 3.9.b. They are mode-1 and mode-2 internal waves with amplitude in the tens of meters, i.e. smaller than the eastward propagating wave. They are generated when tidal currents switch from eastward to westward in the same fashion as previously described for the wave train produced east of the CS (as tidal currents reverse from westward to eastward).

As discussed in Section 3.2.3, a hydraulic control also occurs at the ES. Figure 3.9.b shows the same variations of isopycnal depth in this area as near the CS during the tidal cycle $t \in [\ 7.5\ T,\ 8.5\ T\ ]$, but not on the following cycle anymore. In the latter case, the computed Froude number does not exceed 0.7, as opposed to previous cycles ($t \in [\ 6.5\ T,\ 7.5\ T\ ]$ and $t \in [\ 7.5\ T,\ 8.5\ T\ ]$) or later ones ($t \in [\ 9.5\ T,\ 10.5\ T\ ]$ and $t \in [\ 10.5\ T,\ 11.5\ T\ ]$). In these cases, the variations are similar and hydraulic control occurs at ES. The sequence is as in CS, with a hydraulic control briefly lost at the barotropic flow reversal. Then internal mode-1 waves of 50-m amplitude at a depth of 300 m are released and propagate toward the CS. In Figure 3.9.c, a mode-1 wave can be found at 5.87°W. These waves dissipate in the area near the sill as the absolute value of the barotropic current decreases.

In Figure 3.9.c, two vertical lines are drawn in the TN. They refer to measurements made by Farmer and Armi (1988) : the lines indicate the first two baroclinic modes locations three and a half hours after high tide. The right-hand vertical line corresponds to a mode-1 wave and is in agreement with the simulation. However, in **SimRef**, the distance between the two modes is twice as large as in the observations. Based on observed wave arrivals at various stations, Farmer and Armi (1988) estimated the propagation speed of both mode-1 and mode-2 waves at about 1 to 2.5 m/s for mode 1 and 1 to 1.5 m/s for mode 2. The wave train they observed contained two to three large-amplitude waves, the first one having an amplitude of 100 m. Additional observations by Sánchez Garrido et al. (2008) in the TN region give a propagation speed for mode-1 waves ranging in 1.2 m/s and 2 m/s with a large variation in the velocity of two consecutive wave trains due to the weight of the tidal diurnal inequality (K1 and O1).

The mode-1 dynamics simulated in **SimRef** are consistent with these observations reported by Farmer and Armi (1988) in terms of propagation speed and longitudinal position. However, the simulated mode-2 wave seems too slow and its amplitude too large. Its slower propagation might be due to an underestimation of the barotropic flow that carries the mode-2 within the TN as our 2D vertical approach does not catch well the tunneling effects of this narrowing. This would not affect the mode-1 wave as much, because its linear propagation speed is more intense and the barotropic current advection becomes comparatively small.

The brief hydraulic control loss observed when the tidal currents reverse does not reflect the quasi-permanent control thought to be taking place at ES. In this case, no internal waves packet can be emitted from the ES.

3.2.4 Sensitivity Testing

The reference configuration presented in the previous section is based on several physical and numerical choices which are now investigated; mostly the impact of the forcing amplitude, momentum balance (hydrostatic approximation) and numerical parameters (spatial resolution, advection schemes).

Tidal regime

An additional simulation, **SimS**, is first performed similarly to **SimRef** changing only the tidal forcing amplitude. The imposed tidal current amplitude at the western boundary is now increased up to 0.6 m/s, so that it reaches 1.3 m/s over the CS. This corresponds to a spring-tide regime.

Figure 3.10 presents a comparison between **SimS** and **SimRef**. In Figure 3.10.a, the contours of supercritical regions ($F > 1$) show the CS hydraulic jump extends further east in **SimS**. As a result, a mode-1 disturbance (denoted "a" in Figure 3.10.a) is trapped at 5.725°W longitude. It propagates eastward when the flow becomes subcritical but the faster bore that is crossing the CS can rapidly catch it up. The outflowing Mediterranean water vein on the westward side of the sill is also thicker in **SimS** and so is the supercritical area. In addition, a new supercritical region appears on the western slope of a secondary relief at 5.83°W longitude (denoted "b" in Figure 3.10.a) with trailing lee waves.

The Figure 3.10.b shows an eastward propagating mode-1 solitons packet. Since the initial stratifications are similar, linear phase velocities are the same in **SimRef** and **SimS** at the beginning. The amplitude of the first trough of the train is 50-m larger in **SimS** than in **SimRef**. This should result in increased propagation speed of the solitons in **SimS**, in contradiction with a slower propagation seen in Figure 3.10.b. It can be explained by the stronger tidal currents advection in the opposite direction in **SimS**. A mode-2 wave is also generated in both **SimS** and **SimRef**, but is only visible in **SimRef** in Figure 3.10.b as it quickly dissipates in **SimS** due to stronger tidal currents. Consistent with our results, Farmer and Armi (1988) show that the ISW amplitude increases with the tidal current during the spring-tide / neap-tide cycle. In addition, two concomitant hydraulic jumps were observed in the strait during spring tide ((Sánchez Garrido et al., 2011)) : they exhibit a transverse asymmetry, as the second jump only appears in the northern part of the strait. This could not be confirmed in the present 2D configuration.

Nonhydrostatic Balance and Numerical Factors

The consequences of several numerical choices are now investigated by running five additional simulations whose differences with **SimRef** are laid out in Table 3.3. In particular, the sensitivity to both vertical and horizontal resolution is targeted. A hydrostatic kernel and a WENO5-Z advection scheme for momentum Borges et al. (2008) are also tested and compared with **SimRef**. We focus on the impact of these modifications on two types of small-scale processes studied in the previous sections : the primary (KH) instability generation in the hydraulic jump at the CS, and the eastward propagating solitary waves generated at the same place.

TABLE 3.3: Parameters of numerical sensitivity experiments. If not explicitly indicated, t_s and t_f are the same as in Table 3.1.

SimH	Hydrostatic equations ($t_s = 0.5s \quad t_f = 0.25s$)
SimW	WENO5-Z momentum advection scheme
SimV	80 σ-levels
SimL	220-m horizontal resolution ($t_s = 4s \quad t_f = 0.5s$)
SimLH	220-m horizontal resolution with hydrostatic equations ($t_s = 2s \quad t_f = 1s$)

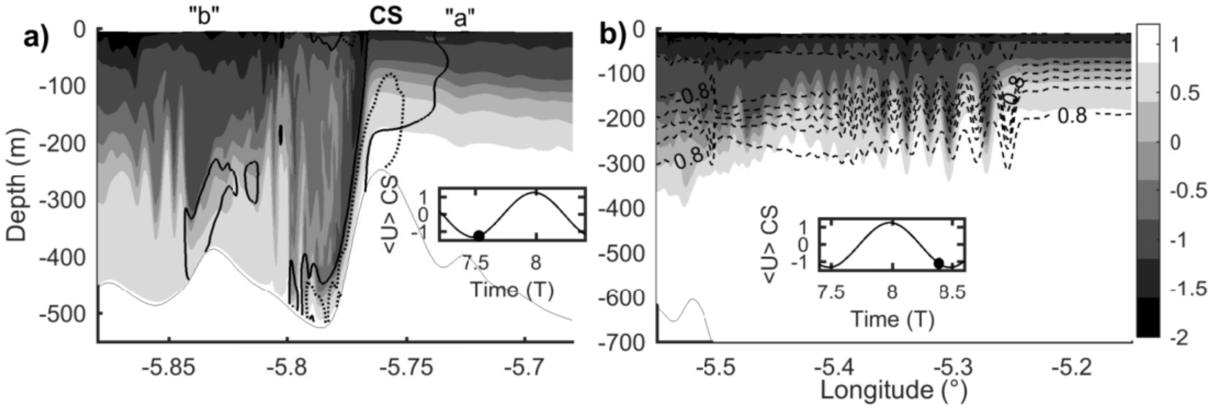

FIGURE 3.10: Comparison of experiments **SimS** and **SimRef** showing the effect of tidal amplitude on the generation of solitary waves. a) Relative density (kg/m^3) in **SimS** during a hydraulic jump ($t = 7.5\ T$) at Camarinal Sill. Regions where $F > 1$ are indicated for both **SimS** (bold lines) and **SimRef** (dashed lines). New features appear with stronger tides : a mode-1 disturbance "a" trapped upstream of the CS ; an additional supercritical area ($F > 1$) noted "b" in the bottom layer of a secondary relief. b) Relative density in **SimS** (greyscale) and **SimRef** (dashed lines) at $t = 8.5\ T$, showing the tidal amplitude effect on eastward propagating solitary waves generated at CS.

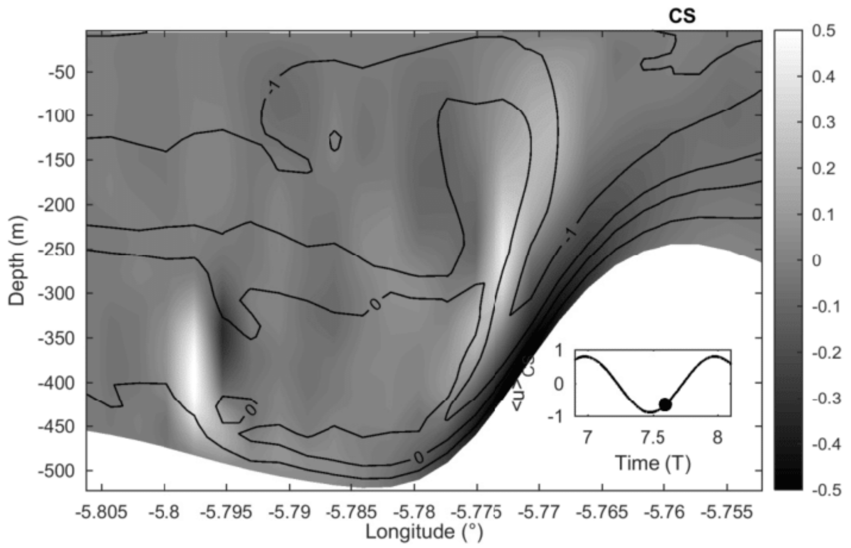

FIGURE 3.11: Vertical velocity (greyscale ; m/s) and isopycnals (black lines ; density anomaly between -1.5 kg m^{-3} and 0.5 kg m^{-3} with an interval of 0.5 kg m^{-3}) in **SimLH**.

Hydraulic Jump and Instabilities Hydraulic controls (Section 3.2.3) occur in all simulations, as revealed by systematic estimations of the Froude numbers. Low Richardson numbers (< 0.25) are also diagnosed for all simulations over at least part of the CS western slope during flood. However, the features that have been identified as KH instabilities in Section 3.2.3 do not appear in all simulations. They are absent in the simulations performed in the hydrostatic framework and/or with low horizontal resolution (**SimL**, **SimLH** and **SimH**). Weak horizontal vorticity tilting under the hydrostatic assumption prevents such instabilities to develop. Instead, a smooth, large recirculation appears west of the CS (Figure 3.11 for **SimLH**).

In the remaining sensitivity experiments (**SimV** and **SimW**), KH instabilities are generated at the edge of the hydraulic jump and their dynamics is overall similar to the one described in

Section 3.2.3 for **SimRef** : pairing of KH billows can occur whereas anti-clockwise vortices induce oscillations of the interface. Fine resolution (a few tens of meters in the present region) and non-hydrostatic equations are both required to explicitly simulate the turbulent cascade onset with KH instabilities between Mediterranean and Atlantic flows.

Interestingly enough, a comparison of Figures 3.6 (nonhydrostatic configuration) with Figure 3.11 (hydrostatic configuration) shows that the fine-scale solution is largely filtered out by the hydrostatic assumption. Without dedicated observations in the area, it remains difficult to conclude that **SimRef** is more realistic, although low Richardson numbers in this region lead us to expect KH instability.

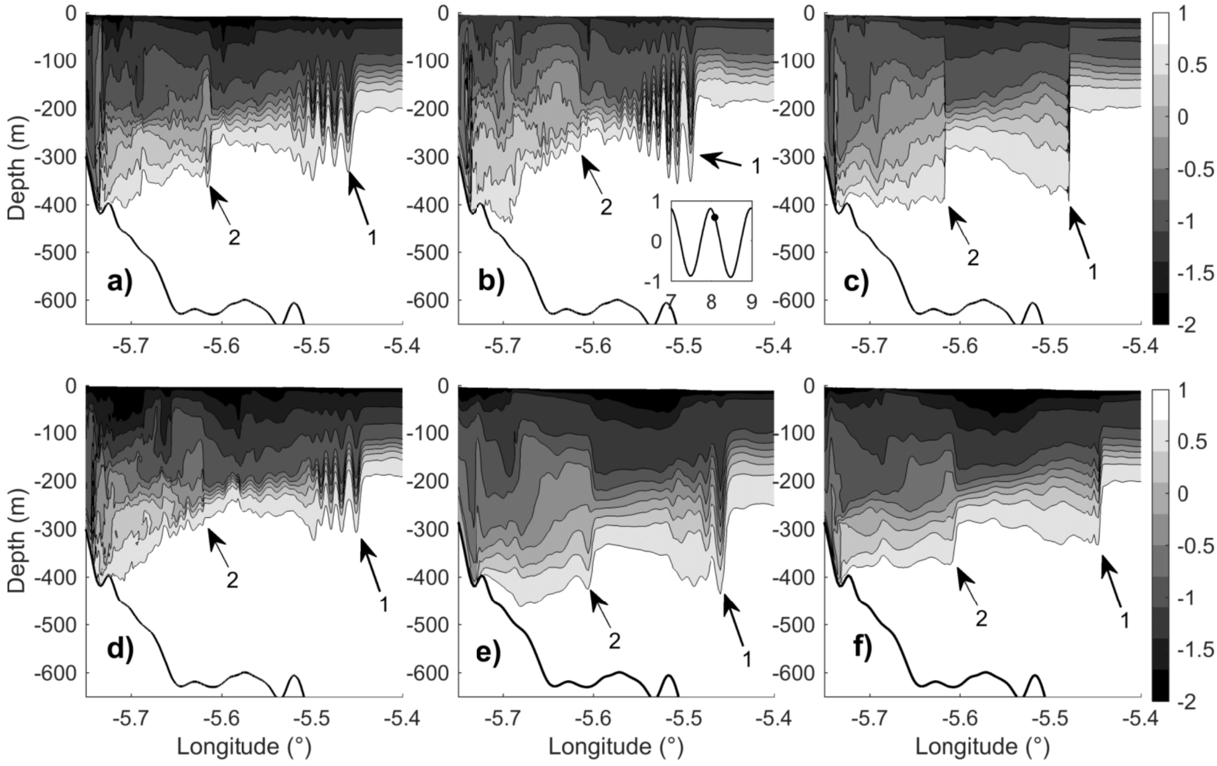

FIGURE 3.12: Internal wave propagation from density field at $t = 8.1T$ in (a) **SimRef** ; (b) **SimW** ; (c) **SimH** ; (d) **SimV** ; (e) **SimL** ; and (f) **SimLH**. Large amplitude mode-1 waves (soliton or bore) are denoted as "1" and mode 2 as "2".

Large Internal Waves As described in Section 3.2.3, mode-1 and mode-2 large amplitude internal waves are generated in the CS vicinity and propagate eastward during each ebb in all nonhydrostatic simulations. Figure 3.12 presents the density fields in the region of the TN at $t = 8.1\ T$. A wave train with a minimum of two solitons can only be identified in the nonhydrostatic experiments. In the hydrostatic cases **SimH** and **SimLH**, the lack of nonhydrostatic dispersion produces internal waves propagating as internal bores. In the nonhydrostatic cases, these internal waves can propagate as trains of solitons with varying numbers of solitons (and celerity) : 6 in **SimRef**, 8 in **SimW**, 4 in **SimV**, and 2 in **SimL**.

This illustrates a second aspect of the effect of hydrostatic assumptions, besides the inhibition of turbulent primary instabilities (KH instabilities in the region of the hydraulic jump). As already noted by previous authors (Sannino et al., 2004), the dispersion needed to balance nonlinear steepening in large-amplitude solitary waves is missing in hydrostatic simulations such as **SimH** and **SimLH** (Figure 3.12).

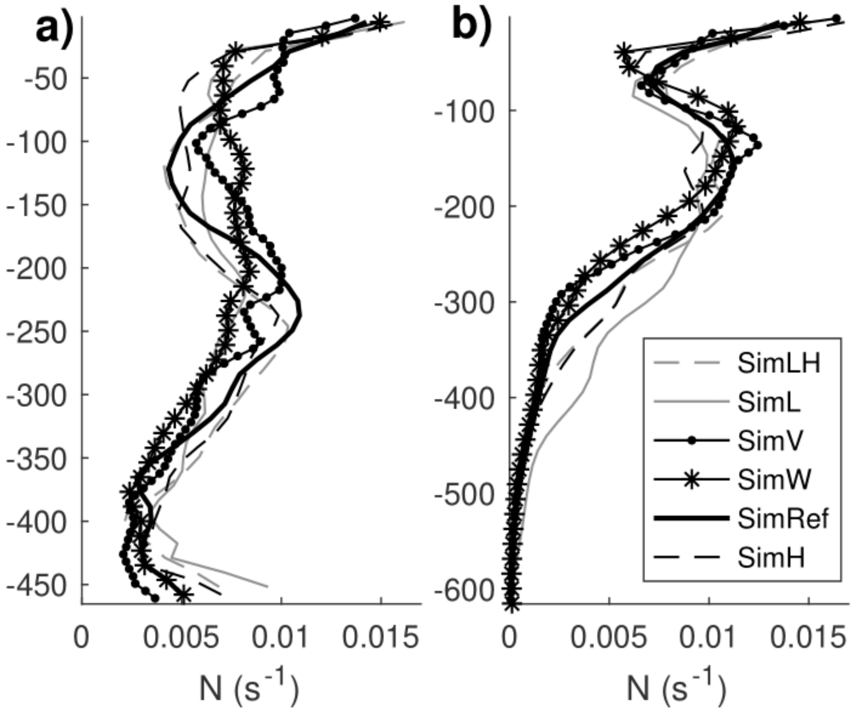

FIGURE 3.13: a) N frequency computed at 5.8°W longitude and time-averaged between 8.2 T and 8.7 T (during flood tide and presence of hydraulic jump). b) Same as (a) but at 5.55°W longitude.

Evolution of Stratification The previous results lead us to anticipate large differences in the way density stratification evolves in **SimRef**, **SimW**, **SimV**, **SimH**, **SimL**, or **SimLH**. To go further, Figure 3.13 shows for each configuration the profiles of Brunt-Väisälä frequency (N defined in Equation 3.2.13) at 5.8°W (a) and at 5.55°W (b). Profiles are time-averaged over one flood.

At 5.8°W, stratification is similar in **SimH** and **SimLH** with an interface region (defined as the region where N is maximal, here $N = 8.10^{-3}$ s^{-1}) located at a depth of 250 m (Figure 3.13.a). The nonhydrostatic simulations **SimRef** and **SimL** present an interface region at a similar depth but the vertical gradients are larger in **SimRef** and smaller in **SimL**. **SimV** shows larger vertical gradients of density (N = 1.1 10^{-2} s^{-1}) and a shallower interface at a depth of 150 m. **SimW** is weakly stratified over most of the water column with no clear interface between the two water masses. This result may seem surprising because the WENO5 scheme is of fifth-order accuracy with more selective quasi-monotonic corrections near shocks than the TVD scheme, and is thus expected to produce less smoothing. This apparent contradiction can be explained by the generation of more intense primary shear instabilities (i.e. with higher values of associated vertical velocity and vertical velocity gradients), which has the effect of diffusing density gradients.

In Figure 3.13.b, averaged N profiles over one flood are shown at 5.55°W longitude in a region subjected to intense internal wave activity. **SimH**, **SimLH** and **SimL** exhibit similar profiles with N slowly decreasing below the interface at 160 m. **SimRef** has a similar interface at 160 m but with higher N value, although weaker stratification appear at the top of the lower layer. **SimV** and **SimW** both have shallower interfaces at 130 m, with N reaching the highest values in **SimV** (N = 1.25 10^{-2} s^{-1}), as the enhanced vertical resolution allows the representation of stronger gradients.

Clear conclusions cannot yet be drawn concerning mixing. KH instabilities are expected in the region of the hydraulic jump and downstream. They lead to more stirring and consequently open up new opportunities to improve modelling of the route to mixing. Further investigation and diagnostics are now required to better understand the energy cascades. In particular, the present comparison between WENO5 and TVD advection schemes (and their implicit dissipation) indicates that numerical choices may unfortunately still have large consequences. Therefore, the role of physical and numerical closure must be considered comprehensively (Marchesiello et al., 2011; Soufflet et al., 2016).

3.2.5 Discussion and Conclusion

The present study focuses on small-scale dynamics in the Strait of Gibraltar and on the capacity of a new split-explicit, free-surface, nonhydrostatic regional oceanic model (CROCO) to represent such dynamics. Both objectives were pursued in parallel and several seminal results are obtained.

The study confirms that the generation of large-amplitude mode-1 and mode-2 internal waves in the Strait of Gibraltar as well as the onset of stratified turbulence and its energy cascade can be simulated with a computationally-efficient 2D vertical section. The characteristics of the simulated internal waves compare qualitatively well with published observations and previous numerical studies. Internal tides dynamics and shear instability in the hydraulic jump area are then analysed in more details, revealing characteristics and mechanisms.

The results of the study rely on a new type of nonhydrostatic, non-Boussinesq, free-surface kernel (Auclair et al., 2018) implemented in the CROCO model. The resulting compressible oceanic model is presented in a realistic nonhydrostatic configuration for the first time. Sensitivity tests confirm that a nonhydrostatic (here non-Boussinesq) kernel is required (i) to simulate ISW trains and (ii) to explicitly simulate the onset of stratified turbulence energy cascade, provided that resolution is increased from about 200 m to 50 m. We conclude that resolutions finer than a few hundred meters are required in addition to a refinement of dynamical equations (relaxation of hydrostatic assumption) in order to solve the dominant dynamical processes in a key region of the Mediterranean.

Detailed characteristics of the vertical 2D configuration are also given with particular attention to the bathymetry and to the representation of the Coriolis force (implicit representation of funnelling effect in the strait). The proposed approach offers a computationally affordable way to make preliminary investigations of internal-wave dynamics in regions where these waves are important. However, the vertical 2D configuration is limited by the simplified representation of bathymetry and associated biases in the velocity shear between in-flowing Atlantic Waters and out-flowing Mediterranean waters. The inclusion of restratification processes (surface and boundary forcing) would allow the model to remain accurate for a greater number of tidal cycles — the present configuration is considered accurate within three days after the spin-up period, before mixing starts to homogenise the water masses. Several remaining processes could not be considered : the transverse propagation of ISWs in the Strait of Gibraltar (Sánchez Garrido et al., 2011; Vlasenko et al., 2009) and in the Alboran Sea ; the hydraulic control at the TN (Farmer and Armi, 1988; Sannino et al., 2009b) ; the boiling-water over the CS (Bruno et al., 2002) or reflections on the strait's coasts.

Only the "onset" of turbulence cascade could be simulated showing complex dynamics occurring in the area of the hydraulic jump at CS, with some small scale features identified as primary Kelvin-Helmholtz instabilities. Although this 2D study highlights how interesting this area can be, there is no doubt that simulation of secondary KH instabilities and subsequent energy cascade as well as the long term impact of these small scale processes on Mediterranean and North Atlantic circulation will require a fully 3D LES approach as well as dedicated field campaigns that explore these fine-scale processes.

3.2.6 Appendices

Appendix : evaluation of the first internal Rossby radius

The first internal Rossby radius is defined as :

$$R = \frac{\sqrt{g'h}}{f} \tag{3.2.15}$$

At the Gibraltar Strait's latitude, the Coriolis parameter is $f = 8.5 \times 10^{-5}\ s^{-1}$. The numerator $c^* = \sqrt{g'h}$ is the phase speed of the linear interfacial waves, into which the reduced gravity is :

$$g' = g\frac{\rho_M(S_M) - \rho_A(S_A)}{\rho_0} \tag{3.2.16}$$

where $\rho_M(S_M) - \rho_A(S_A) \approx 2\ kg/m^3$. If the reference density is set to $\rho_0 = 1033.7\ kg/m^3$ and the gravity acceleration by $g = 9.81\ m^2/s$, $g' = 0.02\ m/s^{-2}$ which is in agreement with in situ data (cf Bryden et al. (1994)). h is a characteristic height given by :

$$h = \frac{h_1 h_2}{h_1 + h_2} \tag{3.2.17}$$

where h_1 and h_2 are respectively the upper and lower layer thicknesses. Picking up the data values from Farmer and Armi (1988) (Table 3.2, first line), we obtain a range of $h = 50 - 100\ m$, which combined with the previous values for g' and f leads to R ranging in 11.5 km (east of Camarinal Sill) to 16 km (west of Camarinal Sill).

$\sqrt{g'h}$ can be replaced by the mode-1 internal waves speed (c_1), which is estimated in the present study (Appendix 3.2.6) for the 3T-averaged stratification (**SimRef**) presented in Figure 3.5. c_1 ranges between 0.8 m/s (at Camarinal Sill) and 1.8 m/s (in the eastern part of the strait), giving an estimated range of Rossby Radius c_1/f between 9.5 and 21 km for the simulated section.

Appendix : computation of a Froude number

A single value of mode-n linear internal wave phase speed (c_n) can be computed for a flat-bottom and a linear stratification. This velocity can then be compared at each depth with the magnitude of local horizontal currents (u) to estimate when and where internal waves can propagate against currents. A diagnostic tool is the ratio of velocities, i.e. a Froude number (F_n) defined as $F_n = u/c_n$. $c_n = \omega/k_n$ where ω is the wave frequency, here the M2-tidal frequency, and k_n are eigenvalues obtained by solving numerically the Sturm-Liouville problem associated with the linear propagation equation (Gill, 1982) :

$$W_n'' + k^2\frac{N^2 - \omega^2}{\omega^2 - f^2}W_n = 0 \tag{3.2.18}$$

with bottom and surface boundary conditions $W_n(0) = 0$ and $W_n(-H) = 0$. W_n gives the structures of vertical modes. For each point on the x-axis, the profile N(z) is computed with Equation 3.2.13 from the 3T-averaged stratification in **SimRef** (shown in Figure 3.5).

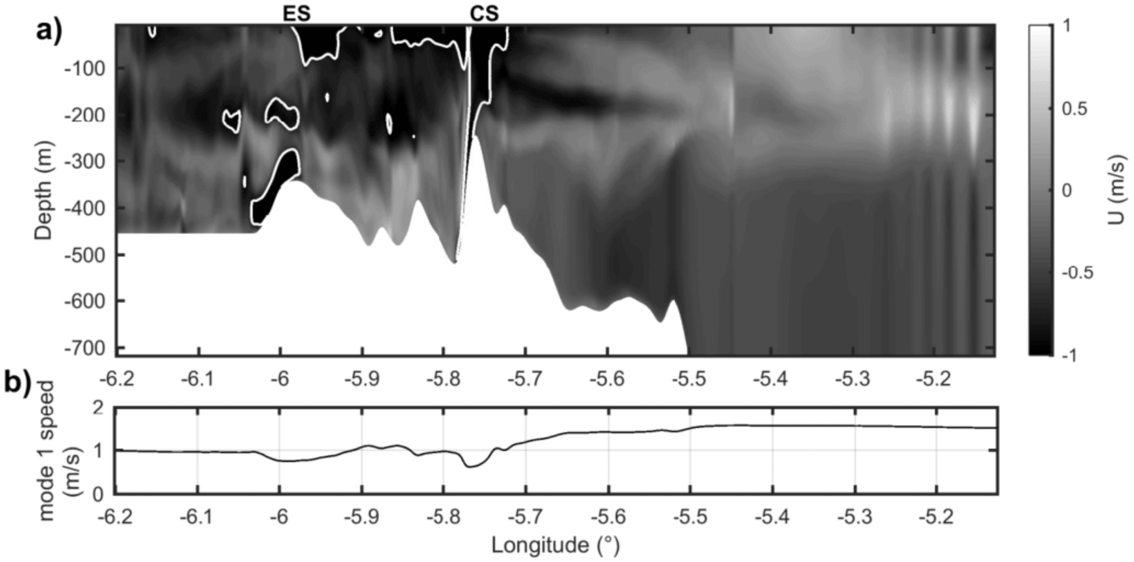

FIGURE 3.14: a) Field of longitudinal velocity ($u(x,z)$) at $t = 8.5\ T$ with contours of mode-1 supercritical region (F>1) calculated from a 3T-averaged stratification. b) Computed speed of mode-1 linear internal waves ($c_1(x)$) from a 3T-averaged stratification in configuration **SimRef**.

The value of the first mode phase speed $c_1(x)$ is indicated in the lower panel of Figure 3.14 and compared to the longitudinal velocity $u(x,z)$ at $t = 8.5\ T$ plotted in the upper panel. The areas where $u(x,z) > c_1(x)$ (equivalent to Froude number F_1 larger than 1) are presented in the upper panel as well. The flow inside those contours is called supercritical.

Appendix : computation of Okubo-Weiss parameter

The Okubo-Weiss parameter (OW) is defined as

$$OW = s_n^2 + s_s^2 - \Omega^2 \tag{3.2.19}$$

With s_n the normal strain component, s_s the shear strain component and Ω the vorticity. Usually, it is used in a xy-plane (e.g., for tracking eddies in Chelton et al. (2007)), but it is computed here in the zx-plane with the strains and vorticity expressed as :

$$s_n = \frac{\partial w}{\partial z} - \frac{\partial u}{\partial x} \quad , \quad s_s = \frac{\partial u}{\partial z} + \frac{\partial w}{\partial x} \quad , \quad \omega = \frac{\partial u}{\partial z} - \frac{\partial w}{\partial x} \tag{3.2.20}$$

Negative values of OW indicate a greater role of rotation over deformation, and thus the presence of coherent vortices.

Appendix : a Korteweg-de Vries (KdV) model

Following many studies (Sánchez Garrido et al., 2008; Sannino et al., 2009b; Vlasenko et al., 2009), the large amplitude internal waves of Section 3.2.3 are termed ”ISWs” for Internal Solitary Waves. To confirm that the internal waves observed in this section are ISWs, they are

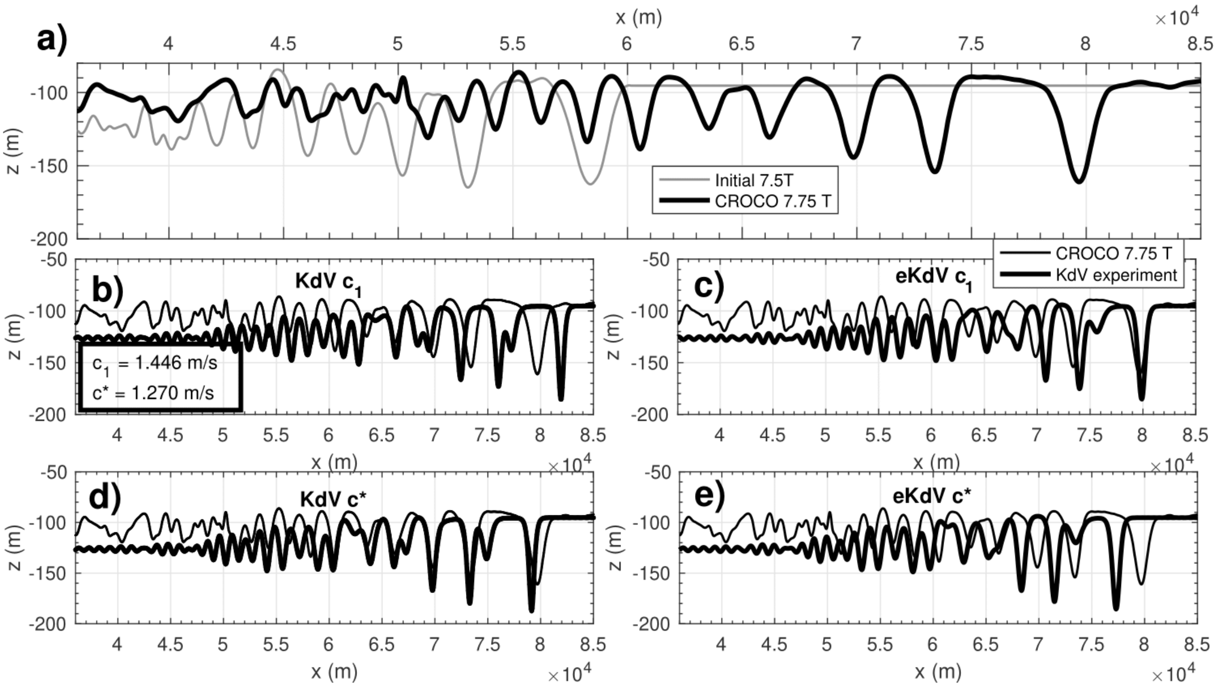

Figure 3.15: a) Isopycnal $\rho' = -0.2$ kg/m^3 simulated by CROCO in **SimRef+** at $t = 7.5\,T$ (grey line ; the interface depth is left constant downstream of the wave) and at $t = 7.75\,T$ (black line). b-e) Evolution of the interface simulated by KdV or eKdV (bold) and **SimRef+** (solid line) at $t = 7.75\,T$. Two propagation speeds are used : c_1 (b,c) and c^* (d,e) (see text for details).

now compared with solutions of the Korteweg-de Vries equation which is recalled below. The solutions of this equation satisfy a balance between nonhydrostatic dispersion and nonlinear advection. Nonlinear advection steepens the wave front, whereas nonhydrostatic dispersion reduces steepening by transferring energy from large to small scales, resulting in a relatively stable entity called a ”solitary” wave, or soliton.

The Korteweg-de Vries (KdV) equation describes the evolution of an infinitely thin interface in a two-layer system with constant bottom topography :

$$\frac{\partial\zeta}{\partial t} + c^*\frac{\partial\zeta}{\partial x} \underbrace{+\frac{3}{2}\frac{h_1-h_2}{h_1h_2}c^*\zeta\frac{\partial\zeta}{\partial x}}_{A} \underbrace{+\frac{1}{6}h_1h_2c^*\frac{\partial^3\zeta}{\partial x^3}}_{B} \underbrace{-\frac{3}{8}\zeta^2c^*\frac{h_1^2+6h_1h_2+h_2^2}{8(h_1h_2)^2}}_{C} = 0 \tag{3.2.21}$$

where c^* is the interfacial speed of small-amplitude internal waves : $c^* = \sqrt{g'h} = R\,f$ and ζ is the vertical displacement of the interface. g' and h have already been defined in Appendix 3.2.6. The first two terms on the left-hand-side of Equation 3.2.21 are those involved in the classical propagation equation for a small-amplitude, linear, interfacial wave travelling in the x-direction at speed c^*. The third term (bracket A) is a first-order approximation (with respect to amplitude) of nonlinear advection. Term (B) is a dispersive term. The fifth term (C) is a higher-order non-linear term associated with a second order development for advection. The complete Equation 3.2.21 will be referred to as "extended KdV" (or "eKdV"), whereas the same equation without term (C) will simply be referred to as "KdV" (Dossmann, 2012).

The simulated large amplitude waves presented in this study are compared with the solutions of the KdV or eKdV equation to gain insight into their dynamics. For optimal comparison, a new simulation, called **SimRef+** was carried out. Its characteristics are similar to **SimRef** (Table 3.1), except that (i) the eastern boundary is shifted 42-km to the east into the Mediterranean sea and (ii) the tidal forcing is stopped after only 7.25 periods. The first eastward-propagating train of mode-1 waves generated by the tide at the CS is compared with the propagation given by numerical integration of the KdV and eKdV equations (Equation 3.2.21).

The vertical displacement of isopycnal $\rho' = -0.5\ kg/m^3$ is extracted[5] at $t_0 = 7.5\ T$ when the mode-1 ISW train propagates over a region of constant depth ($H = 890\ m$) east of TN (Figure 3.15), so as to get closer to the KdV framework. The position of the chosen isopycnal surface at this time is shown in Figure 3.15.a. At that time, the distance between the first and second solitons of the train is 5 km ; the first soliton has an amplitude of 75 m and the train includes 7 solitons. This isopycnal is chosen as initial state for the KdV or eKdV model. The KdV and eKdV equations are integrated either with the interfacial wave speed ($c^* \approx 1.27\ m/s$) or with mode-1 velocity ($c_1 = 1.45\ m/s$; see Appendix 3.2.6 for details on c_1 evaluation).

Figures 3.15.b-e compare the interface depth obtained at $t = t_0 + 0.25\ T$ in the KdV and eKdV models with the position of the $-0.5\ kg/m^3$ isopycnal in **SimRef+**. In the latter, the distance between the first two solitons has grown since $t = t_0$ and reaches 7 km with an amplitude of 70 m for the first trough. The train is now made of 11 solitons : the first three have decreasing amplitudes, then two smaller solitons of comparable amplitude (40 m) and one soliton of greater amplitude, followed by solitons with decreasing amplitude again.

In the KdV solution obtained with propagation speed c* the first solitary wave is slightly slower but its amplitude is markedly larger (Figure 3.15.d). The remaining solitons of the train are well located, but a secondary trough is generated between the first two solitons whereas it is absent in **SimRef+**.

Using the larger mode-1 speed c_1 instead of c^* (Figure 3.15.b), the train of solitons in KdV is too fast. When the eKdV equation is used with speed c^* (e), the solitons are too slow, whereas this same extended equation with c_1 (c) leads to a correct displacement of the solitons. Overall, the temporal evolution of solitary waves in **SimRef+** is consistent with the solutions of the KdV or eKdV equation (Equation 3.2.21). However, the KdV or eKdV framework remains an inviscid simplification. Note that closer evolution of soliton amplitudes between KdV or eKdV and **SimRef+** solutions can be obtained by simply adding a diffusive term in KdV or eKdV equation. This also slows down propagation in KdV, and to a lesser extent in eKdV (not shown).

The KdV or eKdV model also involves adjustable parameters, such as the linear wave speed, which ranges between the interfacial speed c^* and the mode-1 speed c_1, each being one particular approximation of the wave's behaviour.

That being said, the wave trains in **SimRef+** are appropriately modeled as KdV or eKdV ISWs, which confirms (i) the propagation of interfacial troughs as trains of solitons and (ii) CROCO's ability to simulate the subtle balance between nonhydrostatic effects (responsible for dispersion) and nonlinear advection.

Acknowledgments This work was partly funded by the DGA "Etude Amont" Protevs driven by the Shom. It was granted access to the HPC ressources of CALMIP supercomputing center under the allocation P18017. We also gratefully thank the computer team of the *Laboratoire d'Aérologie* for its support. Margaux Hilt's PhD thesis was funded by a MESRI scholarship.

---

[5] Due to the extension of the domain to the east, a new value of ρ_0 is computed : $\rho_0 = 1033.9\ kg/m^3$ to optimize computations.

-4- Simulation des grandes structures turbulentes (LES, 3D) dans le détroit de Gibraltar

4.1 Résumé en français.

Présentation. Ce chapitre détaille l'étude de la dynamique de fine échelle dans le détroit de Gibraltar, basée d'une part sur les résultats d'une configuration numérique dite à "haute résolution" (§4.2), d'autre part sur l'analyse d'un choix d'observations *in situ* effectuées au cours de la campagne de mesures *Protevs Gibraltar 2020* (§4.3).

Les simulations analysées dans la Section 4.2 s'inscrivent dans la continuité de celles présentées dans le Chapitre 3 : aucun forçage atmosphérique n'est intégré, cependant l'écoulement est tri-dimensionnel et prend en compte des forçages réalistes : une initialisation et des forçages aux frontières issus du modèle opérationnel de l'"Agenzia Nazionale per le Nuove tecnologie, l'Energia e lo Sviluppo economico sostenibile" (ENEA, Rome) ainsi qu'une bathymétrie à haute résolution (SHOM) sont utilisés. La stratification des masses d'eaux et les ondes de marées sont ainsi représentées de façon plus réaliste. Le choix de ne pas inclure le forçage atmosphérique dans cette première génération de configuration à haute résolution vise à simplifier l'analyse des mécanismes et des processus à l'oeuvre dans cette région réputée très riche d'un point de vue dynamique. Une seconde génération de configurations déjà en place sera analysée dans une prochaine étude afin d'enrichir la dynamique simulée et d'aller vers plus de réalisme.

Le développement et l'analyse de la maquette numérique constituent la première partie de ce chapitre. L'étude s'est focalisée sur la variabilité durant un cycle "morte-eau" / "vive-eau", c'est-à-dire la variabilité liée à l'intensité du forçage de marée semi-diurne. Ainsi, trois situations sont plus spécifiquement analysées correspondant à une période de morte-eau (SimNT), une période de vive-eau (SimST), et une période intégrant la partie croissante du cycle (SimIT).

L'analyse s'effectue par le biais de divers diagnostics mis au point au cours de la thèse. Les différentes configurations de l'écoulement (subcritique ou surcritique) des masses d'eaux méditerranéennes et atlantiques sont présentées, ainsi que la propagation des solitons et la génération d'instabilités primaires de cisaillement. Dans ce dernier cas, un test de sensibilité aux schémas de fermeture turbulente a été réalisé.

L'étude détaillée de la dynamique de la région du détroit à partir de ces simulations a aidé à préparer la campagne Protevs/Gepeto Gibraltar 2020, qui s'est déroulée en Octobre 2020. Elle a en outre contribué à l'analyse des mesures réalisées durant cette même campagne (§4.3).

Les observations présentées dans la Section 4.3 sont essentiellement des données issues de trois mouillages, un premier positionné au seuil de Camarinal (mouillage Mo2), et deux autres juste à l'est visant à intercepter le train de solitons se propageant après relaxation du ressaut hydraulique (mouillages Mo4 et Mo5). Dans la présente analyse, seule une partie des données est présentée : elle correspond à la période durant laquelle tous les mouillages sont présents sur zone. Comparaison est faite avec les "pseudo-observations" mimant des données de mouillage dans les simulations numériques de la première partie du chapitre (Section 4.2).

Principaux résultats. La simulation numérique des grandes structures turbulentes dans la région du détroit de Gibraltar a donné plusieurs résultats originaux. Trois configurations dynamiques de l'écoulement au-dessus du seuil de Camarinal ont été proposées et analysées. Elles correspondent à trois configurations typiques de forçage par la marée dans cette région. Les périodes choisies se distinguent par la présence (ou l'absence) de ressauts hydrauliques ainsi que par leur localisation spatiale. Les ressauts sont associés aux transitions surcritiques / subcritiques des eaux atlantiques et méditerranéennes. Ces configurations sont qualifiées de *no-jump* (pas de ressaut détecté), *s-jump* (ressaut à l'aplomb de la partie la moins profonde du seuil) et *w-jump* (ressaut localisé au-dessus de la pente ouest du seuil).

La distinction des situations *s-jump* et *w-jump* avait déjà été proposée dans une étude antérieure (Sánchez-Garrido et al., 2011). Toutefois, dans la présente étude, en situation *w-jump* les deux ressauts restent distincts de part et d'autre du seuil, alors que ces deux mêmes ressauts sont déplacés sur l'ouest du seuil dans l'étude proposée par Sánchez-Garrido et al. (2011).

Les marées de plus faible amplitude en périodes de mortes-eaux correspondent à une situation *no-jump*, les plus fortes en périodes de vives-eaux à la situation *w-jump*. La situation *s-jump* est un cas intermédiaire. Les simulations réalisées montrent que la relaxation du ressaut hydraulique débouche bien sur la propagation d'un train d'ondes solitaires. Cependant, elles montrent aussi clairement que la propagation de l'onde longue de marée barocline à travers le détroit sans présence préalable de ressaut (situation *no-jump*) peut elle aussi dégénérer en un train de solitons sous l'effet de mécanismes non-linéaires. Dans ce cas, le nombre de solitons du train se propageant en mer d'Alboran est réduit, l'amplitude de l'anomalie de profondeur de l'interface initiale étant elle-même plus faible.

Outre la propagation du soliton, la simulation à haute résolution permet (comme au Chapitre 3) de simuler explicitement des instabilités de cisaillement dans le courant de densité à l'ouest du seuil de Camarinal durant les périodes de reflux de la marée (*outflow*). Les zones probables de leur génération ne changent pas entre les situations *no-jump* et *s-jump* et sont centrées sur les deux sillons nord et sud de part et d'autre du point culminant du seuil de Camarinal. En situation *w-jump*, cette génération se fait à toutes les latitudes.

Une étude de sensibilité de la simulation de ces instabilités aux schémas de fermeture turbulente (schéma dit de "Smagorinsky" avec ajustement des paramètres ou schéma GLS) a permis de mettre en exergue l'impact de ces fermetures sur la composition hydrologique du courant méditerranéen via le mélange avec les eaux atlantiques.

Campagne Protevs Gibraltar 2020. Les simulations numériques à haute résolution ont enfin été confrontées aux observations réalisées dans le cadre de la campagne d'observations Protevs Gibraltar 2020 à la laquelle j'ai activement participé à l'automne 2020. Même si cette analyse demeure préliminaire (cette campagne s'est tenue durant ma dernière année de thèse et a été très contrainte par la pandémie de COVID), un certain nombre de résultats ont d'ores et déjà pu être mis en évidence :

- Sur les cinq types de situations observées aux mouillages Mo4 et Mo5, quatre sont illustrées dans les simulations numériques proposées. Seul une situation ressemblant à un bore interne est absent des simulations numériques.
- Deux des situations correctement reproduites correspondent à des trains de solitons associés à la relaxation des ressauts hydrauliques internes, confirmant ainsi la qualité des simulations

numériques proposées.

— L'analyse d'une image SAR coïncidant avec la période de la campagne Protevs Gibraltar 2020 montre la présence d'une onde solitaire en mer d'Alboran alors que le passage de cette onde n'est pas détecté au préalable par les mouillages Mo4 et Mo5. Cette observation sur l'image SAR confirmerait les résultats des simulations numériques et l'existence d'un second mécanisme de génération dans le détroit. Le train d'ondes solitaires pourrait en effet être généré lors de la propagation non-linéaire de l'onde de marée barocline dans le détroit.

Cette première confrontation des simulations numériques aux observations a aussi permis de mettre en évidence ou de confirmer les limites de l'approche proposée en modélisation. Les forçages atmosphériques ont par exemple été volontairement négligés afin de simplifier la dynamique dans la région du détroit, ouvrant ainsi la porte à une analyse approfondie des mécanismes impliqués. Une configuration numérique de seconde génération, plus réaliste, basée sur un raffinement de la dynamique simulée dans la région du détroit de Gibraltar a d'ores et déjà été mise en place. Ce raffinement s'appuie sur trois niveaux de grilles de résolutions respectives 900 m, 180 m et enfin 60 m. Cette nouvelle configuration numérique a pour double vocation de raffiner l'analyse de la campagne Gibraltar 2020 et de préparer la campagne Gibraltar 2022 centrée sur les grandes structures turbulentes dans la région du détroit.

4.2 3D LES in the strait of Gibraltar

4.2.1 Introduction

The Atlantic - Mediterranean exchange occurring in the Strait of Gibraltar has been explored summarily in a previous section (Section 3.2). The consequences at basin scale broadly consists in Mediterranean waters leaving the Strait at depth (as what has been dubbed the 'Mediterranean outflow') whereas Atlantic waters enter the Mediterranean basin in the surface layer.

Those Atlantic waters entering through the Strait of Gibraltar are the principal contribution to the Mediterranean inflowing water budget : the average transport of Atlantic waters at Gibraltar is of the order of 1 Sv whereas the net exchange itself is of the order of 0.1 Sv. This positive entry offsets the otherwise net evaporation occurring on the integrated surface over the Mediterranean basin (Bryden et al., 1994). Since the Mediterranean basin is otherwise closed, Mediterranean waters leaving the Strait of Gibraltar are the result of the transformations of the surface circulating Atlantic water mass into intermediate and deep water masses in the various seas. More details are provided in this section on the characteristics of the strait, on the exchange, its variability, and on the fine-scale processes that take place during this exchange.

A clear objective of the numerical approach proposed in the present chapter is the explicit representation of these fine scales in the Strait of Gibraltar in order to better simulate the route toward mixing in this peculiar region of the ocean. Large Eddy Simulation (LES) is implemented to simulate the primary instabilities developing at depth between the Mediterranean and Atlantic water masses.

Circulation in neighbouring areas (Gulf of Cadix and Alboran Sea)

Atlantic side of the Strait of Gibraltar. The surface waters that enter the strait are North Atlantic Central Water (NACW) and Surface Atlantic Waters (SAW) (Millot, 2014; Naranjo et al., 2015). They are carried by the Portugal and Azores Currents into the Strait of Gibraltar as part of the eastern branch of the north-Atlantic subtropical gyre (Barton, 2001).

The Mediterranean water mass that was transported out of the strait as the Mediterranean outflow circulates at depth below this surface circulation in the Northern Atlantic. This outflow first enters the Gulf of Cadix, turning north due to geostrophy and flowing along the continental slope (Price et al., 1993; Gasser et al., 2017). West of the Gulf of Cadiz, it stabilizes to its neutral buoyancy level at 1000-m depth as the "Mediterranean water mass" (Price et al., 1993).

Meddies are salty lenses of water that can persist for years and can be found far in the open Atlantic ocean. They are generated along the canyons and caps encountered by the Mediterranean outflow in the region of the Gulf of Cadiz (Bashmachnikov et al., 2015).

The Mediterranean water mass participates in the global circulation of the Northern Atlantic overturning circulation. It increases the salinity of the whole Northern Atlantic basin by spreading in the open ocean at around 1000m, whether as slowly decaying meddies or as water carried by subsurface currents to join the basin scale circulation at higher latitudes (Price et al., 1993; Jia et al., 2007).

Mediterranean side of the strait of Gibraltar. Surface waters leaving the strait at the eastern end enter the Alboran Sea as the Atlantic Jet (AJ). The circulation of the Alboran sea can vary in time. The most common state is organized around two anticyclonic gyres : the Western Alboran Gyre (WAG) and the Eastern Alboran Gyre (EAG). However, it is not uncommon that only one of these two gyres is present (Heburn and La Violette, 1990). The AJ is coupled to the WAG when the latter is present and usually constitutes its northern branch. The AJ also delimits the front of the upwelling occurring due to wind stress in the north-western Alboran Sea (Sarhan et al., 2000). The AJ variability is mainly due to meteorological and tidal forcing, and can destabilize this system (Sánchez-Garrido et al., 2013; Lorente et al., 2019).

At depth, several components of the Mediterranean water masses enter the strait. In the Alboran Sea, they are identified as LIW (for Levantine Intermediate Water) and WMDW (for West Mediterranean Deep Water). Additional water masses from the western Mediterranean basin like TDW (for Tyrrhenian Deep Water) have also been detected (Millot, 2014). An arrangement of these water masses according to latitudes has been observed : TDW, LIW and other intermediate waters are more abundant in the northern part of the Alboran sea, whereas WMDW is mostly present in its southern part (Millot, 2014). As the depth decreases from the Alboran sea to the Strait of Gibraltar, it is more difficult for deeper WMDW to pass through the strait; its input can be modulated by mechanisms such as the strength of the WAG or the overall production of WMDW linked to the strength of winter convection (Naranjo et al., 2012).

Transformation of the water masses. Both the inflowing (in reference to the Mediterranean basin) Atlantic waters or the outflowing Mediterranean waters incorporate signatures of respectively the Mediterranean (Macias et al., 2006) and Atlantic waters (Millot, 2007; García-Lafuente et al., 2011). This is due to the mixing driven by small-scale processes of variable strength occurring in the Strait of Gibraltar.

Morphology, barotropic tides and atmospheric forcing.

The Strait of Gibraltar is tilted at approximately 15° from the west-east direction. Away from the continental shelf, Camarinal Sill (CS) is the shallowest section of the strait with an average depth of about 300 m (see Figure 4.1). The strait is narrow and deep east of Camarinal Sill. The shallower west side of CS is divided by two troughs on each side of a submarine mount called Majuan Bank. The northern trough is shallower than the southern one, which includes another sill, called Espartel Sill (ES). Those two troughs are the main pathways of the Mediterranean outflow towards the Gulf of Cadix. Most of the flow follows the southern, deeper path (Sánchez-Román et al., 2009).

There is an important influence of the semi-diurnal tide in the Strait, with the principal constituent being M2. It induces high-frequency oscillations of the currents. The amplitude of the associated sea level anomaly decreases from west to east, with a complex phase diagram due to the strait being at the junction between the Mediterranean and Atlantic basins (García Lafuente et al., 1990; Candela et al., 1990).

Wind is funnelled through the strait and is mostly zonal, either blowing westward or eastward with gusts reaching 25 m/s (Candela et al., 1989). Wind stress affects the first tens of meters of the circulation in the strait (Candela et al., 1989), which can be sufficient to affect the Atlantic Jet as either an increase or decrease in flow velocity, sometimes even stopping the jet (García Lafuente et al., 2002b). Change in the strength of the AJ affects its tilt as it enters the Alboran Sea and how it interacts with the WAG. Otherwise, the integrated effect of atmospheric pressure over the Mediterranean basin influences the net flow through the strait and leads to subinertial variability of the exchange (García Lafuente et al., 2002a).

Baroclinic exchange and small-scale processes at the tidal time-scale

During the flood (resp. ebb) tide, barotropic currents at Camarinal Sill are oriented westward (resp. eastward). These currents associated with the barotropic tide have the same amplitude as the mean baroclinic exchange and modulate it at tidal time-scale. They can reverse the flow of Mediterranean and/or Atlantic waters in certain sections (Sánchez-Román et al., 2012), and they have a pronounced neap-spring tide cycle.

The circulation can thus be splitted into a low-frequency time-average component of the mean exchange and a high-frequency, eddy-flux-like, tidal anomaly. The latter has a large impact on the exchange flow (Naranjo et al., 2014) and can even have a larger amplitude than the former at CS (Vargas et al., 2006). Consequently, various small-scale processes arise during the tidal cycle that can be identified in the Strait of Gibraltar.

Firstly, due to the limited horizontal and vertical extent of the strait, the time-averaged exchange flow and the depth-averaged barotropic tidal currents are channeled in the strait. A consequence is that the flow in the strait can become supercritical with respect to internal gravity wave propagation, meaning that the velocity of the currents are larger than the velocity of the internal gravity waves. This can be the case for the Mediterranean waters circulating west of Camarinal Sill, or for the Atlantic waters in the eastern, narrowest section of the strait known as Tarifa Narrows (Farmer and Armi, 1988).

Hydraulic control of the exchange flow only occurs episodically at CS. More generally, the location and the variability of the occurrence of supercritical flows can yet vary depending on the type of diagnosis used to characterize such events (see for instance Farmer and Armi (1988); Vargas et al. (2006); Sannino et al. (2007); Sánchez-Román et al. (2012)).

In the region of CS, the development of two hydraulic jumps when hydraulic control occurs reflects the underlying bathymetry of the sill and can be observed on satellite imagery (Brandt et al., 1996; Sánchez-Garrido et al., 2011). In particular, the modelling study of Sánchez-Garrido et al. (2011) notes influence of the tidal forcing on the shape of the hydraulic jump. They found that on spring tides, both hydraulic jumps are swept to the west of CS.

The hydraulic jump remains approximately 4 hours in the region of Camarinal during outflows (Farmer and Armi, 1988; Vlasenko et al., 2009). During this particular period, an intense mixing of Mediterranean and Atlantic waters occurs (Wesson and Gregg, 1994; Macias et al., 2006; García-Lafuente et al., 2011). Strong billows are indeed induced by Kelvin-Helmoltz instabilities in the lee of the hydraulic jump. These billows are then advected westward by the Mediterranean flow (Wesson and Gregg, 1994). In addition, the establishment of the hydraulic jump matches with the presence of chlorophyll-rich waters in the center of the strait , a signal later transported toward the Mediterranean by the Atlantic inflow (Bruno et al., 2013).

As the tidal flow weakens before the switch to ebb tide, hydraulic control is lost, the depressed anomaly of the interface between Mediterranean and Atlantic waters propagates as a Large Amplitude Internal Wave (LAIW). It takes the form of a solitary bore before transforming into an Internal Solitary Wave (ISW) (Farmer and Armi, 1988). An ISW is a particular type of internal wave satisfying a balance between non-linear advection of momentum and non-hydrostatic dispersion, which makes the initial wave expand into a train of ISWs (Vlasenko et al., 2000). The signature of such solitary waves have been extensively observed both at the surface (as areas of alternating surface roughness) and inside teh water column (as anomaly in tracer and velocity fields) in the east portion of the Strait of Gibraltar and the west of the Alboran sea (Ziegenbein (1970); Farmer and Armi (1988); Watson and Robinson (1990); Sánchez Garrido et al. (2008) to cite a few). As of now, the location of their breaking or of any other mechanisms of dissipation is unknown.

ISWs are generated during each tidal cycle except when westward current are not strong enough for the hydraulic control to set up. This can be the case during the neap tide part of the fortnightly cycle (Watson and Robinson, 1990).

The hydraulic control, the hydraulic jump and the generation mechanism of large internal tides can be simulated numerically by hydrostatic models but a non-hydrostatic model is required to simulate the propagation of ISWs or the large turbulent eddies and primary instabilities induced by the baroclinic exchange flow (Brandt et al., 1996; Vlasenko et al., 2009).

Toward Large Eddy Simulation (LES)

The small-scale processes are consequently responsible for the mixing of Atlantic and Mediterranean waters in the Strait of Gibraltar, and the modification of the characteristics of the water masses involved in the baroclinic exchange at Gibraltar. It yet remains difficult to clearly isolate the retroaction of such small-scale processes on the circulation and more generally on the large-scale processes observed in the Mediterranean basin (García-Lafuente et al., 2017). The enhanced mixing in the strait must in any event be parameterized in coarsely-resolved global or even in regional models and the modification of water-mass characteristics has an impact on the circulation in both the Mediterranean and the northern Atlantic basins.

Sánchez-Garrido et al. (2011) provides to our knowledge, the most resolved numerical simulation of the area until the present study, with a curvilinear grid of resolution approximately 50m for the x direction and 200m for the y direction in the vicinity of Camarinal Sill, as well as vertical z-levels of resolution 7.5m in the upper 300m

Based on the preliminary numerical study presented by Hilt et al. (2020) (Chapter 3 of the present manuscript), the 3D s-coordinate, non-hydrostatic, free-surface model CROCO is implemented in the region of Gibraltar with a horizontal resolution of a few tenths of meters. This chapter will show that such a high resolution grid is sufficient to resolve at least the largest scales of the mixing processes in the strait, i.e. the largest turbulent eddies or primary instabilities.

A specific focus is made on different tidal forcing configurations during a neap-spring tidal cycle and on the way the flow characteristics and the intensity of mixing processes are affected by this variability.

The numerical simulation framework based on three simulation periods is presented in Section 4.2.2. Various diagnosis that have been implemented in the numerical experiments are described in Section 4.2.3. Section 4.2.4 presents results pertaining to : the hydrological state of the flow depending on the strength of barotropic tidal currents ; the propagation of ISWs ; the areas of generation of primary instabilities ; and a comparison of several turbulence closure schemes.

4.2.2 Numerical configuration

Numerical framework

Numerical configurations are based on CROCO-NBQ and build on Hilt et al. (2020), see Section 3.2. Most numerical parameters are summarized in Table 4.1, with the three chosen simulation periods indicated in Table 4.2. A non-linear equation of state and a no-slip condition at the bottom have also been implemented. A simple Smagorinsky-like turbulent closure scheme ('Smago' in Table 4.3) (Smagorinsky, 1963), prescribes diffusivities and viscosity as :

$$A = C_s\, L^2\, D \tag{4.2.1}$$

with C_s a coefficient, L a typical length-scale taken as either $(\Delta x \Delta y)^{1/2}$ or Δz, and D the deformation rate.

The characteristic Smagorinsky coefficient C_s is chosen equal to 0.05 in most simulations as presented in Table 4.3. At the end of Section 4.2.4, several other Smagorinsky coefficients are further tested (10^{-3},10^{-2},10^{-1}), and compared with the use of a GLS k-ϵ turbulent closure scheme (Umlauf and Burchard, 2003), to evaluate the consequences on the simulated dynamics.

A crucial aspect in the elaboration of such high-resolution numerical configurations of the Strait of Gibraltar is the realism (and quality) of bathymetry data. Indeed the topography of the strait has significant (not to say major) consequences on the local and regional dynamics. Here, a 100-m-resolved MNT SHOM bathymetry has been used and adapted to model requirements and is presented in Figure 4.1.

Initialization and open-boundary conditions (which include tidal forcing) are based on a simulation of the operational Mediterranean and Black sea model developed by ENEA (Rome) using MitGCM. This ENEA configuration, presented in Palma et al. (2020), can be viewed as a parent simulation that forces the boundary after the initialization. It has a horizontal resolution in the strait reaching a hundred of meters, with 100 vertical z-levels inhomogeneously distributed (Δz from 2 to 62m in the upper 1500m of the water column). By contrast, the simulations discussed in the next sections have a horizontal resolution of 45 m and 40 evenly spaced vertical σ-levels. As noted in Table 4.1, this is sufficient to provide a higher resolution in the vertical direction than in the horizontal for the whole simulation domain. For example, at CS, vertical resolution varies from approximately 7.5 m at the shallowest point of the sill, to approximately 12.5 m downslope.

No wind forcing nor atmospheric fluxes are specified at the surface of the ocean in the studied configurations. This choice is not a consequence of any numerical constraints or malfunctions but is dictated by the will to address the complex dynamics of the region step-by-step, concentrating first on the exchange and tidal flow crossing strait of Gibraltar and on the fine scales developing at depth in a realistic context (apart from the atmospheric forcing).

To somehow reduce the computational cost of the various numerical configurations, the first six hours can be considered as a spin-up period and are simulated with CROCO's hydrostatic kernel over the same 45-m-horizontal-resolution grid. The last field of this simulation is used as a restart file to initialize the fully non-hydrostatic and compressible simulation. This 6-hours spin-up is made necessary by the large ratio existing between the forcing grid length-scale of the MitGCM ENEA coarse-grid field and the CROCO grid length-scale (a ratio reaching 15 to 30 depending on the studied configurations).

Grid Extension	6°4.8'W 5°3.4'W ; 35°23.8'N 36°27.4'N	
Number of horizontal grid points	2049x2621	
Number of vertical σ-levels	40	
$\Delta x = \Delta y$	45 m	
Depth	Min	Max
	26 m	960 m
Δz	0.7 m	24 m
Internal time-step (Δt_s)	1 s	
External time-step (Δt_f)	1/11 s (change 1/14)	
Advection scheme	WENO-5	
Viscosity ν	10^{-6} m^2/s	
Diffusivity K_ρ, K_S, K_T	10^{-6} m^2/s	
Sound wave pseudo-velocity C_s	400 m/s	
Tidal components (from ENEA)	M_2, S_2,K_1, O_1	

Table 4.1: Simulation parameters

Situation	Simulation name	Dates (UTC)
Intermediate Tide	SimIT	10/09/2017 19h00 - 13/09/17 01h00
Neap Tide	SimNT	13/09/2017 16h00 - 15/09/17 17h00
Spring Tide	SimST	19/09/2017 22h00 - 21/09/17 23h00

Table 4.2: Start and end dates of CROCO simulations corresponding to intermediate, neap and spring tides.

Tidal forcing and simulation period

Tidal forcing is integrated to the forcing of both horizontal currents and sea level anomaly at the lateral eastern and western boundaries (the only open boundaries in the domain). As indicated in Table 4.1, it comprises four tidal harmonic components (M_2, S_2, K_1, O_1). To limit computational costs, simulations are run for two-day periods of 3 characteristic flow configurations of September, 2017 (i.e. close to equinox). The start and end dates of each CROCO simulation are prescribed in Table 4.2. They do not include the 6-hour-hydrostatic spin-up period.

The comparison of the sea-level anomaly near Tarifa (5.6° West, 36.01° North) in both the parent MitGCM and CROCO simulations and the corresponding tidal gauge data (from Puertos del Estado [1]) are shown in Figure 4.2. This comparison shows that the CROCO configurations

---

[1] http ://www.puertos.es/

remain close to the parent MitGCM implementation except during the neap tide period. At this time, the relative importance of the tidal barotropic currents is reduced compared to the ones of the exchange, the difference in the dynamic in the Strait may induce difference in the propagation of the tidal signal in the Strait.

Closure scheme	Simulation name
Smago 0.005	SimIT, SimNT, SimST
Smago 0.001	SimIT-S001
Smago 0.01	SimIT-S01
Smago 0.1	SimIT-S1
GLS K-ϵ	SimIT-Kep

TABLE 4.3: Simulation names and turbulent closure schemes

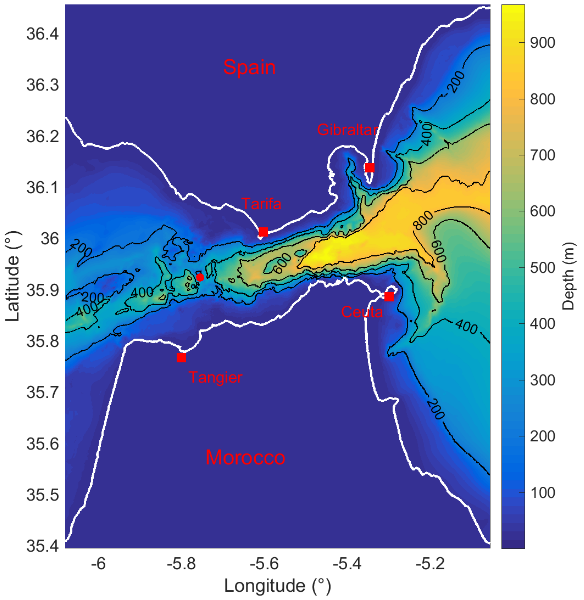

FIGURE 4.1: Area and Bathymetry used for the simulations. The red dot denotes the point at Camarinal Sill where the zonal barotropic current is taken as reference in following figures.

Water masses.

Figure 4.3.A and B show the $\theta - S$ diagrams in the eastern and western parts of the domain computed for the field of tracers used to initialize the simulation SimIT.

At the eastern boundary (Figure 4.3.B), the signatures of a deep water mass and of an intermediate water mass that correspond respectively to WMDW and LIW can be identified. The latter is present mostly in the northern part of the domain. The simulated waters are however saltier and warmer than the corresponding water masses observed in the region as per Naranjo et al. (2014).

At the western boundary now, the signature of two Mediterranean water masses corresponding to the two pathways of the Mediterranean outflow, centered around 35.8°North and 35.9°North,

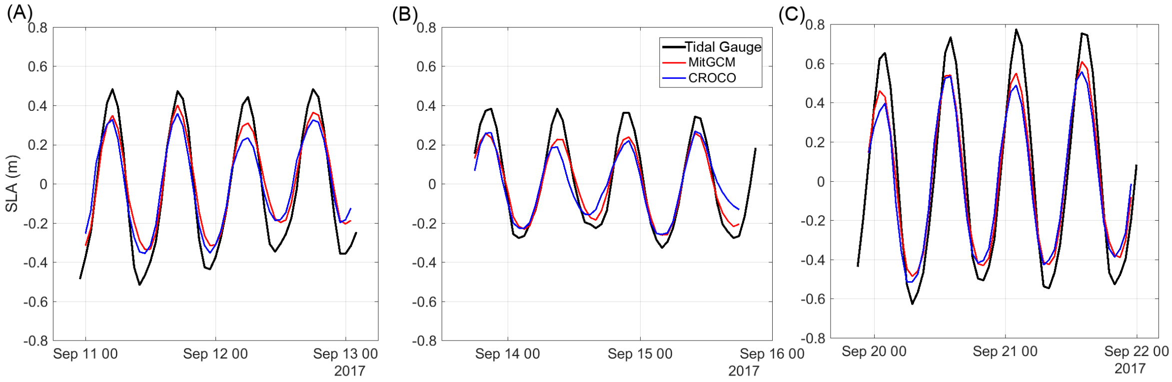

FIGURE 4.2: Sea level-anomaly at Tarifa : tidal gauge data (black), nearest grid point for parent MitGCM simulation (red) and CROCO simulation (blue) during ME (a), MM (b) and VE (c) events.

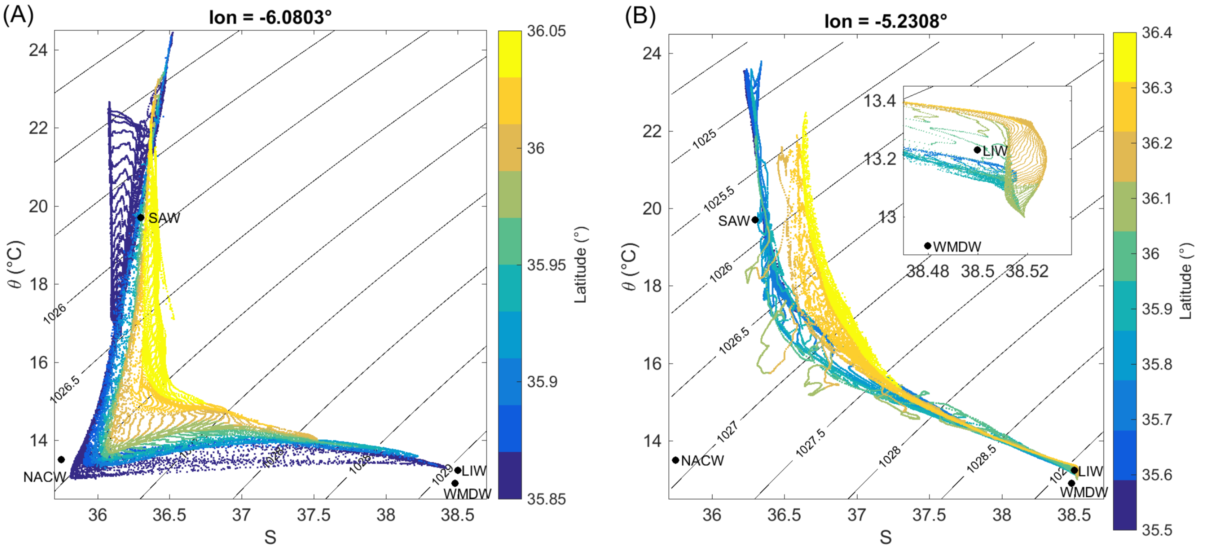

FIGURE 4.3: θ-S diagrams computed at 6.08° W (a) and 5.23° W at first time step of SimIT. Color indicates the latitude of each grid point. Definition of the water masses according to Naranjo et al. (2014) are also indicated.

can be identified. As far as Atlantic waters are concerned, NACW are mostly present on the western part of the domain. Its signal is minimized in the east of the domain, where surface waters are seen in Figure 4.3.B to be saltier and colder over 36.2°N than at other latitudes.

4.2.3 Numerical diagnosis

Hydraulic control

The flow in the Strait of Gibraltar can shift from subcritical to supercritical in only a few hours. Diagnosing the hydraulic state of the flow at each instant of the tidal cycle is then a necessity, and must be done locally to account for the complex bathymetry of the region. The definition of an instantaneous and local internal Froude number was already presented in Chapter 3 (see Appendix 3.2.6), and is here refined not as a Froude number for the flow at a peculiar grid point but to characterize either the flow of the Atlantic or Mediterranean layer in the water column at a given coordinate. To do so, the superposition of the Atlantic and Mediterranean water masses (when effective) is chosen as a simple two-layer representation of the stratification.

As seen in Figure 4.3, salinity is probably the most pertinent tracer to differentiate these waters in the region of the strait due to the large contrast of salinity existing between Mediterranean and Atlantic water masses. The determination of this reference salinity S_I is further elaborated on in Appendix 4.4 it is taken as varying along the west-east direction in the strait as a hyperbolic tangent function of longitude centered at CS to account for the different water mass composition in the eastern and western part of the Strait of Gibraltar.

$$S_I(l) = tanh(\frac{l - L_{CS}}{dl})\frac{S_M - S_m}{2} + \frac{S_M + S_m}{2} \tag{4.2.2}$$

with $L_{CS} = 5.75^o$, $dl = 0.25^o$, the location and width of the Camarinal Sill in degrees, $S_M = 37.39$ and $S_m = 37.1$ the max and minimum interface values taken respectively east and west of the sill.

With the Atlantic and Mediterranean layers defined in relation to $S_I(l)$, the Froude layer number for internal gravity waves is computed for a given water column as :

$$F_1^{Med,Atl} = \left(\frac{U^2_{Med,Atl}}{g'H}\right)^{\frac{1}{2}}, \text{ with } g' = g\frac{\rho_{Med} - \rho_{Atl}}{\rho_0}, \text{ and } H = \frac{h_{Med}h_{Atl}}{h_{Med} + h_{Atl}} \tag{4.2.3}$$

where $\rho_{Med,Atl}$ is the averaged density, and $U_{Med,Atl}$ the averaged velocity norm, in either the Atlantic or Mediterranean layer of thickness $h_{Med,Atl}$. $c_1 = \sqrt{g'H}$ is the phase speed of internal wave for a two layer model (Cushman-Roisin and Beckers, 2011). $F_1 > 1^{Med,Atl}$ means that the flow in the relevant layer is supercritical.

Hydraulic jump detection, modification of flow : velocity jump

However, the necessity to caricature the stratification, but also to evaluate a local phase velocity of internal waves based on this stratification, renders the evaluation of a local Froude number rather complex and, as a consequence, can somehow blur the characterization of the local regime of the dynamics. One process that needs to be properly evaluated is the presence of the hydraulic jump over Camarinal Sill, a feature of the flow that has a role in both the generation of ISWs and in local mixing of the water masses.

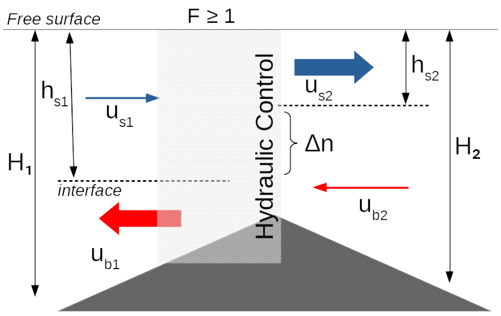

FIGURE 4.4: Schematic of flow upstream and downstream of hydraulic jump at Camarinal Sill in the Strait of Gibraltar. The grey shaded rectangle indicates an area of supercritical flow in the lee of which the jump is formed.

A simple diagnosis for the detection of the hydraulic jump at Camarinal Sill in numerical simulations is now proposed, based on the impact such a structure is known to have on the flow. As schematized on Figure 4.4, a hydraulic jump (also called hydraulic drop) induces a drop of the interface depth (note that part of the variation in depth of the interface is also due to the varying bathymetry). The flow in the Strait is channeled by the bathymetry (for the Mediterranean flow at least) and the coast (for the Atlantic flow). If the width of the channel does not vary much from one side of the hydraulic jump to the other, there must be conservation of the water flux from a downstream section to an upstream section of the hydraulic jump. The variation of the interface depth (and so of the layer thickness h_{s1} to h_{s2} in Figure 4.4), therefore causes an increase (or a decrease depending on the reference layer) of the flow velocity downstream of the jump (for example, from u_{s2} to u_{s1} in the upper layer of Figure 4.4). An expression for this jump in velocity can be found and a threshold value can be deduced to indicate the formation of a hydraulic jump between two grid points separated by a distance sufficient to be located respectively downstream and upstream of the hydraulic jump.

The drop in the interface depth to be considered between those two points is noted $\varDelta n = h_{s2} - h_{s1}$, the variation of bottom depth $\varDelta H = H_2 - H_1$ and the velocity difference in the bottom layer $\varDelta u_b = u_{b2} - u_{b1}$. In the bottom layer, the conservation of the flux leads to :

$$u_{b1}(H_1 - h_{s1}) = u_{b2}(H_2 - h_{s2}) \tag{4.2.4a}$$

$$= u_{b1}(\varDelta H + \varDelta n) + u_{b1}(H_1 - h_{s1}) + \varDelta u_b(H_2 - h_{s2}) \tag{4.2.4b}$$

$$\varDelta u_b = -u_{b1}\frac{\varDelta H + \varDelta n}{H_2 - h_{s2}} \tag{4.2.5}$$

For the surface flow :

$$\varDelta u_s = -u_{s1}\frac{\varDelta n}{h_{s2}} \tag{4.2.6}$$

The velocity in the area of the hydraulic jump must validate the condition of (at least) critical flow, i.e. Froude number ≥ 1 at the shallower location (grey shaded area of Figure 4.4). A minimal condition for hydraulic jump is consequently $u_i = c$ (from $F = 1$, with u_i the velocity of flow in a given layer) : the flow velocity must be equal to the local phase speed of internal waves. If in the situation presented in Figure 4.4, the flow the shaded area denotes a transition to supercritical flow, an expression for $u_{b,s1}$ is given by the definition of the baroclinic velocity of internal waves in a two-layer model :

$$|u_1| = c = \sqrt{g'\frac{(H_1 - \varDelta n - h_{s2})(\varDelta n + h_{s2})}{H_1}} \tag{4.2.7}$$

In this formulation, H_1,H_2 and$\varDelta H$ are the local depths of the water column at any coordinate. $\varDelta n$, h_{s2} and g' are *a priori* unknown.

But the values of $\varDelta u_b$ and $\varDelta u_s$ are used as theoretical threshold to be compared to the actual variation of the flow between two grid points in the model. So this threshold only needs to be chosen small enough so that a larger increase of the flow velocity can be attributed to a hydraulic jump. Here the distance between those two points is of 250 m (5 grid points), so that the jump has a noticeable amplitude. The set of parameters ($\varDelta n$, h_{s2}, g') is chosen empirically. Here the vertical excursion of the interface is $\varDelta n = 30\ m$, the depth of the Atlantic layer is $h_{s2} = 50\ m$ (Farmer and Armi, 1988), and the reduced gravity is $g' = 0.02\ m.s^{-2}$ (Bryden et al., 1994). This diagnosis is only used in the area of Camarinal Sill.

Q parameter and derivated diagnosis

The studied configurations are all based on grid resolutions of a few tenths of meters, an objective being the explicit simulation of at least the largest turbulent eddies. The region of the Mediterranean outflow is of particular interest since large velocity shears are known to be associated there to a large vertical density (salinity) stratification, and may overcome this stratification's stabilizing effect to give rise to the development of shear instabilities.

A dedicated diagnosis is now proposed to "detect" primary instabilities and more specifically to identify Kelvin-Helmholtz instabilities potentially developing in this region. A careful inspection of the relative-vorticity vector can fulfill this purpose and a dedicated scalar diagnostic based on the components of this relative vorticity is retained, Q (Cucitore et al., 1999). It is a generalization of the Okubo-Weiss parameter retained in Hilt (2020) (Chapter 3, see Appendix 3.2.6) to the present 3D realistic configurations.

$$Q = -\frac{1}{2}\frac{\partial u_i}{\partial x_j}\frac{\partial u_j}{\partial x_i} = \frac{1}{2}(\Omega_{ij}\Omega_{ij} - S_{ij}S_{ij}) \tag{4.2.8}$$

with u_i the components of velocity vector, and S_{ij} and Ω_{ij} are respectively the strain-rate tensor and vorticity tensor. When $Q > 0$, rotation is larger than shear.

Statistical description of the field of this parameter Q are carried out in the following sections. In particular, the easy to implement standard deviation of parameter Q is :

$$std(Q)(\mathbf{x}, t) = \sqrt{\overline{Q(\mathbf{x}, t)^2} - \overline{Q(\mathbf{x}, t)}^2} \tag{4.2.9}$$

where the overbar denotes an average over 30 minutes, a time-scale considered here as larger than the time-scales of the fine-scale dynamical structures the present study is interested in, but over which the variations of the large-scale flow are not too important.

This description in standard deviation is compared to Singular Value Decomposition (SVD) presented in Appendix 4.6. SVD computations requires a priori the storage of the field to be decomposed. Contrary to the computation of the standard deviation of Q, this could not be made online and SVD have consequently been computed off-line. This necessitates high frequency 3D outputs to pick up the relevant structures, so for storage space reason SVD could only be carried out on limited areas.

4.2.4 Fine scales in the strait of Gilbraltar

Hydraulically controlled layer and hydraulic jumps, neap-spring tide variability

Figures 4.5 to 4.7 present several diagnosis for a series of maximal outflows and inflows with variable strength of the tidal forcing in configurations SimNT, SimST, then SimIT (Tables 4.2 and 4.3). The corresponding diagnosis are presented in paragraph 4.2.3 : the blue and red shaded regions correspond to areas of supercritical flows in either the Atlantic (red) or Mediterranean(blue) layers. On top of these shaded regions, the locations of hydraulic jumps are indicated as black dotstogether with the areas of large standard deviations of parameter Q (the latter is discussed in Section 4.2.4). In the various extended grey areas, the salinity in the bottom level is below the interfacial salinity as defined in Equation 4.2.2, and thus Atlantic waters are exclusively present in the water column.

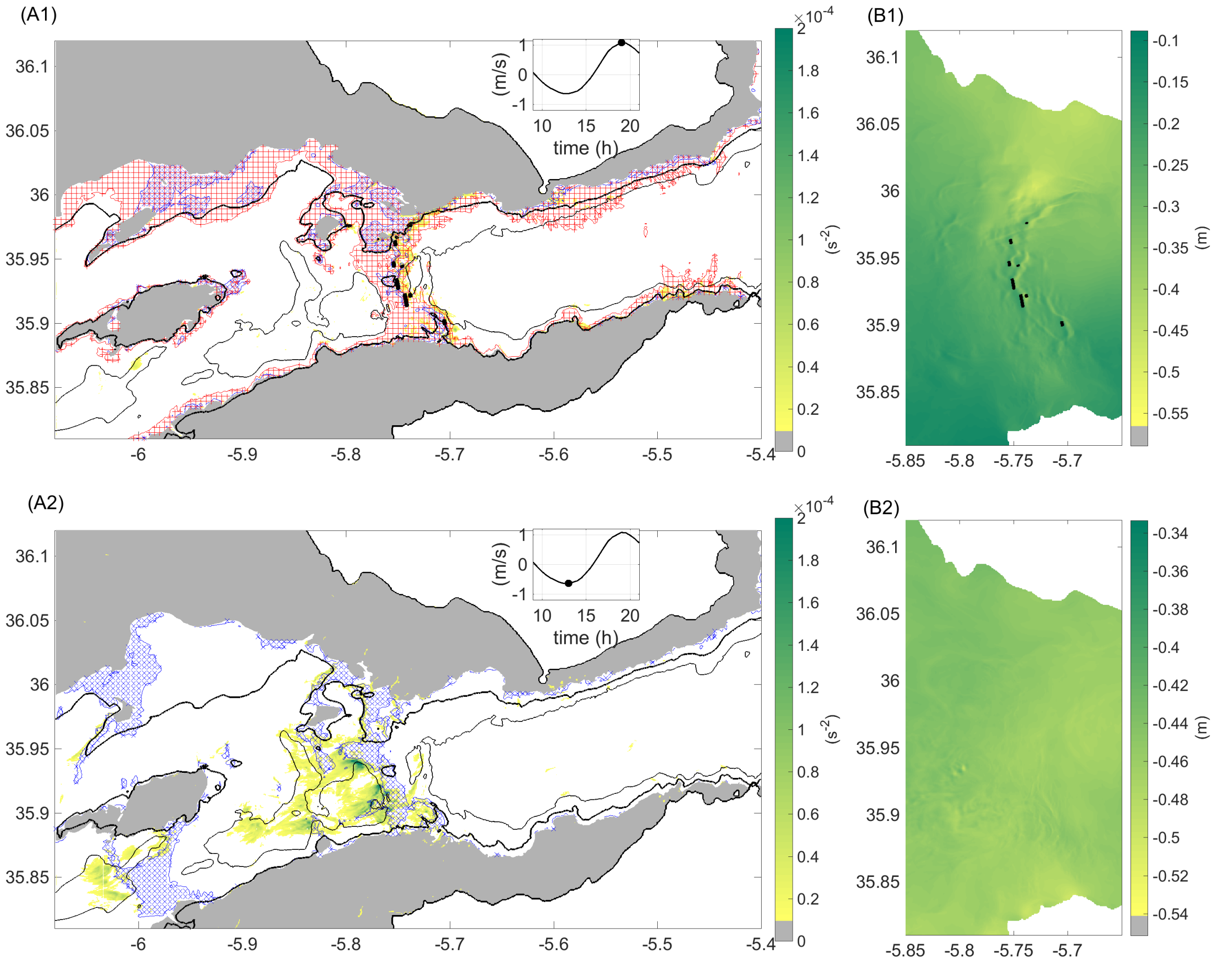

FIGURE 4.5: (A1 and A2) Consecutive inflow and outflow in configuration SimNT, *no-jump* case. The blue (red) shaded areas correspond to supercritical Mediterranean (Atlantic) layers (§4.2.3). Black dots show locations where a hydraulic jump has been detected (§4.2.3). The grey areas denote where $S_{bottom} < S_{interface}$, the salinity in the bottom grid point is lesser than the interface salinity defined in Section 4.2.3. Colorbar is related to the standard deviation of parameter Q (Section 4.2.3, only values above $10^{-5} s^{-2}$ are represented). Barotropic zonal currents at CS (point indicated in Figure 4.1 are also indicated). Two black isobathes contours are shown : 200 m (bold) and 400 m (thin). (B1 and B2) field of sea level anomaly in the area of CS and black dots indicating detection of a hydraulic jump as in (A1 and A2).

Figure 4.5 presents a neap-tide situation of weak barotropic currents ($< 1\ m/s$ for the depth averaged zonal velocity at a shallow point of CS) in both outflow and inflow conditions. Figure 4.6 corresponds to strong barotropic currents ($\geq 1.5\ m/s$) in inflow and outflow conditions during a spring-tide period. Finally, Figure 4.7 corresponds to a period of outflow with intermediate-strength ($\approx 1\ m/s$) of the barotropic currents.

Firstly, two veins of Mediterranean water separated by Majuan Bank are systematically found west of CS in Figure 4.5 to 4.7. The southern vein does not change much across situations. In the northern channel, however, an area of possible circulation of the Mediterranean outflow (non-grey area) roughly centered at 36°N ;5.95°W with bottom depth of 200m is seen as variable. This area is larger during outflows (compare for example Figures 4.6.A1 and 4.6.A2), as Mediterranean waters are driven up-slope by the westward barotropic current. But the flow presents an additional southern component that bends back into the deeper main northern channel (see Figure 4.1 for a

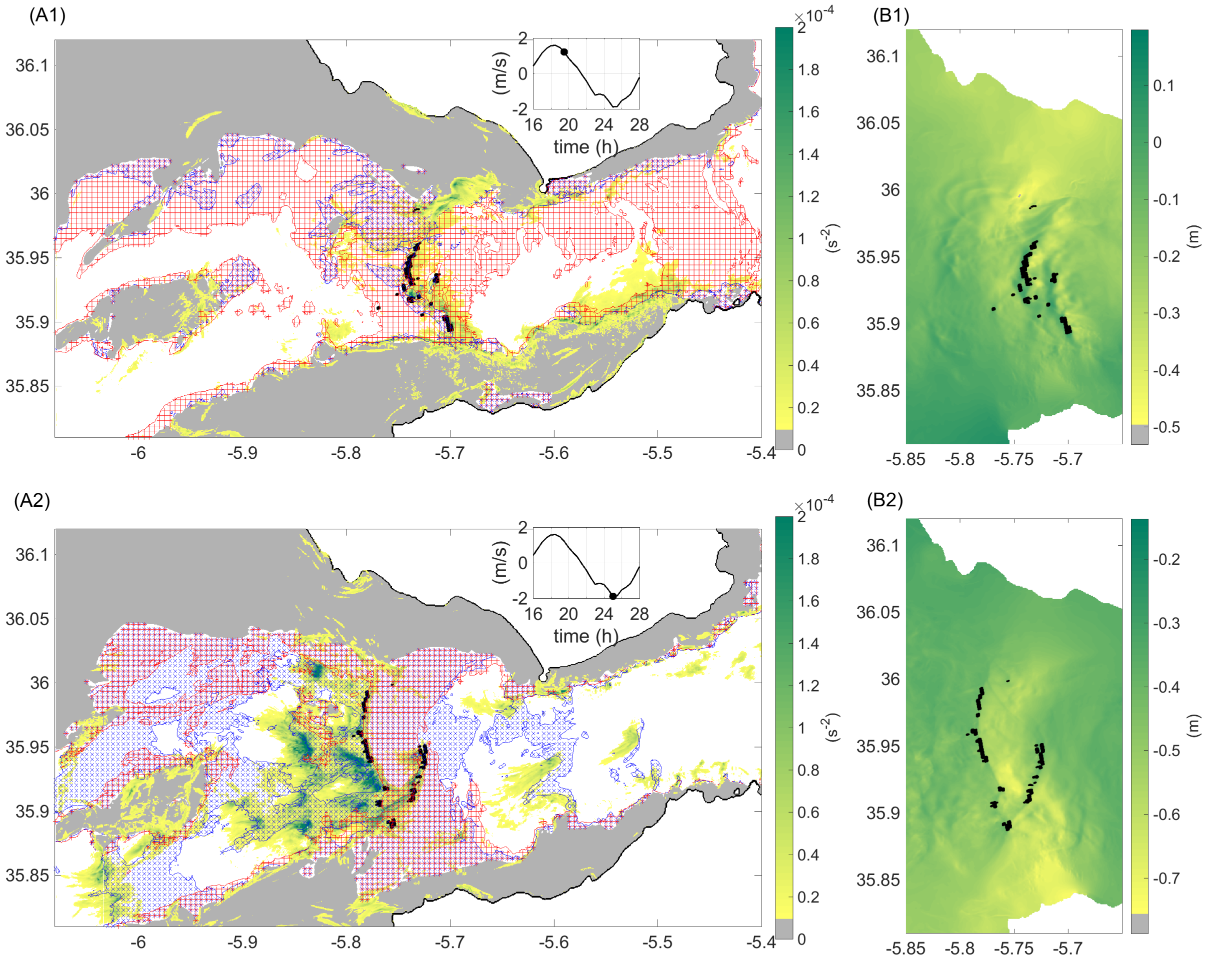

FIGURE 4.6: Same as Figure 4.5 but for simulation SimST in inflow and outflow of type *w-jump*

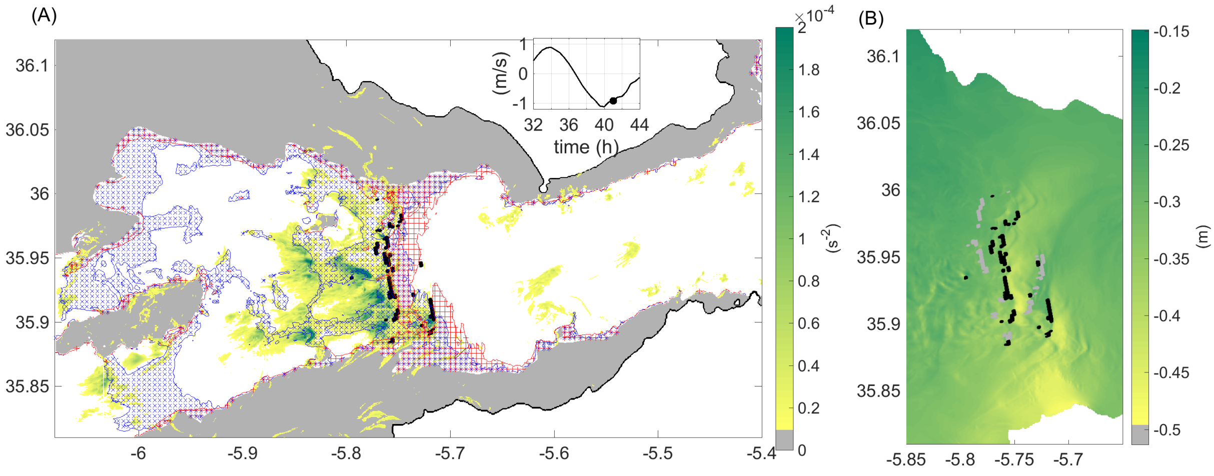

FIGURE 4.7: Same as Figure 4.5 but for simulation SimIT and an outflow of type s-jump. The sea surface anomaly (SLA) shows the signature of the hydraulic jump of spring tide outflow

better view of the bathymetry of this area).

For all cases, supercritical areas of the Atlantic (Mediterranean) layer can be found mostly east (west) of 5.8 º W which corresponds to the western slope of CS. During inflows in Figure 4.5.A1 and 4.6.A1, the Mediterranean layer becomes supercritical over several non-extensive regions (patches are observed). In outflows in Figures 4.5.A2, 4.6.A2 and 4.7.A, the Mediterranean layer is supercritical at both Camarinal, Espartel sills and in the northern channel. During the spring tide outflow period, there is not much difference between the intermediate and spring tide outflow periods with an expansion of the areas of supercritical Mediterranean flow.

For the intermediate and spring tide outflow cases, the Atlantic layer is supercritical at CS and in the shallower areas on the west part of the Strait. During the neap tide period (see Figure 4.5.A2) it isn't supercritical anywhere.

In cases for which both the Mediterranean and Atlantic layers are supercritical at CS, a hydraulic jump is detected. It is located for outflows at the western transition between supercritical and subcritical Atlantic flow that overlays supercritical Mediterranean flow. For inflows it is located east of the supercritical to subcritical transition for the Mediterranean layer, under a supercritical Atlantic flow.

This configuration leads to an area of high gradients of free-surface elevation (Figures 4.6.B2 and 4.7.B). For outflow cases, two hydraulic controls are detected in the area of Camarinal Sill, a western one (west of 5.75°W in Figure 4.7.B) linked to the sill itself, and an eastern one (east of 5.725°W in Figure 4.7.B) linked to secondary bathymetric features.

Among the simulated tidal cycles, three regimes can be encountered at CS for the outflow periods from small to large amplitude of the tidal currents : (i) no hydraulic jump (*no-jump*), (ii) the western hydraulic jump is located right above the sill (Figure 4.7, *s-jump*), and (iii) the western hydraulic jump is located over the western slope of CS (Figure 4.6.A2 and B2, *w-jump*). In this latter case, the western hydraulic jump actually develops over the sill's crest as in the *s-jump* case but since the tidal currents continue to strengthen, the area of supercritical Atlantic flow broadens. The junction between supercritical and critical flow is shifted west over the slope of the Sill where a hydraulic jump can be observed. The same evolution applied to the eastern hydraulic jump, see Figure 4.7.B for a comparison of the positions of hydraulic jumps between the two cases.

A hydraulic jump also appears during certain inflows, it remains in the same area over the east slope of CS regardless of the strength of tidal currents. It is more well-defined when barotropic currents are stronger, compare Figures 4.5.B1 and 4.6.B1. In simulations, this hydraulic jump crosses the sill toward the east before the transition to flood tide, as in the case of jumps generated during outflow. However in the inflow case no further propagation as a noticeable wave can be found.

Further discussion of the generation of the hydraulic jump over Camarinal Sill and the evolution of the criticality of the flow is presented in Appendix 4.5, applied to the spring tide outflow case.

Further east in the strait, another area of supercritical Atlantic layer appears during inflows. During neap-tide (Figure 4.5.A1), it takes the appearance of a patch near the north shore in Tarifa Narrows at 5.59^o W. During spring tide (Figure 4.6.A1), this patch extends over a larger area and a secondary area of supercritical Atlantic flow exists between 5.5^o W and 5.4^o W, extending from the northern to the southern side of Tarifa Narrows.

Figures 4.8.A and B shows the divergence of surface currents in Tarifa Narrows while a train of ISW is propagating there. In both figures, it is visible as an alternation of negative and positive surface currents divergence (when seen from west to east) between 5.4°W and 5.45°W. Figure 4.8.A corresponds to a barotropic current of intermediate strength in SimIT during inflow and Figure 4.8.B to a strong barotropic current during the inflow of another tidal cycle in SimST (the time is the same as in Figure 4.6.A2). The areas of critical Atlantic layer flow are also shown as a black meshed area.

In Figure 4.8.A, two distinct areas of supercritical Atlantic flow are located immediately west of the ISWs and in the northwest at 36°N, both as moderately extended patches. Looking at Figure 4.5.A1 the situation is similar for that inflow of SimNT. In Figure 4.8.B, for which the barotropic currents are stronger, the first patch overlays half of the propagating train of ISWs and joins the northwestern patch, so that the flow of the whole Atlantic layer is supercritical at this moment and at all latitudes between 5.4°W and 5.45°W.

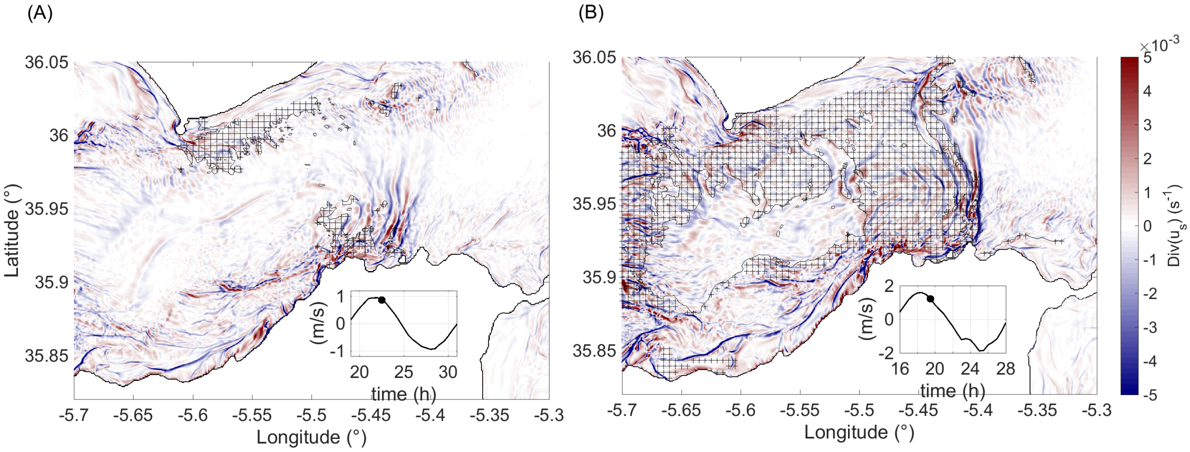

FIGURE 4.8: Divergence of the surface current (color) and areas of supercritical Atlantic layer (black hatches) at t = 22.5 h in SimIT (A) and t = 19.5 h in SimST (B)

Propagation of Solitons (ISWs)

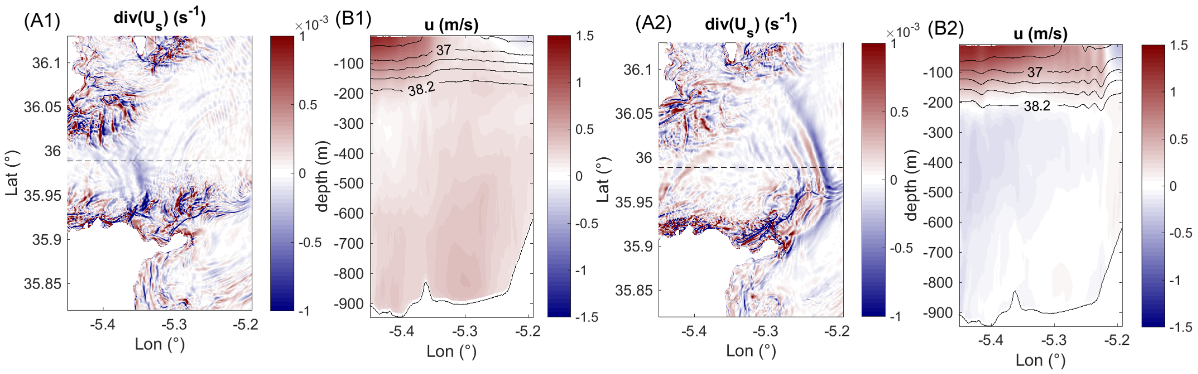

FIGURE 4.9: Divergence of surface current (A1, A2) and vertical sections (B1, B2) of salinity (black isohalines) and zonal velocity *u* (color) in SimNT at t = 20 h (A1,B1) and 22 h (A2,B2) of simulation.

Generation in *no-jump* condition. Solitary waves are observed in the three simulations after the relaxation of both *s-jump* and *w-jump* type of hydraulic jump at CS (Figure 4.8), but propagation also occurs in simulation in the *no-jump* case. Figures 4.9.A1 and A2 also depict the divergence of surface currents but at the eastern exit of the strait, at two consecutive times

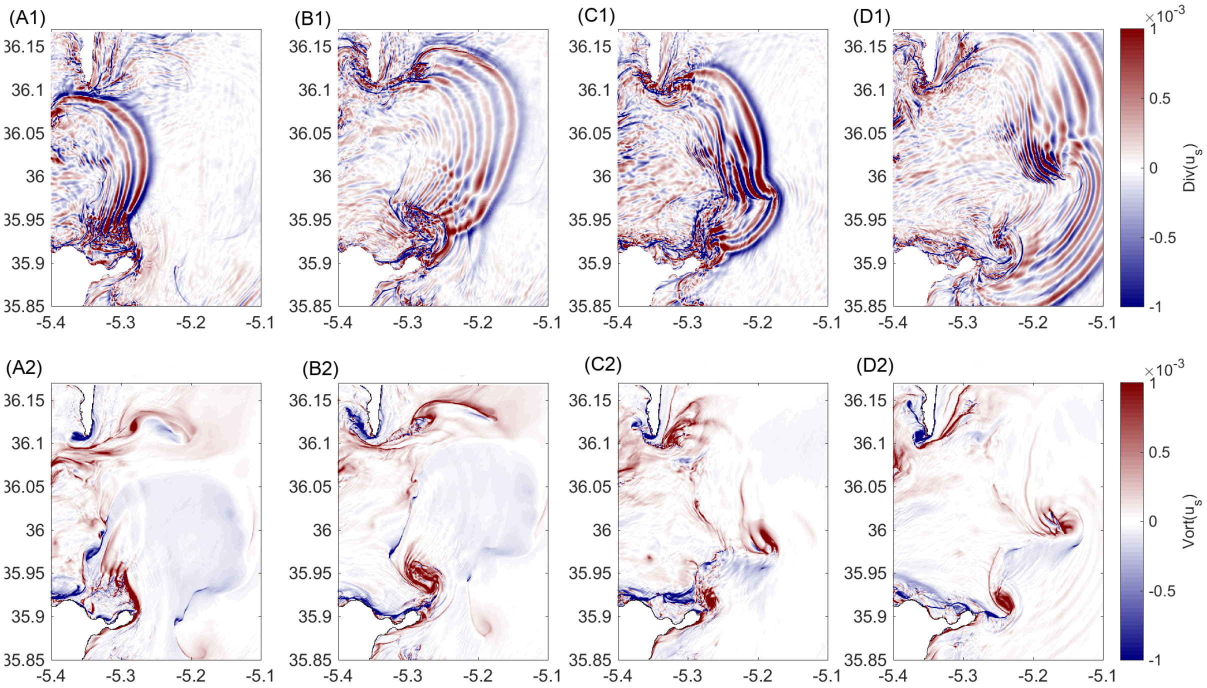

Figure 4.10: Divergence of surface current (upper row) at t = 10.5 h, 12.5 h, then 23 h and 25 h of simulation SimST, and z-axis vorticity of surface current (lower row) for the same instants.

during ebb tide following a no-jump outflow in simulation SimNT. Figures 4.9.B1 and B2 are vertical sections of the zonal current and salinity at the same dates. Despite taking place after a *no-jump* outflow, a train of ISWs can be observed in Figures 4.9.A2 and B2. This train, that ends up propagating in the Alboran sea, appears after the propagation of the baroclinic tide in Figure 4.9.B1 creates a growing front with isohalines steepening due to non-linear effects. As is the case for the ISWs generated at CS, non-hydrostatic dispersion balances this effect and creates a train of ISWs. In SimNT this process occurs following every *no-jump* outflows.

However, compared to the upper row of Figure 4.10 (also showing the divergence of surface currents during two inflow periods following the presence of a hydraulic jump at CS), the train of ISWs visible at the surface in the Alboran Sea after a *no-jump* outflow is less extended, consisting of fewer waves (3 in Figure 4.9.A2, and 5 in Figure 4.10.A2).

Interaction with submesoscale eddies. Figures 4.10.A1 and B1 then Figures 4.10.C1 and D1, show two consecutive inflow periods in the SimST configuration, for which train of soliatry waves propagate eastward following hydraulic jump release at Camarinal Sill. The lower row of Figure 4.10 exhibits the z-component of the surface vorticity at the same instants. In the first two figures of each row, a train of ISWs leaves the strait and enters into the Alboran sea. The number of solitons in the train increases during this period. A filament of positive vorticity is formed by interaction with the southern coast (Peninsula of Almina) in Figure 4.10.A2 and develops into a cyclonic eddy in Figure 4.10.B2. In Figure 4.10.C2, one tidal cycle later, the eddy is located at 5.2 ° W and 36° N and the train of ISWs of the next ebb tide is refracted by this eddy in Figure 4.10.C1 : its southern part is indeed accelerated whereas its northern part is decelerated by the induced currents. At the same time, a new vortical structure can be observed off the southern shore. In Figure 4.10.D2 this structure has also evolved into a cyclonic eddy, centered at 35.92°N ;5.25°W, that propagates in the Alboran sea while the previous eddy has been advected to the north-east by currents of the West Alboran Gyre. Meanwhile, the interaction between the solitary waves and the previous cyclonic eddy has resulted into an interference pattern in the wave packet in figure (D1).

In the simulations, this process of generation of cyclonic eddies off the coast of the peninsula of Almina occurs each time a train of solitary waves exits the strait. The train of ISWs generated at the next tidal cycle gets diffracted on this eddy, creating local modifications of the structure of the train.

Dynamical structures at Camarinal Sill, primary instabilities

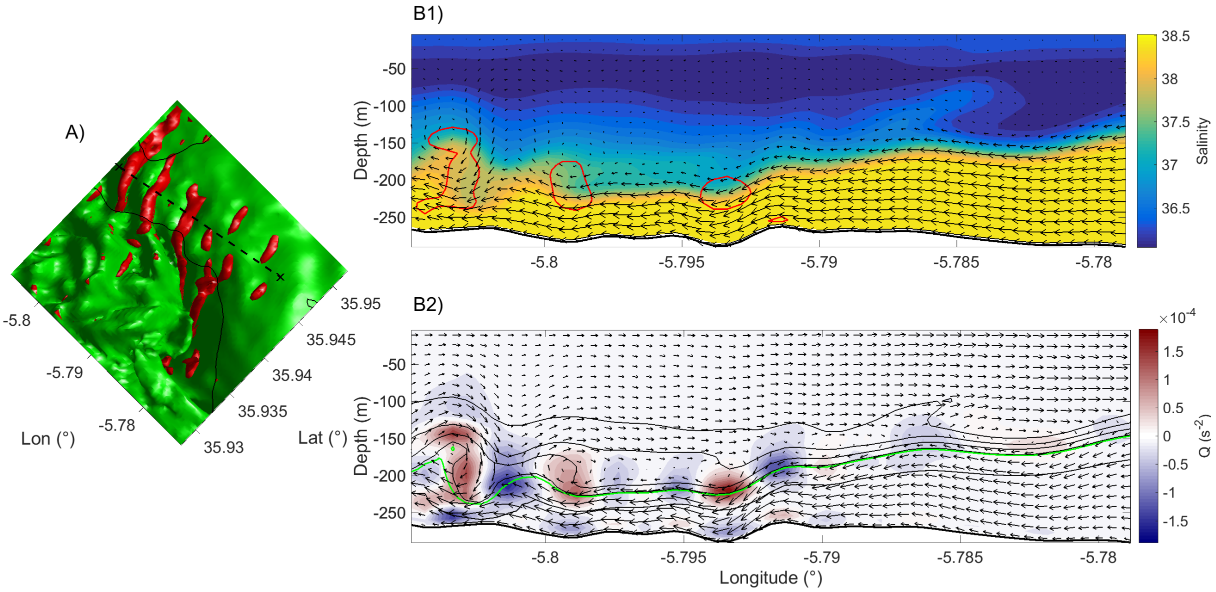

FIGURE 4.11: (A) Bird's eye view of isohaline surface $S = 38.1$ (green) and $Q = 5.10^{-5}\ s^{-2}$ surfaces (red) in a small area west of CS at t=4H in SimIT. 300-m depth isobath (black line) and position of the vertical section for B1 and B2 (dotted black line). (B1) Vertical section of salinity (color), (u,w) vectors and isoline $Q = 5.10^{-5}\ s^{-2}$ (red). (B2) The same vertical section as (B1) with parameter Q (color), isohalines (black lines and green line for $S = 38.1$), and vectors (u',w) where u' is the residual of u minus its barotropic component.

Standard deviation of parameter Q. Along with the features of the flow already discussed previously, Figures 4.5, 4.6 and 4.7 indicate patches of high standard deviation of parameter Q (defined in §4.2.3). Figure 4.11 gives an example of what the instantaneous field of Q looks like in simulation SimIT. Figure 4.11.A presents a 3D bird's view of a procession of tube-like structures for which $Q = 5.10^{-5}\ s^{-2}$ (in red) over a surface of constant salinity (in green). Those features are present in a small area immediately northwest of Camarinal Sill during an outflow and are moving westward. Figures 4.11.B1 and B2 are vertical sections. Figure 4.11.B1 shows the contour of $Q = 5.10^{-5}\ s^{-2}$ (in red) along with the (u,w) component of velocity and the salinity in this section. In this velocity field, three areas of highly positive parameter Q are positioned in the haloclyne between the Mediterranean and Atlantic waters.

In Figure 4.11.B2, instead of (u,w) is plotted (u',w) with $u' = u - |u|$ where $|u|$ is the barotropic (vertically averaged) component of the zonal velocity. It highlights the area of shear between the

Mediterranean vein and the Atlantic waters, but also confirms that the high positive values of Q are associated with areas of rotating fluid, for example at 5.798°W and 200m deep.

Those kind of structures are numerous and are carried westward by the Mediterranean outflow, they are for example transported 1 km downflow of the generation area in a little over 10 minutes. This means that over a single grid cell, the temporal evolution of Q shows oscillations between high positive values (at the center of a billow or a vortex for instance) and low negative values (sheared layers between two consecutive billows for instance) as between the two westernmost vortexes of Figure 4.11.B2. At such a grid point, the standard deviation of parameter Q is large. Thus, this proxy is used in Figures 4.5, 4.6 and 4.7, where the maximal value of standard deviation in the water column is depicted. It indicates the areas where primary shear instabilities are advected by the Mediterranean outflow. The higher the value of standard deviation is, the closer they are to the generation site.

Neap-spring tide cycle in the Strait. Comparing the fields of standard deviation of Q in Figures 4.5, 4.6 and 4.7, the extension of patches of standard deviation is maximal during all outflow periods, and the spring tide inflow of Figure 4.6.A1 although the values of standard deviation for this latter case are not as large and the patch itself is not as extended. During the outflow cases, high values of standard deviation extend from the west of CS at 5.79 ° W and west of secondary bathymetric features in Tangier basin at 5.84 ° W. This values are higher for the two cases where a hydraulic jump is present at CS (*s-jump* and *w-jump*). There is also a smaller amplitude signal at ES.

More local patches exist east and west of CS, but with relatively small values of standard deviation that may not be associated with shear instabilities but with propagating internal gravity waves.

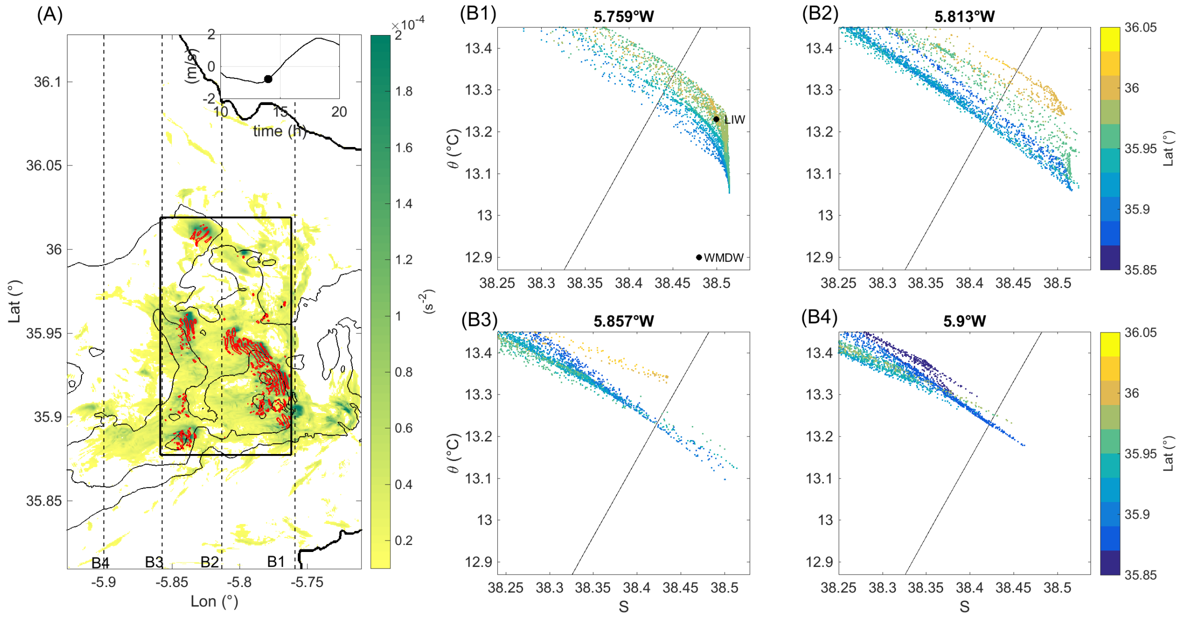

FIGURE 4.12: (a) Standard deviation of parameter Q over 30-min-periods at $t = 14\,h$ in SimST (color) and isocontour of $Q = 5.10^{-5}s^{-2}$ from the high-frequency singular vector of SVD performed in the rectangular black box during the outflow period. Black dashed lines indicate the longitude at which $\theta - S$ diagrams are plotted. (B1, B2, B3, and B4) $\theta - S$ diagrams, zoomed in the area of the Mediterranean water masses, in color is the latitude of each point.

Mixing along the path of the Mediterranean Outflow. Figure 4.12.A superposes the standard deviation of Q and the singular vector of Singular Value Decomposition (SVD, see Appendix 4.6) performed on the 3D field of this same parameter Q during an outflow of SimST. The singular vector depicted is the fifth one of the decomposition, the most high-ranked singular vector for which temporal evolution shows high frequency variability (timescale in minutes), associated with propagation of vortices (the higher ranked singular vectors (not shown) have low frequency variability and structure associated with the large-scale flow itself). Figures 4.12.B1 to 4.12.B4 are θ-S diagram showing the signature of all the simulation grid-points at a given longitude at t=14h of simulation, during flood tide, and zoomed in on the domain of Mediterranean waters.

As expected, in Figure 4.12.A the contours of parameter $Q = 5.10^{-5}\ m^2 s^{-2}$ of the singular vector (in red) are colocalized with the highest values of standard deviation of Q, i.e. on the western slope of CS (between 5.73°W and 5.8°W) and on the western slope of secondary sills in Tangier Basin (at around 5.84°W). At this latter location, three main areas appear for the generation and propagation of primary instabilities, from south to north : 35.88°N, 35.95°N and 36°N. Those are the same latitudes along which the Mediterranean water masses are homogenizing in the θ-S diagrams of Figures 4.12.B2 and 4.12.B3. This is in accordance with previous results showing that the instabilities develop along the path the Mediterranean vein takes in the lee of salient bathymetric features.

This organisation in different veins centered at different latitudes is absent in Figure 4.12.B1. At 5.76° W, still over the crest of Camarinal Sill, the composition of Mediterranean waters remains similar to the one found in Figure 4.3 at the east entry of the strait, indicating that only minimal mixing occurred for those waters in the eastern portion of the strait.

The waters of the different Mediterranean vein's pathway are not homogeneous directly downflow of CS, highlighting how gradual the process of mixing is. While the primary instabilities are generated, diapycnal mixing itself, through the rest of the turbulent cascading process achieved by subgrid processes, has not yet occurred entirely. It is in Figures 4.12.B3 and 4.12.B4 that the Mediterranean veins are distinct and homogeneous, with the southern veins of the Mediterranean outflow being comprised of waters with higher density. In Figure 4.12.B4 the northernmost signal, of waters propagating over 36°N, has been eroded and shows up outside of the zoomed area of this figure in the θ-S diagram.

Neap-spring tide cycle at CS. The singular vectors of SVD are now studied over outflows of simulations SimNT, SimIT and SimST, varying the strength of barotropic tidal currents, specifically over the area of Camarinal Sill. Figures 4.13.A1, B1, C1 present the singular vector of parameter Q for the outflows of Figures 4.5, 4.7,and 4.6 respectively.

Along those, vertical sections of salinity are plotted in Figures 4.13.A2, B2, C2. These sections are plotted along latitude 35.94° N. Figures 4.13.D and 4.13.E are histograms giving respectively the height above the seafloor and the latitude of the grid points of the singular vectors of figures (A1,B1,C1) for which Q is larger or equal to $5.10^{-5}\ s^{-2}$. On vertical sections, positive values of Q parameter are associated with specific billow structures of salinity that develop in the gravity current along the west slope of the CS, as was the case in Figure 4.11.

Those structures are generated for each outflow case at a depth of around 100m above the seafloor for both hydraulic jump cases, and 70m above the seafloor for the no-jump case (Figure 4.13.D). Instabilities are also more numerous for the w-jump outflow case in SimST (Figure C1), developing along all latitudes as seen in Figure 4.13.E. Whereas, in the other two cases instabilities are not present between the interval of 35.925°N and 35.932°N west of the shallowest

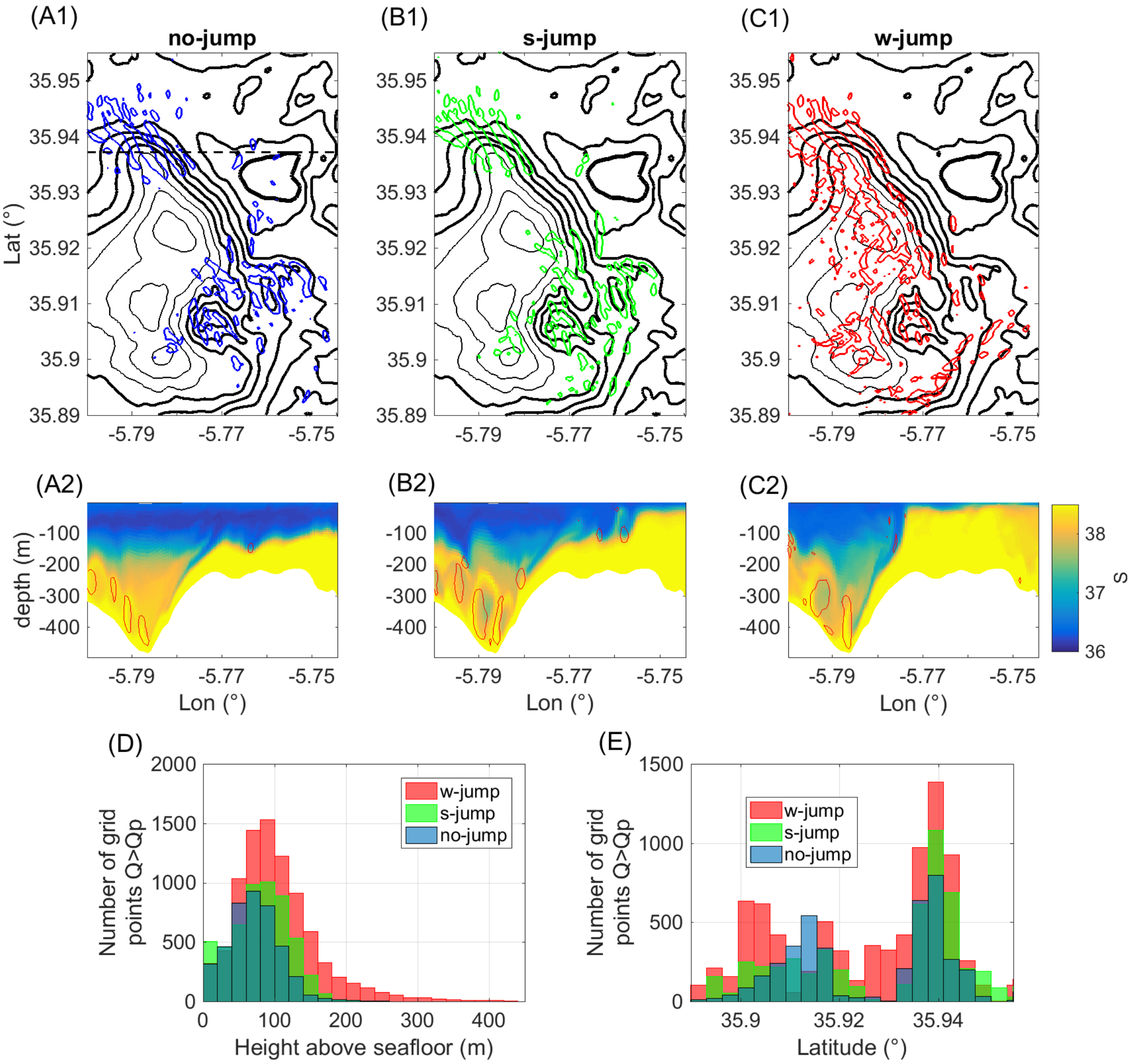

FIGURE 4.13: (A1, B1, C1) Contours of parameter Q = 5.10^{-5} s^{-2} in the first high-frequency singular vector of SVD performed during outflow of Figures 4.5.A2,4.7 and 4.6.A2 respectively. Isobathes in black : 200 m (thicker), 250 to 450 m (thick) and 500 to 600 m (thin). (A2, B2, C2) Vertical sections of salinity (color) and contours of Q-parameter = 5.10^{-5} s^{-2} at latitude 35.9372° N at the same dates. (D) histogram of the height of the grid points of each singular vector shown in A1, B1 and C1 above the seafloor. (E) Same as (D) but showing the latitude of the grid points.

part of CS.

Looking at the vertical section of Figure 4.13.C2, in the w-jump case the interface drop of the western hydraulic jump of CS is over the western slope at 5.775°W, contrary to Figure B2 of the s-jump outflow type for which it is positioned at 5.755°W. In that s-jump case as well as the no-jump case of Figure A2, the dynamic over the slope is a density current. It is in this density current that the simulated primary instabilities are mainly seen, so that the distribution in latitude is close for those two cases in Figure 4.13.E. In the w-jump case, this density current of Mediterranean waters crossing the sill is colocalized with the hydraulic jump, including west of the shallowest point of CS at $35.935^{/}circ$N. Only in the case when the hydraulic jump is localised on the west slope of the sill can the Mediterranean waters flow over this shallow depth as the rapid Mediterranean vein in which primary shear instabilities can develop.

In the vertical sections of Figures B2 and C2 the aspect the salinity billows structured by this instabilities is similar, with the core of the billows having low salinity that can reach 37 psu compared to the ambient waters around 38 psu. Note that as this longitude, corresponding to the area of the θ-S diagram of Figure 4.12.B2, the outflow is still heterogeneous. The aspect of the billows in the no-jump case of Figure 4.13.A2 is different and does not incorporate as much low salinity waters.

Closure schemes. Four additional simulations are now presented to investigate and better understand the impact of the turbulent scheme : the first three are based on different implementations of the Smakorinsky turbulent scheme and the latest uses the GLS K-ϵ scheme (see Table 4.3). In Figures 4.14.A1, A2, A3 and A4, vertical sections of salinity during the first outflow after $t = 5\ h$ of a *no-jump* outflow case are presented. Values are indicated for the Richardson gradient number $Ri = 0.25$ (black) and $Q = 5.10^{-5}\ s^{-2}$ (red). Ri is calculated from fields of density and velocity averaged over half an hour to filter out the propagating structures.

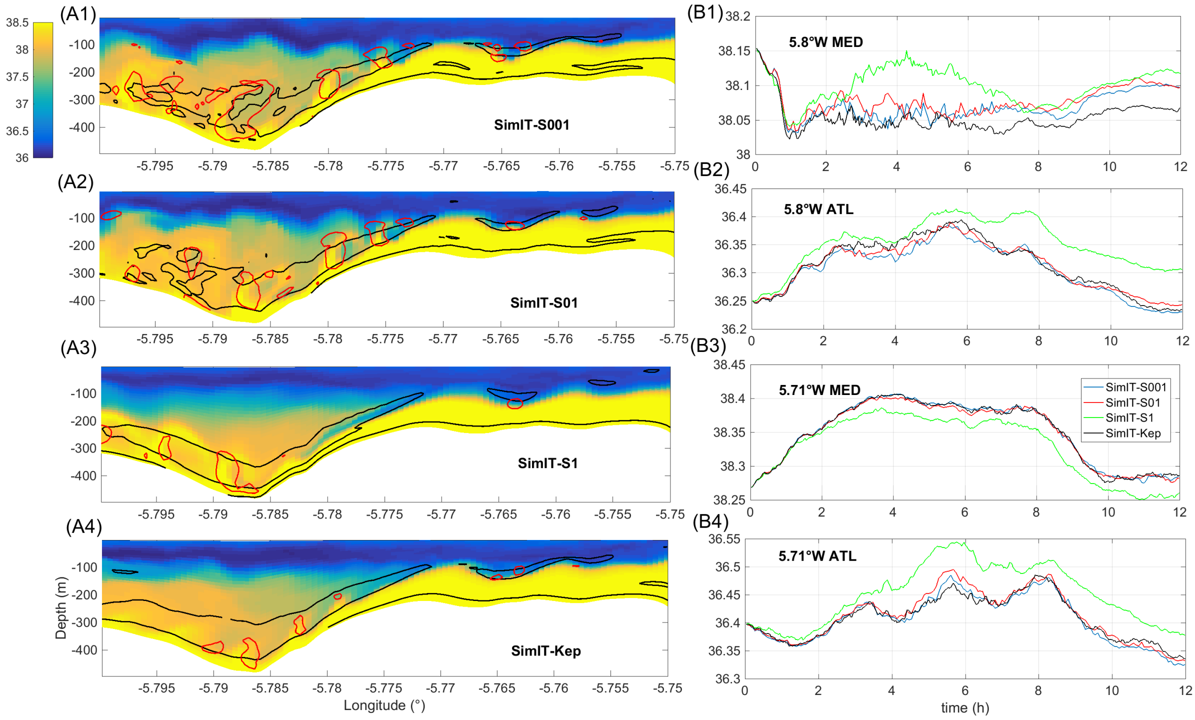

FIGURE 4.14: (A1, A2, A3, A4) Vertical section of salinity (color), contours of $Q = 5.10^{-5}\ s^{-2}$ (red) and Richardson gradient number = 0.25 (black) at a latitude of 35.9372^o N in SimIT-S001 (A1), SimIT-S01 (A2), SimIT-S1 (A3) and SimIT-Kep (A4) respectively, 4 h after the initialization. (B1,B2,B3 and B4) Averaged salinity across the Mediterranean (B1 and B3) or Atlantic (B2 and B4) layer at two different longitudes, east (B1 and B2) or west (B3 and B4) of Camarinal Sill.

Figures 4.14.B1, B2, B3, and B4 show the salinity averaged in the Mediterranean (B1, B3) and Atlantic (B2, B4) layers as defined in paragraph 4.2.3, west (B1,B2) and east (B3,B4) of CS. Keep in mind that averaged values are shown, and that as previously discussed and shown in Figure 4.12, at this longitude west of CS, the different veins of the Mediterranean outflow do not have yet homogeneous characteristics. Primary shear instabilities carry waters of lesser salinity into the outflow, but it has not yet been homogenized by further mixing processes.

The decrease in salinity of the layer this provokes depends of the turbulent closure scheme, but in a counterintuitive way. Looking first at averaged layer salinities east of the sill in Figures 4.14.B3 and B4, simulations SimIT-S001, SimIT-S01 and SimIT-Kep lead to the same salinities for the Mediterranean layer, whereas differences can be observed punctually in the Atlantic layer. The simulation presenting the largest differences is SimIT-S1 : the Mediterranean layer is less saltier by 0.4psu after t=2h, whereas the Atlantic layer is, in contrast, saltier by 0.5 psu compared to the other simulations. This is expected since in SimIT-S1, the mixing coefficient is larger, hence there is more diffusion across the interface between Atlantic and Mediterranean waters.

However west of the sill in SimIT-S1, both the Atlantic and Mediterranean layers are saltier than in the three other simulations, especially between 2 and 8 hours following the initialization. This cannot obviously be explained by an increase of the dissipation that would lead to a salinity of the Mediterranean layer lesser than in the other simulations, the same way than it does at the eastern section.

At 5 hours of simulation, the vertical sections of Figures 4.14.A1,A2,A3 and A4 show that instabilities develop. The area where Ri is lower than 0.25 begins at 5.77° W in all the simulations, indicating shear instabilities could develop from this point in the gravity current. This is the case for SimIT-S01, SimIT-S001 and SimIT-Kep, but instabilities are only found downslope of an intrusion of Atlantic waters at 5.783° W in simulation SimIT-S1 (Figure A3).

In simulations SimIT-S001 and SimIT-S01 (Figures A1 and A2), instabilities arise earlier in the hydraulic jump, so that the waters at the center of the billows (for example at 5.778°W) are of small salinity and originate in the Atlantic layer, whereas in SimIT-S1 the billows are forming by incorporating ambient mixed waters of the Mediterranean vein to the new saltier Mediterranean waters that cross the sill. This means that, in SimIT-S1, less Atlantic water is integrated to the Mediterranean outflow when going through CS compared to the other simulations, resulting in Figure 4.14.B1 to a saltier Mediterranean layer than in the other three simulations.

In the case of implementation of $K-\epsilon$ turbulent scheme in simulation SimIT-Kep, the billows, and more generally the instabilities, are less-developed with smaller values of parameter Q in Figure A4 and a less-salty outflow in Figure B1. This signal persists 7 h after the initialization when the flow reverses and no instabilities are generated anymore across all simulations. For SimIT-S1, at this point the salinity averaged in the Mediterranean layer is closer to the other simulations with Smagorinsky schemes, possibly because the increased diffusion in the pycnocline may counteract the previous enhanced injection of Mediterranean water.

4.2.5 Discussion & conclusions

Fines scales in Gibraltar strait.

The variability of the hydraulic control and the variability of the other dynamical features during the neap-spring tidal cycle have been explored with high resolution, non-hydrostatic, free-surface simulations of the region of the Strait of Gibraltar. No permanent supercritical flow has been identified in the various simulations and only intermittent events of such flows have been observed during the tidal cycle. The location and the extension of the area of supercritical flows depend on the strength of the barotropic currents. During flood tide when both Atlantic and Mediterranean layers are critical at Camarinal Sill, two hydraulic jumps are generated and explicitly simulated. The western one is located at the time of maximum amplitude of the western tidal currents either over the shallowest part of the sill (*s-jump* case), or over its western slope (*w-jump* case).

For the western jump, this displacement during spring tide is similar to the behaviour that was simulated by Sánchez-Garrido et al. (2011). However, these authors found that for this intensity of the tidal forcing the eastern hydraulic jump was also swept on the western slope of CS, while in our case this eastern hydraulic jump, while being swept westward, remains close to its initial position east of the sill, and is still a distinct hydraulic jump. This discrepancy may arise mainly from differences in bathymetric data between the two models : the eastern bathymetric feature is not as prominent in Sánchez-Garrido et al. (2011) as in the present study.

The generation of a hydraulic jump is also seen in simulations on the east side of CS during the ebb tide, but its release with the disappearance of hydraulic control does not lead to the formation of westward propagating ISWs.

Another secondary generation process for ISWs has been brought to light. To our knowledge, previous studies focused so far exclusively on the generation of ISWs following the collapse of the hydraulic control at "high tide" in the region of the strait. In simulations carried out in this chapter during tidal cycles with no critical flow over the sill and no hydraulic jump, the propagation of a long internal wave at ebb tide induces, through non-linear steepening of the wave and non-hydrostatic dispersion, the generation of a smaller (less extended) train of ISWs in the eastern part of the strait.

During each simulated tidal cycle, a cyclonic eddy is formed along the coast of the Peninsula of Almina (southern part of the eastern exit of the strait of Gibraltar). This eddy is advected by the flow in the Alboran sea and interacts with the trains of ISWs, inducing a local diffraction of the solitons.

Several other dynamical features have been explicitly simulated such as the billows resulting from shear instabilities and developing in the lee of CS. In simulations, these billows are associated with high positive values of parameter Q. This parameter is used as a proxy for their detection and analysis. The billows are generated at the interface of Mediterranean and Atlantic waters and they are advected by the Mediterranean outflow while carrying waters of lesser density originating from the interface or the Atlantic layer. They are also present above secondary bathymetry accidents in Tangier basin and above ES. They can be observed during outflows of any intensity, but their spreading changes with the intensity of tidal currents, due to the existence and to the position of the western hydraulic jump at CS. They play an important role in the way the simulated Mediterranean and Atlantic waters mix, changing the hydrological features of the Mediterranean vein. In numerical simulations, this mixing is sensitive to the dynamic of the instabilities, and this dynamic is piloted by the turbulent dissipation scheme.

A conclusion is that the hydrological and dynamical properties of the Mediterranean waters entering in the northern Atlantic basin are greatly influenced by the configuration of the flow in the region of CS. Both the volume of these Mediterranean waters and their mixing with the Atlantic waters can indeed vary during the neap-tide cycle.

In the present numerical configurations, only the largest primary instabilities and thus only the upper part of the direct turbulent cascade were explicitly simulated. The road to mixing consequently depends on the quality of the turbulence closure scheme that leads to the mixing of the water masses and this dependency has been summarily evaluated by testing several schemes with well-known properties.

No atmospheric forcing were specified at the surface of the ocean in the configurations presented in this section other than those integrated in the parent simulation. This means that the upper layer is not too realistically represented in particular in the region of Tarifa Narrows where wind stress is expected to be the largest. This choice remains yet consistent with the desire to simplify (but not over simplify) the "fine" dynamical structures in the complex region of the strait of Gibraltar. The depiction of fine scale dynamics in a numerical model can nonetheless be used to help in the interpretation of *in situ* data in the area of the Strait of Gibraltar, which presents several very localized and distinct phenomena that evolve relatively rapidly during the tidal cycle.

LES in the Strait of Gibraltar.

To our knowledge, the present study is the first three-dimensional realistic simulation to represent explicitly the beginning of the turbulent cascade in the region of the Strait of Gibraltar. However, only the primary instabilities developing at the interface between Mediterranean and Atlantic water masses have been explicitly simulated. Other primary instabilities with length scales of a few meters or less can be expected in the surface and bottom layers. Such dynamical structures remain implicit and are modelled as subgrid processes with the 45m-resolution grid used in the present numerical configurations.

As a consequence the numerical configurations of this study is proposed as a Large Eddy Simulation of the inner water column, for which a resolution of a few tenths of meters both in the horizontal and vertical directions is sufficient in the Strait of Gibraltar to simulate explicitly primary instabilities.

In the real ocean, such primary instabilities devolve into secondary (then tertiary, etc.) instabilities that break their structure in various ways (Mashayek and Peltier, 2012). How fast the transition between primary and secondary instabilities occurs will command the characteristics of the water masses in the Strait of Gibraltar. Since this evolution does not occur with a still too coarse grid, the evolution of this instabilities is "unnatural".

Moreover, the tools employed here to examine the rise of those instabilities in LES are limited and somewhat rudimentary in reflecting on the stochastical nature of the turbulent process. It has been shown that the choice of subgrid dissipation parametrization generally influences the primary instabilities dynamics, and it is crucial to develop accurate, dedicated tools to properly evaluate the diapycnal mixing provoked by those structures and confrontation to *in situ* evaluations. Investigation of such a tool makes up the last chapter (Chapter 5) of the present manuscript.

Finally, compared to the kilometric horizontal-grid length-scales classically proposed, the much higher resolutions proposed here obviously lead to an increase of the computer coast to cover the region of the strait. This was achieved thanks to the performances of the CROCO model inherited in part from ROMS time-splitting and numerical schemes (Shchepetkin and McWilliams, 2005) in which a non-hydrostatic, compressible kernel has been added (Auclair et al., 2018; Hilt et al., 2020). This study is consequently a first step toward a downscaled, embedded, explicit simulation of the large turbulent structures, and the feedback of explicit mixing in the water column on the larger-scale circulation.

The present work is thus a first LES exploration in *Terra Incognita* (Scotti, 2010; Wyngaard, 2004).

4.3 A first evaluation of LES with in-situ & remote observations

The pertinence and the accuracy of the high-resolution Large Eddy Simulations performed so far crucially need to be evaluated based on in-situ or remote observations of both the regional and fine scales of the real ocean. The observation of the latter is somehow difficult at least when these fine scales are localized in small, transient spots. In turn, LES can then appear as a well-adapted tool to help designing the campaign.

In the present section, only a selection of in-situ and remote observations of Gibraltar 2020 campaign is studied. While the exploitation of campaign data is incomplete, some observations are still presented to represent the complete work that was carried out during my Ph-D to provide an as-rigorous-as-possible work including both development of LES, investigation of LES dynamics and evaluation with dedicated observations. Further treatment of in-situ observations and the preparation of the Gibraltar 2022 campaign are still being carried out.

4.3.1 Field campaign Gibraltar 2020 (an overview)

The field campaign of in situ measurements Gibraltar 2020 has been carried out by SHOM during the fall of 2020 in the Strait of Gibraltar and in the western part of the Alboran sea aboard the research and survey ship *L'Atalante*. This campaign and the following Gibraltar 2022 campaign are part of the PrometeVs program and LEFE-GEPETO project. On-site measures were taken by ship-based instruments from 8/10/2020 to 20/10/2020. Among those, sampling of the water column at both end of the strait were realized; at the eastern end of the strait on the 14th and 15th October, and at its western end on the 16th of October.

Additionally, five moorings were deployed as presented in Table 4.4, locations are also indicated in Figure 4.15.A2. Mooring Mo1 is positioned west of the slope of Camarinal Sill. Mooring Mo3 is placed in the southern deep half of CS whereas Mo2 is positioned in a shallow area at the center. Mo4 and Mo5 are positioned near each other at some distance east of CS. Three of the moorings (Mo1, Mo3 and Mo5) are equipped with CTD sensors to provide hydrological characteristics of the water masses, and the other two (Mo2 and Mo4) with ADCP sensors to sample the currents in the water column. Sampling frequencies range from a few tens of seconds to one minute.

Mooring	type	position	date (UTC)
Mo1	CTD	35° 55.264'N; 5° 46.739'W	8/10/2020 15h - 9/11/2020 12h
Mo2	ADCP	35° 55.761'N; 5° 45.288'W	8/10/2020 5h - 17/10/2020 15h
Mo3	CTD	35° 54.719'N; 5° 44.459'W	8/10/2020 13h - 22/10/2020 21h
Mo4	ADCP	35° 55.870'N; 5° 41.020'W	8/10/2020 7h - 17/10/2020 14h
Mo5	CTP	35° 56.229'N; 5° 41.026'W	8/10/2020 9h - 1/11/2020 14h

TABLE 4.4: Name, type of sensors, coordinates and date of deployment for moorings during Gibraltar 2020 field campaign.

In Section 4.3.4, mooring data from Mo2, Mo4 and Mo5 are analyzed for a first observation period covering the ten-day period 8/10 to 18/10 during which, as indicated in Table 4.4, both types of moorings data are available.

4.3.2 Insights from LES simulations in preparation of Gibraltar 2020

The numerical simulations presented in Section 4.2 are based on a high-resolution, non-hydrostatic model. Atmospheric fluxes are neglected as a first step toward realistic, high- resolution Large Eddy Simulation of the region of Gibraltar strait. This simulations provide information on the flow and processes occurring in the strait that were used to design the Gibraltar 2020 campaign.

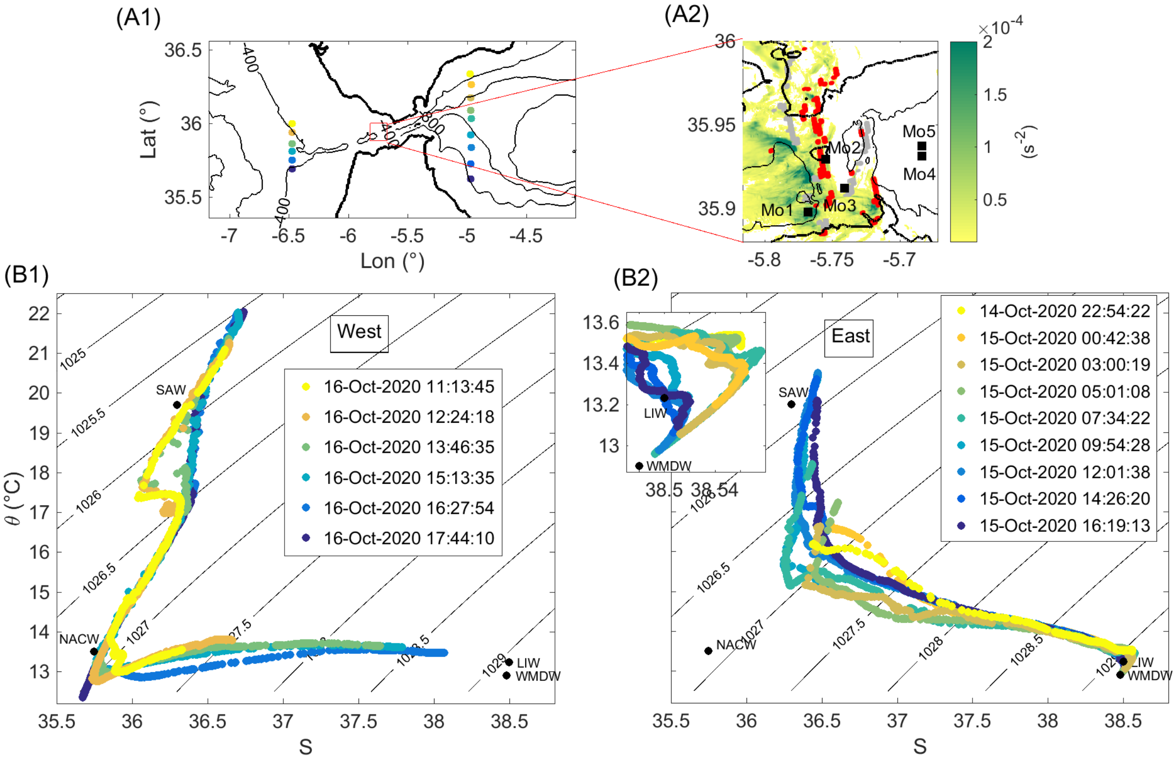

FIGURE 4.15: (A1) Water column sampling sites for (B1) and (B2). (A2) locations of moorings deployed during Gibraltar 2020 (black squares), over the map of standard deviations of parameter Q (colorbar) and the location of the hydraulic jumps of w-type and s-type from high-resolution numerical modelling of the strait of Gibraltar, as presented in Section 4.2. (B1 and B2) Θ-S diagrams for the series of water column sampling carried out respectively at the western and eastern exit of the Strait, water mass definitions according to Naranjo et al. (2015).

The field of standard deviation of parameter Q and the localization of the hydraulic jumps in figure (4.15.b) are for instance issued from those simulations. In combination with external restrictions such as the dense maritime traffic, strong currents and steep slopes of the area, such diagnosis and others were studied to chose the mooring deployment as well as the transect plans for the campaign (not shown). As an example, Mo1 was positioned down the western slope of the sill, i.e. down-flow of a potential primary instability generation area (see Sections 4.2.3 and 4.2.4 for a discussion of this diagnosis in high-resolution numerical simulation).

Figure 4.16 features a comparison between a SAR image (figure (A)) of the strait of Gibraltar with the surface signature of a propagating ISW just east of CS, and the corresponding field of norm of the gradient of surface currents in SimIT at the same date (figure (B)), showing a traveling wave in the same vicinity. Whereas the shape of the train itself differs in the model and observed fields, the simulation gives an accurate idea of the propagation speed of ISWs in the strait of Gibraltar. This was used to predict the position of ISW in relation to the tidal cycle as predicted by the Spanish institute Puertos del Estado[2]. The anticipation of position of ISWs train was accurate at least in the strait of Gibraltar itself. In the Alboran Sea, where the influence of the gyre on the form of the wave packet is important, prediction was not as accurate, with time of arrival being greatly delayed compared to our predictions.

Beyond the propagation speed, the high resolution of the model means that the shape of individual solitary waves is accurate as it propagates. This is used in the following Section 4.3.4 to help in the interpretation of mooring data from Mo4 and Mo5.

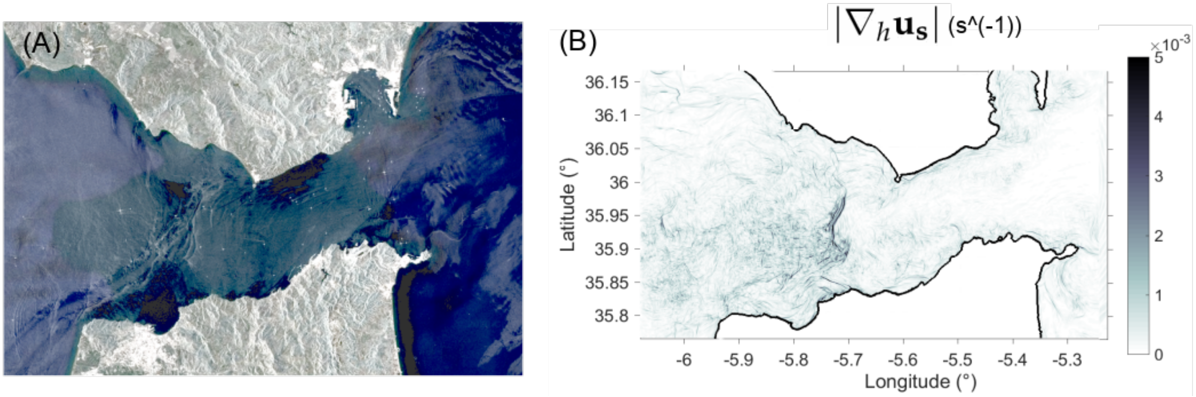

FIGURE 4.16: (a) Sentinel-1 Synthetic Aperture Radar (SAR) image (12/09/2017 - 6h18pm UTC). (b) Norm of the gradient of surface horizontal velocity (s^{-1}) in the simulation SimIT (12/09/2017 - 6h30pm or t = 35h30 in simulation time) presented in Section 4.2.

4.3.3 Overview of the mesoscale circulation during the observation period

The in-situ time period covers one (for ship-based instruments and ADCP moorings) or two (for CTD moorings) neap-spring tide cycles. Figure 4.19.B shows the depth-averaged zonal component of the current measured at CS (data from Mo2 mooring). The measures begin during the neap-tide part of the fortnightly cycle. The west Alboran Gyre was also present in the West Alboran Sea during the field campaign (not shown).

Figures 4.15.B1 and B2 present the $\theta - S$ diagrams from ship-based water column sampling. For both figures, each color refers to a different sampling station indicated in Figure 4.15.A1.

On the west end of the strait (Figure 4.15.B1), no Mediterranean water was sampled at the southernmost station and a well-mixed signal could be identified at the northernmost station, delimiting the path of the Mediterranean outflow between 35.7° and 36° N. Among the signals of Mediterranean outflow waters, the two northernmost stations that reach depths shallower than 400 m (orange and yellow) show an enhanced mixing with NACW.

On the east end of the Strait (Figure 4.15.B2), WMDW can be found at depth for all stations except the northernmost (yellow). For the next two stations south of the latter, as well as the two southernmost stations, WMDW is mixed with intermediate waters.

The five northernmost stations' surface waters have signal of lower temperature than the SAW signal at the rest of the stations. This could be due to the northern stations being affected by the upwelling from the Iberian coast. The intermediate Mediterranean waters sampled at these stations are also warmer and saltier compared to the signal of the remaining four, which is interpreted as LIW.

---

[2] http ://www.puertos.es/

4.3.4 Solitary waves at Mo4 and Mo5 mooring and currents over CS at Mo2 mooring

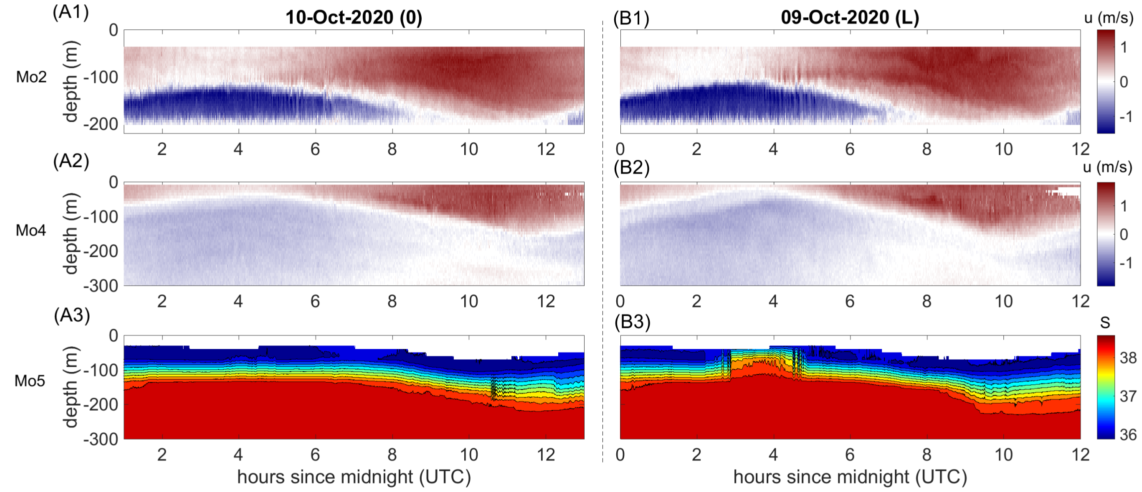

FIGURE 4.17: Time-series of mooring data over the water column from Mo2 (upper row), Mo4 (center row) and Mo5 (lower row) mooring. The zonal component of currents is represented for Mo2 and Mo4 mooring, and the measured salinity at Mo5 mooring.

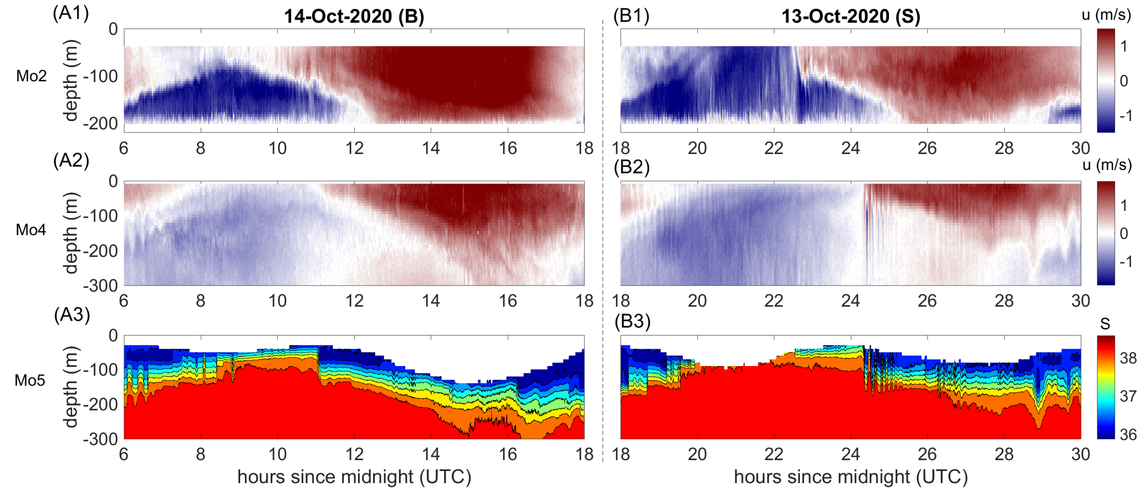

FIGURE 4.18: same as Figure 4.17 for different time-periods.

Figures 4.17 to 4.19.a present depth-time records of the zonal velocity (for Mo2 and Mo4 mooring) and salinity (for Mo5 mooring) for five different M2 tidal periods. Tilting by the strong currents provoked the depths of the CTD sensors of the Mo5 mooring to change overtime, sometime loosing the signal from tens to a hundred of meters at the top of the water column (for example see Figure 4.18.A3 at 15hUTC). Additionnally, note that whereas the whole water column is presented in those figures for the Mo2 data, only the upper 300 m (of a 500-m-deep water column) are represented here for Mo4 and Mo5 data for a better visualization.

Similarly, Figure 4.20 presents the zonal velocity and salinity of the upper 300 m of simulated data at a grid point of coordinate (35.937°N;5.706°W), near Mo4 and Mo5, from the simulations SimNT (Figures 4.20.A and B), SimIT (C) and SimST (D) of Section 4.2. Although those simulations cover a different time-period, the simulated fields present similar patterns of internal waves traveling in the water column as the observed data.

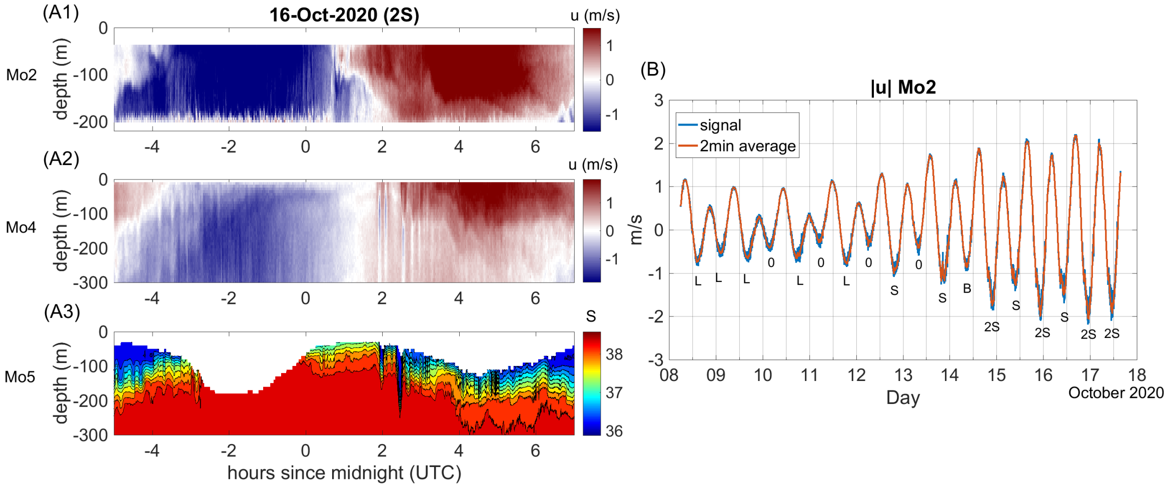

FIGURE 4.19: (A1 to A3) Same as Figure 4.17 but for a different time-period. (B) Time-series of depth-averaged signal of the zonal component of currents from Mo2 data (in blue the instant signal recorded, in red the 2 minutes average). For each outflow is indicated the type of signal that is observed at Mo4 and Mo5 mooring (see text).

Currents at Mo2 and Mo4 moorings

In the observations of currents made at mooring Mo2, periods of inflows and outflows can be distinguished respectively as having mostly eastward or westward components over the water column. During inflow periods, there are always at least two hours during which the whole flow measured by the captors is eastward (for example between 10 and 12 hours in Figure 4.17.A1). During outflows, the current can be westward at all captors, as is the case in Figures 4.18.B1 and 4.19.A1, but this is not necessarily the case.

In Figures 4.17.A1 and B1, for example, the baroclinic exchange structure of currents is still distinctive during outflows, with a weak eastward flow in the upper 120 m of the water column over a strong westward current. Figure 4.18.A1 presents another case for which the flow in the upper water column becomes momentarily weakly westward between t = 7 h and t = 9 h, with a still clear shear interface at 100-m deep.

In the numerical simulations performed in Section 4.2, an entirely westward flowing water column at Mo2 mooring corresponds to an area a hydraulic jump is present. In Figure 4.15.A2, this location corresponds to the upflow area of the two types of hydraulic jumps identified in Section 4.2 (s-jump and w-jump), and depicted respectively as grey and black points.

At mooring Mo4, the flow of the water column can become unidirectional during both outflow and inflow periods during the spring tide part of the fortnightly cycle. In this occasions, a shear area still subsists that matches with the salinity interface between Mediterranean and Atlantic waters identified at mooring Mo5 (see for example at t = 14 h in Figure 4.18.A2 and A3 at depth ranging between 150 and 200 m).

Propagation of high frequency waves

It is on the salinity interface observed at Mo5 mooring that the signal of propagating internal gravity waves can be spotted, sometimes matching with anomalies in the current field of mooring Mo4.

Figures 4.17.B3 at t = 3 h, 4.18.A3 at t = 8h30, and 4.18.B3 at t = 19h30, show as a recurring

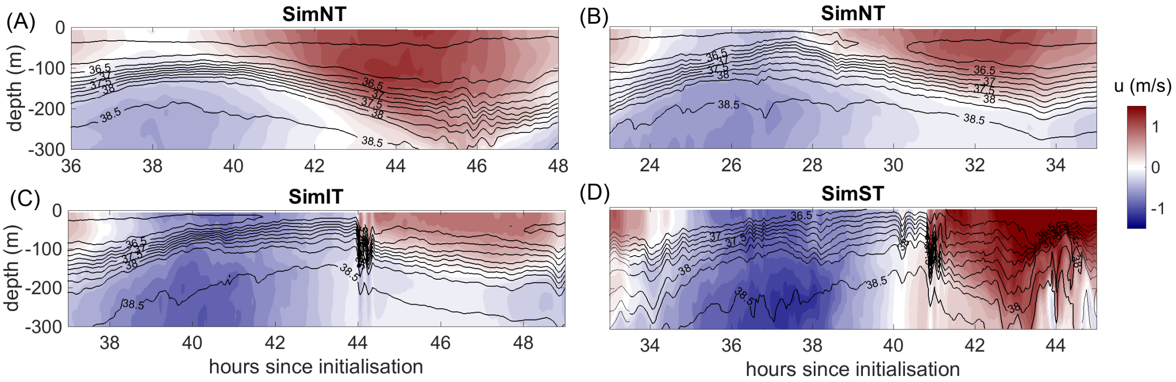

FIGURE 4.20: Time series of salinity (black lines) and zonal velocity (color) in the upper 300 m in simulations SimNT(A and B), SimIT (C) and SimST (D) of Section 4.2 at the gridpoint of coordinates (35.937°N ;5.706°W). Abscises is simulation time.

feature an abrupt lifting of the interface, that does not appear in the simulations data of Figure 4.20.

Another recurring signal in Mo5-mooring data are the large amplitude troughs that can be seen during the inflow period of the tidal cycle. In this data set, it appears clearly in observation data made at t = 29 h in Figure 4.18.B3. In simulation data (for example t = 49 h in Figure 4.20.C), this signal corresponds to a westward traveling train of ISWs that is generated by reflection off the Moroccan coast of the well-known eastward traveling ISWs train that is generated at CS.

The focus is now made on the signal showing up at Mo4 and Mo5 mooring, usually 3 hours or sooner after the maximal outflow at Mo2 mooring. Five distinctive types of signals are identified and categorized with letters o, L, B, S, and 2S :

— Linear-internal tide (o), Figures 4.17.A2-A3 : the depth of the salinity interface at Mo5 mooring and maximum shear at Mo4 mooring evolves linearly, except for some low amplitude traveling waves at the interface in Mo5 mooring at t = 10h30. At Mo2 mooring (Figure 4.17.a1), there is a distinctive shear in the water column during the preceding outflow, with slightly positive velocity in the upper layer. This signal is also seen in SimNT as shown in Figure 4.20.A.

— Small-amplitude internal wave (L), Figures 4.17.B2-B3 : in the salinity data, there is a signal that looks like two internal waves of relatively small amplitude (10 m) at Mo5 mooring at t = 4h30. At Mo4 mooring, the depth of maximum shear of zonal velocity still evolves in a linear manner as in the previous (o) case. At Mo2 mooring (Figure 4.17.A1), the interface of westward flow evolves at the same depth as in the (o) case but in the upper layer velocity becomes almost nil from t = 1 h to t = 3h30. This signal is also seen in SimNT in Figure 4.20.B at t = 28.5 h of simulation, and is associated there in the velocity field with a mode-1 anomaly.

— Internal-traveling bore (B), Figures 4.18.A2-A3 : at Mo5 mooring, the salinity interface drops by 50 m at t = 11 h which resembles the signal of a westward-propagating internal bore. At Mo4 mooring, however, the depth of maximum shear still evolves linearly, but before the arrival of the internal bore signal, the flow in the water column is negative at all depths. At Mo2 mooring over CS, the upper layer velocity is nil or lightly negative during the outflow. This type of signal is not recovered in the simulations that have been performed.

— Train of internal-solitary waves (S), Figures 4.18.B2-B3 : a succession of seven troughs goes though Mo5 mooring starting at t = 24h15. The first one has an amplitude of 80 m. At Mo4 mooring, this series corresponds to mode-1 anomalies of the velocity field. At Mo2 mooring, the flow is westward throughout the water column during the preceding outflow, with an abrupt return to a sheared two-layer state at t = 22h30, corresponding to the loss of hydraulic control and the release of the western hydraulic jump over CS. In simulations, this type of signal is seen for instance in simIT and presented in Figure 4.20.C with two troughs at t = 44 h. In these simulations, this type of signal at mooring Mo4 and Mo5 follows the release of a s-jump type of hydraulic jump (i.e., at maximum outflow, the western hydraulic jump is located over the shallowest part of CS).

— Two close trains of internal-solitary waves (2S), Figures 4.19.A1-A2 : five troughs can be seen propagating at Mo5 mooring starting at t = 2 h, but are not propagating in order of decreasing amplitude. The first trough has an amplitude of 80 m and is followed by two short-wavelength, small-amplitude troughs. Then at t = 2h30, an over-100-m amplitude trough propagates at Mo5 mooring. It is in turn followed by a smaller-amplitude trough. The mode-1 anomaly of the velocity field is seen clearly at Mo4 mooring for the first two waves, then the fourth larger amplitude one. At Mo2 mooring, as in the previous (S) case, the flow through the water column transitions from wholly westward to sheared two-layer at t = 1 h. In numerical simulation SimST (Figure 4.20.D), four waves can be identified. They follow this pattern, the first two waves have decreasing amplitude, the third has a larger amplitude than the first two, and the fourth has a smaller amplitude. In this case, this pattern corresponds to two different trains of ISWs. The first (second) train corresponds to the previously released hydraulic jump east (west) of CS. In the numerical simulations, this signal follows the release of a w-jump (i.e., at maximum outflow the west hydraulic jump is located over the western slope of CS).

Both S and 2S signals are linked to westward flow of the whole water column at CS, which should indicate that, as in the numerical simulations, a hydraulic jump was present west of Mo2 mooring.

The 2S case can be observed in numerical simulations and in Figure 4.20.D. The amplitude of the first wave which corresponds to the eastern hydraulic jump of CS can however be very small. While the wave(s) produced by the release of the eastern hydraulic jump are always present, at the latitude of moorings Mo4 and Mo5, its amplitude depends (i) on the northern extent of the eastern hydraulic jump at maximum outflow (i.e., how high a latitude it reaches) and (ii) on the initial angle taken by the released non-linear wave as it first propagates in a slightly southern direction.

As the two sets of ISWs propagate further in the strait, the second train overtakes the first one. Indeed the propagation speed of ISWs depends on their amplitude (the larger the faster), so eventually they appear as a merged and sorted train of ISWs. For instance, the "S" structure in simulation appears because the wave released by the western hydraulic jump of CS overtook the eastern one(s) sooner due to their initial closeness.

So although it appears here that two cases are distinct (the S case following an s-jump and the 2S case following a w-jump), there might be a possibility that slowly propagating waves from an s-jump could also appear as a 2S structure at Mo4 and Mo5 mooring, and conclusion cannot be reached on the structure of the two hydraulic jumps at CS only on the basis of the signal at Mo4 and Mo5 moorings.

4.3.5 Transition between outflow types & ISWs generation in Gibraltar strait

The classification of the previous section is applied to signals at Mo4 and Mo5 mooring following each outflow of the first observation period and is marked as annotations in Figure 4.19.B.

A pattern emerges linking outflow type and strength of the averaged currents at CS. The beginning of the period corresponds to the neap-tide part of the fortnightly cycle, and either (L) or (o) type of outflows are detected, with no hydraulic jump at CS. The first solitary wave is observed at Mo4 and Mo5 mooring the 12/10/2020. Due to the diurnal variation of semidiurnal flow, the tidal flow over the following period is weaker (less than 1 m/s) and the signal at Mo4 and Mo5 moorings is an (o) case.

Except for one specific (B) case (14/10/2020), during the remainder of the period, trains of ISWs (with either a S or 2S structure) are propagating through Mo4 and Mo5 mooring. The stronger outflows lead to (2S) signals in agreement with the numerical simulations presented in Section 4.2. Under especially strong outflows, the internal hydraulic jump generated over CS is swept downstream as a w-jump, resulting in an initially increased distance between the eastern and western jumps. This distance may not be overcome as quickly upon release of the hydraulic jump as in the s-jump case. This explains the distinction between S and 2S cases, however as explained previously, for some outflows, the distinction between the two may remain subjective.

Only one (B) case is observed, it was not featured in numerical simulations so it is less evident whether it can be attributed to the presence of a hydraulic jump over CS. Whereas the variation with depth of currents at Mo2-mooring site in the preceding outflow shows a shallower interface and more westward currents in the upper layer than for the (o) and (L) cases, it may be more akin to a near supercritical flow regime engendering some form of propagating steepening interfacial disturbance.

It was seen in Section 4.2.4 that, in numerical simulations, even if no hydraulic jump occurs at CS, the flow of the barotropic tide in the strait of Gibraltar can lead to the steepening of a long interfacial wave that later develops into a train of ISWs. This train contains a lesser number of ISWs than in the release of hydraulic jump case as it propagates toward the Alboran Sea.

Figure 4.21 is a SAR image taken during the Gibraltar 2020 campaign in the morning of October, 9. A curved surface signature of higher reflectivity can be seen in the Alboran Sea, looking like the front of an ISW (for example in Figure 4.16.A). But looking at Figure 4.19.B, all preceding outflows are of the "L" case for the signal at Mo4 and Mo5 mooring at this date, with no hydraulic jump at CS. The small amplitude internal gravity wave that was observed at Mo5 mooring, if propagating east, could be responsible for the signal in the Alboran Sea that looks like a lone ISW, and is similar to what was encountered in simulations.

4.3.6 Discussion & perspectives

A first confrontation between numerical LES and observations has been carried out showing at least a qualitative agreement. Similarities are found between simulated fields and four of the five types of signals encountered in data of moorings Mo4 and Mo5. Two of those signals, namely "S" and "2S" structures have been shown to be trains of ISWs propagating after the release of the hydraulic jumps at Camarinal Sill. This release induces indeed a westward flow in the whole water column in Mo2 mooring data.

Concerning the signal associated to "L" structures, the presence of the hydraulic jump is doubtful, but Figure 4.21 provides a satellite image of what appears to be the signal of a lone

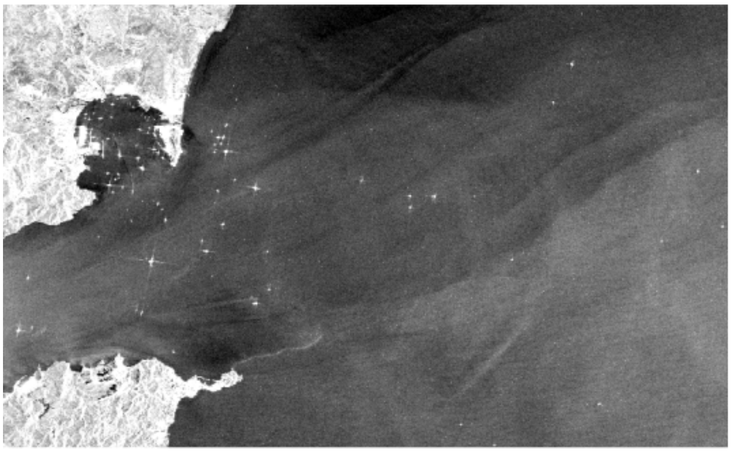

FIGURE 4.21: Sentinel-1 Synthetic Aperture Radar (SAR) image from 09/10/2020 - 6h18am UTC.

large-amplitude internal wave propagating in the Alboran Sea after such an outflow. According to this observation, and in agreement with numerical simulations, the mechanism of release of the hydraulic jump might not be the only mechanism responsible for the generation of the observed ISWs in the strait of Gibraltar and in the western part of the Alboran sea. ISWs trains are indeed observed in other areas of the global ocean, without being linked to the establishment and to the release of a hydraulic jump (see for example Chen et al. (2017)).

Looking at the barotropic currents observed at the Mo2 mooring, there is a pattern linking the amplitude of the tide to the signal observed at the Mo4 and Mo5 moorings. Indeed there seems to be a threshold over which hydraulic jumps and solitary waves can be observed. The reproduction of this threshold in numerical simulations of the strait of Gibraltar is expected to be complex. Even in high-resolution regional modelling such as in Section 4.2, the transition between regimes with or without hydraulic jumps depends greatly to the numerical configuration. The quality and realism of the simulated stratification, for example, play a crucial role in controlling the "criticality" of the atlantic-mediterranean exchange flow and consequently in setting the date of appearance of the hydraulic jump. The quality of the water masses simulated numerically can obviously depend greatly on the quality of the atmospheric and large-scale forcing, knowing that the former has been neglected in the present configurations. Other important physical factors are the high-sensitivity to the quality of the high-resolution bathymetric data and to the tidal forcing.

Several improvements shall be studied in the future :

- Atmospheric fluxes are specified at the surface of the ocean. This provides a better representation of the stratification in the upper surface and has important consequences on the characteristics of the pycnocline and thus on the characteristics of the internal waves, bores and solitons.

- The high-resolution dynamics in the strait of Gibraltar can now be explicitly simulated by downscaling the regional circulation (from the Gulf of Cadix to midway of the Alboran Sea). A three-step embedding has already been carried out using AGRIF library from 900-m to 60-m resolution simulations through a 180-m resolution implementation.

4.4 Appendix : Interface determination between Atlantic and Mediterranean waters

The choice is made to analyze the flow in the Strait of Gibraltar as a two-layer exchange flow based on salinity.

To determine this salinity, first profiles of salinity in the three simulations are fitted to hyperbolic tangent formulations following Sannino et al. (2007). However, contrary to Sannino et al. (2007) that used this definition to consider the interface as a distinct third layer of finite thickness with its own dynamic, here only the median value of the hyperbolic tangent profile is taken as salinity of the interface between Atlantic and Mediterranean waters.

Profiles are analyzed for all three simulations at sections of constant longitude and for various timesteps in the tidal cycle, thus giving both time and spacial variation in this salinity value.

However, the choice is made to only retain a longitudinal variation for the definition of the interfacial salinity and so for each longitudinal section in each simulation, a value is averaged in time and latitude that is presented in Figure 4.22. On this figure is also plotted the finally chosen expression for the value of the salinity interface in the Strait of Gibraltar that reflects the asymmetry of water mass composition with respect to Camarinal Sill :

$$S_I(l) = tanh(\frac{l - L_{CS}}{dl})\frac{S_M - S_m}{2} + \frac{S_M + S_m}{2} \tag{4.4.1}$$

with $L_{CS} = 5.75^o$, $dl = 0.25^o$, the location and width of the Camarinal Sill in degrees, $S_M = 37.39$ and $S_m = 37.1$ the max and minimum interface values taken respectively east and west of the sill.

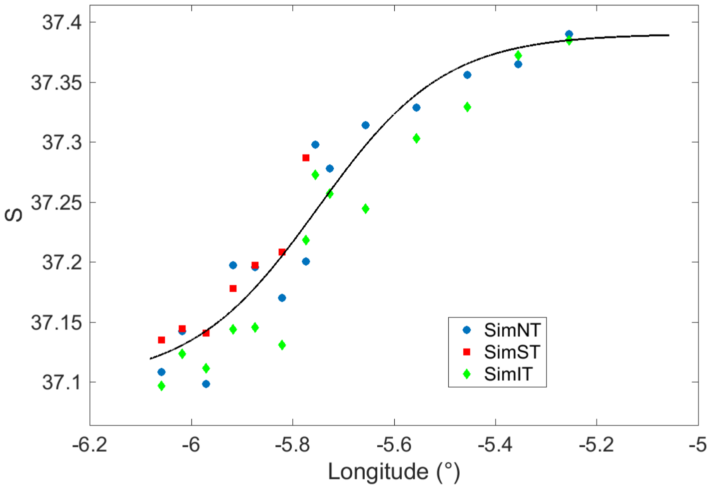

FIGURE 4.22: Value of salinity of the interface between Atlantic and Mediterranean waters from either average of the median values of fitted hyperbolic tangent profiles in simulations SimNT (blue circles), SimIT (green diamonds) and SimST (red squares) at various longitude, or the curve of equation $S_I(l)$ (black line, see text).

This definition is applied online in simulation to define the Atlantic and Mediterranean layers, compute average velocity and Froude number, and reduce variables outputs.

4.5 Appendix : Discussion of diagnosis for supercritical flow and position of hydraulic jump

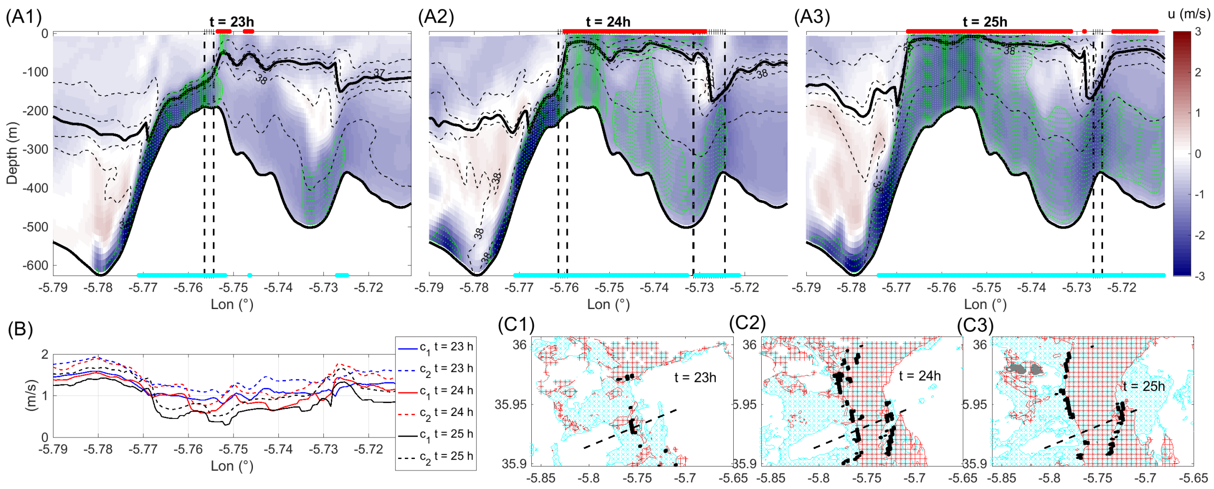

Figure 4.23: (A1 to A3) Comparison in vertical sections at Camarinal Sill of several diagnosis for t = 23, 24 and 25 hours in SimST. Zonal velocity in the section (colorbar), with isohalines in thin dashed lines and the interface as defined in Appendix 4.4 in thick black line. The green shaded area denotes the grid points for which $F_2 \geq 1$ (see text). On the upper (lower) boundary of each figures, red (cyan) denotes $F_1^{Atl} \geq 1$ ($F_1^{Med} \geq 1$) (see text). Horizontal thick dashed lines indicate the hydraulic jump position diagnosis. (B) baroclinic velocity c_1 (plain lines) and mode-1 internal wave velocity c_2 (dashed lines) computed for each vertical section. (C1 to C3) Extension of areas of $F_1^{Med} \geq 1$ (cyan) and $F_1^{Atl} \geq 1$ (red), as well as detection of the hydraulic jump (black dots) in the area of Camarinal Sill for each instant of vertical sections A1 to A3 (section location in dashed line).

Figure 4.23.A1 to A3 present vertical sections at Camarinal Sill, several diagnosis are highlighted. In particular, the depth of the interface as defined in Appendix 4.4 is presented at different moments of the outflow of SimST. As well are indicated the first two diagnosis of Section 4.2.3 :

- The areas for which the flow in the Mediterranean or Atlantic layer as defined by the above-mentioned interface is supercritical ($F_1^{Atl,Med} \geq 1$).
- The position of the hydraulic jump due to the jump in velocity in each layer is evaluated.

Another quantity is represented as green areas. Those areas denote local supercritical flows at model's grid points with a Froude number larger than 1 ($F_2 \geq 1$) that is defined in a different manner than in Section 4.2.3.This new Froude number is given by

$$F_2 = \frac{|\mathbf{u_h}|}{c_2} \tag{4.5.1}$$

with $|\mathbf{u_h}| = \sqrt{u^2 + v^2}$ the norm of the horizontal velocity at each grid point and c_2 an evaluation of the phase speed of the first mode for linear internal wave. This evaluation is carried out by making the approximation for all water columns of a flat-bottom and linear stratification in order to solve numerically the Sturm-Liouville problem associated with the linear propagation equation (Gill, 1982) :

$$W_n'' + k^2 \frac{N^2 - \omega^2}{\omega^2 - f^2} W_n = 0 \tag{4.5.2}$$

for $n = 1$ with bottom and surface boundary conditions $W_n(0) = 0$ and $W_n(-H) = 0$. ω is the wave frequency, here the M2-tidal frequency, and the value of N is taken as the average value over the water column : $c_2 = \omega/k_1$ (this method was already used in Chapter 3).

Figures A1 to A3 and the corresponding Figures C1 to C3 depict the development of the hydraulic jump (*w-jump*) in the spring tide configuration SimST. Figures A1 to A3 are vertical sections orthogonal to the Camarinal Sill that show the flow of Mediterranean Waters under Atlantic waters. The evolution of the criticality of the flow as the tidal variation of the currents strengthen the westward flow can be analyzed, with a comparison between results given by the evaluation of the two Froude numbers F_1 and F_2.

In Figure A1, the Mediterranean waters flow on the western side of the sill as a supercritical gravity current while a hydraulic jump is being formed over a shallower section of the Camarinal sill at 5.755^{o}W. The supercriticality of the Mediterranean waters on the west slope of the sill extends further in F_2 than F_1^{Med} since the latter averages on a layer defined by an interface which is higher in the water column than the shear front of the density current. The detection of the hydraulic jump is close to a noticeable drop of the interface's depth. East of this point there is a bit of overlap between areas of $F_1^{Med} \geq 1$ and $F_1^{Atl} \geq 1$. The area of $F_2 \geq 1$ in the Mediterranean layer can be found downstream whereas the same supercritical region for the Atlantic layer can be found upstream of the drop in the interface's depth.

In Figure A2, one hour later, the position of the hydraulic jump has evolved and moved further west at 5.76^{o}W. The area of supercritical flow has extended east of this point, both for the Mediterranean and the Atlantic layers as the interface is shoaling upflow of the jump. A second hydraulic jump is detected around 5.73^{o}W, associated with the transition to subcritical flow of Atlantic layer and a near vertical drop of the interface. This drop was already present in Figure A1 but with a smaller amplitude and only associated with a non extensive area of $F_1^{Med} \geq 1$ and $F_2 \geq 1$ near the bottom of the water column.

At $t = 25h$ in Figure A3, the westward current is maximal. Extensive area for supercritical flow according to $F_1^{Med,Atl}$. In the evaluation of F_2, the flow is supercritical in the whole water column over an area that extends from 5.77^{o}W to 5.74^{o}W. East of this area, there is extended supercrical flow in the bottom layer, that reaches the interface in the area of the second hydraulic jump. The first hydraulic jump is not detected anymore by the relevant diagnosis while it has fused with the gravity current on the west slope of the sill. Looking at Figure C3 however, this is the case for an area around the section but the detection of the hydraulic jump still occurs at other latitudes.

In Figure B are indicated the theoretical speeds of internal waves, either as the baroclinic speed c_1 or the speed of the first mode waves c_2 for each time of the section. The evaluation of c_1 is always smaller than that of c_2. While c_1 is compared to the averaged speed in a layer in the definition of $F_1^{Med,Atl}$ assumed here, c_2 is compared to local flow at the grid point to define F_2. With $c_2 > c_1$, if c_2 was compared to the average flow in either the Mediterranean or Atlantic layer, the regions of supercritical flow detected in this way would be less extended than the ones seen in Figures C1 to C3.However, in general in Figures A1 to A3, the region where $F_1^{Med,Atl} \geq 1$ corresponds to $F_2 \geq 1$ being true through a good vertical extension for the relevant layer, despite the evaluations of internal waves they are based on being dissimilar (those evaluations are as well made based on theoretical developments for cases far from the complex bathymetry and stratification found here. There is as well some coherence with the results of the hydraulic jump detection criteria, despite the latter does not take into account the interface depth and relying on arbitrary parameters so that its efficiency is sensitive to the complex evolutions of the flow.

All those diagnosis, though rudimentary, are complementary, and allow to have an idea of the evolution of the flow conditions at Camarinal Sill. In the first instants of the apparition of the hydraulic jump as an interface depth discontinuity, the transition of the Atlantic layer from west to east (i.e. alongflow), from supercritical to subcritical over the shallowest part of the sill is mirrored in the bottom Mediterranean layer by a transition from subcritical to supercritical flow associated with the gravity current on the western slope of the sill. Those two transitions coincide with the detection of a hydraulic jump. But as the latter remains while currents strengthen, its position seems to correlate with the transition from supercritical to subcritical in the Atlantic layer as the flow of Mediterranean waters becomes supercritical over a larger area. This extension of supercritical flow of Mediterranean waters to a secondary seamount on the east slope of Camarinal Sill, linked with the shoaling of the Atlantic layer that extends the area of supercritical Atlantic flow, also gives rise to another hydraulic jump at this location.

4.6 Appendix : Singular Value Decomposition (SVD)

Incomplete Singular Value Decomposition (SVD) consists in finding a basis of k [3] singular values and orthonormal singular vectors for a matrix A (complex or real), so that :

$$A = U\Sigma V^* \tag{4.6.1}$$

If A has dimensions G x T, U is a G x k matrix, while V (and its conjugate V^*) is a k x T matrix. U and V are called the left and right singular vectors respectively, and Σ is the diagonal k x k matrix of singular values associated to each couple of singular vectors.

To analyze a time-varying signal of a variable ψ on a 3D grid of G grid points, the spatial field of each of the T time-steps is appended into one column of length G to create the GxT matrix A, where T are the number of iterations of the 3D field.

After proceeding with the SVD of this matrix A, the 3D spatial structure of the i^{th} left-singular vector is recomputed together with its time-evolution (i^{th} right-singular vector).

In Section 3.2, SVD is applied to the complex field $\psi = w + i\,u$. In Section 4.2, SVD is applied to the field of the real quantity Q.

---

[3] In an incomplete decomposition, k the number of singular values on which to decompose A can be specified.

-5- Énergie potentielle disponible : un outil adapté au diagnostic du mélange turbulent

5.1 Résumé en français

Après avoir développé et analysé une simulation originale des grandes structures turbulentes dans le détroit de Gibraltar, dans le cinquième et dernier chapitre de ce manuscrit est abordée la problématique de l'évaluation du mélange turbulent dans une simulation numérique des grandes structures turbulentes. Sous de nombreux aspects, la quantification et la localisation de ce mélange turbulent via celle des flux diapycnaux dans l'océan est un problème délicat.

Les premières pierres d'un cadre théorique rigoureux ont en effet été posées il y a maintenant plus d'un demi-siècle par E. Lorenz (Lorenz, 1955) avant qu'un algorithme simple ne soit proposé à la fin du siècle précédent par Winters et al. (1995) pour intégrer ce raisonnement à partir d'une analyse appuyée sur un raisonnement très physique. La simplicité de cette application algorithmique en fait la force mais aussi d'une certaine façon la faiblesse, en particulier à cause des hypothèses très fortes sur lesquelles elle est fondée. Une hypothèse simplificatrice centrale est celle de la constance du volume de fluide, hypothèse qui devient problématique lorsque le domaine considéré pour le bilan d'énergie potentielle est constitué de colonnes d'eau de mer dont la surface libre et donc la hauteur évoluent au cours du temps.

Dans une première section de ce chapitre (§5.3), une équation d'évolution complète est tout d'abord proposée pour l'énergie potentielle de référence. L'équation proposée intègre en particulier la somme des contributions de la variation de surface en dz^*/dt ($z^*(\rho)$ représentant ici la cote d'une particule de masse volumique ρ dans le profil de référence réarrangé). A partir de cette équation d'évolution, l'algorithme classique proposé par Winters et al. (1995) est généralisé à une somme de colonnes océaniques : une diffusivité efficace est ainsi calculée à partir d'un bilan complet d'énergie potentielle (plus spécifiquement d'énergie potentielle de référence ou BPE en anglais) via la relation de l'Équation 5.3.15.

Cet algorithme généralisé est ensuite appliqué à un ensemble de configurations de complexité croissante, chaque configuration permettant d'analyser et d'évaluer la pertinence de la quantification et de la localisation du mélange turbulent. Une équation d'advection-diffusion d'un traceur passif est tout d'abord étudiée dans le cadre de stratifications linéaires puis "bi-couche". Le mélange induit par les oscillations libres d'une cuve stratifiée ou dans un écoulement bi-couche instable ou par un écoulement dans la région du détroit de Gibraltar est lui-aussi analysé. Ces trois dernières configurations sont simulées numériquement avec le code océanique à toit libre CROCO dans sa version compressible et non-hydrostatique.

Une première conclusion est que la généralisation de l'algorithme de Winters et al. (1995) permet une évaluation rigoureuse et "suffisamment" précise du mélange turbulent (comparée aux erreurs induites par son évaluation). L'efficacité de l'algorithme doit toutefois encore être optimisée afin que ce dernier ne soit appliqué à très haute résolution à des régions océaniques d'extension conséquente.

5.2 Introduction

In the present chapter, a substantial step is made toward the quantification of mixing in realistic ocean configurations. The objective is to generalize Winters et al. (1995)'s framework, in which mixing is linked to the evolution of potential energy, to the real ocean made of volume-varying ocean columns.

The most rigorous approach of the *mixing*-related issues has undoubtedly been proposed by Lorenz (1955), and was recently extended to a fully compressible context by Tailleux (2009) and lately Tailleux (2013). It is based on the concept of Background and Available gravitational Potential Energy (hereafter respectively BPE and APE) as a decomposition of the total gravitational Potential Energy (PE). The author defines first APE as the potential energy released when reorganizing adiabatically the flow so that it reaches its state of minimal potential energy. This minimal value corresponds to the BPE, that can also be expressed as the difference between the PE and the APE. The BPE compartment, thus defined, grows monotonically under diabatic mixing, offering a well-defined tool to evaluate this mixing.

The BPE potential energy compartment is defined with respect to a "reference" state of minimum possible potential energy, often called the *Lorenz reference state* (Saenz et al., 2015). Winters et al. (1995) proposed an algorithm to compute (i) this reference state by an adiabatic reorganisation of the fluid density, (ii) an approximation of the diffusivity responsible for diapycnal mixing for a constant-volume region.

But this approach remains challenging when applied in a realistic context, for instance over a limited area of a free-surface, varying-bathymetry ocean. A "limited area" raises indeed many questions on boundary fluxes and the validity of the state of minimal energy, whereas a free surface or a varying bathymetry complicate the computation of the reference state.

In recent developments, local expressions of the available potential energy under a Boussinesq approximation have been derived (Winters and Barkan, 2013) in contrast to the usually vertical integrated potential energy. Lately Howland et al. (2020a,b) also quantified both mixing and available potential energy in vertically periodic simulations of a stratified flow, making a first step toward domains with varying vertical boundaries.

Both Saenz et al. (2015) and Tailleux (2018) insist on the fact that the Lorenz reference state of absolute minimum potential energy is difficult to define and compute (due to the numerical cost of the sorting algorithm, the non-linearity of the EOS, etc.). As a consequence, these studies are dedicated to the evaluation of the errors and discrepancies when simpler and easier-to-obtain reference states are defined. Saenz et al. (2015) additionally describes in detail an algorithm to compute Lorenz' reference state in an efficient way.

In this chapter, several developments are made to evaluate the evolution of BPE in a s-coordinate numerical model for a free-surface ocean, and the feasibility of quantifying mixing processes from this evaluation. In particular, a general evolution equation for the Background Potential Energy (BPE) is derived to take into account the evolution in time of the volume (and as a consequence of the potential energy) of water columns due to free-surface anomalies. Based on such an evolution equation, Winters et al. (1995)'s algorithm can then be generalized to realistic numerical ocean configurations. To do so, additional difficulties need to be solved in order to take into account : (i) bathymetry variations, (ii) variations of grid-cell volume in terrain-following s-coordinates, and (iii) diffusive and advective fluxes through open boundaries. In particular for this last point, the diapycnal fluxes associated *in fine* to mixing are known to be several orders of magnitude smaller than the advective fluxes associated for instance to ocean tides, and the computation of the terms of the balance equation must be carried out with care to preserve an overall high accuracy.

The generalized algorithm proposed in this chapter takes root in the "milestone" publication by Winters et al. (1995). Later developments to gain efficiency are not yet implemented because (i) the cases studied so far do not require too large computations, and (ii) Winters et al. (1995)'s approach is to be used as a reference and, as a consequence, needs to be implemented first. The aim of this chapter is not only to evaluate the relevance and efficiency of the method but also to point out where the approach needs to be further refined.

This algorithm and other developments are presented in Section 5.3.4 of this chapter. It is applied first in Section 5.4 to a simple advection - diffusion equation using homogeneous grid cells. In a second step, CROCO ocean model is implemented in test-case configurations of Section 5.5. Those configurations are of increasing complexity in terms of bathymetry and dynamics ; the last, most realistic configuration being the vertical section of Gibraltar Experiment (SimRef) presented in Chapter 3.

5.3 Mixing in a general volume-varying ocean region

5.3.1 Decomposition of potential energy balance in a free-surface ocean

The Lorenz reference state is the state of the stratification after the adiabatical reorganization of Lorenz (1955). It consists in attributing a reference depth z^* to each fluid parcel corresponding to its depth in the reference density profile. This reference profile is constructed by redistributing adiabatically the fluid particles in such a way that the heaviest particles are located at the deepest depths, i.e. below the lightest particles. The potential energy associated to this state is the BPE (noted PE_B in subsequent equations) of the initial state before reorganisation, and can be expressed as :

$$PE_B = \int_x \int_{-1}^{0} g\rho z^* \, h dxds \tag{5.3.1}$$

The evolution of BPE, through the evolution of the stratification profile z^*, reflects the adiabatic mixing processes that can then be quantified.

The expression of the evolution of a specific quantity integrated in a time-varying volume is addressed in the Appendices 5.7 of the present chapter. In particular, an expression of the evolution of the quantity $\mathcal{A} = \int_x \int_{-1}^{0} \rho A h \, dxds$ in vertical s-coordinate is derived using mass conservation and the state equation in Appendix 5.7.3. It is applied in the two following paragraphs in order to express the evolution of PE and BPE (the evolution of APE can be retrieved from deducting the latter from the former).

5.3.2 Balance of PE in s-coordinates

The evolution of the specific PE can be obtained from the general evolution equation in s-coordinates derived in Appendix 5.7.3 by setting $A = gz$:

$$\frac{dE_p}{dt} = g \int_x \int_{-1}^{0} \left. \frac{\partial \rho h z}{\partial t} \right|_s dxds \tag{5.3.2a}$$

Replacing A in Equation 5.7.45, that uses as evolution equation for density the Equation 2.2.6 :

$$\frac{dE_p}{dt} = g\int_x\int_{-1}^{0} \rho h \left.\frac{\partial z}{\partial t}\right|_{xs} dxds \tag{5.3.3a}$$

$$- g\left[\int_{-1}^{0} \rho hzu\, ds\right]_x + g\int_x\int_{-1}^{0} \rho hu \left.\frac{\partial z}{\partial x}\right|_{ts} dxds \tag{5.3.3b}$$

$$- g\left[\int_x \left.\frac{\partial \rho z v_s}{\partial s}\right|_{tx} dx\right]_0^1 + g\int_x\int_{-1}^{0} \rho v_s \left.\frac{\partial z}{\partial s}\right|_{tx} dxds \tag{5.3.3c}$$

$$+ g\left[\int_{-1}^{0} hz\kappa^h \left.\frac{\partial \rho}{\partial x}\right|_{ts} ds\right]_x - g\int_x\int_{-1}^{0} h\kappa^h \left.\frac{\partial z}{\partial x}\right|_{ts} \left.\frac{\partial \rho}{\partial x}\right|_{ts} dxds \tag{5.3.3d}$$

$$+ g\left[\int_x z\frac{\kappa^v}{h} \left.\frac{\partial \rho}{\partial s}\right|_{tx} dx\right]_0^1 - g\int_x\int_{-1}^{0} \frac{\kappa^v}{h} \left.\frac{\partial z}{\partial s}\right|_{tx} \left.\frac{\partial \rho}{\partial s}\right|_{tx} dxds \tag{5.3.3e}$$

With v_s the vertical velocity through $s = cst$ surfaces that was defined in Section 2.2.2 of Chapter 2. The advective flux of PE (fourth term at the RHS) can be integrated by part leading to :

$$\frac{dE_p}{dt} = \underbrace{g\int_x\int_{-1}^{0} \rho h \left.\frac{\partial z}{\partial t}\right|_{xs} dxds}_{(1)} \tag{5.3.4a}$$

$$- g\left[\int_{-1}^{0} \rho hzu\, ds\right]_x + \underbrace{g\int_x\int_{-1}^{0} \rho hu \left.\frac{\partial z}{\partial x}\right|_{ts} dxds}_{(2)} \tag{5.3.4b}$$

$$- \underbrace{g\left[\int_x \rho z v_s\, dx\right]_0^1}_{=0} + \underbrace{g\int_x\int_{-1}^{0} \rho h v_s\, dxds}_{(3)} \tag{5.3.4c}$$

$$+ g\left[\int_{-1}^{0} hz\kappa^h \left.\frac{\partial \rho}{\partial x}\right|_{ts} ds\right]_x - g\int_x\int_{-1}^{0} h\kappa^h \left.\frac{\partial z}{\partial x}\right|_{ts} \left.\frac{\partial \rho}{\partial x}\right|_{ts} dxds \tag{5.3.4d}$$

$$+ g\left[\int_x z\frac{\kappa^v}{h} \left.\frac{\partial \rho}{\partial s}\right|_{tx} dx\right]_0^1 - g\int_x\int_{-1}^{0} \kappa^v \left.\frac{\partial \rho}{\partial s}\right|_{tx} dxds \tag{5.3.4e}$$

where the advection of PE at the surface and at the bottom vanishes. At the RHS, terms (1), (2) and (3) can be gathered to recover the buoyancy flux component (ϕ_z) of Winters et al. (1995).

$$\frac{dE_p}{dt} = \underbrace{\int_x\int_{-1}^{0} \rho g h v_z \, dxds}_{=(1)+(2)+(3)\equiv\phi_z} \tag{5.3.5a}$$

$$- g\left[\int_{-1}^{0} \rho h z u \, ds\right]_x \tag{5.3.5b}$$

$$+ g\left[\int_{-1}^{0} hz\kappa^h \left.\frac{\partial\rho}{\partial x}\right|_{ts} ds\right]_x - g\int_x\int_{-1}^{0} h\kappa^h \left.\frac{\partial z}{\partial x}\right|_{ts}\left.\frac{\partial\rho}{\partial x}\right|_{ts} dxds \tag{5.3.5c}$$

$$+ g\left[\int_x z\frac{\kappa^v}{h}\left.\frac{\partial\rho}{\partial s}\right|_{tx} dx\right]_0^1 - g\int_x\int_{-1}^{0} \kappa^v \left.\frac{\partial\rho}{\partial s}\right|_{tx} dxds \tag{5.3.5d}$$

5.3.3 Balance of BPE in s-coordinates

The same Equation 5.7.45 derived in Appendix 5.7.3 can alternatively be used for $A = gz^*$, the specific BPE, leading to :

$$\frac{dPE_B}{dt} = g\int_x\int_{-1}^{0} \left.\frac{\partial\rho h z^*}{\partial t}\right|_s dxds \tag{5.3.6a}$$

and then

$$\frac{dPE_B}{dt} = g\int_x\int_{-1}^{0} \rho h\left.\frac{\partial z^*}{\partial t}\right|_{xs} dxds_{\;(1)} \tag{5.3.7a}$$

$$- g\left[\int_{-1}^{0} \rho h z^* u \, ds\right]_x + g\int_x\int_{-1}^{0} \rho h u\left.\frac{\partial z^*}{\partial x}\right|_{ts} dxds_{\;(2)} \tag{5.3.7b}$$

$$- 0 + g\int_x\int_{-1}^{0} \rho v_s\left.\frac{\partial z^*}{\partial s}\right|_{tx} dxds_{\;(3)} \tag{5.3.7c}$$

$$+ g\left[\int_{-1}^{0} hz^*\kappa^h \left.\frac{\partial\rho}{\partial x}\right|_{ts} ds\right]_x - g\int_x\int_{-1}^{0} h\kappa^h \underbrace{\left.\frac{\partial z^*}{\partial x}\right|_{ts}}_{=\frac{dz^*}{d\rho}\left.\frac{\partial\rho}{\partial x}\right|_{ts}}\left.\frac{\partial\rho}{\partial x}\right|_{ts} dxds \tag{5.3.7d}$$

$$+ g\left[\int_x z^*\frac{\kappa^v}{h}\left.\frac{\partial\rho}{\partial s}\right|_{tx} dx\right]_0^1 - g\int_x\int_{-1}^{0} \frac{\kappa^v}{h}\left.\frac{\partial z^*}{\partial s}\right|_{tx}\left.\frac{\partial\rho}{\partial s}\right|_{tx} dxds \tag{5.3.7e}$$

The terms associated to the particulate derivative of z^* can be gathered from terms (1), (2) and (3) :

$$\frac{dPE_B}{dt} = \underbrace{g\int_x\int_{-1}^{0}\rho h\frac{dz^*}{dt}\,dxds}_{(1)+(2)+(3)} \tag{5.3.8a}$$

$$-\underbrace{g\Big[\int_{-1}^{0}\rho hz^*u\,ds\Big]_x}_{\approx F_A} \tag{5.3.8b}$$

$$+\underbrace{g\Big[\int_{-1}^{0}hz^*\kappa^h\frac{\partial\rho}{\partial x}\Big|_{ts}\,ds\Big]_x}_{F_D^{(h)}}\underbrace{-g\int_x\int_{-1}^{0}h\kappa^h\frac{dz^*}{d\rho}\frac{\partial\rho}{\partial x}\Big|_{ts}^{2}\,dxds}_{\phi_D^{(h)}} \tag{5.3.8c}$$

$$+\underbrace{g\Big[\int_x z^*\frac{\kappa^v}{h}\frac{\partial\rho}{\partial s}\Big|_{tx}\,dx\Big]_0^1}_{F_D^{(v)}}\underbrace{-g\int_x\int_{-1}^{0}\frac{\kappa^v}{h}\frac{dz^*}{d\rho}\frac{\partial\rho}{\partial s}\Big|_{tx}^{2}\,dxds}_{\phi_D^{(v)}} \tag{5.3.8d}$$

where F_A is the lateral (horizontal) advective flux of BPE at the boundary, $F_D^{(v)}$ and $F_D^{(h)}$ are the vertical and horizontal diffusive fluxes, $\phi_D^{(v)}$ and $\phi_D^{(h)}$ are the diapycnal vertical and horizontal fluxes.

Time variations of z^*

The first RHS term of Equation 5.3.8,

$$g\int_x\int_{-1}^{0}\rho h\frac{dz^*}{dt}\,dxds \tag{5.3.9}$$

is akin to a vertical buoyancy-flux term for the z^* reference state. It vanishes for a volume of integration with fixed-in-time boundaries (Winters et al. (1995), Huang (1998) and many others...). But it has no particular reason to vanish when movements of the free-surface are taken into account. This paragraph constitutes a proposition for its development in this case.

Going back to a more general notation of our integral volume V_ζ and following Huang (1998), z^* can be expressed as a function of the volume $v(\rho)$ of fluid with a density larger than ρ :

$$v(\rho) = \iiint_\zeta H(\rho(\mathbf{x}',t) - \rho(\mathbf{x},t))d\mathbf{x}' \tag{5.3.10}$$

where H is the Heaviside function, equals to 0 for $\rho(\mathbf{x}',t) < \rho(\mathbf{x},t)$, $1/2$ for $\rho(\mathbf{x}',t) = \rho(\mathbf{x},t)$, and 1 for $\rho(\mathbf{x}',t) > \rho(\mathbf{x},t)$. In the reference profile, a given density is associated to a reference depth. This volume can then be expressed as $v(z^*)$, the volume of water between the bottom and depth z^* in the water column :

$$v(z^*) = \int_{bottom}^{z^*} S(z')dz' \tag{5.3.11}$$

with $S(z)$ the area at depth z.

Using the s-coordinate formulation of Reynolds transport theorem of Equation 5.7.27 in the Appendix's section 5.7.1 :

$$\frac{dz^*}{dt} = \left(\frac{d\,v(z^*)}{dz^*}\right)^{-1} \frac{d\,v(\rho)}{dt} \tag{5.3.12a}$$

$$= \frac{1}{S\,(z^*(\rho))} \frac{d}{dt} \iiint_{V_\zeta} H\,(\rho(\mathbf{x}', t) - \rho(\mathbf{x}, t))\, d\mathbf{x}' \tag{5.3.12b}$$

$$= \frac{1}{S\,(z^*(\rho))} \iiint_{V_\zeta} \frac{\partial}{\partial t} H\,(\rho(\mathbf{x}', t) - \rho(\mathbf{x}, t))\, d\mathbf{x}' \tag{5.3.12c}$$

$$+ \frac{1}{S\,(z^*(\rho))} \iint_{S_{surf}} H\,(\rho(\mathbf{x}', t) - \rho(\mathbf{x}, t))\, \frac{\partial \zeta(x', t)}{\partial t} dS' \tag{5.3.12d}$$

In which S_{surf} is the free-surface. As a consequence, the first RHS term expressed in Equation 5.3.9 can be rewritten as ϕ_ζ :

$$\phi_\zeta = \iiint_{\mathbf{V}_\zeta} \rho(\mathbf{x}, t) g \frac{dz^*}{dt} d\mathbf{x} \tag{5.3.13a}$$

$$= \underbrace{\iiint_{\mathbf{V}_\zeta} \frac{\rho(\mathbf{x}, t) g}{S\,(z^*(\rho))} \iiint_{V_\zeta} \frac{\partial}{\partial t} H\,(\rho(\mathbf{x}', t) - \rho(\mathbf{x}, t))\, d\mathbf{x}' d\mathbf{x}}_{=0} \tag{5.3.13b}$$

$$+ \iiint_{\mathbf{V}_\zeta} \frac{\rho(\mathbf{x}, t) g}{S\,(z^*(\rho))} \iint_{S_{surf}} H\,(\rho(\mathbf{x}', t) - \rho(\mathbf{x}, t))\, \frac{\partial \zeta(x', y', t)}{\partial t} dS' d\mathbf{x} \tag{5.3.13c}$$

The first term at the RHS vanishes as shown for instance by Huang (1998). The second term, however, will be *a priori* non-zero for any case with a moving free-surface.

Note that with the definition of the Heaviside function, a way to interpret this term is that the contribution of the evolution of the free-surface elevation is only taken into account in the evolution of BPE for fluid parcels as light as the ones at the surface (ie, the parcels at the free-surface themselves), or lighter than them. Those parcels are placed near the top of the reference state's profile, so that $S\,(z^*(\rho))$ is in most cases the area at the level of the free-surface (but not the area of the deformed free-surface itself).

5.3.4 Generalized algorithm to evaluate effective diffusivity

The evolution of BPE is integrated in the following framework, that is applied invariably to each configuration of Sections 5.4 and 5.5 of this chapter :

1. The volume of available ocean water located below a given depth $V(z)$ is evaluated at all depths. For non-moving bathymetry cases, this step is carried out only once.
2. At a given time, the *reference* density profile $\rho^*(z)$ is obtained following Winters et al. (1995) by sorting the stratification, filling from bottom to top the total available ocean volume as determined in the previous step with water parcels of increasing density. In "small"-extent configurations (such as the 2D vertical sections of this chapter), this sorting does not incur too large computations.

3. The depth of a given density $z^*(\rho, t) = z^*(\mathbf{x}, t)$ can in turn be obtained as the inverse function of the reference, sorted density profile $\rho^*(z)$.
4. The Background Potential Energy $PE_B(t)$, together with its evolution in time and the RHS terms of Equation 5.3.8, can then be computed based on $z^*(\rho, t)$ for the ocean region considered.
5. An "effective" diffusivity κ_{eff} can finally be evaluated in a chosen area based on the generalized evolution equation of BPE (Equation 5.3.8).

Indeed, in Equation 5.3.8, the horizontal and vertical diffusivities (respectively κ_h and κ_v) are the two unknowns of the problem. Here they are considered as homogeneous for the volume of ocean to which the algorithm is applied. Furthermore, in most cases studied hereafter, diffusivity has to be chosen isotropic, leading to $\kappa_h = \kappa_v = \kappa$. Indeed, the balance equation only provides one equation and, as a consequence, it can only lead to the determination of one unknown diffusivity without resorting to a parameterized expression of diffusivity. In this case, the effective diffusivity (κ_{eff}) can be obtained by reformulating the evolution Equation 5.3.8 as :

$$\frac{dPE_B}{dt} = \underbrace{g\int_x\int_{-1}^{0}\rho h\left.\frac{dz^*}{dt}\right|_{xs} dxds}_{\phi_\zeta} \tag{5.3.14a}$$

$$\underbrace{-g\Big[\int_{-1}^{0}\rho h z^* u\, ds\Big]_x - g\Big[\int_x \rho z^* v_s\, dx\Big]_0^1}_{F_A} \tag{5.3.14b}$$

$$+\,\kappa_{eff}\underbrace{\Big[+g\Big[\int_{-1}^{0} hz^*\left.\frac{\partial\rho}{\partial x}\right|_{ts} ds\Big]_x + g\Big[\int_x z^*\frac{1}{h}\left.\frac{\partial\rho}{\partial s}\right|_{tx} dx\Big]_0^1\Big]}_{F_D} \tag{5.3.14c}$$

$$+\,\kappa_{eff}\underbrace{\Big[-g\int_x\int_{-1}^{0} h\frac{dz^*}{d\rho}\left.\frac{\partial\rho}{\partial x}\right|_{ts}^2 dxds - g\int_x\int_{-1}^{0}\frac{1}{h}\frac{dz^*}{d\rho}\left.\frac{\partial\rho}{\partial s}\right|_{tx}^2 dxds\Big]}_{\phi_D} \tag{5.3.14d}$$

In essence, the balance is first computed with $\kappa_{eff} = 1\ m^2/s$ and both diffusive terms ϕ_D and F_D have high values. An instantaneous evaluation of diffusivity is then given by :

$$\kappa_{eff} = \frac{\frac{dPE_B}{dt} - (\phi_\zeta + F_A)}{F_D + \phi_D} \tag{5.3.15}$$

The treatment of this evolution equation needs to be achieved with a particular care. Indeed, the term (ϕ_ζ) associated to dz^*/dt can hardly be evaluated directly. It is computed as the sum of terms (1), (2) and (3) in Equation 5.3.6 in order to maintain the required accuracy without adding to the computational cost.

Additionally, in the first test-cases presented and discussed in Section 5.4, configurations are cyclic in both horizontal and vertical directions, so the formulation of Equation 5.3.14 retains advective and diffusive fluxes through the top and bottom boundaries. This is otherwise not the case in Section 5.5.

5.4 Explicit and implicit mixing in an advection-diffusion equation

The evolution of the explicit (physical) and implicit (numerically induced) mixing is first tackled in the 2D vertical section of a flow governed by an advection - diffusion equation. As indicated previously, to avoid the heavy numerical treatment of tracer fluxes through lateral boundaries, the configuration is chosen cyclic in both directions.

The advection - diffusion governing the local evolution of a passive tracer ψ is given by :

$$\frac{\partial \psi}{\partial t} = -u\frac{\partial \psi}{\partial x} - w\frac{\partial \psi}{\partial z} + \kappa^{h}_{exp}\frac{\partial^2 \Psi}{\partial x^2} + \kappa^{v}_{exp}\frac{\partial^2 \psi}{\partial z^2} \tag{5.4.1}$$

with $\kappa^{h,v}_{exp}$ the given explicit (known) diffusion coefficient (for most cases $\kappa^{h}_{exp} = \kappa^{v}_{exp}$). Total volume is supposed to remain constant so that the RHS term ϕ_{ζ} of Equation 5.3.14 integrates to zero. No cases with vertical velocity are presented ($w = 0$ and $v_s = 0$) so the second term of F_a is also zero. Depending on the test-case considered, the initial field of passive tracer is either equal to $\psi_1(x) = cos(2\pi x/L_x)$ or to $\psi_2(x, z) = Re(e^{i2\pi x/L_x}e^{i2\pi z/L_z})$.

5.4.1 Local diffusion test configuration (BPE_{exp})

The first implementation is that of a diffusive but advection-free flow ($u = 0\ m/s$). The main numerical parameters are given in Table 5.1.

Configuration BPE_{exp}	*Parameters*
Numerical Model	Advection-diffusion equation of passive tracers
L_x	30 m
L_z	30 m
Δx	0.5 m
Δz	0.5 m
Δt	10 s
Time stepping	RK3
Diffusivity	$Left : \kappa^{h}_{exp} = \kappa^{v}_{exp} = 10^{-5}\ m^2/s.\ Right : \kappa^{h}_{exp} = \kappa^{v}_{exp} = 10^{-3}\ m^2/s.$
Advection	none
Initial field	$\psi(x, z,\ 0) = \psi_2(x, z)$

Table 5.1: BPE_{exp} configuration : numerical parameters.

The chosen initial passive tracer field is given by $\psi_2(x, z)$ and is shown in Figure 5.1.A1. To evaluate the capacity of the algorithm to deal with local variations of mixing (i.e. when the intensity of turbulent mixing is varying in space), the explicit diffusivity κ_{exp} of Equation 5.4.1 is non-homogeneous over the domain. It is two order of magnitude greater over the right half (from 15 m to 30m along the x-axis in Figure 5.1.A1) of the domain (10^{-3} vs. $10^{-5}\ m^2/s$ in the left half), so that as can be seen in Figure 5.1.A2 gradients are smoothed faster in this part of the grid.

The evaluation of κ_{eff} presented in the previous section is carried out either for each half domain or for the whole domain. Three $z^*(\rho)$ reference profiles (respectively z^*_{left}, z^*_{right} and z^*_{all}) are consequently computed with the sorting algorithm considering only the fluid parcels in the left sub-domain, the right sub-domain, or the whole domain. Examples of those profiles are presented in Figures 5.1.B1 and B2.

Figures 5.1.C to F present the terms of Equation 5.3.14 computed from the evolution of each reference profiles. It must be noted that neither the diffusive term ϕ_D nor dPE_B/dt computed for the whole domain are equal to the sum of those terms computed on each half domain (for example $\phi^{all}_D \neq \phi^{left}_D + \phi^{right}_D$). This is due to the different definition of $z^*(\psi)$ depending on the domain

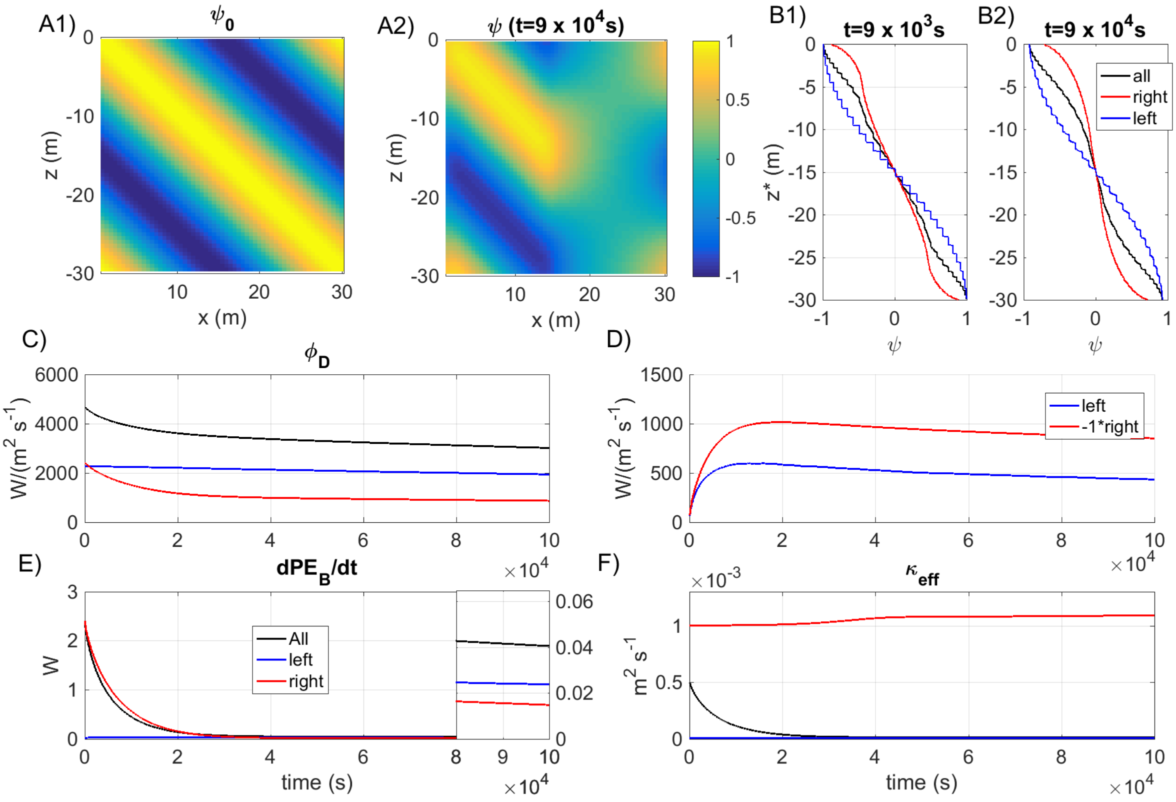

FIGURE 5.1: (A1 and A2) Initial field of tracer ψ, and tracer field after $t = 100s$ of simulation. (B1 and B2) Reference profiles $z^*(\psi)$ at $t = 9.10^3 s$ and $t = 9.10^4 s$ of simulation computed either with the fluid parcels of the left-half sub-domain (blue), the right-half sub-domain (red), or the complete domain (black). (C, D and E) RHS (C and D) and LHS (E) terms of Equation 5.3.14 computed on the different (sub-)domains. F_D^{right} is indicated with a factor -1 in (D). (F) κ_{eff} as evaluated in Equation 5.3.15 with the previous terms on the different (sub-)domains.

extension over which the sorting algorithm is used. In the same way, the diffusive fluxes F_D of Figure 5.1.D do not cancel each other from one half domain to the other past the initialization.

If the effective diffusivity (κ_{eff}) is evaluated over each half of the domain, Figure 5.1.E shows that the algorithm provides the correct value of the diffusivity with : $\kappa_{eff} \approx \kappa_{exp}$, as the ratio of Equation 5.3.15 is near constant. In contrast, if κ_{eff} is evaluated over the whole domain, it is initially equivalent to the overall explicit mean diffusivity $(\kappa^{left} + \kappa^{right})/2 = 5.10^{-4}\ m^2/s$ but it decreases afterwards with time, approaching the value of κ_{exp}^{left} after $t \approx 3.10^4\ s$. So the global effective diffusivity is finally close to the smallest value in the domain κ^{left}. This smallest value is associated with the area of the domain in which gradients of the tracer field are at that time less affected by dissipation, with a slower evolution of z^* as seen in Figures 5.1.B1 and B2.

Indeed, a characteristic time-scale associated with diffusion can be evaluated for each half subdomain as

$$T_\kappa = \frac{L_\kappa^2}{\kappa} \tag{5.4.2}$$

T_κ should represent an order of magnitude for the time span required to achieve the complete homogenisation of the tracer field over the characteristic length L_κ. Taking $L_\kappa = 15\ m$, $T_\kappa^{left} = 2.25\ 10^7\ s$ and $T_\kappa^{right} = 2.25\ 10^5\ s$. The smoothing of tracer gradients in the right part of the domain should occur more rapidly than in the left part, so it is expected that after a period of about T_{κ}^{right}, the effect of κ_{right} in a global evaluation of mixing over the complete domain is negligible.

5.4.2 Implicit diffusion case (BPE_{imp})

A similar flow configuration is now investigated with homogeneous κ_{exp} when advection is not neglected anymore ($u \neq 0$, Table 5.2).

Configuration BPE_{imp}	*Parameters*
Numerical Model	Advection-diffusion equation of passive tracers
L_x	30 m
L_z	20 m
Δx	0.5 m or 1.5 m
Δz	0.5 m
Δt	0.1 s
Time stepping	RK3
Diffusivity	UP1 case : 0 m^2/s, UP3 case see Table 5.3
Advection	U = 0.1 m/s with UP1 or UP3 advective schemes.
Initial field	With UP1 scheme : $\psi(x, z,\ 0) = \psi_2(x, z)$. With UP3 scheme : $\psi(x, z,\ 0) = \psi_1(x)$

TABLE 5.2: BPE_{imp} configuration : numerical parameters.

The objective with this new implementation is to evaluate the implicit diffusion κ_{imp} due to upstream (UP1 or UP3) advective schemes. The effective diffusivity can be compared to the value obtained analytically for each upstream scheme.

First order upstream scheme (UP1)

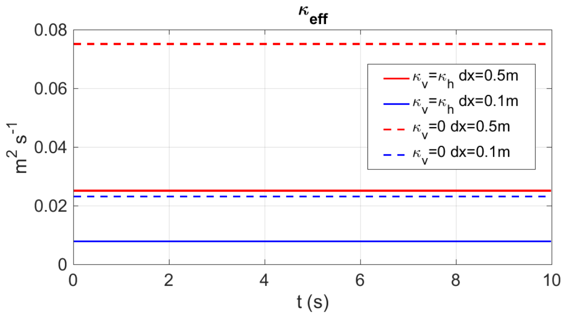

FIGURE 5.2: κ_{eff} computed in the case of an implicit diffusion with RK3-UP1 schemes for $\Delta x = 0.5m$ (red) or $\Delta x = 0.1m$ (blue). In the computation of κ_{eff}, either isotropic diffusion is assumed ($\kappa^v = \kappa^h$, lines) or that diffusion is only applied in the horizontal direction ($\kappa^v = 0$, dashed lines)

The initial field is the same as in the previous BPE_{exp} configuration ($\psi_2(x, z)$, see Figure 5.1.A1). Advective fluxes are now based on a first-order upstream scheme (UP1) and no explicit harmonic diffusion ($\kappa_{exp} = 0$) is specified for now, so all diabatic evolution of ψ will be due to the implicit effect of the advection scheme. The modified equation for the discrete advection equation can be derived analytically :

$$\frac{\partial\psi}{\partial t} + U\frac{\partial\psi}{\partial x} = \frac{1}{2}U\Delta x\frac{\partial^2\psi}{\partial x^2} + O(\frac{\partial^3\psi}{\partial x^3}) \tag{5.4.3}$$

This leads to an analytical formulation of the implicit diffusion coefficient for the UP1 advective scheme :

$$\kappa_{imp}^{h} \approx \frac{1}{2}U\Delta x \tag{5.4.4}$$

The implicit diffusivity consequently varies linearly with the grid scale and for $\Delta x = 0.5\ m$ (respectively $\Delta x = 1.5\ m$), it can reach $\kappa_{imp}^{h} = 0.025\ m^2/s$ (respectively $0.075\ m^2/s$).

Figure 5.2 shows that the correct value of the implicit diffusivity ($\kappa_{eff} = \kappa_{imp}$) can be recovered with the BPE algorithm only if the vertical component of the diffusion flux (ϕ_D in Equation 5.3.14) is not taken into account, i.e. when only the along-flow diffusion flux is considered. If both the horizontal and vertical components of the fluxes are retained in the evolution equation, the BPE algorithm leads to a smaller value of the effective diffusivity as part of the mixing is attributed to vertical diabatic fluxes.

Third order upstream scheme (UP3)

In this third configuration, the initial tracer field is now $\psi(x,\ 0) = \psi_1(x)$ (see Figure 5.3.A). A third-order upstream advective scheme (UP3) is now associated to the RK3 time-stepping with a non-vanishing horizontal velocity. The modified equation leads this time to a 4th-order diffusion term :

$$\frac{\partial\psi}{\partial t} + U\frac{\partial\psi}{\partial x} = \underbrace{\frac{1}{120}(5C^3 - 10)U\Delta x^3}_{k_4}\frac{\partial^4\psi}{\partial x^4} + O(\frac{\partial^5\psi}{\partial x^5}) \tag{5.4.5}$$

where $C = U\Delta t/\Delta x$ is the advection Courant number. With $C = 2.10^{-2}$ in the present configuration, the fourth order diffusivity takes the value $k_4 = -1.10^{-3}m^4/s$. Note that the BPE algorithm gives an implicit diffusion in form of a second-order diffusivity κ_{eff}.

This second-order effective diffusivity is evaluated for several experiments relying on this configuration (Table 5.3). In those experiments, in addition to the effect of the implicit diffusivity from the $UP3$ scheme, explicit harmonic diffusion is added, so that the effective diffusivity should be the sum of both contributions $\kappa_{eff} \approx \kappa_{exp} + \kappa_{imp,2}$. The computed effective diffusivity shows high-frequency oscillations with a non-negligible relative amplitude (not shown). Those oscillations are found regardless of the value of κ_{exp}. To filter out these oscillations, the value of κ_{eff} indicated in Table 5.3 has been averaged over the whole simulation time. Once κ_{exp} is removed from κ_{eff}, a unique value of $\kappa_{imp,2}$ is recovered at $4.65.10^{-5}\ m^2/s$ for all experiments.

To compare the effective second-order diffusivity ($k_{imp,2} = \kappa_{eff} - \kappa_{exp}$) with the analytical fourth-order diffusivity k_4, Figure 5.3.B shows the evolution of the spatial derivative of the passive tracer field (ψ) with the resulting second and fourth-order diffusion schemes. The resulting trends are close to each other. Note however that the second-order and fourth-order advection terms do not operate in a similar way in wave-number space. Indeed, the fourth order is a more selective filter, smoothing more specifically small-scale gradients of passive tracer. This might be sufficient to explain the differences observed in Figure 5.3.B.

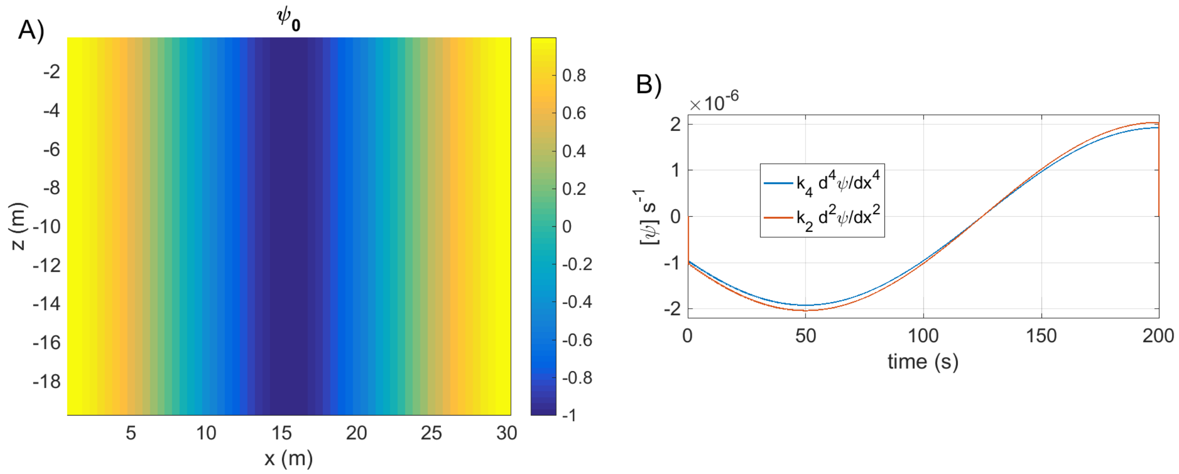

FIGURE 5.3: (A) Initial tracer field. (B) Comparison of the fourth-order (with an analytical diffusivity k_4) and second-order (with a diffusivity k_2 deduced from κ_{eff} in Table 5.3) formulation of diffusion at a random grid point.

κ_{exp}	-10^{-4}	$-4.65.10^{-5}$	-10^{-5}	0	10^{-5}	10^{-4}
κ_{eff}	$-5.35.10^{-5}$	$3.5.10^{-8}$	$3.65.10^{-5}$	$4.65.10^{-5}$	$5.65.10^{-5}$	$14.65.10^{-5}$
$\kappa_{imp,2}$	$4.65.10^{-5}$					

TABLE 5.3: Explicit diffusion coefficient (κ_{exp}) given to simulation, effective coefficient (κ_{eff}) computed from BPE analysis and implicit second-order coefficient ($\kappa_{imp,2}$) by deducting one from the other (all in m^2/s)

5.4.3 Diffusion and advection timescales (BPE_{ts})

A third and last experiment (BPE_{ts}) based on the advection-diffusion equation 5.4.1 is now presented to better understand the limitation of the BPE algorithm in terms of characteristic time and length scales. The idea is that the BPE algorithm can only give an accurate, valuable value of the effective diffusivity if (i) this diffusivity can be considered as homogeneous and can thus be extracted from the integral of the diapycnal flux in Equation 5.3.14 and (ii) diapycnal fluxes can be evaluated over time-scales smaller than the time-scale of the diapycnal fluxes at stake but larger than the remaining dynamical time-scales in the studied ocean region. Table 5.4 presents the physical and numerical parameters chosen for this experiment. The configuration is similar to BPE_{exp} with different values of κ_{exp} over each half of the domain, but with active advection by a second-order centered scheme (C2) known to lead to a vanishing implicit dissipation. This experiment is made twice with different velocities u, results are presented in Figures 5.4.A1 to A3 for $u_1 = 2\ 10^{-4}\ m/s$ and Figures B1 to B3 for $u_2 = 2\ 10^{-3}\ m/s$.

Characteristic timescales are evaluated for advection, ($T_{adv} = L_{adv}/U$), and for diffusion ($T_\kappa = L_\kappa^2/\kappa$), where L_i is the characteristic length-scale over which the flow is affected by each process. In this configuration, the explicit diffusion coefficient takes a different value in each half-domain so $L_\kappa = 15\ m$, whereas advection occurs with the same exact value over the whole domain so that $L_{adv} = 30\ m$. The value of advection however will change between two experiments.

This leads to the following time-scales : $T_\kappa^{left} = 2.25\ 10^7\ s$, $T_\kappa^{right} = 2.25\ 10^5\ s$ (regardless of the chosen velocity), and (depending on the value of U) $T_{adv}^{U_1} = 1.5\ 10^5\ s$ or $T_{adv}^{U_2} = 1.5\ 10^4\ s$. As

Configuration BPE_{ts}	*Parameters*
Numerical Model	Advection-diffusion equation of passive tracers
L_x	30 m
L_z	30 m
Δx	0.5 m
Δz	0.5 m
Δt	10 s
Time stepping	RK3
Diffusivity	Left : $\kappa_{exp} = 10^{-5}\ m^2/s$. Right : $\kappa_{exp} = 10^{-3}\ m^2/s$.
Advection	$U_1 = 2.10^{-4}\ m/s$, $U_2 = 2.10^{-3}\ m/s$ with C2 advective scheme.
Initial field	$\psi(x,\ 0) = \psi_1(x)$

TABLE 5.4: BPE_{ts} configuration : numerical parameters.

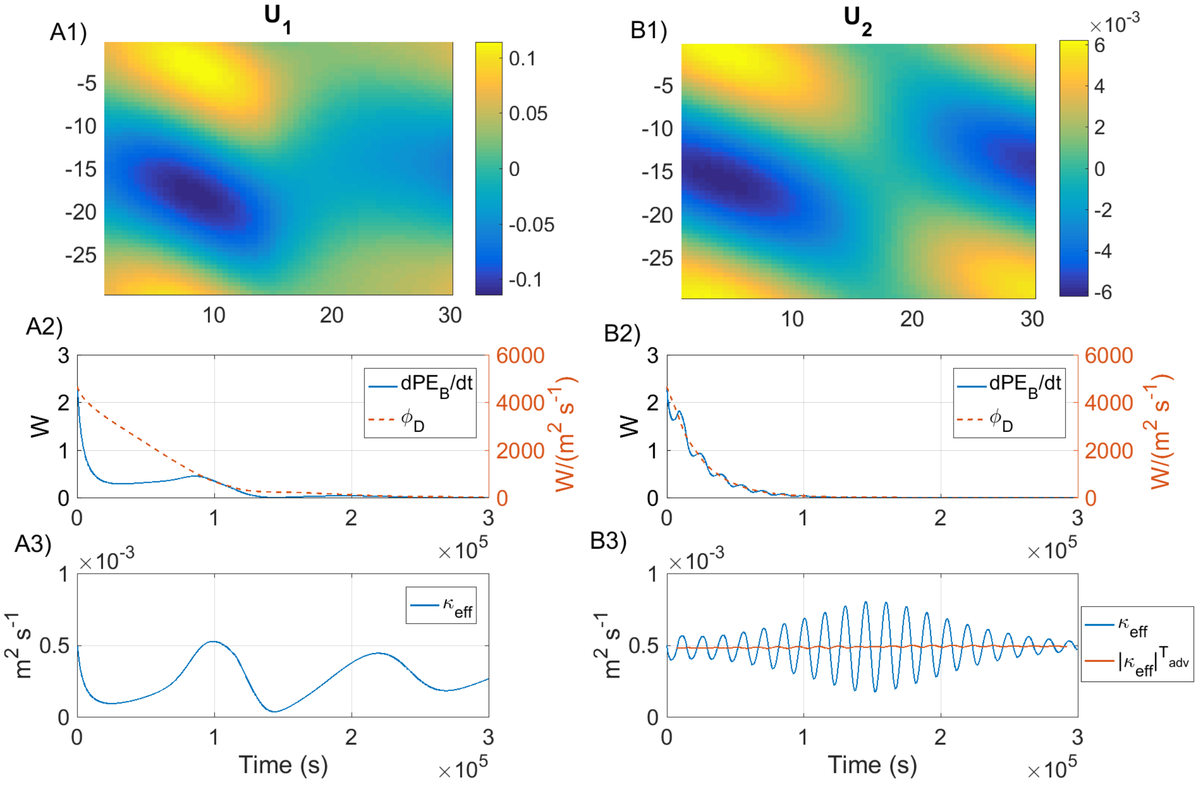

FIGURE 5.4: (A1 and B1) Field of tracer ψ at $t =\ 1.35\ 10^5\ s$ after initialisation for $u = 2.10^{-4}\ m/s$ (A1) and $u = 2.10^{-3}\ m/s$ (B1). (A2 and B2) Evolution of BPE (blue) and of term ϕ_D (red) of Equation 5.3.14 for each experiment. (A3 and B3) Value of instantaneous $\kappa_{eff}(t)$ as computed in Equation 5.3.15 (blue) for each experiment. In (B3) is also plotted in red the sliding averaged value of κ_{eff} for a window $T_{adv} = T_{adv}^{U2} = 1.5\ 10^4 s$.

a consequence :

$$T_{adv}^{U_2} << T_{adv}^{U_1} < T_{\kappa}^{right} << T_{\kappa}^{left} \tag{5.4.6}$$

Figures 5.4.A1 and B1 show the flow field after $t = 1.35\ 10^5\ s$ for both values of the advective velocity. For the smallest advective velocity $U = U_1$ (figure A1), $t < T_{adv}^{U_1}$ so no advective cycle as been completed yet. For an advective velocity one order of magnitude greater

$U = U_2$ (figure B1), $t >> T_{adv}^{U_2}$ and several advection cycles have happened, leading in the whole domain to smaller extrema of ψ than in the $U = U_1$ case.

Figures 5.4.A3 and B3 additionally show the variations with time of the effective diffusivity κ_{eff} computed over the whole domain for each case (from the evaluations of ϕ_D and dPE_B/dt in Figures A2 and B2). With advective velocity U_1 (Figure A3), the time-scales T_κ^{right} and $T_{adv}^{U_1}$ are close ($O(10^5\ s)$), the effective diffusivity is initially close to the prescribed averaged explicit diffusivity ($5\ 10^{-4}\ m^2/s$) but quickly decreases. Figure 5.4.A3 shows two oscillations of κ_{eff} with a period of $\approx 1.2\ 10^5 s$, a minimum (maximum) value reached of $3.8\ 10^{-5}\ m^2/s$ ($5\ 10^{-4}\ m^2/s$). Those oscillations are not regular and seem to arise from resonance between the advective and dissipative timescales $T_{adv}^{U_1}$ and T_κ^{right}, they do not average to the median value of diffusivity. With a much larger advective velocity U_2 (figure B3) now, the effective diffusivity oscillates around the averaged explicit advective velocity. The time-scale of the oscillations is now smaller : it remains very close to the advective time-scale $T_{adv}^{U_2}$, with an envelope at a smaller frequency that could be linked to T_κ^{right}. When a sliding average operator with time window $T_{adv}^{U_2}$ is applied to the effective diffusivity most of the oscillations are cleared of the signal.

When the effective diffusivity is computed independently over each sub-domain, the expected prescribed values of κ^{right} and κ^{left} are recovered with small amplitude oscillations at the advective time-scale (not shown).

5.4.4 Partial conclusion

The various experiments carried out in the frame of this simple but complete advection- diffusion configuration confirms that Winters et al. (1995)'s BPE algorithm can lead to a quantification but also to a localization of the turbulent mixing coefficient in regional ocean configurations. This includes an evaluation of the implicit dissipation induced by advective schemes. Quantification is achieved through the determination of an effective diffusivity, to be viewed as an average for the region (viewed as a sum of water-columns) over which the evolution Equation 5.3.14 has been evaluated. However, in this advection- diffusion configuration, advection through areas of localized diffusion leads to oscillations of the evaluated effective diffusivity at the advection time-scale.

5.5 Toward an evaluation of mixing in real ocean

Several additional test configurations of increasing complexity are now presented to progress toward an evaluation of mixing in a "real ocean" with the "generalized" BPE algorithm presented in §5.3.4. The algorithm is applied to output fields of numerical simulations made with the non-hydrostatic CROCO model. These fields are obtained while prescribing a diffusion κ_{exp}, however the model's dynamics allow for the development of features such as instabilities that, through subgrid parameterization or implicit diffusion, lead to *a priori* unknown mixing intensity. The consequences of the variations of the ocean free-surface are thus first explored in the case of the free oscillations of a stratified tank (§5.5.1). Mixing is then finally evaluated with the BPE algorithm when Kelvin-Helmholtz instabilities are developing (§5.5.2) and in the region of Gibraltar strait (§5.5.3).

5.5.1 Free oscillations of a stratified tank

Linear stratification and free surface : induced mixing (BPE_{tank})

As shown in §5.3.1, variations of the ocean free-surface's elevation induce several adaptations of the evolution equation of BPE and, as a consequence, they have a significant impact on the evaluation of mixing in realistic configurations. The present configuration focuses on the mixing of a stratified fluid induced by the natural (free) oscillations of a stratified tank initially subjected to a gradient of free-surface anomaly. The physical and numerical parameters are presented in Table 5.5.

Configuration BPE_{tank}	*Parameters*
Numerical Model	CROCO (compressible, non-hydrostatic kernel)
L_x	50 m
L_z	10 m
Δx	0.2 m
Δz	$\approx\ 0.2\ m$
Δt	close to CFL requirements in test-configurations
Diffusivity	$\kappa_{exp} = 4.10^{-6}\ m^2/s$

TABLE 5.5: BPE_{ts} configuration : numerical parameters.

The initial perturbation of the ocean free-surface is chosen equal to :

$$\zeta(x, t = 0) = \zeta_0\ cos\left(\frac{\pi x}{L_x}\right) \tag{5.5.1}$$

with $\zeta_0\ =\ 2\ mm$.

The initial sinusoidal anomaly of the free-surface elevation induces natural oscillations of the linearly stratified flow presented in Figure 5.5.A due to the propagation and resonance of surface gravity waves of speed $c\ =\ sqrtgL_Z\ \approx\ 9.9\ m/s$. The free-surface then evolves as a standing wave with period $T_\zeta\ =\ 2L_x/c\ =\ 10\ s$. The induced currents in the fluid are expected to lead to diapycnal fluxes and, as a consequence, participate to increased turbulent mixing.

Figures 5.5.B1-B2 and C1 to C3 show the evolution with time of the various terms in the balance Equation 5.3.14. Computations are successively carried out for the whole domain (Figures 5.5.B1 and B2) or for the right half domain (Figures 5.5.C1 to C3).

As could be expected, the oscillations of the free-surface clearly governs not only the variations of the first term (ϕ_ζ) of this balance equation but also the variations of the overall BPE variations (dPE_B/dt), with oscillations at period T_ζ of both signal in Figure 5.5.B2, C1 and C2.

If the balance equation is evaluated over the whole domain, the free-surface term of the evolution equation explains the oscillations of (dPE_B/dt) (Figure 5.5.B1) and the prescribed explicit diffusivity is recovered with good accuracy (Figure 5.5.B2) with only some spurious small amplitude noise already present in the evaluation of $dBPE/dt$.

If the balance equation is now evaluated over the right half domain only (Figures 5.5.C1 to C3), ϕ_ζ is approximately equal to F_a the sum of the advective flux of BPE through the (vertical) lateral boundary of this sub-domain (Figure 5.5.C1). Note that the terms of the evolution equation are all several orders of magnitude larger than when the balance equation is evaluated over the whole domain. The effective diffusivity is still recovered with good accuracy (Figure 5.5.C3).

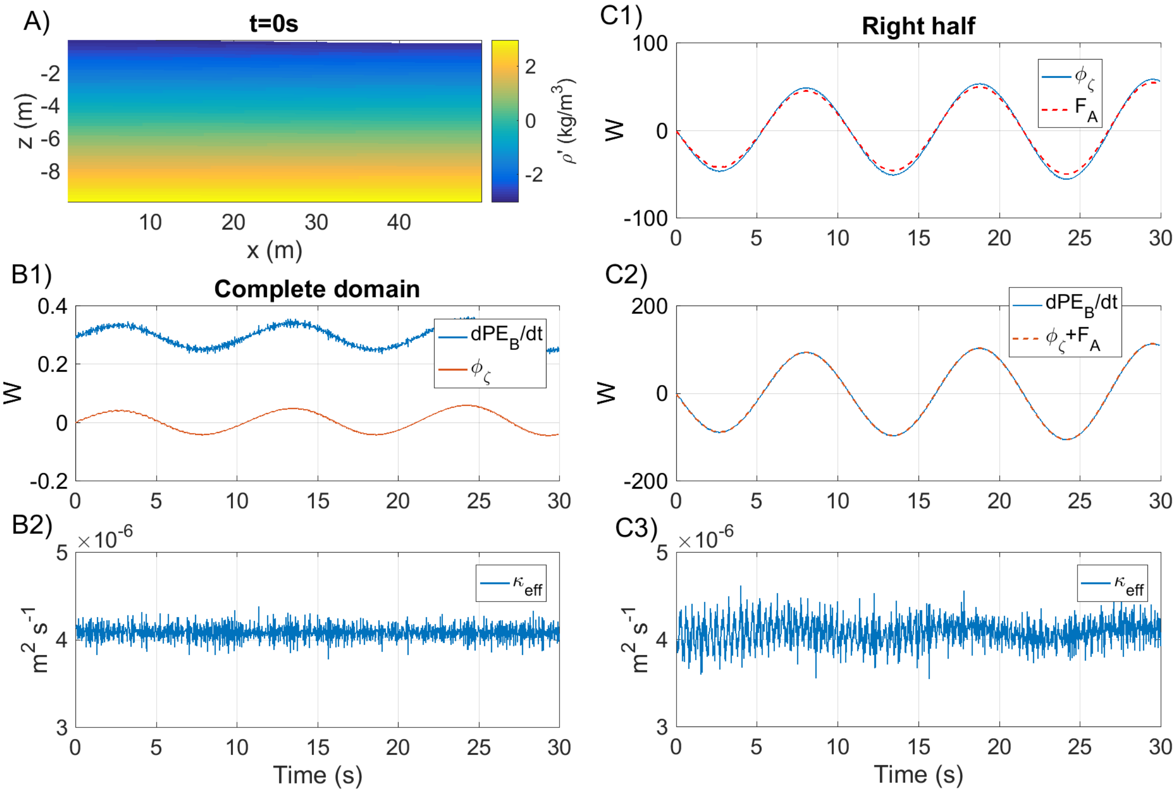

FIGURE 5.5: (A) Initial tracer field of the BPE_{tank} configuration. (B1 and B2) Time evolution of some terms of the balance equation 5.3.14 over the whole simulated domain. (C1 to C3) same as B1 and B2 but for an evaluation carried out only over the right half of the domain.

These results confirm the pertinence of the proposed BPE balance Equation 5.3.14 and reinforce the choices made to evaluate numerically the BPE algorithm. Even in a case where the induced mixing is several order of magnitudes smaller than the other terms of the balance equation, the explicit diffusivity can therefore be recovered both globally and locally based on Equation 5.3.15, provided that the term ϕ_ζ is taken into account.

Pycnocline and free surface (BPE_{tank2})

The mixing induced by the natural oscillations in a tank are now explored for a two-layer stratification (i.e. for a sharp ocean pycnocline). Most parameters of Table 5.5 remain unchanged except for the prescribed diffusivity now put at $10^{-4} m^2/s$.

Two types of "interfacial" gravity waves can now propagate in this stratified tank : surface gravity waves with a phase speed of $\sqrt(gL_z) \approx 9.9\ m/s$ and internal gravity wave with a baroclinic wave speed of $\sqrt(g'h_1(L_z - h_1)/L_z = 0.33\ m/s$ (h_1 being the depth of the pycnocline).

The free-surface is supposed to be initially at rest whereas the sinusoidal-shaped initial stratification is shown in Figure 5.6.A. Both the interface and the free-surface evolve into standing waves with periods of respectively $T_\eta = 300\ s$ and $T_\zeta = 10\ s$.

As with the previous configuration the evolution of the terms of the balance Equation 5.3.14 are first evaluated over the whole domain in Figures 5.6.B1 to B3, then over one half in Figures 5.6.C1 to C4.

The evaluation of κ_{eff} carried out on the entire domain (Figure 5.6.B3) is close to the

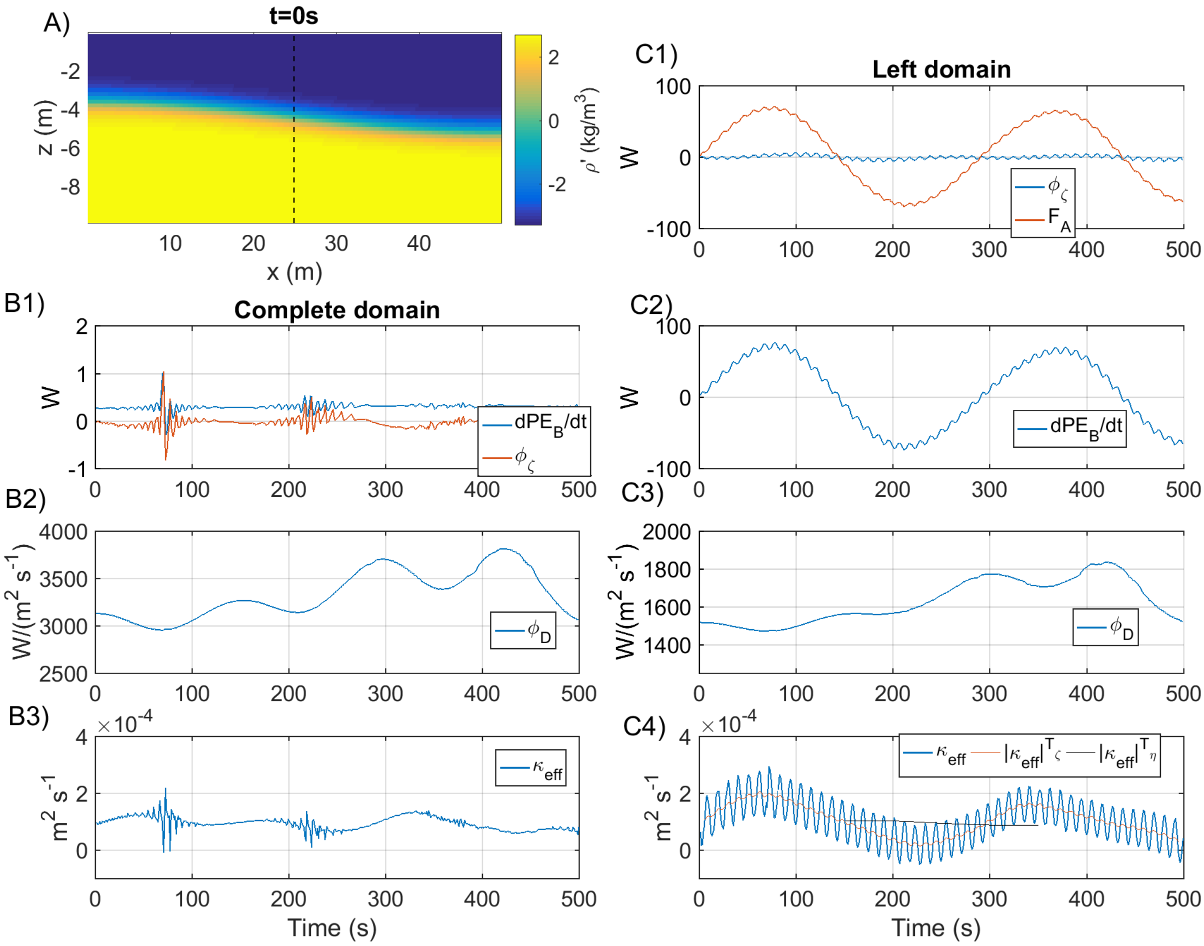

FIGURE 5.6: (A) Initial tracer field of the BPE_{tank2} configuration. (B1 to B3) Evaluation of the time evolution of some terms of the balance equation 5.3.14 over the whole simulated domain. (C1 to C4) Same but for an evaluation carried out only on the left half of the domain.

prescribed diffusivity with a regular pattern of noise (first at $t = 80\ s$), that could come from interaction of the pycnocline with the boundaries of the closed domain.

In the left half domain, $F_A >> \phi_\zeta$ (Figure 5.6.C1) in contrast to the previous case, with the evolution in the trend of BPE (Figure 5.6.C2) mainly explained by the advective flux. The term ϕ_ζ still retains a non-negligible part of the high-frequency variability. The evolution of κ_{eff} in this half domain now clearly shows two oscillations frequency, as shown in Figure 5.6.C3, corresponding to T_ζ and T_η. When the signal is averaged over this latter period, the prescribed diffusivity is found again. The diffusivity κ_{eff} evaluated on the right domain (not shown) has an evolution symmetric relative to this average to the one in the left domain.

Note that the oscillations of the evaluated diffusivity have such a large amplitude that it occasionally reaches negative values, especially for evaluation in the half domain. This indicates the occurrence of re-stratification processes.

Pycnocline, free surface and bottom bathymetry (BPE_{tank3})

The last experiment carried out for the tank configuration includes variations of the bathymetry. The objective is to evaluate the limitations of the BPE algorithm for non-flat domains. The physical and numerical parameters are the same as those given in Table 5.5 except for the depth

L_z which now varies linearly between 10 to 9.25 m, the width L_x is now 10 m, and the prescribed diffusivity is $10^{-6} m^2/s$.

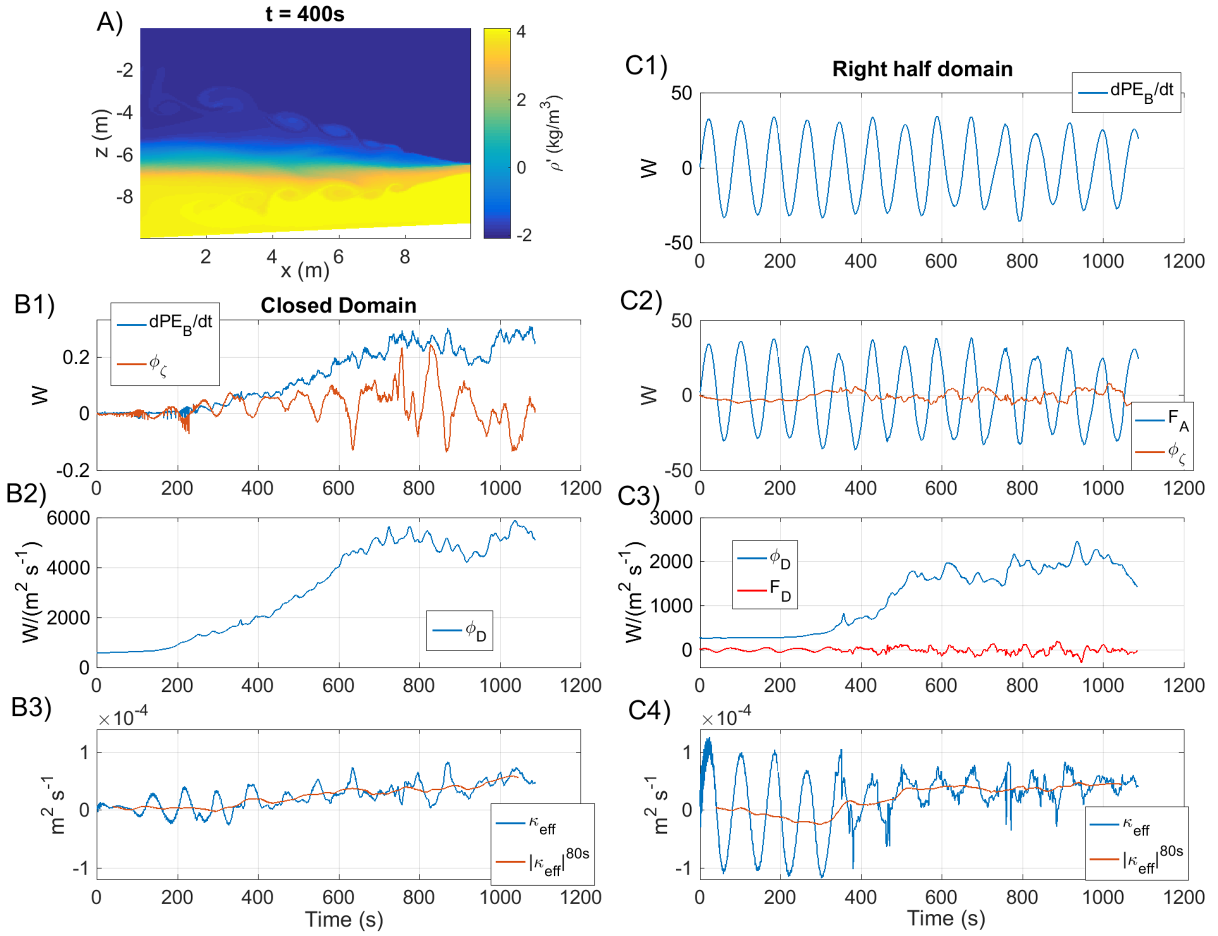

FIGURE 5.7: (A) Initial tracer field of the BPE_{tank3} configuration. (B1 to B3) Evaluation of the time evolution of some terms of the balance equation 5.3.14 over the whole simulated domain. (C1 to C4) Same but for an evaluation carried out only on the left half of the domain.

The phase speed of internal, interfacial waves is in this case approximately equal to 0.32 m/s. As the bathymetry is no longer flat, the interface's depth is not a simple standing wave any more. A corresponding general time-scale for the propagation of gravity waves is approximately $T_\eta = L_x/c = 30\ s$.

In this configuration, the movements induced by the initial slope of the pycnocline lead to Kelvin-Helmholtz instabilities after approximately 400s as depicted in Figure 5.7.A.

As for previous configurations, Figures 5.7.B1 to B3 present terms of the balance of the evolution of BPE and the evaluation of κ_{eff} for the algorithm applied to the whole domain, while it is applied only to the right half in Figures 5.7.C1 to C4.

The BPE evolution equation evaluated over the whole domain shows an increase of both dPE_B/dt and ϕ_D (Figure 5.7.B1 and B2). The term associated to the free-surface oscillations (ϕ_ζ) is shown to oscillate at a period of 80 s.The same type of oscillations can be observed on the variations of κ_{eff} (Figure 5.7.B3).

For the balance evaluated over the right half domain, the advective flux term (F_a) shows larger amplitude oscillations than ϕ_ζ that contribute to most of the evolution of BPE (Figure 5.7.C1 and C2). This oscillations are once again at the time-scale (80 s) and are found in the evaluated κ_{eff} (Figure 5.7.C4).

When κ_{eff} evaluated over both domains is averaged over $t = 80s$, the prescribed value of diffusivity is at first recovered for the first 250s of simulations in the whole domain. In the right half of the domain, it first decreases and becomes negative as the perturbations of the stratification are amplified due to interaction with the slope, then increases back at $t = 350s$ as instabilities begin to develop. This increase is also visible in the entire domain, for which the value of effective diffusivity becomes one order of magnitude greater than the prescribed value at $6.10^{-5}\ m^2/s$.

5.5.2 Kelvin-Helmholtz Instability (BPE_{kh})

The following configuration focuses on the large turbulent eddies associated to Kelvin-Helmholtz instabilities based on a previous study by Penney et al. (2019). The corresponding physical and numerical parameters are given in Table 5.6.

Configuration BPE_{kh}	*Parameters*
Numerical Model	CROCO (compressible, non-hydrostatic kernel)
L_x	256 m
L_z	256 m
Δx	2 m
Δz	$\approx\ 2\ m$
Boundary conditions	Cyclic
Δt	Close to CFL requirements in test-configurations.
Diffusivity	$\kappa_{exp} = 10^{-4}\ m^2/s$

Table 5.6: BPE_{kh} configuration : numerical parameters.

The initial field is a two-layer vertical stratification $\Delta\rho = 2.5\ kg/m^3$ associated to a two-layer sheared horizontal current $\Delta U = 2\ m/s$ in the vertical direction ($u = 1\ m/s$ at the bottom and $u = -1\ m/s$ at the top). The domain is cyclical in the horizontal direction.

Two unstable billows develop over the domain during the simulated period, as shown by the evolution of the density field after $t = 200\ s,\ 400\ s,\ 600\ s$ and $800\ s$ in Figures 5.8.A1 to A4.

Figure 5.8.B shows the evolution of the reference profile at the same times. Figures 5.8.C, D and E in the lower row provide the various terms involved in the BPE balance equation 5.3.14.

The surface-induced ϕ_ζ term remains small in the balance, and here the evolution of BPE is mostly due to the diapycnal fluxes ϕ_D. The effective diffusivity κ_{eff} indeed increases significantly after 200 s as the Kelvin-Helmholtz instability and its associated billows develop. It reaches a maximal value after $t = 600s$ which coincides with the maximum amplitude of the diapycnal term ϕ_D along with the development of secondary instabilities as depicted in Figure 5.8.A3. Once the Kelvin-Helmholtz instability has mixed the density field, the reference profile at $t = 800s$ (in purple in Figure 5.8.B) exhibits an intermediate homogeneous layer located between $z^* = 110\ m$ and $z^* = 140\ m$, which coincides with a decrease of the effective diffusivity κ_{eff} as the flow is no more under the influence of the shear instability.

5.5.3 Gibraltar strait configuration ($SimRef$)

The induced mixing in the vertical section of the Strait of Gibraltar is finally investigated in the simplest two-dimensional configuration of ocean flow describing its tidal dynamics and main

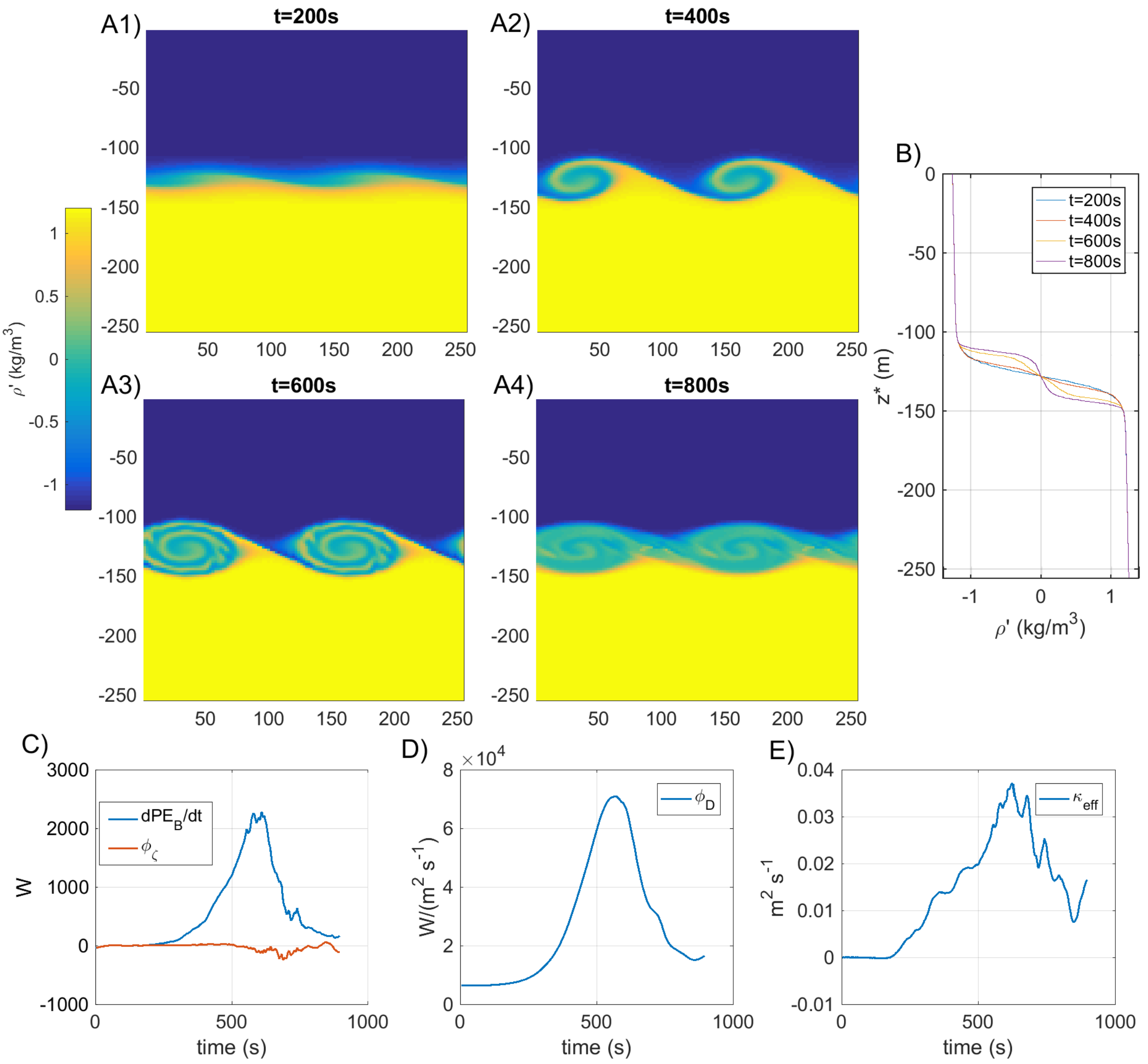

FIGURE 5.8: (A1 to A4) Tracer field simulated in the BPE_{kh} configuration for $t = 200,\ 400,\ 600,\ 800 s$. (B1) Reference profile from the sorting of the tracer field at the same times in the simulation. (C, D and E) Evaluation of the time evolution of some terms of the balance equation 5.3.14 over the whole simulated domain.

bathymetric features (SimRef) originally presented in Chapter 3.

The initial time ($t = 0\ s$) is now chosen for simulation time $t_{SimRef} = 6.29\ T$, i.e. at the beginning of the first outflow following the spin-up period so that the algorithm is applied to four tidal cycles of $T = 12.4\ h$.

The BPE evolution balance is evaluated over sub-domains of limited extension covering the eastern part of the Strait, the western part, and the western slope of Camarinal Sill (respectively noted E,W and CSw in Figure 5.9.A1). In the latter sub-domain (CSw) fine-scale processes, large turbulence eddies and thus mixing are supposed to occur, while solitary wave trains propagate in the east domain (E, see Figure 5.9.A2). Figure 5.10 presents the evaluation of the effective diffusivity κ_{eff} for each domain, along with the remaining terms of Equation 5.3.14.

The evolution of dPE_B/dt (Figures 5.10.A1, B1 and C1) is a noisy signal not easily interpreted, the "noise" being largely explained by the sum of the non-diffusive terms F_a and ϕ_ζ (Figures

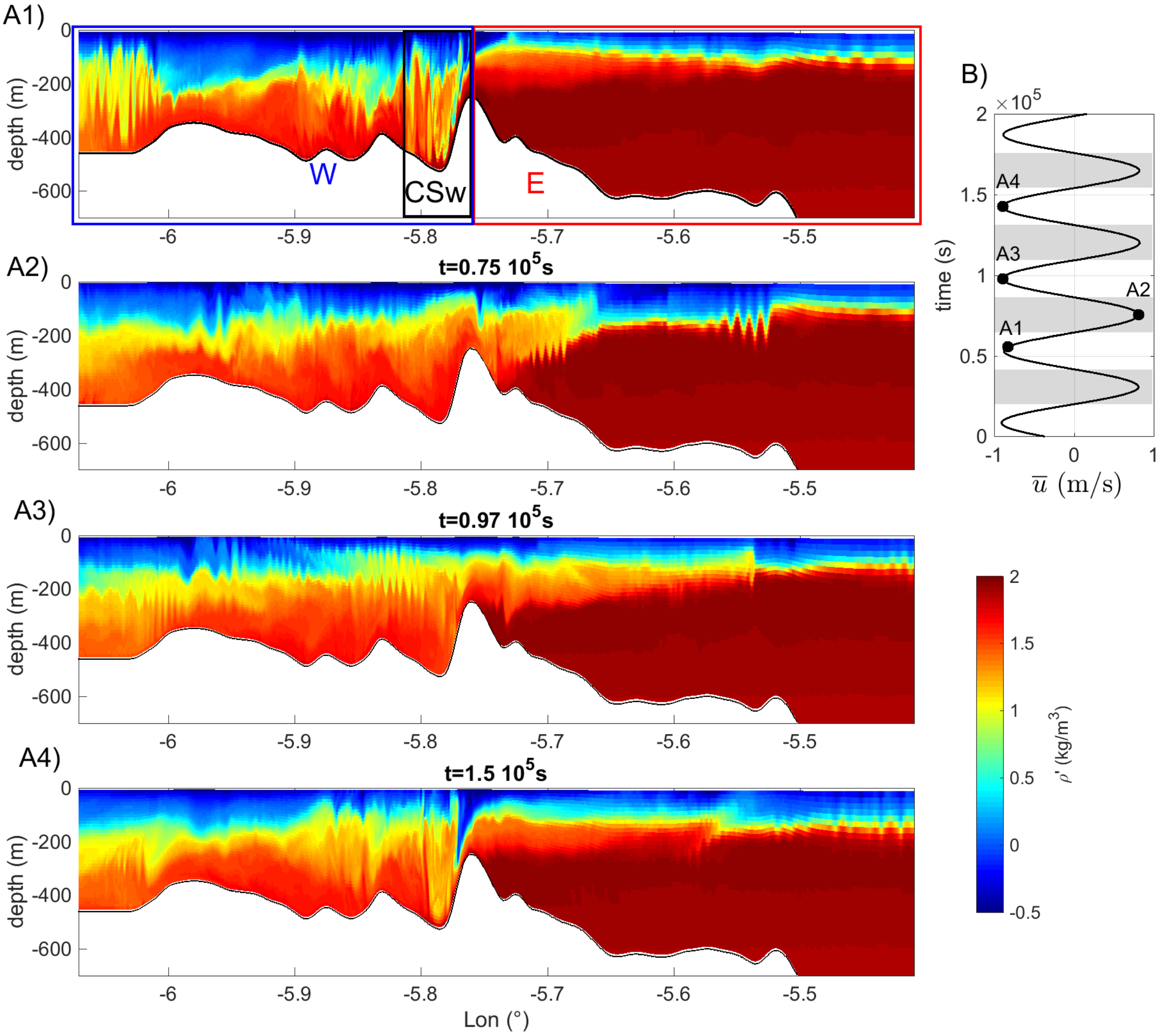

FIGURE 5.9: (A1 to A4) Simulated field of density anomaly ρ' in simulation SimRef of Chapter 3 at various times. In (A1) are shown the locations of the sub-domains for which local sorting is carried out to give the temporal evolution of Figure 5.10. (B) Time evolution of the barotropic current over the shallowest point in the domain at Camarinal Sill, with black dots indicating the instant of figures (A1 to A4).

A2, B2 and C2). Those two terms have the same order of magnitude but their general trend is symmetrical to the other in regard to 0. Diffusive fluxes through the lateral boundaries (F_D) are negligible compared to the diapycnal flux ϕ_D (Figures A3, B3 and C3) and are not plotted.

The evolution in time of the effective diffusivity κ_{eff} (Figures 5.10.A4, B4 and C4) is in contrast noise-free. In the eastern part of the domain (E), this evolution is sinusoidal of period T in agreement with the evolution of barotropic currents (indicated in Figure 5.9.B) : it is positive when the barotropic component of the current is positive.

In the western part of the domain (W) and in its sub-domain (CSw), this semi-diurnal periodicity is readily apparent, not as regular oscillations this time but rather as intermittent episodes (bursts) of high (positive) effective diffusivity κ_{eff} during outflows (when the barotropic component of the current is this time negative). Those bursts reach higher values in the sub-domain of the sill's slope (CSw), the contribution of mixing in this area being averaged out in the evaluation made over the greater west (W) domain. This burst is also of limited amplitude for

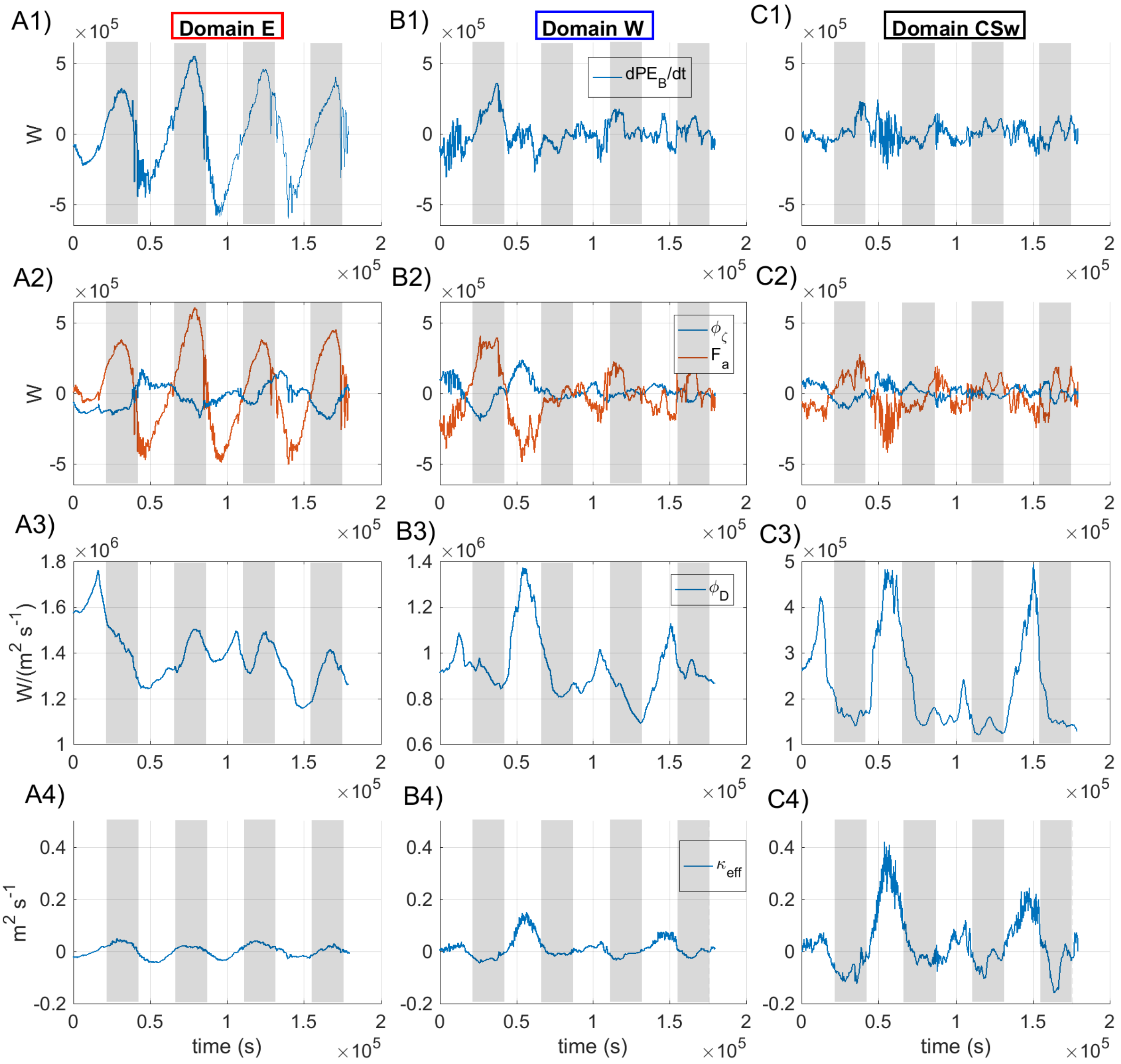

FIGURE 5.10: Evaluation of the time evolution of the terms of the balance equation 5.3.14 in each domain of SimRef as defined in Figure 5.9.A1. Upper row is the time derivative of BPE, second row is ϕ_ζ (blue) and F_a (red), third row is ϕ_D, bottom row is the evaluated κ_{eff}. Grey shaded areas delineate periods of inflow (positive or eastward barotropic currents).

the third outflow (around $t = 10^5 s$) because, as can be seen in Figure 5.9.A3, the usual hydraulic jump is absent compared to the previous and next outflows (see Figure 5.9.A1 and A4).

Due to this different dynamics of consecutive outflows, there are still important variations in the signal of κ_{eff} when it is averaged in time over one tidal period T. Thus Table 5.7 gives the value of this evaluated effective diffusivity as a time-average taken over either two or four tidal cycles. Those values are indeed greater in the sub-domain CSw localised on the west side of Camarinal Sill, especially they are close to one order of magnitude greater there than in the sub-domain E east of this sill. This confirms the faculty of the algorithm to help localize mixing, even in a complex flow area, as it is west of Camarinal Sill that the most intense mixing takes place in the strait of Gibraltar.

	E	W	CSw
$\lvert\kappa\rvert_1^{2T}$	0.002	0.015	0.037
$\lvert\kappa\rvert_2^{2T}$	0.001	0.009	0.021
$\lvert\kappa\rvert^{4T}$	0.002	0.012	0.029

Table 5.7: Time-averaged effective diffusivity κ_{eff} (in m^2/s) in each sub-domain of SimRef (Figure 5.9.A1). Averaging is made either over the first two tidal periods ($|\kappa|_1^{2T}$), the last two periods ($|\kappa|_2^{2T}$), or all four tidal periods ($|\kappa|^{4T}$).

5.6 Discussion and conclusion

A complete analysis of the Background Potential Energy (BPE) evolution equation has been carried out in several test-configurations of increasing complexity, ending with an application to the real ocean in the region of the strait of Gibraltar. This analysis is based on original analytical developments (to our knowledge at least) to derive an as-complete-as-possible evolution equation of BPE for free-surface water columns (§5.3.1). Original developments have also been proposed to evaluate numerically this evolution in non-flat regions of the ocean simulated with terrain-following, s-coordinate numerical models. The efficiency of the proposed implementation of the BPE algorithm remains affordable in terms of computing costs and memory storage for the hierarchy of configurations proposed, but new approaches need to be implemented to compute the reference state in a cost-efficient way (Saenz et al., 2015) for 3D LES of more extended regions.

In a free-surface domain with opened lateral boundaries, advection and motion of the free surface make $PE_B = \iiint_V \rho g z^* d\tau$ evolve with the reorganisation of the mass field (through F_a) and with the change of the water-column volume (through ϕ_ζ). In most studied configurations, those two terms are of the same order of magnitude and are the largest contributions to dPE_B/dt. The fluxes associated to the effective diffusivity κ_{eff} are found to complete the balance and the effective diffusivity reflects (or at least should reflect) diapycnal mixing : it quantifies the averaged turbulent mixing occurring over the domain of integration (a sum of water columns). This averaging effect is in part due to the choice of a homogeneous value of κ_{eff} over the selected domain.

Several assumptions could additionally be reconsidered or at least evaluated with care.

The isotropy of the effective diffusivity ($\kappa_h = \kappa_v = \kappa$) should be reconsidered when the implicit numerical diffusion of the advection schemes is at stake : implicit diffusion is indeed added specifically along the advection direction and diffusivity is not isotropic anymore.

The evaluations of the effective diffusivity has been made offline which leads to an additional limitation. Indeed, if an open-boundary configuration is studied, the sampling frequency must be chosen with care and must in particular remain high enough not to induce numerical truncations or artefacts.

Another consequence of our protocol is that this effective diffusivity value can have contributions on timescales similar to other dynamical processes. For example, the signal of advection through areas of varying mixing intensity (experiment BPE_{ts} of §5.4) appears in the evaluation of κ_{eff} as the timescale of advection is usually small compared to the timescale of diffusive mechanisms. This is especially the case in the evaluation of κ_{eff} over domains with open boundary fluxes, in which case the oscillations of this evaluation can become negative (§5.5.1 and following), indicating re-stratification periods, whereas mixing is supposed to be an irreversible process. In Equation 5.3.15 this can be explained by negative values of $dBPE/dt$ which are not offset in the numerator by $F_a + \phi_\zeta$. It still needs to be assessed whether this is due to a bad evaluation of those fluxes (with important errors in the subtraction of this two terms of high order of magnitude compared to κ), or numerical re-stratification in the model itself, or if it is more fundamentally linked to the difference of time-scales between advection and diffusive processes that would make an instantaneous evaluation of effective diffusivity not reflect the dynamical adjustment of the advected structures due to mixing

Given the latter interpretation, for the present study, the time-averaging of the effective diffusivity was used to retrieve coefficients representative of processes over extended time periods coherent with dissipation processes, but it may be more pertinent to integrate the time-averaging process into the balance equation itself.

Finally, this study only focuses on the APE/BPE subdivision of the gravitational potential energy of the ocean. More information on the underlying effects of the simulated dynamics on the evolution of BPE and diabatic mixing could be gained by evaluating transfers with and between other energy compartments, such as the kinetic energy of the flow (Floor et al., 2011).

5.7 Appendices to *The evolution equation of BPE*

5.7.1 Reynolds Theorem

Flux through a surface

Based on (Delhaye, 2008), let $\mathbf{v}_\Sigma$ be the velocity of a material surface in the fluid :

$$\mathbf{v}_\Sigma = \left.\frac{\partial \mathbf{x}}{\partial t}\right|_\Sigma \tag{5.7.1}$$

with $\mathbf{x}$ the position of the current point where the velocity is computed. This velocity is undetermined since the tangential component is itself undetermined. Only its normal component ($\mathbf{n}_\Sigma.\mathbf{v}_\Sigma$) can be computed and isolated. This component is different from the vertical component of $\mathbf{v}_\Sigma$ of Equation 2.2.12. Demonstrations and further expressions of the normal component can be found in Griffies (2004), Griffies (2012) and Delhaye (2008).

$$\left.\frac{\partial z}{\partial t}\right|_s = \left.\frac{\partial s}{\partial t}\right|_z \left.\frac{\partial z}{\partial s}\right|_t = h\,||\nabla s||\,\mathbf{n}_\Sigma.\mathbf{v}_\Sigma \tag{5.7.2}$$

Metric tensor formulations lead to :

$$dS_\Sigma = h\,||\nabla s||\,dS \tag{5.7.3a}$$

$$hdS = \mathbf{n}_\Sigma.\mathbf{v}_\Sigma dS_\Sigma \tag{5.7.3b}$$

Formulations of the Reynolds Transport Theorem (& Leibniz Rule)

Demonstration. The difficulty to compute :

$$\frac{d}{dt}\iiint_{\mathcal{V}_M(t)} \rho A d\tau \tag{5.7.4}$$

is due to the fact that for a general time-varying volume $\mathcal{V}(t)$ the differentiation cannot be taken through the internal sign. To do so, we can however consider a change of coordinates to volume-attached coordinates (Hirasaki, 2021). Let $\mathcal{J}$ be the Jacobian (determinant of the

Jacobian matrix) of the change of variables from Cartesian coordinates $(\mathbf{x}, t)$ to volume varying coordinates $(\boldsymbol{\xi}, t)$. Integrating volume is $\mathcal{V}(t) = \mathcal{V}_\xi = \mathcal{V}_\xi(t)$.

Kinematic evolution of material particulate ("dilation kinematic theorem") is then nothing but Reynolds'transport theorem (which is equivalent to Leibniz derivation rule to 3D volumes) (Hirasaki, 2021). Caution : the demonstration given in (Hirasaki, 2021) is for a material volume $\mathcal{V}_M$. As the demonstration is kinematic, it is generalized here to a general volume moving thought the fluid flow ($\mathcal{V}(t)$). This problem is dealt with in Jakobsen (2014) (and further references are given in there). As a consequence for a general volume $\mathcal{V}(t)$ moving at a 3D velocity $\mathbf{v}_\Sigma$:

$$\frac{dJ}{dt} = J\nabla.\mathbf{v}_\Sigma \tag{5.7.5}$$

which is reminiscent of the kinematic evolution of the specific volume of a fluid particle :

$$\frac{d\tau}{dt} = \tau\nabla.\mathbf{v} \tag{5.7.6}$$

sometime written :

$$\frac{d\delta\tau}{dt} = \delta\tau\nabla.\mathbf{v} \tag{5.7.7}$$

which is noting but the continuity equation written for the specific volume. With the natural change of variable, the derivation can enter the integral sign and :

$$\frac{d}{dt}\iiint_{\mathcal{V}(t)} \rho A d\tau = \frac{D}{Dt}\iiint_{\mathcal{V}(t)} \rho A d\tau = \frac{D}{Dt}\iiint_{\mathcal{V}(t)} \rho A d\mathbf{x} \tag{5.7.8a}$$

$$= \frac{D}{Dt}\iiint_{\mathcal{V}_\xi} \rho A J d\boldsymbol{\xi} \tag{5.7.8b}$$

$$= \iiint_{\mathcal{V}_\xi} \frac{D\rho A}{Dt} J d\boldsymbol{\xi} + \iiint_{\mathcal{V}_\xi} \rho A \frac{DJ}{Dt} d\boldsymbol{\xi} \tag{5.7.8c}$$

$$= \iiint_{\mathcal{V}_\xi} \frac{D\rho A}{Dt} J d\boldsymbol{\xi} + \iiint_{\mathcal{V}_\xi} \rho A \nabla.\mathbf{v}_\Sigma \, J d\boldsymbol{\xi} \tag{5.7.8d}$$

where :

$$\frac{D\bullet}{Dt} = \left.\frac{\partial\bullet}{\partial t}\right|_\xi + \mathbf{v}_\Sigma.\nabla_{t,\xi}\bullet \tag{5.7.9}$$

Following Truesdell and Toupin (1960), a more general formulation can thus be recovered for a time-dependant volume $\mathcal{V}(t)$ moving with a velocity $\mathbf{v}_\Sigma$:

$$\frac{d}{dt}\iiint_{\mathcal{V}(t)} \rho A d\tau = \iiint_{\mathcal{V}(t)} \frac{D\rho A}{Dt} d\boldsymbol{x} + \iiint_{\mathcal{V}(t)} \rho A \nabla.\mathbf{v}_\Sigma \, d\mathbf{x} \tag{5.7.10a}$$

$$= \iiint_{\mathcal{V}(t)} \left.\frac{\partial \rho A}{\partial t}\right|_{xz} d\tau + \oiint_{S(t)} \rho A \mathbf{v}_\Sigma.\mathbf{n}_\Sigma dS_{Sigma} \tag{5.7.10b}$$

This is the generalized (Reynolds) transport theorem or the generalized Leibnitz theorem. Caution : the derivative D/Dt is associated to $\mathbf{v}_\Sigma$.

Closed time-dependent volume $\mathcal{V}(t)$. Several formulations of this kinematic theorem can be given :

$$\frac{d}{dt}\iiint_{\mathcal{V}(t)} \rho A d\tau = \iiint_{\mathcal{V}(t)} \left.\frac{\partial \rho A}{\partial t}\right|_{xz} d\tau + \oiint_{\mathcal{V}(t)} \rho A \mathbf{v}_\Sigma . d\mathbf{S} \tag{5.7.11a}$$

$$= \iiint_{\mathcal{V}(t)} \left(\left.\frac{\partial \rho A}{\partial t}\right|_{xz} + \nabla.(\rho A \mathbf{v}_\Sigma) \right) d\tau \tag{5.7.11b}$$

$$= \iiint_{\mathcal{V}(t)} \left(\rho \left.\frac{\partial A}{\partial t}\right|_{xz} + A \left.\frac{\partial \rho}{\partial t}\right|_{xz} + \rho \mathbf{v}_\Sigma . \nabla A + A \nabla.(\rho \mathbf{v}_\Sigma) \right) d\tau \tag{5.7.11c}$$

$$= \iiint_{\mathcal{V}(t)} \rho \frac{DA}{Dt} d\tau + \iiint_{\mathcal{V}(t)} A \left(\left.\frac{\partial \rho}{\partial t}\right|_{xz} + \nabla.(\rho \mathbf{v}_\Sigma) \right) d\tau \tag{5.7.11d}$$

This can also be written :

$$\frac{d}{dt}\iiint_{\mathcal{V}(t)} \rho A d\tau = \iiint_{\mathcal{V}(t)} \left(\rho \left.\frac{\partial A}{\partial t}\right|_{xz} + A \left.\frac{\partial \rho}{\partial t}\right|_{xz} + \rho \mathbf{v}_\Sigma . \nabla A + A \mathbf{v}_\Sigma . \nabla \rho + A \rho \nabla . \mathbf{v}_\Sigma \right) d\tau \tag{5.7.12a}$$

$$= \iiint_{\mathcal{V}(t)} \rho \frac{DA}{Dt} d\tau + \iiint_{\mathcal{V}(t)} A \frac{D\rho}{Dt} d\tau + \iiint_{\mathcal{V}(t)} \rho A \nabla . \mathbf{v}_\Sigma d\tau \tag{5.7.12b}$$

or alternatively :

$$\frac{d}{dt}\iiint_{\mathcal{V}(t)} \rho A d\tau = \iiint_{\mathcal{V}(t)} \rho \frac{dA}{dt} d\tau + \iiint_{\mathcal{V}(t)} \left(A \frac{d\rho}{dt} + \nabla . \left[\rho A (\mathbf{v}_\Sigma - \mathbf{v}) \right] + \rho A \nabla . \mathbf{v} \right) d\tau \tag{5.7.13a}$$

$$= \iiint_{\mathcal{V}(t)} \rho \frac{dA}{dt} d\tau + \iiint_{\mathcal{V}(t)} \nabla . \left[\rho A (\mathbf{v}_\Sigma - \mathbf{v}) \right] d\tau \tag{5.7.13b}$$

where $\mathbf{v}_\Sigma$ is defined as the velocity of the closed surface of $\mathcal{V}(t)$ and is more generally the 3D displacement velocity of the volume $\mathcal{V}(t)$. Caution : this has nothing to do with the velocity of the fluid in this volume except in the following particular case when considering a material volume, i.e. in the Lagrangian approach. These general formulations and demonstrations are useful in s-coordinates.

Material volume $\mathcal{V}_M(t)$ (kinematics & dynamics)

Formulation of the transport theorem. A material volume $\mathcal{V}_M(t)$ is defined as a volume containing exactly the same fluid particles as time goes on. Simplifications to obtain the simple expression of the integral variations in the case of a moving material volume are based on the use of the continuity equation or conservation of mass.

As the control volume is advected by mean flow (Lagrangian approach), $\mathbf{v}_\Sigma = \mathbf{v}$:

$$\frac{d}{dt}\iiint_{\mathcal{V}_M(t)} \rho A d\tau = \iiint_{\mathcal{V}_M(t)} \rho \frac{dA}{dt} d\tau + \iiint_{\mathcal{V}_M(t)} A \frac{d\rho}{dt} d\tau + \iiint_{\mathcal{V}_M(t)} \rho A \nabla . \mathbf{v} d\tau \tag{5.7.14}$$

and thus :

$$\frac{d}{dt}\iiint_{\mathcal{V}_M(t)} \rho A d\tau = \iiint_{\mathcal{V}_M(t)} \rho \frac{dA}{dt} d\tau + \iiint_{\mathcal{V}_M(t)} A \underbrace{\left(\left.\frac{\partial \rho}{\partial t}\right|_{xz} + \nabla.(\rho \mathbf{v}) \right)}_{=0} d\tau \tag{5.7.15a}$$

$$= \iiint_{\mathcal{V}_M(t)} \rho \frac{dA}{dt} d\tau \tag{5.7.15b}$$

This is a generalization to 3D volume of the Leibniz rule. The time dependency of the integral volume $\mathcal{V}_M(t)$ is for a Lagrangian evolution with time-dependent boundaries. The present formulation is to be used for time-dependent boundaries whatever the velocity $\mathbf{v}_\Sigma$ inside the volume.

Material volume $\mathcal{V}_M(t)$ in Lagrangian material coordinates. The same exact approach and demonstration can be carried out in the case of a material volume as in the general case. Let in this case $\mathcal{J}$ be the Jacobian (determinant of the Jacobian matrix) of the change of variables from Cartesian coordinates $(\mathbf{x}, t)$ to material coordinates $(\boldsymbol{\xi}, t)$. Integrating volume is $\mathcal{V}(t) = \mathcal{V}_\xi$. Kinematic evolution of material particle ("dilation kinematic theorem") reads (Hirasaki, 2021) :

$$\frac{dJ}{dt} = J \nabla.\mathbf{v} \tag{5.7.16}$$

which is reminiscent of the kinematic evolution of a control volume given in Equation 5.7.6. With this kinematic theorem :

$$\frac{d}{dt}\iiint_{\mathcal{V}_M(t)} \rho A d\tau = \frac{d}{dt}\iiint_{\mathcal{V}_M(t)} \rho A d\mathbf{x} \tag{5.7.17a}$$

$$= \frac{d}{dt}\iiint_{\mathcal{V}_s} \rho A J d\boldsymbol{\xi} \tag{5.7.17b}$$

$$= \iiint_{\mathcal{V}_\xi} \frac{d\rho A}{dt} J d\boldsymbol{\xi} + \iiint_{\mathcal{V}_\xi} \rho A \frac{dJ}{dt} d\boldsymbol{\xi} \tag{5.7.17c}$$

$$= \iiint_{\mathcal{V}_\xi} \frac{d\rho A}{dt} J d\boldsymbol{\xi} + \iiint_{\mathcal{V}_\xi} \rho A \nabla.\mathbf{v} \; J d\boldsymbol{\xi} \tag{5.7.17d}$$

This leads finally to :

$$\frac{d}{dt}\iiint_{\mathcal{V}_M(t)} \rho A d\tau = \iiint_{\mathcal{V}_\xi} \left(\frac{\partial \rho A}{\partial t} + \nabla.(\rho A \mathbf{v}) \right) J d\boldsymbol{\xi} \tag{5.7.18a}$$

$$= \iiint_{\mathcal{V}_M(t)} \left.\frac{\partial \rho A}{\partial t}\right|_{xz} d\tau + \oiint_{\mathcal{V}_M(t)} \rho A \mathbf{v}.d\mathbf{S} \tag{5.7.18b}$$

Reynolds transport theorem is recovered for a material volume, understood as a volume containing the same fluid particles. This last relation can be viewed as the difference between the time variation of the extensive variable inside the domain and the advective flux through the "control" surface matching at time "t" with material volume.

Time-independent "control" volume $\mathcal{V}_0$. In the particular case when the volume (and thus his surface) is independent of time, then $\mathbf{v}_\Sigma = 0$ and as a consequence :

$$\frac{d}{dt}\iiint_{\mathcal{V}_0} A d\tau = \iiint_{\mathcal{V}_0} \frac{\partial A}{\partial t} d\tau \tag{5.7.19}$$

5.7.2 Formulations based on total derivatives (toward Lagrangian relations...)

Note that the continuity equation can be written :

$$\frac{d\,\delta\tau}{dt} = \frac{\partial v_k}{\partial x_k}\delta\tau = \nabla.\mathbf{v}\,\delta\tau \tag{5.7.20}$$

and so for a closed, moving volume $\mathcal{V}(t)$:

$$\begin{aligned}
\frac{d}{dt}\iiint_{\mathcal{V}(t)} \rho A d\tau \quad &= \iiint_{\mathcal{V}(t)} \rho\frac{DA}{Dt} d\tau + \iiint_{\mathcal{V}(t)} A\frac{D(\rho d\tau)}{Dt} && \text{(5.7.21a)}\\
&= \iiint_{\mathcal{V}(t)} \rho\frac{DA}{Dt} d\tau + \iiint_{\mathcal{V}(t)} A\frac{D\rho}{Dt} d\tau + \iiint_{\mathcal{V}(t)} \rho A\frac{Dd\tau}{Dt} && \text{(5.7.21b)}\\
&= \iiint_{\mathcal{V}(t)} \rho\frac{DA}{Dt} d\tau + \iiint_{\mathcal{V}(t)} A\frac{D\rho}{Dt} d\tau + \iiint_{\mathcal{V}(t)} \rho A\nabla.\mathbf{v}_\Sigma\, d\tau && \text{(5.7.21c)}\\
&= \iiint_{\mathcal{V}(t)} \rho\frac{DA}{Dt} d\tau && \text{(5.7.21d)}
\end{aligned}$$

where $D\bullet/Dt = \partial\bullet/\partial t + \mathbf{v}_\Sigma.\nabla\bullet$. The last simplification is associated to the conservation of mass when written :

$$\frac{D\rho}{Dt} = -\rho\nabla.\mathbf{v}_\Sigma \tag{5.7.22}$$

If the volume is now a material volume and is thus advected by the mean flow (Lagrangian approach), $\mathbf{v}_\Sigma = \mathbf{v}_M$ and $D./Dt = d./dt$:

$$\begin{aligned}
\frac{d}{dt}\iiint_{\mathcal{V}_M(t)} \rho A d\tau \quad &= \iiint_{\mathcal{V}_M(t)} \rho\frac{dA}{dt} d\tau + \iiint_{\mathcal{V}_M(t)} A\frac{d\rho}{dt} d\tau + \iiint_{\mathcal{V}_M(t)} \rho A\nabla.\mathbf{v} d\tau && \text{(5.7.23a)}\\
&\left[= \iiint_{\mathcal{V}_M(t)} \rho\frac{dA}{dt} d\tau + \iiint_{\mathcal{V}_M(t)} A\underbrace{\left(\frac{\partial\rho}{\partial t} + \underbrace{\mathbf{v}.\nabla\rho + \rho\nabla.\mathbf{v}}_{=\nabla.(\rho\mathbf{v})}\right)}_{=0} d\tau\right] && \text{(5.7.23b)}\\
&= \iiint_{\mathcal{V}_M(t)} \rho\frac{dA}{dt} d\tau + \iiint_{\mathcal{V}_M(t)} A\underbrace{(-\rho\nabla.\mathbf{v} + \rho\nabla.\mathbf{v})}_{=0} d\tau && \text{(5.7.23c)}\\
&= \iiint_{\mathcal{V}_M(t)} \rho\frac{dA}{dt} d\tau && \text{(5.7.23d)}
\end{aligned}$$

recovering the results from the Eulerian approach and the previous more general formulation.

Rate of change of integrals in s-coordinate

In s-coordinates, the ocean column behaves as a material volume in the vertical direction but not in the horizontal direction where it a fixed-in-time control volume. For a volume associated to the s-coordinate grid : $\mathbf{v}_\Sigma = \mathbf{v}_h + \mathbf{v}_z - \mathbf{v}_s$. This is the vertical velocity of the iso-s surfaces. The integration volume in s-coordinates is a sum of "waters columns" and is named $\mathcal{V}_s$.

Kinematic-Dynamic evolution (Left-Hand-Side). In an Eulerian approach, the depth-to- surface integration can be carried out using Equation 2.5.19 with $J = h(t, \mathbf{x}, z)$:

$$\frac{d}{dt}\iiint_{\mathcal{V}_s} \rho A \; d\tau = \iiint_{\mathcal{V}_s} \frac{d\rho A}{dt} \; d\tau \tag{5.7.24a}$$

$$= \iiint_{\mathcal{V}_s} \frac{\partial \rho A}{\partial t} d\tau + \iiint_{\mathcal{V}_s} \nabla.(\rho A \mathbf{v}_\Sigma) d\tau \tag{5.7.24b}$$

$$= \iiint_{\mathcal{V}_s} \frac{\partial \rho A}{\partial t} d\tau + \iint_S \rho A \; \mathbf{v}_\Sigma.\mathbf{n}_\Sigma \; dS_\Sigma \tag{5.7.24c}$$

Griffies (2004), Griffies (2012) and Delhaye (2008) provides a reformulation of the latest term in Cartesian coordinates :

$$\frac{d}{dt}\iiint_{\mathcal{V}_s} \rho A \; d\tau = \iiint_{\mathcal{V}_s} \frac{\partial \rho A}{\partial t} \underbrace{d\tau}_{dxdydz} + \iint_S \rho A \left.\frac{\partial z}{\partial t}\right|_s \underbrace{dS}_{dxdy} \tag{5.7.25}$$

using the central relation (2.121) of (Griffies, 2012) and in §6 of (Griffies, 2004) :

$$\mathbf{v}_\Sigma.\mathbf{n}_\Sigma \; dS_\Sigma = \left.\frac{\partial z}{\partial t}\right|_s \; dS \tag{5.7.26}$$

Since the ocean bottom boundary is supposed to remain stationary, this leads eventually to :

$$\frac{d}{dt}\iiint_{\mathcal{V}_s} \rho A \; d\tau = \iiint_{\mathcal{V}_s} \frac{\partial \rho A}{\partial t} \underbrace{d\tau}_{dxdydz} + \iint_{S_{surf}} \rho A \; \frac{\partial \zeta}{\partial t} \underbrace{dS}_{dxdy} \tag{5.7.27}$$

Using the kinematic condition. Caution : to recover this relation based on the kinematic condition, one has to remember that $\mathbf{v}_\Sigma$ is indeterminate (Delhaye, 2008). Its component tangent to the iso-s surface depends in particular on the parametrization of this surface. The component orthogonal to this surface can however be computed. As a consequence, one has to consider the product $\mathbf{v}_\Sigma.\mathbf{n}_\Sigma$ rather than $\mathbf{v}_\Sigma$ alone.

The previous relation can then be recovered writing :

$$\frac{d}{dt}\iiint_{\mathcal{V}_s} \rho A \; d\tau = \iiint_{\mathcal{V}_s} \frac{\partial \rho A}{\partial t} d\tau + \iint_S \rho A \; \mathbf{v}_\Sigma.\mathbf{n}_\Sigma \; dS_\Sigma \tag{5.7.28a}$$

$$= \iiint_{\mathcal{V}_s} \frac{\partial \rho A}{\partial t} d\tau + \iint_{S_{surf}} \rho A \; (\mathbf{u}_\Sigma - \mathbf{w}_\Sigma).\mathbf{n}_\Sigma \; dS_\Sigma \tag{5.7.28b}$$

$$= \iiint_{\mathcal{V}_s} \frac{\partial \rho A}{\partial t} d\tau + \iint_{S_{surf}} \frac{\rho A}{\|\nabla s\|} \left(\nabla_z s.\mathbf{u} - \frac{h}{h}(\frac{\partial s}{\partial t} + \nabla_z s.\mathbf{u})\right) \underbrace{dS_\Sigma}_{= \sqrt{1+S^2} dS} \tag{5.7.28c}$$

Since $h\,\|\nabla s\| = \sqrt{1+S^2}$, we can recover :

$$\frac{d}{dt}\iiint_{\mathcal{V}_s} \rho A\, d\tau = \iiint_{\mathcal{V}_s} \frac{\partial \rho A}{\partial t} d\tau + \iint_{S_{surf}} \rho A \frac{\partial s}{\partial t} dS \tag{5.7.29}$$

Then knowing that :

$$\frac{\partial s}{\partial t} = \frac{\partial z}{\partial t} - \frac{\partial \zeta}{\partial t} \tag{5.7.30a}$$

$$= \frac{\partial \zeta}{\partial t} = \left.\frac{\partial \zeta}{\partial t}\right|_s \tag{5.7.30b}$$

we can conclude that :

$$\frac{d}{dt}\iiint_{\mathcal{V}_s} \rho A\, d\tau = \iiint_{\mathcal{V}_s} \frac{\partial \rho A}{\partial t} d\tau + \iint_{S_{surf}} \rho A \frac{\partial \zeta}{\partial t} dS \tag{5.7.31}$$

In s-coordinates. This result can also be recovered considering Reynolds transport theorem and the fact that $\mathbf{v}_s$ vanishes over both the bottom and surface boundaries. This latest formulation can be recovered from the expression in Cartesian coordinates since

$$\frac{d}{dt}\iiint_{\mathcal{V}_s} \rho A\, d\tau = \iiint_{\mathcal{V}_s} \frac{\partial \rho A}{\partial t} d\tau + \iint_{S} \rho A \left.\frac{\partial z}{\partial t}\right|_s dS \tag{5.7.32}$$

The first term on the right hand side can be rewritten :

$$\iiint_{\mathcal{V}_s} \frac{\partial \rho A}{\partial t} d\tau = \iiint_{\mathcal{V}_s} \left(\left.\frac{\partial \rho A}{\partial t}\right|_s - \frac{1}{h}\frac{\partial \rho A}{\partial s} \left.\frac{\partial z}{\partial t}\right|_s \right) h\, dsdxdy \tag{5.7.33a}$$

$$= \iiint_{\mathcal{V}_s} \left(\left.\frac{\partial \rho h A}{\partial t}\right|_s - \rho A \left.\frac{\partial h}{\partial t}\right|_s - \left.\frac{\partial}{\partial s}\left(\rho A \frac{\partial z}{\partial t}\right)\right|_s + \rho A \underbrace{\frac{\partial^2 z}{\partial s \partial t}}_{\partial h/\partial t|_s} \right) dsdxdy \tag{5.7.33b}$$

Canceling the second, third and fourth terms together and using the Green-Ostrogradsky theorem lead to :

$$\frac{d}{dt}\iiint_{\mathcal{V}_s} \rho A\, d\tau = \iiint_{\mathcal{V}_s} \left(\left.\frac{\partial \rho h A}{\partial t}\right|_s \pm \left.\frac{\partial}{\partial s}\left(\rho A \frac{\partial z}{\partial t}\right)\right|_s \right) dsdxdy \tag{5.7.34a}$$

$$= \iiint_{\mathcal{V}_s} \left.\frac{\partial \rho h A}{\partial t}\right|_s dsdxdy \tag{5.7.34b}$$

Lagrangian approach. We can recover the relation for the evolution over a material volume such as a sum of water columns :

$$\frac{d}{dt}\iiint_{\mathcal{V}_s} \rho A d\tau = \iiint_{\mathcal{V}_s} \rho \frac{dA}{dt} d\tau + \iiint_{\mathcal{V}_s} \nabla.\left[\rho A(\mathbf{v}_\Sigma - \mathbf{v})\right] d\tau \tag{5.7.35a}$$

$$= \iiint_{\mathcal{V}_s} \rho \frac{dA}{dt} d\tau + \iint_{S_{surf}} \rho A(\mathbf{v}_\Sigma - \mathbf{v}).\mathbf{n}_\Sigma dS_\Sigma \tag{5.7.35b}$$

Griffies (2004) (page 140) further shows that, at the surface :

$$\mathbf{n}_\Sigma.(\mathbf{v}_\Sigma - \mathbf{v}) = \frac{h}{\sqrt{1+S^2}} \underbrace{\frac{ds}{dt}}_{=1/h\ w_s} \tag{5.7.36}$$

and using $w_s = h\dot{s}$ thus :

$$\frac{d}{dt}\iiint_{\mathcal{V}_s} \rho A d\tau = \iiint_{\mathcal{V}_s} \rho \frac{dA}{dt} d\tau + \iint_{S_{surf}} \rho A \underbrace{w_s}_{=0} dS \tag{5.7.37a}$$

5.7.3 Conservation of an extensive quantity in a free-surface ocean

To develop diagnostics in a realistic free-surface ocean, the conservation or at least the evolution of a given property defined as $\mathcal{A} = \iiint_{\mathcal{V}(t)} \rho A d\tau$ where A is a given specific [1] property must be calculated in a region of the ocean with a varying upper surface. For a general time-dependent volume $\mathcal{V}(t)$ moving with a velocity $\mathbf{v}_\Sigma$, a formulation of the Reynolds transport theorem (or Leibnitz theorem) is given by Truesdell and Toupin (1960) and reformulated in Appendix 5.7.1 :

$$\frac{d}{dt}\iiint_{\mathcal{V}(t)} \rho A d\tau = \iiint_{\mathcal{V}(t)} \frac{D\rho A}{Dt} d\boldsymbol{x} + \iiint_{\mathcal{V}(t)} \rho A \nabla.\mathbf{v}_\Sigma \, d\mathbf{x} \tag{5.7.38a}$$

$$= \iiint_{\mathcal{V}(t)} \left.\frac{\partial \rho A}{\partial t}\right|_{xz} d\tau + \oiint_{S(t)} \rho A \mathbf{v}_\Sigma.\mathbf{n}_\Sigma dS_\Sigma \tag{5.7.38b}$$

with the material derivative D/Dt here associated to $\mathbf{v}_\Sigma$:

$$\frac{D\bullet}{Dt} = \left.\frac{\partial \bullet}{\partial t}\right|_\xi + \mathbf{v}_\Sigma.\nabla_{t,\xi}\bullet \tag{5.7.39}$$

In oceanic configurations, $\mathcal{V}(t)$ can be chosen as $\mathcal{V}_s$, a sum of water columns. In the absence of shoaling processes, this volume's boundaries only move in the vertical direction with the elevation of the free-surface. It is then possible to express $\mathcal{A}$ in s-coordinates with the Jacobian of transformation equal to $\mathcal{J} = h$:

$$\frac{d}{dt}\iiint_{\mathcal{V}_s} \rho A \, d\tau = \frac{d}{dt}\iiint_{\mathcal{V}_s} \rho A \, h ds dx_s dy_s \tag{5.7.40}$$

In this case, with the definition of constant-s surfaces, the boundaries of volume $\mathcal{V}_s$ are constant and the time-derivative can directly be applied through the integral as :

$$\frac{d}{dt}\iiint_{\mathcal{V}_s} \rho A \, h ds dx_s dy_s = \iiint_{\mathcal{V}_s} \left.\frac{\partial h \rho A}{\partial t}\right|_s ds dx_s dy_s \tag{5.7.41a}$$

$$= \iiint_{\mathcal{V}_s} \rho h \left.\frac{\partial A}{\partial t}\right|_s ds dx_s dy_s + \iiint_{\mathcal{V}_s} A \left.\frac{\partial \rho h}{\partial t}\right|_s ds dx_s dy_s \tag{5.7.41b}$$

This formulation is based on Reynolds transport theorem (see Appendix 5.7.1).

---

[1] Specific : per unit mass of the flow.

To simplify notations and without any loss of generality, integrals should in the following be restricted to the (x, z) vertical plane and subscript s should be abandoned :

$$\mathcal{A} = \int_x \int_{-1}^{0} \rho A \, h dx ds \tag{5.7.42}$$

The conservation of mass in Equation 2.5.19 and the formulation of evolution of ρ in Equation 2.5.20 of Appendix 2.5 can be used, leading to :

$$\frac{d}{dt} \int_x \int_{-1}^{0} \rho A \, h ds dx = \int_x \int_{-1}^{0} \left.\frac{\partial A}{\partial t}\right|_s \rho h ds dx \tag{5.7.43a}$$

$$- \int_x \int_{-1}^{0} A \left.\frac{\partial \rho h u}{\partial x}\right|_{ts} dx ds \tag{5.7.43b}$$

$$- \int_x \int_{-1}^{0} A \left.\frac{\partial \rho v_s}{\partial s}\right|_{tx} dx ds \tag{5.7.43c}$$

$$+ \int_x \int_{-1}^{0} A \frac{\partial}{\partial x}\left(h\kappa^h \left.\frac{\partial \rho}{\partial x}\right|_{ts} \right)_{ts} dx ds \tag{5.7.43d}$$

$$+ \int_x \int_{-1}^{0} A \frac{\partial}{\partial s}\left(\frac{\kappa^v}{h} \left.\frac{\partial \rho}{\partial s}\right|_{tx} \right)_{tx} dx ds \tag{5.7.43e}$$

Various fluxes can be simplified in this expression :

$$\frac{d}{dt} \int_x \int_{-1}^{0} \rho A \, h ds dx = \qquad \int_x \int_{-1}^{0} \rho h \left.\frac{\partial A}{\partial t}\right|_{xs} dx ds \tag{5.7.44a}$$

$$- \int_x \int_{-1}^{0} \left.\frac{\partial \rho h A u}{\partial x}\right|_{ts} dx ds + \int_x \int_{-1}^{0} \rho h u \left.\frac{\partial A}{\partial x}\right|_{ts} dx ds \tag{5.7.44b}$$

$$- \int_x \int_{-1}^{0} \left.\frac{\partial \rho A v_s}{\partial s}\right|_{tx} dx ds + \int_x \int_{-1}^{0} \rho v_s \left.\frac{\partial A}{\partial s}\right|_{tx} dx ds \tag{5.7.44c}$$

$$+ \int_x \int_{-1}^{0} \frac{\partial}{\partial x}\left(hA\kappa^h \left.\frac{\partial \rho}{\partial x}\right|_{ts} \right)_{ts} dx ds - \int_x \int_{-1}^{0} h\kappa^h \left.\frac{\partial A}{\partial x}\right|_{ts} \left.\frac{\partial \rho}{\partial x}\right|_{ts} dx ds \tag{5.7.44d}$$

$$+ \int_x \int_{-1}^{0} \frac{\partial}{\partial s}\left(A \frac{\kappa^v}{h} \left.\frac{\partial \rho}{\partial s}\right|_{tx} \right)_{tx} dx ds - \int_x \int_{-1}^{0} \frac{\kappa^v}{h} \left.\frac{\partial A}{\partial s}\right|_{tx} \left.\frac{\partial \rho}{\partial s}\right|_{tx} dx ds \tag{5.7.44e}$$

Integrating by parts the advective and diffusive flux integrals in both the vertical and horizontal directions finally leads to :

$$\frac{d}{dt}\int_x\int_{-1}^{0}\rho hA\,dxds = \int_x\int_{-1}^{0}\rho h\frac{\partial A}{\partial t}\bigg|_{ts}dxds \tag{5.7.45a}$$

$$-\left[\int_{-1}^{0}\rho hAu\,ds\right]_x + \int_x\int_{-1}^{0}\rho hu\frac{\partial A}{\partial x}\bigg|_{ts}dxds \tag{5.7.45b}$$

$$-\left[\int_x\rho Av_s\,ds\right]_0^1 + \int_x\int_{-1}^{0}\rho v_s\frac{\partial A}{\partial s}\bigg|_{ts}dxds \tag{5.7.45c}$$

$$+\left[\int_{-1}^{0}hA\kappa^h\frac{\partial\rho}{\partial x}\bigg|_{ts}ds\right]_x - \int_x\int_{-1}^{0}h\kappa^h\frac{\partial A}{\partial x}\bigg|_{ts}\frac{\partial\rho}{\partial x}\bigg|_{ts}dxds \tag{5.7.45d}$$

$$+\left[\int_x A\frac{\kappa^v}{h}\frac{\partial\rho}{\partial s}\bigg|_{tx}dx\right]_0^1 - \int_x\int_{-1}^{0}\frac{\kappa^v}{h}\frac{\partial A}{\partial s}\bigg|_{tx}\frac{\partial\rho}{\partial s}\bigg|_{tx}dxds \tag{5.7.45e}$$

This latest relation can also be formulated as a function of dA/dt :

$$\frac{d}{dt}\int_x\int_{-1}^{0}\rho hA\,dxds = \int_x\int_{-1}^{0}\rho h\frac{dA}{dt}\,dxds \tag{5.7.46a}$$

$$-\left[\int_{-1}^{0}\rho hAu\,ds\right]_x - 0 \tag{5.7.46b}$$

$$+\left[\int_{-1}^{0}hA\kappa^h\frac{\partial\rho}{\partial x}\bigg|_{ts}ds\right]_x - \int_x\int_{-1}^{0}h\kappa^h\frac{\partial A}{\partial x}\bigg|_{ts}\frac{\partial\rho}{\partial x}\bigg|_{ts}dxds \tag{5.7.46c}$$

$$+\left[\int_x A\frac{\kappa^v}{h}\frac{\partial\rho}{\partial s}\bigg|_{tx}dx\right]_0^1 - \int_x\int_{-1}^{0}\frac{\kappa^v}{h}\frac{\partial A}{\partial s}\bigg|_{tx}\frac{\partial\rho}{\partial s}\bigg|_{tx}dxds \tag{5.7.46d}$$

with $\left[\int_x\rho Av_s\,ds\right]_0^1 = 0$ since v_s is void at the bottom and top boundaries.

-6- Conclusion et Perspectives

6.1 Première incursion en *Terra Incognita* dans le détroit de Gibraltar

Durant mes trois années de thèse de doctorat, je me suis attachée à mener à bien une exploration des *fines échelles* dans la région du détroit de Gibraltar. Cette incursion en *Terra Incognita* avaient deux types d'objectifs : sur la dynamique des fines échelles tout d'abord (et la perspective de mieux comprendre les processus de fine échelle dans la région du détroit : ressaut, ondes internes solitaires, grandes structures turbulentes...), mais aussi sur la mise en place, la réalisation et l'évaluation de simulations numériques explicites (dites *LES zonale*) de ces grandes structures turbulentes.

Je me suis par conséquent appuyée sur une simulation numérique explicite et originale des *grandes structures turbulentes* à très haute résolution (seulement quelques dizaines de mètres) dans la région du détroit. La simulation numérique ne pouvant en aucun cas répondre à elle seule à l'ensemble des questions qui se posaient, j'ai effectué des allers-retours entre mes outils numériques et l'observation de l'océan réel. Si la majeure partie de mon travail de thèse a été consacrée à l'élaboration et à la description d'un écoulement océanographique local au moyen de l'outil numérique, j'ai en effet eu l'occasion de toucher à d'autres aspects de l'océanographie physique. En plus de développements plus conceptuels sur l'évaluation du mélange, j'ai eu la chance de pouvoir interagir étroitement avec mes collègues du SHOM lors de la préparation, la conduite et l'exploitation d'une campagne de mesures dédiée à la problématique des fines échelles dans la région du détroit de Gibraltar.

6.2 Des avancées de plusieurs ordres

Avec le soutien du Groupement de Recherche CROCO, j'ai mis en place une hiérarchie de maquettes numériques à très haute résolution dans la région du détroit de Gibraltar : maquettes bi-dimentionnelles (Chapitre 3) puis tri-dimentionnelles (Chapitre 4). Le choix assumé avec cette démarche de modélisation a été de proposer des maquettes de plus en plus réalistes, mais sans complexifier trop rapidement la dynamique simulée au détriment de la compréhension des processus et mécanismes complexes rencontrés dans cette région océanique très particulière.

L'abandon de l'hypothèse hydrostatique (ou des paramétrisations non-hydrostatiques) a été un préalable à la modélisation des fines échelles océaniques. Le passage à une dynamique non-hydrostatique permet en effet de représenter explicitement l'accélération verticale des processus de sous-mésoéchelle comme les courants gravitaires ou les cheminées convectives. Il est de même essentiel pour la simulation explicite de processus tels que les ondes solitaires, pour lesquelles la dispersion non-hydrostatique est un mécanisme clé aux côtés de l'advection non-linéaire. Tous ces exemples sont fondamentalement non-hydrostatiques, et la simulation explicite est particulièrement nécessaire dans l'étude de la propagation des ondes de leur lieu de génération à leur dissipation où elles participent activement au mélange diabatique.

De tels processus de sous-mésoéchelle peuvent conduire à des instabilités primaires de cisaillement, les grandes structures turbulentes ainsi générées ouvrant la voie à la cascade turbulente directe dite de Richardson-Kolmogorov. Ces grandes structures turbulentes marquent la limite basse en termes d'échelles spatio-temporelle de ce qui est appelé dans ce manuscrit "fines échelles". Elles peuvent intervenir de façon très hétérogènes et intermittentes dans la colonne d'eau, en particulier lorsqu'elles sont liés à l'instabilité de certains processus dits de sous-mésoéchelle, et sont associées à des développements non-hydrostatiques.

La simulation non-hydrostatique de la *Terra Incognita* a été possible avec la levée de l'hypothèse de Boussinesq et, avec elle, celle de l'hypothèse d'incompressibilité. J'ai ainsi pu simuler un océan à toit libre à des coûts en adéquation avec les moyens de calcul à disposition, jusqu'à une résolution de 25 m sur l'horizontal lors de tests de convergence. Cette résolution de l'ordre de quelques dizaines de mètres a permis la simulation d'instabilités primaires de cisaillement.

Cependant, les échelles spatio-temporelles auxquelles apparaissent ces instabilités au sein de la colonne d'eau sont très dépendantes des mécanismes entraînant leur génération. L'échelle des instabilités issues des écoulements de sous-mésoéchelle est généralement éloignée de celle aboutissant à la déstabilisation des couches limites de surface et de fond, dont l'extension spatiale est de l'ordre du mètre voire moins. Ainsi, pour les couches limites de surface et de fond, la modélisation (implicite) de ces "grandes" structures demeure indispensable à ce jour. La configuration numérique proposée pour l'étude des fines échelles correspond donc à une LES zonale, approche pertinente étant donnés les outils numériques et les moyens de calcul à disposition.

Les premières évaluations de la dynamique de fine échelle explicitement simulée dans les maquettes numériques mises en place au cours de ma thèse sont très encourageantes et offrent un premier état des lieux de notre capacité à explorer cette *Terra Incognita* océanique. La confrontation tant aux observations satellites qu'à une première campagne d'observation in-situ et aux marégraphes dans la région du détroit, a montré que les processus "clés" de la dynamique du détroit étaient correctement représentés et localisés (aussi bien spatialement que temporellement) : ressauts hydrauliques ou encore génération, propagation mais aussi réflexion des ondes solitaires de grande amplitude. Un mécanisme de génération secondaire pour les trains d'ondes solitaires (s'ajoutant donc à celui lié aux ressauts hydrauliques) a de surcroît été mis en évidence.

L'étude de la structuration complexe du jet méditerranéen en amont et en aval du détroit, ou celle des caractéristiques des grandes structures turbulentes, demeurent encore exploratoires en ce sens qu'une évaluation précise et vraisemblablement stochastique est à ce jour nécessaire (et en partie planifiée dans le cadre du second volet de la campagne in situ Gibraltar 2022).

Il a aussi été confirmé que la seule implantation d'une maquette numérique non-hydrostatique ne suffit pas à la bonne représentation de la dynamique locale du détroit. La dynamique des fines échelles est évidemment très dépendante de la bonne représentation de la bathymétrie dans la région du détroit (avec toutes les difficultés inhérentes à l'obtention d'une bathymétrie de quelques dizaines de mètres de résolution) mais aussi de son immersion dans une dynamique régionale (à mésoéchelle) réaliste. Concernant la bathymétrie je tiens à remercier le SHOM pour les données bathymétriques de grande qualité sur lesquelles j'ai pu appuyer mes travaux. Concernant la dynamique régionale de moyenne échelle, je souhaite aussi remercier l'ENEA (et en particulier G. Sannino) pour avoir fourni des sorties hydrostatiques du modèle MIT-GCM pour cette région dans le cadre d'une collaboration entamée avec le post-doctorat de L. Bordois.

Je tiens enfin à remercier le groupement MERCATOR pour les données de circulation générale qui ont été utilisées pour divers tests réalisés dans le cadre des travaux de l'équipe.

En ce qui concerne le "forçage" par la circulation de mésoéchelle, un travail de raffinement de la dynamique est encore en cours de déploiement (voir les perspectives ci-après). Un autre point méritant une attention particulière est la simulation de la propagation de l'onde de marée, élément essentiel de la dynamique de fine échelle dans la région du détroit de Gibraltar. En effet, la dynamique de la marée dans cette région de faible étendue jouxtant deux bassins océaniques aussi différents que l'Atlantique Nord et la Méditerranée, relève du véritable challenge. Les premières confrontations aux observations de marégraphes et la bonne représentation des processus que cette marée induit dans le détroit (ressauts hydrauliques ou encore ondes solitaires...) sont très encourageantes. Toutefois un raffinement progressif de la marée semble inéluctable pour espérer aller plus loin en termes de réalisme et de précision des processus induits (voir de nouveau les perspectives ci-après).

6.3 La question du mélange turbulent en *Terra Incognita*

Cette première exploration des grandes structures turbulentes à Gibraltar a confirmé la présence d'instabilités de type Kelvin-Helmholtz à la fois très localisées (à l'interface entre les jets méditerranéens et atlantiques) et intermittentes (bien que très corrélées avec le cycle de marée). J'ai pu montrer que leurs caractéristiques étaient très sensibles au forçage par la marée et ce, de manière fondamentalement non-linéaire puisque liée à la mise en place des ressauts hydrauliques. D'un point de vue numérique cette fois, j'ai aussi mis en évidence leur sensibilité à la modélisation des processus sous-mailles. Dans la mesure où ces structures sont les portes d'entrée de la cascade turbulente directe, leur simulation explicite ainsi qu'une représentation statistiquement correcte de l'amorce de ces cascades menant au mélange est un enjeu "clé" de notre entrée en *Terra Incognita*.

Une question sous-jacente une fois ces grandes structures turbulentes simulées est celle de la quantification du mélange turbulent. Durant ma dernière année de thèse, j'ai mené à bien un travail de fond visant à généraliser l'approche basée sur l'équation d'évolution de l'énergie potentielle disponible (et par là même de l'énergie potentielle de référence) issue des travaux de Lorenz (1955). Ce travail, présenté en Chapitre 5 de ce manuscrit, a montré la nécessité de reformuler ce bilan dans le contexte de colonnes océaniques de volume variable. L'introduction d'un terme lié aux mouvements de la surface libre s'est en particulier révélé indispensable dans la série de configurations tests que j'ai proposée dans ce chapitre. Cette étude demeure évidemment exploratoire, et les choix algorithmiques doivent encore être affinés pour déboucher sur une localisation et une quantification du mélange turbulent dans un contexte pleinement réaliste impliquant en particulier une analyse à très haute résolution sur des régions étendues. Le choix de grandeurs physiques permettant de rendre compte correctement de l'évolution très hétérogène et instationnaire du mélange est encore ouvert à ce jour.

Un autre verrou, peut-être plus conceptuel, est lié à la nécessité de converger sur une "grandeur" (ou un jeu de "grandeurs" liées les unes aux autres) qui serait étudiée dans des contextes aussi différents que l'observation in-situ, la simulation physique (en laboratoire) et la simulation numérique, tout en pouvant être mis en relations. Cette grandeur doit aussi prendre tout son sens et être partagée par les schémas de fermeture turbulente des modèles de circulation générale.

6.4 Perspectives pour les prochaines incursions en *Terra Incognita*

Une conclusion de mes travaux qui s'impose est la nécessité de penser la simulation des *fines échelles océaniques* dans le cadre d'approches par raffinement local. Ceci est essentiel aussi bien pour le forçage par la marée que pour la circulation régionale à mésoéchelle dans le détroit de Gibraltar. En parallèle de mes travaux de thèse, l'équipe CROCO du LAERO a dors et déjà mis en place une maquette basée sur trois niveaux de raffinement pour aboutir à une résolution de quelques dizaines de mètres dans le détroit à partir d'une circulation régionale kilométrique. Des allers-retours entre les simulations numériques sur lesquelles ces maquettes débouchent et l'océan réel sont actuellement en cours dans le cadre des projets in-situ SHOM Prometevs - LEFE Gepeto Gibraltar 2020-2022.

De plus, au cours de mes travaux de thèse, seul l'effet de la fine échelle sur la composition des masses d'eaux a été abordé, mais la question de l'impact du mélange ou de la friction sur la distribution des traceurs passifs biogéochimiques (Penney et al., 2020) et sur la structuration de la vorticité potentielle (Morel et al., 2019) demeure encore ouverte.

Cette thèse propose une simulation originale des grandes structures turbulentes dans un contexte réaliste. Je me suis pour cela appuyée sur un outil de modélisation nouveau au développement duquel j'ai activement participé dans le cadre de mes travaux de thèse : le code CROCO à toit libre non-hydrostatique et compressible (Hilt et al., 2020). Outre la simulation par raffinement locale, cinq pistes d'évolutions sont aujourd'hui soit en cours d'étude, soit encore à l'état de projet. Il est tout d'abord indispensable de penser les schémas sous-mailles dans le contexte d'une LES dite zonale Friess (2010). Cela implique en particulier des allers-retours avec des simulations physiques d'une part et avec l'observation in-situ d'autre part. Dans ce contexte, la convergence de la LES zonale vers des simulations directes (dites DNS) est indispensable et doit être démontrée. Les performances de l'outil numérique doivent évidemment être accrues et de l'importance des gains réalisés dépendra la richesse de la dynamique simulée dans les prochaines années. Le code CROCO dans sa version non-hydrostatique et compressible a pour cela été porté sur la future génération de processeurs hétérogènes CPU / GPU. La compressibilité et plus spécifiquement déjà la propagation acoustique des anomalies de pression est actuellement en cours d'évaluation dans l'outil numérique CROCO en temps que processus[1] : une telle étude va permettre de mieux comprendre la dynamique compressible sous-jacente et donc de mieux l'appréhender dans le contexte des fines échelles océaniques. Enfin une approche stochastique est actuellement lancée dans le cadre du Groupement de Recherche CROCO (Mémin, 2014), la simulation des grandes structures turbulentes devra être pensée ou plus exactement repensée dans un tel contexte.

Enfin, l'exploration des fines échelles initiée durant ma thèse de doctorat est focalisée sur la région du détroit de Gibraltar, qui s'apparente à un écoulement bicouche dans une zone à bathymétrie accidentée. Les outils numériques développés ou en cours de développement ouvrent d'intéressantes perspectives d'applications à d'autres zones d'intérêt, comme les zones de convection profonde, d'autres détroits, des régions d'upwelling côtier ou encore les régions littorales (Marchesiello et al., 2021)...

---

[1] Thèse de doctorat de Pierre-Antoine Dumont, SHOM.

Table des figures

Liste des tableaux

Bibliographie

Auclair, F. (2011). WOcean.fr, Teaching & Reshearch. http ://poc.omp.obs-mip.fr/auclair/WOcean.fr/Html_maps/Site_ENS_map_main.htm.

Auclair, F., Bordois, L., Dossmann, Y., Duhaut, T., Paci, A., Ulses, C., and Nguyen, C. (2018). A non-hydrostatic non-Boussinesq algorithm for free-surface ocean modelling. *Ocean Modelling*, 132 :12–29.

Auclair, F., Bordois, L., Hilt, M., Chassignet, E., Roblou, L., and Nguyen, C. (2019). Modélisation des fines échelles internes dans la région du détroit de Gibraltar. *Contrat SHOM / UPS 16CR01.*, page 101.

Auclair, F., Debreu, L., Duval, E., Hilt, M., Marchesiello, P., Blayo, E., Dumas, F., and Morel, Y. (2021a). Theory and analysis of acoustic-gravity waves in a free-surface compressible and stratified ocean. *Ocean Modelling*, 168 :101900.

Auclair, F., Estournel, C., Floor, J. W., Herrmann, M., Nguyen, C., and Marsaleix, P. (2011). A non-hydrostatic algorithm for free-surface ocean modelling. *Ocean Modelling*, 36(1-2) :49–70.

Auclair, F., Hilt, M., Dumas, F., and et al. (2021b). A non-hydrostatic, compressible, free-surface model of the ocean. *Ocean Modelling*, Soumission en cours.

Augier, P. (2012). Turbulence in strongly stratified fluids : cascade processes. page 236.

Baines, P. G. (1995). *Topographic Effects in Stratified Flows*. Cambridge University Press edition.

Barton, E. (2001). Canary And Portugal Currents. In *Encyclopedia of Ocean Sciences*, pages 380–389. Elsevier.

Bashmachnikov, I., Neves, F., Calheiros, T., and Carton, X. (2015). Properties and pathways of Mediterranean water eddies in the Atlantic. *Progress in Oceanography*, 137 :149–172.

Bethoux, J. (1979). Budgets of the mediterranean sea. Their dependance on the local climate and on the characteristics of the atlantic waters. *Oceanologica Acta*, 2(2) :157–163.

Billant, P., Deloncle, A., Chomaz, J.-M., and Otheguy, P. (2010). Zigzag instability of vortex pairs in stratified and rotating fluids. Part 2. Analytical and numerical analyses. *Journal of Fluid Mechanics*, 660 :396–429.

Biscara, L., Maspataud, A., and Schmitt, T. (2016). Generation of bathymetric digital elevation models along French coasts : Coastal risk assessment. *Hydro International*, 20(6) :26—-29.

Borges, R., Carmona, M., Costa, B., and Don, W. (2008). An improved weighted essentially non-oscillatory scheme for hyperbolic conservation laws. *Journal of Computational Physics*, 227(6) :3191–3211.

Bormans, M. and Garrett, C. (1989). The effect of rotation on the surface inlow through the Strait of Gibraltar. *Jounal of Physical Oceanography*, 19(10) :1535–1542.

Brandt, P., Alpers, W., and Backhaus, J. O. (1996). Study of the generation and propagation of internal waves in the Strait of Gibraltar using a numerical model and synthetic aperture radar images of the European ERS 1 satellite. *Journal of Geophysical Research : Oceans*, 101(C6) :14237–14252.

Bray, N. A., Ochoa, J., and Kinder, T. H. (1995). The role of the interface in exchange through the Strait of Gibraltar. *Journal of Geophysical Research*, 100(C6) :10755–10776.

Bruno, M., Alonso, J. J., Cózar, A., Viad, J., Ruiz-Cañavate, A., Echevarría, F., and Ruiz, J. (2002). The boiling-water phenomena at Camarinal Sill, the Strait of Gibraltar. *Deep-Sea Research II*, 49(19) :4097–4113.

Bruno, M., Chioua, J., Romero, J., Vázquez, A., Macías, D., Dastis, C., Ramírez-Romero, E., Echevarria, F., Reyes, J., and García, C. (2013). The importance of sub-mesoscale processes for the exchange of properties through the Strait of Gibraltar. *Progress in Oceanography*, 116 :66–79.

Bryden, H. and Kinder, T. (1991). Steady two-layer exchange through the Strait of Gibraltar. *Deep Sea Research Part A. Oceanographic Research Papers*, 38 :S445–S463.

Bryden, H. and Stommel, H. (1984). Limiting processes that determine basic features of the circulation in the Mediterranean Sea. *Oceanologica Acta*, 7(3) :289–296.

Bryden, H. L., Candela, J., and Kinder, T. H. (1994). Exchange through the Strait of Gibraltar. *Progress in Oceanography*, 33(3) :201–248.

Candela, J., Winant, C., and Ruiz, A. (1990). Tides in the Strait of Gibraltar. *Journal of Geophysical Research : Oceans*, 95(C5) :7313–7335.

Candela, J., Winant, C. D., and Bryden, H. L. (1989). Meteorologically forced subinertial flows through the Strait of Gibraltar. *Journal of Geophysical Research*, 94(C9) :12667.

Charney, J. G. (1971). Geostrophic Turbulence. *Journal of the Atmospheric Sciences*, 28(6) :1087–1095.

Chelton, D. B., Schlax, M. G., Samelson, R. M., and de Szoeke, R. A. (2007). Global observations of large oceanic eddies. *Geophysical Research Letters*, 34(15).

Chen, Z., Nie, Y., Xie, J., Xu, J., He, Y., and Cai, S. (2017). Generation of internal solitary waves over a large sill : From Knight Inlet to Luzon Strait : GENERATION OF INTERNAL SOLITARY WAVES. *Journal of Geophysical Research : Oceans*, 122(2) :1555–1573.

Cucitore, R., Quadrio, M., and Baron, A. (1999). On the effectiveness and limitations of local criteria for the identification of a vortex. *European Journal of Mechanics B Fluids*, 18(2) :261–282.

Cushman-Roisin, B. and Beckers, J.-M. (2011). *Introduction to geophysical fluid dynamics : physical and numerical aspects*. International geophysics series 101. Academic Press, Waltham, Mass, 2nd edition edition.

de Lavergne, C., Madec, G., Roquet, F., Holmes, R. M., and McDougall, T. J. (2017). Abyssal ocean overturning shaped by seafloor distribution. *Nature*, 551(7679) :181–186.

Debreu, L., Marchesiello, P., Penven, P., and Cambon, G. (2012). Two-way nesting in split-explicit ocean models : algorithms, implementation and validation. *Ocean Modelling*, 49–50 :1–21.

Delhaye, J.-M. (2008). *Thermohydraulique Des Réacteurs Ed. 1*. EDP Sciences.

Dossmann, Y. (2012). *Ondes internes générées sur une dorsale océanique : du laboratoire à l'océan*. Doctoral dissertation, Université Paul Sabatier - Toulouse III.

Egbert, G. D. and Erofeeva, S. Y. (2002). Efficient inverse modeling of barotropic ocean tides. *Journal of Atmospheric and Oceanic Technology*, 19.2 :183–204.

Farmer, D. and Armi, L. (1986). Maximal two-layer exchange over a sill and through the combination of a sill and contraction with barotropic flow. *Journal of Fluid Mechanics*, 164 :53–76.

Farmer, D. and Armi, L. (1988). The flow of atlantic water through the strait of gibraltar. *Progress in Oceanography*, 21(1) :1–103.

Floor, J., Auclair, F., and Marsaleix, P. (2011). Energy transfers in internal tide generation, propagation and dissipation in the deep ocean. *Ocean Modelling*, 38(1-2) :22–40.

Fox-Kemper, B., Adcroft, A., Böning, C. W., Chassignet, E. P., Curchitser, E., Danabasoglu, G., Eden, C., England, M. H., Gerdes, R., Greatbatch, R. J., Griffies, S. M., Hallberg, R. W., Hanert, E., Heimbach, P., Hewitt, H. T., Hill, C. N., Komuro, Y., Legg, S., Le Sommer, J., Masina, S., Marsland, S. J., Penny, S. G., Qiao, F., Ringler, T. D., Treguier, A. M., Tsujino, H., Uotila, P., and Yeager, S. G. (2019). Challenges and prospects in ocean circulation models. *Front. Mar. Sci.*, 6 :65.

Friess, C. (2010). Modélisation hybride RANS / LES temporelle des écoulements turbulents. *Thèse de Doctorat*, page 152.

García Lafuente, J., Almazan, J., Castillejo, F., Khribeche, A., and Hakimi, A. (1990). Sea level in the Strait of Gibraltar : Tides. *International Hydrographyc Review*, 47 :111–130.

García Lafuente, J., Álvarez Fanjul, E., Vargas, J. M., and Ratsimandresy, A. W. (2002a). Subinertial variability in the flow through the Strait of Gibraltar. *Journal of Geophysical Research*, 107(C10) :3168.

García Lafuente, J., Delgado, J., and Criado, F. (2002b). Inflow interruption by meteorological forcing in the Strait of Gibraltar : Inflow interruption in gibraltar strait. *Geophysical Research Letters*, 29(19) :20–1–20–4.

García-Lafuente, J., Naranjo, C., Sammartino, S., Sánchez-Garrido, J. C., and Delgado, J. (2017). The Mediterranean outflow in the Strait of Gibraltar and its connection with upstream conditions in the Alborán Sea. *Ocean Science*, 13(2) :195–207.

García-Lafuente, J., Sánchez-Román, A., Naranjo, C., and Sánchez-Garrido, J. C. (2011). The very first transformation of the mediterranean outflow in the strait of gibraltar. *Journal of Geophysical Research : Oceans*, 116(C7).

Garrett, C., Bormans, M., and Thompson, K. (1990). *The Physical Oceanography of Sea Straits*, chapter Is the exchange through the Strait of Gibraltar maximal or submaximal ?, pages 271–294.

Gasser, M., Pelegrí, J. L., Emelianov, M., Bruno, M., Gràcia, E., Pastor, M., Peters, H., Rodríguez-Santana, Á., Salvador, J., and Sánchez-Leal, R. F. (2017). Tracking the Mediterranean outflow in the Gulf of Cadiz. *Progress in Oceanography*, 157 :47–71.

Gill, A. E. (1982). *Atmosphere-Ocean Dynamics*. Academic Press Inc, San Diego.

Gregg, M., D'Asaro, E., Riley, J., and Kunze, E. (2018). Mixing Efficiency in the Ocean. *Annual Review of Marine Science*, 10(1) :443–473.

Griffies, S. M. (2004). Fundamentals of ocean climate models. page 523.

Griffies, S. M. (2012). Elements of the modular ocean model (MOM). page 632.

Grinstein, F., Margolin, L., and Rider, W. (2007). *Implicit Large Eddy Simulation : Computing Turbulent Fluid Dynamics*. Cambridge University Press edition.

Haynes, P. H. and McIntyre, M. (1990). On the Conservation and Impermeability Theorems for Potential Vorticity. 47(16) :2021–2031.

Heburn, G. W. and La Violette, P. E. (1990). Variations in the structure of the anticyclonic gyres found in the Alboran Sea. *Journal of Geophysical Research*, 95(C2) :1599.

Hilt, M., Auclair, F., Benshila, R., Bordois, L., Capet, X., Debreu, L., Dumas, F., Jullien, S., Lemarié, F., Marchesiello, P., Nguyen, C., and Roblou, L. (2020). Numerical modelling of hydraulic control, solitary waves and primary instabilities in the Strait of Gibraltar. *Ocean Modelling*, 151 :101642.

Hirasaki, G. J. (2021). Chapter 4 - The Kinematics of Fluid Motion. *Web Course*, page 15.

Howland, C. J., Taylor, J. R., and Caulfield, C. P. (2020a). Mixing in forced stratified turbulence and its dependence on large-scale forcing. page 27.

Howland, C. J., Taylor, J. R., and Caulfield, C. P. (2020b). Quantifying mixing and available potential energy in vertically periodic simulations of stratified flows. *arXiv :2008.02515 [physics]*.

Huang, R. X. (1998). Mixing and Available Potential Energy in a Boussinesq Ocean. *Journal of Physical Oceanography*, 28 :10.

Izquierdo, A., Tejedor, L., Sein, D., Backhaus, J., Brandt, P., Rubino, A., and Kagan, B. A. (2001). Control variability and internal bore evolution in the Strait of Gibraltar : A 2-D two-layer model study. *Estuarine, Coastal and Shelf Science*, 53 :637—-651.

Jakobsen, H. A. (2014). *Chemical Reactor Modeling*. Springer International Publishing, Cham.

Jia, Y., Coward, A. C., de Cuevas, B. A., Webb, D. J., and Drijfhout, S. S. (2007). A Model Analysis of the Behavior of the Mediterranean Water in the North Atlantic. *Journal of Physical Oceanography*, 37(3) :764–786.

Kolmogorov, A. (1941). The Local Structure of Turbulence in Incompressible Viscous Fluid for Very Large Reynolds' Numbers. *Akademiia Nauk SSSR Doklady*, 30 :301–305.

Lac, C., Chaboureau, J.-P., Masson, V., Pinty, J.-P., Tulet, P., Escobar, J., Leriche, M., Barthe, C., Aouizerats, B., Augros, C., Aumond, P., Auguste, F., Bechtold, P., Berthet, S., Bielli, S., Bosseur, F., Caumont, O., Cohard, J.-M., Colin, J., Couvreux, F., Cuxart, J., Delautier, G., Dauhut, T., Ducrocq, V., Filippi, J.-B., Gazen, D., Geoffroy, O., Gheusi, F., Honnert, R., Lafore, J.-P., Lebeaupin Brossier, C., Libois, Q., Lunet, T., Mari, C., Maric, T., Mascart, P., Mogé, M., Molinié, G., Nuissier, O., Pantillon, F., Peyrillé, P., Pergaud, J., Perraud, E., Pianezze, J., Redelsperger, J.-L., Ricard, D., Richard, E., Riette, S., Rodier, Q., Schoetter, R., Seyfried, L., Stein, J., Suhre, K., Taufour, M., Thouron, O., Turner, S., Verrelle, A., Vié, B., Visentin, F., Vionnet, V., and Wautelet, P. (2018). Overview of the Meso-NH model version 5.4 and its applications. *Geoscientific Model Development*, 11(5) :1929–1969.

Lapeyre, G. (2000). Topologie du mélange dans un fluide turbulent géophysique. page 205.

Lemarié, F., Burchard, H., Debreu, L., Klingbeil, K., and Sainte-Marie, J. (2019). Advancing dynamical cores of oceanic models across all scales. *Bull. Amer. Meteor. Soc.*, 100(3) :ES109–ES115.

Lilly, D. K. (1983). Stratified Turbulence and the Mesoscale Variability of the Atmosphere. *Journal of the Atmospheric Sciences*, 40(3) :749–761.

Lorente, P., Piedracoba, S., Sotillo, M. G., and Álvarez-Fanjul, E. (2019). Long-Term Monitoring of the Atlantic Jet through the Strait of Gibraltar with HF Radar Observations. *Journal of Marine Science and Engineering*, 7(1) :3.

Lorenz, E. N. (1955). Available Potential Energy and the Maintenance of the General Circulation. *Tellus*, 7(2) :157–167.

Macias, D., García, C. M., Echevarría Navas, F., Vázquez-López-Escobar, A., and Bruno Mejías, M. (2006). Tidal induced variability of mixing processes on Camarinal Sill (Strait of Gibraltar) : A pulsating event. *Journal of Marine Systems*, 60(1-2) :177–192.

Marchesiello, P., Auclair, F., Debreu, L., McWilliams, J., Almar, R., Benshila, R., and Dumas, F. (2021). Tridimensional nonhydrostatic transient rip currents in a wave-resolving model. *Ocean Modelling*, 163 :101816.

Marchesiello, P., Capet, X., Menkes, C., and Kennan, S. C. (2011). Submesoscale dynamics in tropical instability waves. *Ocean Modelling*, 39(1–2) :31–46.

Marchesiello, P., McWilliams, J. C., and Shchepetkin, A. (2001). Open boundary conditions for long-term integration of regional oceanic models. *Ocean modelling*, 3(1) :1–20.

Marshall, J., Adcroft, A., Hill, C., Perelman, L., and Heisey, C. (1997). A finite-volume, incompressible Navier Stokes model for studies of the ocean on parallel computers. *Journal of Geophysical Research : Oceans*, 102(C3) :5753–5766.

Mashayek, A. and Peltier, W. R. (2012). The ‘zoo’ of secondary instabilities precursory to stratified shear flow transition. Part 1 Shear aligned convection, pairing, and braid instabilities. *Journal of Fluid Mechanics*, 708 :5–44.

McWilliams, J. C. (2016). Submesoscale currents in the ocean. *Proceedings of the Royal Society A : Mathematical, Physical and Engineering Sciences*, 472(2189) :20160117.

Mémin, E. (2014). Fluid flow dynamics under location uncertainty. *Geophysical & Astrophysical Fluid Dynamics*, 108(2) :119–146.

Millot, C. (2007). Interannual salinification of the Mediterranean inflow. *Geophysical Research Letters*, 34(21) :L21609.

Millot, C. (2014). Heterogeneities of in- and out-flows in the mediterranean sea. *Progress in Oceanography*, 120 :254 – 278.

Morel, Y., Gula, J., and Ponte, A. (2019). Potential vorticity diagnostics based on balances between volume integral and boundary conditions. *Ocean Modelling*, 138 :23–35.

Naranjo, C., García Lafuente, J., Sánchez Garrido, J. C., Sánchez Román, A., and Delgado Cabello, J. (2012). The Western Alboran Gyre helps ventilate the Western Mediterranean Deep Water through Gibraltar. *Deep Sea Research Part I : Oceanographic Research Papers*, 63 :157–163.

Naranjo, C., Garcia-Lafuente, J., Sannino, G., and Sanchez-Garrido, J. (2014). How much do tides affect the circulation of the Mediterranean Sea ? from local processes in the Strait of Gibraltar to basin-scale effects. *Progress in Oceanography*, 127 :108–116.

Naranjo, C., Sammartino, S., García-Lafuente, J., Bellanco, M. J., and Taupier-Letage, I. (2015). Mediterranean waters along and across the Strait of Gibraltar, characterization and zonal modification. *Deep Sea Research Part I : Oceanographic Research Papers*, 105 :41 – 52.

Pairaud, I. and Auclair, F. (2005). Combined wavelet and principal component analysis (WEof) of a scale-oriented model of coastal ocean gravity waves. *Dynamics of atmospheres and oceans*, 40 :254–282.

Palma, M., Iacono, R., Sannino, G., Bargagli, A., Carillo, A., Fekete, B. M., Lombardi, E., Napolitano, E., Pisacane, G., and Struglia, M. V. (2020). Short-term, linear, and non-linear local effects of the tides on the surface dynamics in a new, high-resolution model of the Mediterranean Sea circulation. *Ocean Dynamics*, 70 :935–963.

Penney, J., Morel, Y., Haynes, P., Auclair, F., and Nguyen, C. (2019). Diapycnal mixing of passive tracers by Kelvin-Helmholtz instabilities. *Journal of Fluid Mechanics*, Under review. :49.

Penney, J., Morel, Y., Haynes, P., Auclair, F., and Nguyen, C. (2020). Diapycnal mixing of passive tracers by Kelvin–Helmholtz instabilities. *Journal of Fluid Mechanics*, 900 :A26.

Price, J. F., Baringer, M. O., Lueck, R. G., Johnson, G. C., Ambar, I., Parrilla, G., Cantos, A., Kennelly, M. A., and Sanford, T. B. (1993). Mediterranean Outflow Mixing and Dynamics. *Science*, 259(5099) :1277–1282.

Riley, J. J., Metcalfe, R. W., and Weissman, M. A. (1981). Direct numerical simulations of homogeneous turbulence in density-stratified fluids. *AIP Conference Proceedings*, 76(1) :79–112.

Saenz, J. A., Tailleux, R., Butler, E. D., Hughes, G. O., and Oliver, K. I. C. (2015). Estimating Lorenz's Reference State in an Ocean with a Nonlinear Equation of State for Seawater. *Journal of Physical Oceanography*, 45(5) :1242–1257.

Salmon, R. (1980). Baroclinic instability and geostrophic turbulence. *Geophysical & Astrophysical Fluid Dynamics*, 15(1) :167–211.

Sammartino, S., García Lafuente, J., Naranjo, C., Sánchez Garrido, J., Sánchez Leal, R., and Sánchez Román, A. (2015). Ten years of marine current measurements in Espartel Sill, Strait of Gibraltar. *Journal of Geophysical Research*, 120(9) :6309—-6328.

Sánchez Garrido, J., Lafuente, J. G., Aldeanueva, F. C., Baquerizo, A., and Sannino, G. (2008). Time-spatial variability observed in velocity of propagation of the internal bore in the Strait of Gibraltar. *Journal of Geophysical Research*, 113(C07034).

Sánchez Garrido, J., Sannino, G., Liberti, L., Lafuente, J. G., and Pratt, L. (2011). Numerical modeling of three-dimensional stratified tidal flow over Camarinal Sill, Strait of Gibraltar. *Journal of Geophysical Research*, 116(C12).

Sánchez-Garrido, J. C., García Lafuente, J., Álvarez Fanjul, E., Sotillo, M. G., and de los Santos, F. J. (2013). What does cause the collapse of the Western Alboran Gyre ? results of an operational ocean model. *Progress in Oceanography*, 116 :142–153.

Sánchez Garrido, J. C., García Lafuente, J., Criado Aldeanueva, F., Baquerizo, A., and Sannino, G. (2008). Time-spatial variability observed in velocity of propagation of the internal bore in the Strait of Gibraltar. *Journal of Geophysical Research*, 113(C7) :C07034.

Sánchez-Garrido, J. C., Sannino, G., Liberti, L., García Lafuente, J., and Pratt, L. (2011). Numerical modeling of three-dimensional stratified tidal flow over Camarinal Sill, Strait of Gibraltar. *Journal of Geophysical Research*, 116(C12) :C12026.

Sánchez-Román, A., García-Lafuente, J., Delgado, J., Sánchez-Garrido, J., and Naranjo, C. (2012). Spatial and temporal variability of tidal flow in the Strait of Gibraltar. *Journal of Marine Systems*, 98–99 :9–17.

Sannino, G., Bargagli, A., and Artale, V. (2002). Numerical modeling of the mean excghange through the Strait of Gibraltar. *Journal of Geophysical Research*, 107.

Sannino, G., Bargagli, A., and Artale, V. (2004). Numerical modeling of the semidiurnal tidal exchange through the Strait of Gibraltar. *Journal of Geophysical Research*, 109(C5).

Sannino, G., Carillo, A., and Artale, V. (2007). Three-layer view of transports and hydraulics in the Strait of Gibraltar : A three-dimensional model study. *Journal of Geophysical Research*, 112(C3) :C03010.

Sannino, G., Garrido, J. S., Liberti, L., and Pratt, L. (2014). *Exchange flow through the Strait of Gibraltar as simulated by a σ-Coordinate Hydrostatic Model and a z-coordinate nonhydrostatic model*, chapter 3, pages 25–50. American Geophysical Union (AGU).

Sannino, G., Herrmann, M., Carillo, A., Rupolo, V., Ruggiero, V., Artale, V., and Heimbach, P. (2009a). An eddy-permitting model of the Mediterranean Sea with two-way grid refinement at the Strait of Gibraltar. *Ocean Modelling*, 30 :56–72.

Sannino, G., Pratt, L., and Carillo, A. (2009b). Hydraulic criticality of the exchange flow through the Strait of Gibraltar. *Journal of Physical Oceanography*, 39 :2779–2799.

Sarhan, T., Garcia Lafuente, J., Vargas, M., Vargas, J. M., and Plaza, F. (2000). Upwelling mechanisms in the northwestern Alboran Sea. *Journal of Marine Systems*, 23(4) :317–331.

Scotti, A. (2010). Large eddy simulation in the ocean. *International Journal of Computational Fluid Dynamics*, 24(10) :393–406.

Shchepetkin, A. F. and McWilliams, J. C. (2005). The regional oceanic modeling system (ROMS) : A split-explicit, free-surface, topography-following-coordinate oceanic model. *Ocean Modelling*, 9(4) :347–404.

Skamarock, W. C., Klemp, J. B., and Dudhia, J. (2001). Prototypes for the WRF (Weather Research and Forecasting) model. In *Preprints, Ninth Conf. Mesoscale Processes, J11–J15, Amer. Meteorol. Soc., Fort Lauderdale, FL.*

Smagorinsky, J. (1963). General circulation experiments with the primitive equations. *Monthly Weather Review*, 91(3) :66.

Soto-Navarro, J., Somot, S., Sevault, F., Beuvier, J., Criado-Aldeanueva, F., García-Lafuente, J., and Béranger, K. (2015). Evaluation of regional ocean circulation models for the Mediterranean Sea at the Strait of Gibraltar : volume transport and thermohaline properties of the outflow. *Climate Dynamics*, 44 :1277–1292.

Soufflet, Y., Marchesiello, P., Lemarié, F., Jouanno, J., Capet, X., Debreu, L., and Benshila, R. (2016). On effective resolution in ocean models. *Ocean Modelling*, 98 :36–50.

St. Laurent, L. and Garrett, C. (2002). The role of internal tides in mixing the deep ocean. *Journal of Physical Oceanography*, 32(10) :2882–2899.

Sánchez-Román, A., Sannino, G., García-Lafuente, J., Carillo, A., and Criado-Aldeanueva, F. (2009). Transport estimates at the western section of the Strait of Gibraltar : A combined experimental and numerical modeling study. *Journal of Geophysical Research*, 114(C6) :C06002.

Tailleux, R. (2009). On the energetics of stratified turbulent mixing, irreversible thermodynamics, Boussinesq models and the ocean heat engine controversy. *Journal of Fluid Mechanics*, 638 :339.

Tailleux, R. (2013). Irreversible compressible work and available potential energy dissipation in turbulent stratified fluids. *Phys. Scr. T*, page 12.

Tailleux, R. (2018). Local available energetics of multicomponent compressible stratified fluids. *Journal of Fluid Mechanics*, 842 :R1.

Truesdell, C. and Toupin, R. A. (1960). *The Classical Field Theories*, volume III/1. of *Principles of Classical Mechanics and Field Theory.* Springer, Berlin, flugge s hanbuch des physik. edition.

Umlauf, L. and Burchard, H. (2003). A generic length-scale equation for geophysical turbulence models. *Journal of Marine Research*, 61(2) :235–265.

Vallis, G. K. (2006). *Atmospheric and Oceanic Fluid Dynamics : Fundamentals and Large-Scale Circulation.* Cambridge University Press, Cambridge.

Vargas, J., García-Lafuente, J., Candela, J., and Sánchez, A. (2006). Fortnightly and monthly variability of the exchange through the Strait of Gibraltar. *Progress in Oceanography*, 70(2-4) :466–485.

Vázquez, A., Stashchuk, N., Vlasenko, V., Bruno, M., Izquierdo, A., and Gallacher, P. C. (2006). Evidence of multimodal structure of the baroclinic tide in the Strait of Gibraltar. *Geophysical research letters*, 33(17).

Vlasenko, V., Brandt, P., and Rubino, A. (2000). Structure of Large-Amplitude Internal Solitary Waves. *Journal of Physical Oceanography*, 30 :14.

Vlasenko, V., Sanchez Garrido, J. C., Stashchuk, N., Garcia Lafuente, J., and Losada, M. (2009). Three-Dimensional Evolution of Large-Amplitude Internal Waves in the Strait of Gibraltar. *Journal of Physical Oceanography*, 39(9) :2230–2246.

Watson, G. and Robinson, I. (1990). A study of internal wave propagation in the Strait of Gibraltar using shore-based marine radar images.

Wesson, J. C. and Gregg, M. C. (1994). Mixing at Camarinal Sill in the Strait of Gibraltar. *Journal of Geophysical Research*, 99(C5) :9847.

Winters, K. B. and Barkan, R. (2013). Available potential energy density for Boussinesq fluid flow. *Journal of Fluid Mechanics*, 714 :476–488.

Winters, K. B., Lombard, P. N., Riley, J. J., and D'Asaro, E. A. (1995). Available potential energy and mixing in density-stratified fluids. *Journal of Fluid Mechanics*, 289 :115–128.

Wyngaard, J. C. (2004). Toward Numerical Modeling in the "Terra Incognita". *Journal of the Atmospheric Sciences*, 61 :11.

Zakharov, V. E., L'Vov, V. S., and Falkovich, G. (1992). *Wave Turbulence*. Springer-Verlag Berlin and Heidelberg GmbH & Co. K, Berlin Heidelberg.

Ziegenbein, J. (1970). Spatial observations of short internal waves in the Strait of Gibraltar. *Deep Sea Research and Oceanographic Abstracts*, 17(5) :867–875.

An exploration of oceanic fine-scale dynamics in the Strait of Gibraltar : numerical simulation, observation, and mixing

This thesis focuses on the so-called *fine-scale* dynamics of the ocean spectrum, ranging from sub-mesoscale processes to the largest turbulent eddy scales leading to the direct Richardson cascade, itself ending up to molecular mixing. The properties of the ocean's water masses are partly ascribed to this irreversible mixing. While energy transfers in the direct cascade are well-known since Kolmogorov (1941)'s work, observations of the instabilities leading to those scales are few and their numerical simulation is seldom carried out, so that fine-scale dynamics constitutes a real *Terra Incognita* (Scotti, 2010).

Improvements in efficiency of computation means and numerical models, along with new algorithms, now allow for the simulation of the largest turbulent eddies and the study of this *Terra Incognita*. An exploration of fine-scale dynamics is performed in the strait of Gibraltar linking the Mediterranean sea to the Atlantic ocean. In this area, water masses of contrasting density meet over an uneven, relatively shallow seafloor, where the tidal amplitude is large. Fine-scale processes are a consequence of these forcing in the strait : an hydraulic control of the flow evolves over each tidal period, generating and then relaxing an internal hydraulic jump. Mixing by shear instabilities is amplified when this jump is active, and the propagation of a train of internal solitary waves toward the Mediterranean sea follows.

The generation of solitary waves and the shear instabilities in the strait of Gibraltar are studied in this manuscript through numerical simulations, and in-situ observations, the latter having been carried out during a dedicated oceanographic campaign.

Simulation of the fine scale dynamics is made possible by the developments of the non-hydrostatic, compressible, free-surface kernel of CROCO detailed in chapter (2).

Regional simulations of the strait are then addressed in two steps : first as a dynamically-simplified 2D configuration then as a 3D, realistic, LES configuration. The latter configuration allows to study the link between tidal forcing, hydraulic control, and mixing, and its evolution during the spring/neap tidal cycle. Indeed, an original explicit simulation of large turbulent eddies has been carried out : the turbulent eddies have consequently been localized in the region of the sills and their intensification with the spring/neap cycle has been highlighted. Propagation of solitary waves in simulations is compared to mooring observations, pointing to a secondary generation mechanism in the strait for neap tide periods.

A sensitivity study of the characteristics of turbulent eddies and water masses to subgrid models is also performed.

The final chapter of this manuscript revolves around the quantification of mixing based on the evolution of potential energy. A new term is added to the evolution equation of this quantity to take into account the variations of volume with free-surface movements. A careful evaluation of this equation in increasingly complex and realistic flow conditions proves that this term cannot be neglected, highlighting its importance when evaluating mixing with sufficient accuracy.

Key words : numerical simulation, Strait of Gibraltar, solitary waves, oceanic fine-scales, large eddy simulation, diapycnal mixing

Exploration des fines échelles océaniques dans le détroit de Gibraltar : simulation numérique, observation et mélange induit

Thèse préparée par **Margaux HILT**
sous la direction de **Francis AUCLAIR** et **Franck DUMAS**
Thèse soutenue le **8 mars 2022** à Toulouse

Cette thèse se focalise sur la région du spectre océanique dit des *fines échelles*, s'étendant des processus de sous-mésoéchelles jusqu'aux grandes structures turbulentes qui amorcent la cascade de Richardson directe menant elle-même au mélange moléculaire. C'est ce mélange, processus irréversible, qui fixe les propriétés des masses d'eaux circulant dans les bassins océaniques. Si la cascade directe est plutôt bien décrite depuis les travaux de Kolmogorov (1941), les instabilités qui l'amorcent dans l'océan sont peu observées et encore moins simulées, le domaine des fines échelles constitue en quelque sorte une « Terra Incognita » (Scotti, 2010).

L'amélioration des performances des moyens de calcul et des modèles numériques, couplés à de nouveaux algorithmes, permettent néanmoins désormais d'aborder la simulation des grandes structures turbulentes et donc d'étudier cette *Terra Incognita*. Une exploration originale de la fine échelle est proposée dans la région du détroit de Gibraltar qui relie la mer Méditerranée à l'océan Atlantique. Là, se rencontrent des masses d'eaux de densités très différentes au-dessus d'un relief accidenté et relativement peu profond où l'amplitude de la marée est non-négligeable. Des processus de fine échelle émergent de l'interaction de ces éléments dans le détroit, rythmé par le cycle de la marée semi-diurne : un contrôle hydraulique du flux dans le détroit évolue au cours du cycle de marée, entraînant la formation puis la relaxation d'un ressaut hydraulique interne. Lorsqu'il est en place, ce ressaut amplifie le mélange lié aux instabilités de cisaillement dans la veine méditerranéenne, et sa relaxation marque le début de la propagation d'un train d'ondes internes solitaires vers la mer Méditerranée.

Propagation des trains de solitons et instabilités de cisaillement dans le détroit de Gibraltar ont été étudiés pendant cette thèse par la simulation numérique, mais aussi au cours d'une campagne d'observation dédiée.

La simulation des fines échelles dans le détroit est rendue possible grâce au développement original du coeur non-hydrostatique, compressible et à toit libre du code CROCO, présenté dans le chapitre 2 de ce manuscrit.

La simulation régionale du détroit est ensuite abordée en deux temps : tout d'abord est élaborée une configuration 2D verticale qui permet d'évaluer les paramètres numériques à un faible coût numérique avec une dynamique correcte à l'échelle de la marée. Cette méthodologie est ensuite appliquée à une configuration 3D réaliste qui constitue une LES océanique originale. Cette maquette a été utilisée pour étudier la variabilité du lien entre forçage de marée, évolution du contrôle hydraulique, et intensité du mélange au cours du cycle mortes-eaux vives-eaux. En effet, les grandes structures turbulentes, simulées explicitement, ont été localisées au niveau des seuils, et une intensification de leur génération est observée en période de vives-eaux. La propagation des trains d'ondes solitaires, quant à elle, est mise en relation avec des observations de mouillage, et révèle un mécanisme secondaire de génération des ondes internes de grande amplitude dans le détroit lors des mortes-eaux.

Une étude de sensibilité des grandes structures turbulentes et, par rétroaction, des caractéristiques des masses d'eaux à la fermeture sous-maille est aussi proposée.

Le dernier chapitre aborde la question de la quantification du mélange diapycnal en se basant sur l'évolution de l'énergie potentielle. Un nouveau terme a été ajouté au bilan de cette quantité pour prendre en compte l'évolution du volume avec les mouvements de la surface libre. L'application a des cas tests de complexité et de réalisme croissants montre que ce terme est non-négligeable, sa prise en compte permettant de proposer une évaluation précise du mélange turbulent.

Mots-clés : simulation numérique, Détroit de Gibraltar, solitons, fine échelle océanique, simulation des grandes structures turbulentes, mélange diapycnal

---

Laboratoire d'Aérologie - Observatoire Midi-Pyrénées
14 avenue Édouard Belin, 31400 Toulouse, FRANCE